Discovery and Characterisation of Gravitationally Lensed Quasars in Wide-field Surveys

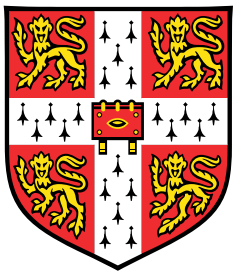

CAMERON LEMON

Supervisors:
RICHARD MCMAHON
and
MATTHEW AUGER

Institute of Astronomy
University of Cambridge

This dissertation is submitted for the degree of
Doctor of Philosophy

Corpus Christi College May 2019

Declaration

This dissertation is the result of my own work and includes nothing which is the outcome of work done in collaboration except as declared in the Preface and specified in the text. It is not substantially the same as any that I have submitted, or, is being concurrently submitted for a degree or diploma or other qualification at the University of Cambridge or any other University or similar institution. It does not exceed 60,000 words, including abstract, tables, footnotes and appendices.

CAMERON LEMON
May 2019

Acknowledgements

I am immensely grateful to both my supervisors, Richard McMahon and Matt Auger. Thank you for your patience. I appreciated every email, office visit, and tea-time conversation. I'd also like to thank Fernanda Ostrovski, Sophie Reed, and Lindsay Oldham for their generous support throughout my PhD. Thank you to everyone at the IoA for always being supportive and keen to help me with my research. Special thanks go to Manda Banerji, Elmé Breedt, Paul Hewett, and Sergey Koposov. Outside of the IoA, I am thankful to everyone I've met through the STRIDES collaboration for their thoughts, motivation, and help over the past few years. In particular, I'd like to thank Paul Schechter for his time and advice.

Thank you to all my officemates and other students for making time in the office enjoyable every day. I'd particularly like to thank Andrew, Aneesh, and Pablo, for all the great times inside and outside the office.

Finally, thank you to my parents, my sisters, my grandma, and Elisabeth for all the unconditional love and support you've given me. I have you all to thank for where I am today.

Abstract

The coincident alignment of two galaxies on the sky can create the rare cosmic phenomenon of strong gravitational lensing, in which light from the more distant galaxy is bent around the foreground galaxy to create multiple, distorted, and magnified images. When the background galaxy hosts a bright active galactic nucleus, a quasar, the system becomes a probe of accretion disk physics, quasar-host galaxy relations, the Hubble constant, the stellar IMF, smooth matter fractions, amongst many other applications.

It has been 40 years since the discovery of the first gravitationally lensed quasar, and dedicated spectroscopic and imaging surveys have added over one hundred new systems to this list. In recent years, the amount of available data across the whole-sky has grown exponentially. Full-sky data from X-ray to radio wavelengths exist, and predictions suggest there are many bright lensed quasars hidden in these datasets. This thesis presents several new techniques to mine these rare systems from whole-sky photometric datasets.

We use the excellent resolving ability of *Gaia*, coupled with other wide-field surveys such as the Dark Energy Survey (DES), Pan-STARRS, and WISE, and present spectroscopic follow-up from the WHT, NTT, and Keck. By looking for multiple *Gaia* detections around photometric quasar candidates, and single *Gaia* detections near morphological galaxies, we have discovered 105 new lensed quasars. We also present a search based on significant offsets in astrometry and flux between *Gaia* and SDSS for spectroscopic quasars, suggesting several promising small-separation lens candidates. We characterise the confirmed systems based on ground-based imaging and the spatially resolved spectra, and comment on the purity, efficiency, and biases in our selection. DES data provides multi-epoch photometry over the baseline of years at optical wavelengths, allowing a colour-independent selection of lensed quasars by looking for nearby variable pairs. We create a parametric modelling pipeline of the DES images to extract lightcurves of system components, and show that it is a highly effective way to remove quasar and star projections before spectroscopic follow-up. We demonstrate that future searches based on detecting variability in multiple images will be biased towards four-image lensed quasars.

Table of contents

List of figures **xiii**

List of tables **xvii**

1 Introduction **1**
1.1 Quasars . . . 1
1.2 Gravitational Lensing . . . 2
1.2.1 Lensing Formalism . . . 3
1.2.2 Applications of Lensing . . . 6
1.3 Lensed Quasar Discovery Surveys . . . 9
1.3.1 HST snapshot surveys . . . 9
1.3.2 CLASS/JVAS . . . 10
1.3.3 SQLS/BQLS . . . 10
1.3.4 MUSCLES . . . 11
1.3.5 STRIDES . . . 11
1.3.6 Other search techniques . . . 11
1.4 Wide-field Surveys . . . 12
1.4.1 Pan-STARRS . . . 12
1.4.2 DES . . . 13
1.4.3 *Gaia* . . . 15
1.4.4 WISE . . . 18
1.5 Predictions . . . 19
1.6 Thesis Outline . . . 23

2 Lensed Quasars from *Gaia* Data Release 1 **25**
2.1 Known Lensed Quasars in GDR1 . . . 25
2.2 Pan-STARRS . . . 27
2.2.1 Photometric quasar candidate catalogues . . . 27

2.2.2 Morphology Selection . . . 28
2.2.3 Final Lens Candidate Catalogue . . . 29
2.2.4 Observations . . . 31
2.2.5 Results . . . 31
2.2.6 Pan-STARRS Modelling . . . 32
2.3 DES . . . 36
2.3.1 Selection . . . 39
2.3.2 Spectroscopy . . . 41
2.3.3 High resolution imaging . . . 41
2.3.4 DES Modelling . . . 46
2.4 Notes on individual systems . . . 46
2.5 Discussion . . . 63
2.5.1 Recovering Known Lenses . . . 63
2.5.2 Comparison to Simulated Lenses . . . 64
2.6 Conclusions . . . 69

3 Resolving Small-separation Lensed Quasars 71
3.1 Close pairs in *Gaia* . . . 71
3.2 A sample of small-separation lensed quasars . . . 72
3.3 Finding quasar lenses in *Gaia* . . . 75
3.3.1 Multiple *Gaia* detections . . . 75
3.3.2 Single *Gaia* detections . . . 76
3.4 Lens candidate selection . . . 82
3.4.1 Multiple detections . . . 84
3.4.2 Single detections . . . 84
3.5 Conclusions . . . 88

4 Lensed Quasars from *Gaia* Data Release 2 89
4.1 *Gaia* DR2 data . . . 90
4.1.1 Detection Rate . . . 90
4.1.2 Proper Motions . . . 91
4.1.3 Astrometric Excess Noise . . . 93
4.1.4 Removing crowded regions . . . 93
4.2 Lens Selection . . . 95
4.2.1 Multiple *Gaia* detections around quasar catalogues . . . 95
4.2.2 Modelling unWISE pixels . . . 96
4.2.3 LRGs with *Gaia* detections . . . 98

4.2.4 Multiple *Chandra* detections . . . 101
4.2.5 Final candidate selection . . . 101
4.3 Results . . . 102
4.3.1 Modelling . . . 102
4.3.2 Notes on Individual Systems . . . 112
4.4 Discussion . . . 132
4.5 Conclusions . . . 134

5 Variability from DES **139**
5.1 A photometry pipeline for lensed quasars . . . 140
5.2 Example Application: ULASJ2343-0050 . . . 142
5.3 Variability of DES systems . . . 146
5.3.1 Removing stellar contaminants . . . 146
5.3.2 J0235-2433 . . . 150
5.3.3 Nearly Identical Quasar Pairs . . . 150
5.4 Variability Selection Bias . . . 152
5.5 Conclusions . . . 155

6 Discussion and Conclusions **157**
6.1 Comparison to Known Lenses . . . 157
6.2 Comparison to Mock Lenses . . . 161
6.3 Prospects for Future Searches . . . 165
6.3.1 *Gaia* . . . 165
6.3.2 Variability . . . 166
6.3.3 Machine Learning . . . 166
6.3.4 Other Datasets . . . 167

References **169**

Appendix A Lens Photometry and Astrometry **183**

Appendix B Inconclusive/Contaminant Systems **191**

List of figures

1.1 Schematic of strong gravitational lensing 4
1.2 Caustics, critical curves, and images for various source positions 5
1.3 Microlensing caustics, critical curves, and images 8
1.4 Pan-STARRS and Dark Energy Survey *grizY* filters. 13
1.5 Dark Energy Survey footprint 14
1.6 *Gaia* CCD schematic 16
1.7 *Gaia* G, BP, and RP bandpasses 17
1.8 G–W1 vs W1–W2 for galaxies, quasars, and stars 19
1.9 Predictions for number of lensed quasars in Pan-STARRS, DES, and *Gaia* against image separation 21
1.10 Full sky predictions for number of lensed quasars against magnitude 22
1.11 Magnitude of combined quasar images against lensing galaxy magnitude in the I-band for the OM10 mock catalogue 24

2.1 Pan-STARRS *gri* colour images of Pan-STARRS-selected lensed quasars . 31
2.2 Spectra of Pan-STARRS-selected lensed quasars 34
2.3 Pan-STARRS *gri* colour images of Pan-STARRS selected NIQs 36
2.4 Spectra of NIQs and binaries from Pan-STARRS selection 39
2.5 Model subtractions of Pan-STARRS-selected lensed quasars 40
2.6 Spectra of DES-selected lensed quasars 42
2.7 DES *gri* colour images of DES-selected lensed quasars 43
2.8 Spectra of NIQs from DES selection 44
2.9 NIRC2 AO data and model subtractions for DESJ0245-0556, DESJ0246-1845, and DESJ0340-2425 45
2.10 SOAR data and model subtractions for DESJ0053-2012, DEJ0150-4041, DESJ0407-1931, DESJ0501-4118, and DESJ0600-4649. 47
2.11 PSJ0030-1525 VST data and model subtractions 48

2.12 NIRC2 AO data for PSJ0140+4107, PSJ0417+3325, PSJ0840+3550, and PSJ0949+4208 50
2.13 NIRC2 AO data and model subtractions for PSJ0630-1201 52
2.14 CFHT *ugr* data and model subtractions for PSJ0941+0518 55
2.15 Caustics and critical curves of the best-fit mass model for DESJ0053-2012 . 57
2.16 DES stacked *gri* data and model subtractions for DESJ0112-1650 58
2.17 VLASS image of DESJ0340–2545 with *Gaia* detections overlaid 61
2.18 NTT spectrum of the lensing galaxy of DESJ0407-1931 62
2.19 DES stacked *gri* data and model subtractions for DESJ2349–4518 62
2.20 Source redshift distribution for *Gaia* DR1-selected lensed quasars 64
2.21 Image separation distribution for *Gaia* DR1-selected lensed quasars 65
2.22 W1 against W1–W2 for all known lenses with at least one *Gaia* detection . 66
2.23 Fainter image magnitude against lensing galaxy magnitude for *Gaia* DR1-selected lensed quasars 67
2.24 Combined image magnitude against lensing galaxy magnitude for *Gaia* DR1-selected lensed quasars 68

3.1 Predicted number of lensed quasars with one or multiple *Gaia* detections against image separation, and measured detection separation distribution in *Gaia* DR1 73
3.2 Known lensed quasars with separations smaller than 2" and multiple *Gaia* DR1 detections 74
3.3 *Gaia* G against astrometric excess noise for galaxies, quasars, stars, and lensed quasars 77
3.4 Synthesised G from SDSS photometry minus *Gaia* G against redshift for spectroscopic quasars 80
3.5 Flux deficit and astrometric offset for lensed quasars and SDSS spectroscopic quasars 83
3.6 SDSS and CFHT/HSC cutouts for small-separation lensed quasar candidates 86
3.7 SDSS and CFHT/HSC/Pan-STARRS cutouts for contaminant systems from the flux deficit/astrometric offset search 86
3.8 KiDS *ugr* data and model subtractions for the lensed quasar candidate SDSSJ1359+0128 87

4.1 Histogram of pair separations for *Gaia* DR1 and DR2 91
4.2 Proper motion significances for stars, quasars, and lensed quasar images . . 92

4.3 *Gaia* G against astrometric excess noise for spectroscopic stars, galaxies, quasars, and known lensed quasar images in *Gaia* DR2 94
4.4 ALLWISE catalogue detection rate of Milliquas quasars against Pan-STARRS *i*-band magnitude 96
4.5 Modelled G–W1 against W1–W2 for components of quasar+star pairs and lensed quasars 99
4.6 unWISE modelled pixels for PSJ0028+0631, PSJ2145+6345, and ULASJ2343-0050 100
4.7 Spectra of *Gaia* DR2-selected lensed quasars and quasar pairs 103
4.8 Pan-STARRS *gri* colour images and *Gaia* detections for *Gaia* DR2-selected lensed quasar candidates 110
4.9 Pan-STARRS *gri* data and model subtractions of *Gaia* DR2 confirmed lensed quasars 113
4.10 BOSS spectrum and model subtraction for J0203+1612 118
4.11 Pan-STARRS *riz* data and model subtractions for J0607-2152 120
4.12 Caustics and critical curves of the best-fit mass model for J0607–2152 . . . 120
4.13 Pan-STARRS *riz* data and model subtractions for J0608+4229 121
4.14 Caustics and critical curves of the best-fit mass model for J0608+4229 . . . 121
4.15 Caustics and critical curves of the best-fit mass model for J0659+1629 . . . 122
4.16 CFHT *r*-band data and PSF subtraction for J0803+3908 123
4.17 Pan-STARRS and VHS data and model subtractions for J0818–2613 124
4.18 Caustics and critical curves of the best-fit mass model for J0818–2613 . . . 125
4.19 SDSS spectrum and model subtraction for J1003+0651 127
4.20 *Chandra* imaging and DECaLS *grz* data and model subtraction for J1307+0642 128
4.21 Predicted cumulative number of lensed quasars as a function of lens galaxy *i*-band magnitude 129
4.22 *gi* HSC data and model subtractions for J2350+3654 133
4.23 Lensing galaxy *i*-band magnitude against source redshift for *Gaia*-DR2 selected lensed quasars 135
4.24 Image separation against source redshift for known lensed quasars 137
4.25 Discovery rate of lensed quasars from 1979 to 2019 138

5.1 DES single-epoch images of ULASJ2343-0050 143
5.2 Example field for PSF selection in the field of ULASJ2343-0050 143
5.3 Best-seeing *grizY* data and models for ULASJ2343-0050 144
5.4 Stacked *grizY* data and models for ULASJ2343-0050 145
5.5 *g*- and *r*-band lightcurves for ULASJ2343-0050 145

5.6 DES z-band lightcurves for a quasar+star system 147
5.7 DES i-band lightcurves for the lensed quasar DESJ0150-4041 148
5.8 Variability measure from the average reduced χ^2 for individual components of lensed quasars, NIQs, and quasar+star projections 149
5.9 DES Y-band lightcurves for the lensed quasar PSJ0235-2433 151
5.10 DES i-band lightcurves for J0229+0320 152
5.11 Predicted numbers of quads and doubles to be discovered through variability from DES i-band single-epoch imaging 154

6.1 Image separation against separation for our sample of *Gaia*-selected lensed quasars and all other lensed quasars 158
6.2 Image separation against lensing galaxy magnitude for the OM10 mock catalogue 159
6.3 Brightest image *Gaia* G magnitude against source redshift for our *Gaia*-selected lensed quasars and all other lensed quasars 160
6.4 Image separation against source redshift for doubles with image separations between 1" and 4" and multiple *Gaia* detections 162
6.5 Image separation against source redshift for quads with image separations between 1" and 4" and at least three *Gaia* detections 163
6.6 Second brightest *Gaia* magnitude against first brightest for known lensed quasars 164
6.7 Examples of visually similar contaminant systems and lensed quasars . . . 168

List of tables

1.1 Pan-STARRS 3π survey details 13
1.2 DES data release 1 details 14
1.3 WISE bandpasses and survey details 18
1.4 Predicted numbers of lensed quasar in *Gaia*, DES, and Pan-STARRS 20

2.1 *Gaia* DR1 detections for known lensed quasars 26
2.2 Number of remaining candidates during Pan-STARRS selection process . . 30
2.3 Observation details of Pan-STARRS-selected candidates 33
2.4 Mass model parameters for Pan-STARRS-selected lensed quasars. 37
2.5 Characteristics of Pan-STARRS-selected lensed quasars 38
2.6 Summary of NIQs and binaries from Pan-STARRS selection 38
2.7 Observation details for DES-selected lensed quasars 41
2.8 Summary of NIQs and quasar pairs from DES selection 46
2.9 Mass model parameters for DES-selected lensed quasars 48
2.10 Galaxy light and mass shape parameters for PSJ0630-1201 53
2.11 Predicted time delays for the image pairs in PSJ0630-1201 54
2.12 DESJ0340-2545 image and galaxy parameters 60
2.13 Summary of DESJ0340–2545 mass models 61
2.14 Numbers of known lensed quasars with multiple detections in *Gaia* DR1 . . 63

3.1 Properties of the small-separation known lensed quasars with multiple *Gaia* DR1 detections 74
3.2 Details of new lensed quasars candidates and contaminant systems 87

4.1 Summary of *Gaia* DR1 and DR2 datasets 89
4.2 Number of *Gaia* detections for known lensed quasars in *Gaia* DR1 and DR2 90
4.3 Number of candidates and selection criteria for *Gaia* DR2 selection methods 101
4.4 Observation details for spectroscopic follow-up of *Gaia* DR2-selected lensed quasar candidates 111

4.5 Mass model parameters for *Gaia* DR2-selected lensed quasars 117

5.1 Astrometry and photometry for ULASJ2343-0050 144

A.1 Pan-STARRS astrometry and photometry of the *Gaia* DR1+Pan-STARRS-selected lensed quasars 184
A.2 Astrometry and photometry of *Gaia* DR1+DES-selected lensed quasars . . 186
A.3 Pan-STARRS astrometry and photometry of *Gaia* DR2+Pan-STARRS-selected lensed quasars. Magnitudes are in the AB sytem. 187

B.1 Inconclusive DES-selected candidates. 191
B.2 Spectroscopically confirmed DES contaminant systems. 191

Chapter 1

Introduction

1.1 Quasars

In the early 1960s, advances in positional localisation of radio sources from the Third Cambridge Catalogue (e.g., Hazard et al., 1963; Matthews and Sandage, 1963) led to blue optical counterparts to several radio objects – a surprising discovery as stars were thought to be particularly weak radio emitters. Spectra of these objects showed unusual broad emission lines, which were found to be coincidental with lines from the hydrogen Balmer series, but redshifted by considerable fractions of the speed of light – 16% and 37% for the first reported cases, 3C273 and 3C48 (Greenstein, 1963; Schmidt, 1963). It was immediately considered that these redshifts were associated with the Hubble expansion and extremely luminous sources (Schmidt, 1963). Lynden-Bell (1969) proposed that the brightness and compactness of quasars was due to accretion onto supermassive black holes, building on the work of Salpeter (1964). This scenario permitted an efficient release of material's rest mass energy as light–up to 40%, compared to nuclear fusion, which is $<$1%. This picture was quickly favoured over the non-cosmological theories such as ejection of quasars by nearby galaxies (e.g., Burbidge and Burbidge, 1967) or screening of atomic nuclei (Cowan, 1968). Observations of quasars over the following decades revealed subsets with different optical, radio, and high-energy characteristics. These objects collectively became known as Active Galactic Nuclei (AGN). Different classifications include Type-1 and Type-2 AGN, Broad Absorption Line quasars (BALs), LINERS, BL Lacs, Flat Spectrum and Steep Spectrum Radio Quasars, Radio Loud and Radio Quiet quasars, blazars, etc. (see, e.g., Padovani et al. (2017) for a comprehensive review of quasar varieties).

This diversity has been largely attributed to different viewing angles of AGN, all with similar geometry (Urry and Padovani, 1995). This picture consists of an accretion disc feeding the supermassive black hole, surrounded by a Broad Line Region, and a thick dusty

torus beyond this (Shakura and Sunyaev, 1973). There also exists a Narrow Line Region, but the details of the dynamics and locations of all these components is still an active area for research (e.g., Borguet and Hutsemékers, 2010).

Quasars play a vital role in our current understanding of the universe, from shaping a galaxy's evolution through feedback (e.g., Fabian, 2012), to probing the earliest epochs of the Universe (e.g., Fan et al., 2019). This thesis concerns the discovery of a very rare population of quasars, not with specific intrinsic properties, but those that are multiply imaged by foreground galaxies.

1.2 Gravitational Lensing

The deflection of light due to mass was considered by Newton in 1704, though the first published calculations were due to Soldner (1801) who considered the bending of light grazing the surface of the Sun using classical mechanics. In 1911, Einstein derived the same value for this deflection angle using the equivalence principle alone. Upon formulating General Relativity and properly accounting for spacetime curvature, Einstein found that the angle of deflection was actually twice the classical value. For a point source mass M, a distance of closest approach b, the speed of light c, and Newton's gravitational constant G, the deflection angle is:

$$\alpha = \frac{4GM}{bc^2} \tag{1.1}$$

This prediction was famously tested and verified in 1919 by Eddington and collaborators by measuring the displacement of stars near the Sun during a solar eclipse. Predictions from General Relativity are in agreement with the most precise measurements made today (e.g., Abbott et al., 2016). Einstein's theory still stands as our best description of gravity.

The possibility of multiple paths from source to observer, and thus observation of multiple images, was discussed by Chwolson (1924) and Einstein (1936), and the effect was concluded to be unobservable with a star acting as the lens. However, Zwicky (1937) soon suggested that galaxies and galaxy clusters could act as gravitational lenses, commenting that "some of the massive and more concentrated nebulae may be expected to deflect light by as much as half a minute of arc". Over 40 years later, the first gravitational lens was discovered. During observations to identify optical counterparts to radio sources, Walsh et al. (1979) discovered a pair of quasars, separated by 6.2 arcseconds, with identical spectra at a redshift of z=1.41. This system, Q0957+561, also known as the Twin Quasar, was suggested to be a gravitational lens, with the lensing galaxy being detected soon after at a redshift of z=0.36, thus confirming this interpretation (Stockton, 1980; Young et al., 1980). The following

year, the first quadruply-imaged lensed quasar was discovered, PG1115+080 (Weymann et al., 1980), and several more lenses were serendipitously discovered over the next decade. Targeted surveys were set up by the 1990s, and at the time of writing, more than 300 gravitationally lensed quasars are now known. To describe the specifics of such surveys and the lensed quasars, we will first need to review the basic formalism of gravitational lensing.

1.2.1 Lensing Formalism

Understanding the theory and mechanisms behind lensing is key to performing useful science with such systems. In what follows we outline the basic theory of gravitational lensing and how it may be applied to derive parameters such as lensing mass and the Hubble constant.

Figure 1.1 shows a basic lensing schematic for one lightray from source to observer. The lens causes a deflection of the light by an angle $\hat{\alpha}$, causing a source to be viewed at an angle θ for the observer, when it actually subtends an angle β. The angular diameter distances, D_L, D_S and D_{LS} are from observer to lens, observer to source and lens to source respectively. Note that the latter is not necessarily equal to the sum of the first two depending on the cosmology. These angles are geometrically related by the lens equation, equation 1.2, where $\hat{\alpha}$ depends on θ as the deflection depends on the impact parameter, $\xi = D_L\theta$.

$$\beta = \theta - \frac{D_{LS}}{D_S}\hat{\alpha}(\theta) \tag{1.2}$$

This encodes how the source position, β, is connected to the image position, θ. The physics of the lensing potential is described by $\hat{\alpha}$.

For very simple mass distributions, the deflection angle can be calculated analytically. For example, equation 1.1 is the deflection for a point mass lens. If this mass were to lens a coaxial source, we would expect a circular image of the source — an Einstein ring — with angular radius $\theta_E = \left(\frac{4GM}{c^2 D}\right)^{1/2}$ where $D = \frac{D_L D_S}{D_{LS}}$. In reality, lenses are extended in three dimensions and the full deflection angle can be found numerically by integrating the Green's function solution from equation 1.1 weighted by the mass density at each point in the lens. Since the lens is much thinner than the relevant source-lens-observer distances, the thin lens approximation can be applied, reducing the deflection angle to a two dimensional integral of the projected surface density weighted by the Green's function.

Axisymmetric projected mass densities will always produce two images (and perhaps a demagnified third central image) of a small background source, however an asymmetry caused by an elliptical mass distribution or external perturbation allows 2 further images for certain source positions. For such lenses, there are two curves in the image plane, called critical curves, at which the magnification formally becomes infinite. Objects lying on the

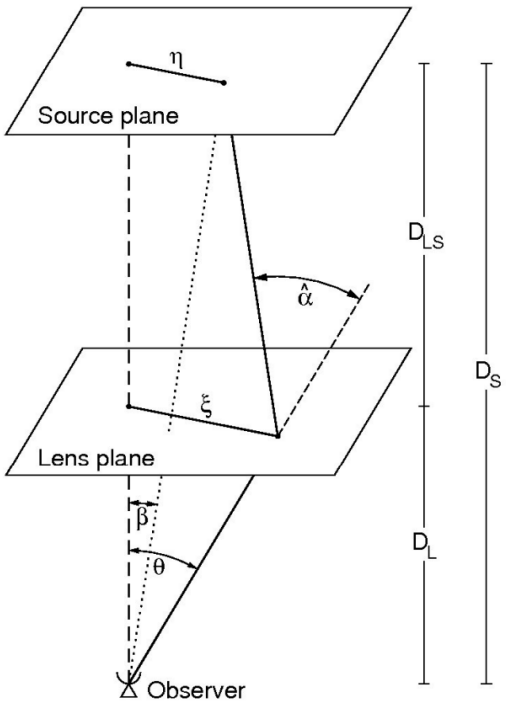

Fig. 1.1 A schematic of strong lensing of a source by a lens. Parameters are defined in the text. Figure taken from Bartelmann and Schneider (2001).

inner (outer) critical curve are stretched radially (tangentially). These curves can naturally be traced back to the source plane to find where images must lie for maximum magnification. The inner (outer) critical curve maps to the outer (inner) source plane caustic. Burke (1981) showed that lenses with smooth surface mass densities always produce an odd number of images. However, one image is a central image that is strongly demagnified, often leading to just two or four observable images, hereafter doubles and quads. The caustics have the property of dividing the source plane according to the number of observed images; crossing a caustic will always change the number of images by 2. Figure 1.2 shows the source plane caustics for a typical lensing potential, with the corresponding images and critical curves for different source positions.

Since many lenses have four images, axisymmetric lens models are not sufficient to model such systems. Throughout this thesis, we will use a simple elliptical mass distribution, the singular isothermal ellipsoid (SIE) (Kormann et al., 1994), which has the benefit of having only 3 free parameters yet still being able to reproduce simple lensing observables (Keeton et al., 1998). The density profile for a SIE is given in equation 1.3 and the Einstein radius for a Singular Isothermal Sphere (SIS) in equation 1.4.

$$\rho\,(x,y) = \frac{\sigma^2}{2\pi G\,(x^2 + y^2/q^2)} \tag{1.3}$$

$$\theta_E = 4\pi\left(\frac{\sigma}{c}\right)^2 \frac{D_{LS}}{D_S} \tag{1.4}$$

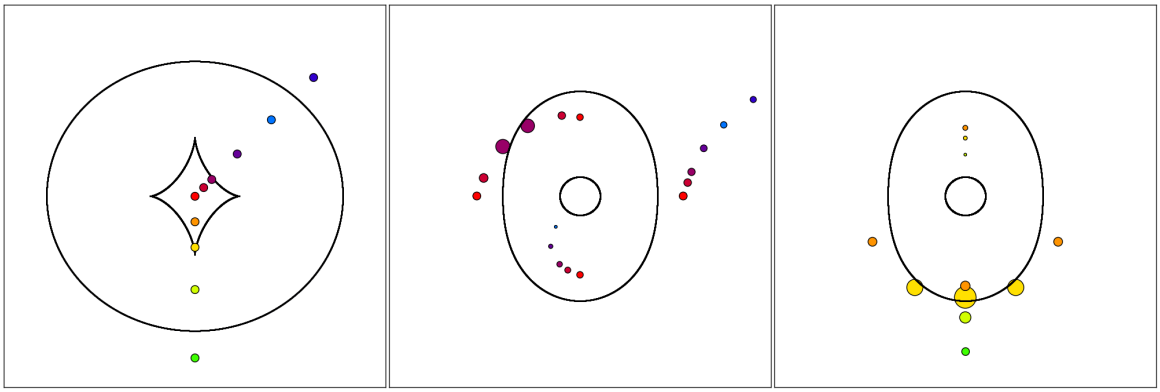

Fig. 1.2 How different source positions (left) create different images depending on their position relative to the source plane caustics, separated into sources towards the fold of the inner caustic (middle), and towards a cusp of the inner caustic (right).

The time delay of an image relative to the unlensed source can be calculated as a combination of the geometric path difference and potential time delay, known as the Shapiro time delay. Equation 1.5 shows how a time delay may be calculated from a lensing potential, $\psi(\theta)$. Since the angular diameter distances depend on cosmological parameters, measuring relative time delays is a method to determine these parameters, with particular sensitivity to the Hubble constant.

$$\Delta t(\theta,\beta) = \frac{D_L D_S}{D_{LS}}(1+z_L)\left[\frac{(\theta-\beta)^2}{2} - \psi(\theta)\right] \tag{1.5}$$

An application of Fermat's principle of extremal time delays reproduces the lens equation (equation 1.2), with images forming at maxima, minima, and saddle points of the time delay surface.

Solving the lens equation for image positions in two dimensions is difficult due to the general non-linearity in θ. Throughout this thesis, we will use two sets of software to solve the lens equation for a variety of different mass models: (i) LENSMODEL (Keeton, 2001), and (ii) a Python-based deflection calculation module including a lens equation solver. We often use both sets of software as a consistency check, but each has its own advantages. The former is used for plotting critical curves and caustics, while the latter is used for all statistical sampling methods.

1.2.2 Applications of Lensing

We will briefly discuss several ways lensed quasars have been used to probe astrophysics and cosmology. For more in-depth reviews of these topics, see, e.g., Courbin et al. (2002), Jackson (2013), and Treu and Ellis (2015). The motivation behind the work presented in this thesis is to build a larger sample of known lensed quasars. Before the release of the datasets used in this thesis, only $\sim$150 lensed quasars were known, limiting the power of the following science cases.

Magnification of Distant Sources

To understand galaxy evolution and cosmology, we must make observations of the high-redshift universe, but this requires high-resolution instruments and large photon collecting area or long exposures. While this can be possible with radio interferometry, or 10m-class telescopes with adaptive optics, gravitational lensing offers a way to push observations to yet higher signal-to-noise and resolution. We provide just three examples of how gravitational lensing has helped our understanding of astrophysics. At X-ray wavelengths, Reis et al. (2014) used the $\approx$50 times magnification of the quadruply imaged lensed quasar in RXJ1131-1231 to collect the signal-to-noise to measure the spin of a supermassive black hole at z=0.66 (Sluse et al., 2003). At radio wavelengths, Hartley et al. (2019) used VLBI observations of the quadruply imaged lensed quasar, HS0810+2554, to probe 0.27 parsec scales at z=1.51 and reveal jets in a sub-micro-Jansky radio-quiet quasar. Finally, Ding et al. (2017) have used *HST* imaging of lensed quasars and their host galaxies to study quasar-host galaxy relations out to $z \sim$4.5, showing black hole growth likely predates the growth of the host galaxy.

Time Delay Cosmography

It was first discussed by Refsdal (1964) that the time delay from equation 1.5 can be measured for a variable source and provides a way of measuring the Hubble constant. Refsdal originally proposed that the sources be supernovae, yet the following decades revealed that lensed quasars were more plentiful and applicable to this time delay measurement. Early measurements of time delays were difficult due to seasonal gaps, long time delays, and microlensing. Even after such measurements were robustly made by the late 1990s (e.g., Kundić et al., 1997; Schechter et al., 1997), lens model degeneracies caused large systematic uncertainties in inferring the Hubble constant. These degeneracies include a mass-sheet degeneracy (Falco et al., 1985), which allows a family of solutions to fit the data, each with different predicted time delays. To overcome these problems, recent analyses by H0LiCOW have included constraints from the lensed quasar host galaxy (Suyu et al., 2017)

and characterisation of galaxies along the line-of-sight matched to simulations (e.g., Sluse et al., 2017). Detailed modelling of just four gravitationally lensed quasars has yielded a measurement of the Hubble constant to 3% (Birrer et al., 2019; Bonvin et al., 2018), agreeing with local distance ladder measurements based on Type Ia Supernovae.

Blinded time delay measurements of mock LSST lightcurves imply that LSST will provide 400 robust time delays for lensed quasars by 2030 (Liao et al., 2015), albeit with less ancillary data than for current time delay lenses. Linder (2011) has predicted that just 150 time delay lenses can offer significant complementarity to other cosmological probes, possibly improving the dark energy figure of merit by almost a factor 5.

Microlensing

Soon after the discovery of the first gravitational lens, Chang and Refsdal (1979, 1984) suggested that the brightness of lensed quasar images can be significantly affected by stars in the lensing galaxy. Gott (1981) suggested that this effect could be caused by compact dark matter, and hence be a probe to detect such objects, and this idea was later extended to within our galaxy (Paczynski, 1986). Due to the relative movement of the source, lens, and observer, these variations can last weeks to years at optical wavelengths and pose a nuisance signal when measuring time delays. However, as the brightness variations depend on the density of stars, dark matter fractions, and quasar accretion disc size-temperature profiles, it can be used as a probe to measure these astrophysical quantities. Figure 1.3 shows the caustic and critical curves associated with a collection of stars drawn from a Salpeter Initial Mass Function, and demonstrates that each star causes at least one additional splitting of the quasar image. This effect is called *microlensing*, since typical separations for the bright images is on the order of microarcseconds, and hence only the total brightness change can be observed (e.g., Irwin et al., 1989). However, since the quasar accretion disc has a size comparable to that of the star's Einstein radius, there can be a strong colour dependence of the microlensing signal (e.g., Mosquera et al., 2009). Through multi-wavelength measurements of lensed quasars, a consensus is now emerging that quasar accretion discs are larger than predicted by standard thin-disc models and have flatter temperature-radius profiles (e.g., Blackburne et al., 2011; Morgan et al., 2018).

The microlensing magnification distribution depends on the local stellar mass surface density; no stars will lead to no microlensing, while a very large stellar mass fraction will also look smooth as the stars begin to significantly overlap (e.g., Jiménez-Vicente et al., 2015). This sensitivity to the stellar mass density provides the only means of measuring stellar masses (rather than total mass) in unresolved stellar populations (e.g., Bate et al., 2011).

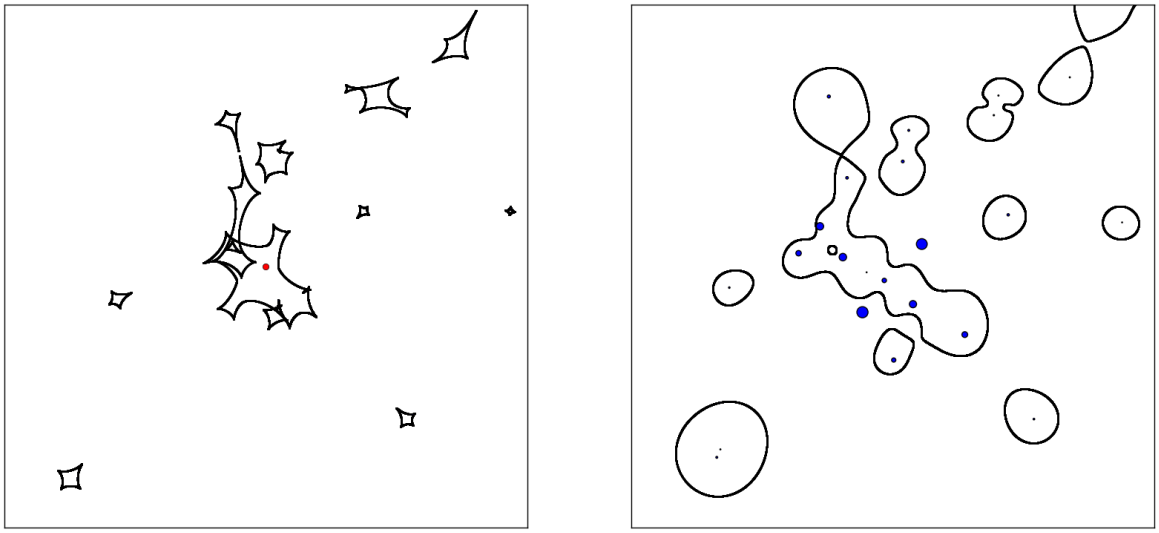

Fig. 1.3 An example of the effect of stars in the lensing galaxy on an individual macroimage of the lensed quasar. Left: caustic curves in the source plane, with the background quasar image overlaid in red. Right: critical curves in the image plane, with blue points representing the many images of the source quasar. The size of the microimages represents their flux. In this example, the already-magnified quasar image is further magnified by 53%.

A lensed quasar discovery project must keep in mind the effects of microlensing, for this can change the brightness ordering of images that smooth macromodels predict. Surprisingly, microlensing affects images differently depending on their order of arrival. Schechter and Wambsganss (2002) showed that typical values of dark matter fractions and magnifications can lead to saddle points being suppressed, i.e., expecting these images to be a magnitude fainter than for a smooth model half of the time. It is therefore important to understand which images are saddle points. We defer to Saha and Williams (2003) for a full description of saddle points in various lensed quasar configurations.

Dark Matter Substructure

Gravitational lensing is the most powerful technique for probing the mass structure of distant galaxies, where resolved stellar dynamics are currently not possible. Although several degeneracies exist in lens modelling, such as the mass-sheet degeneracy (Falco et al., 1985), robust measurements of total masses within the Einstein radius have been made, with a general consensus that mass profiles are well-fit by near-isothermal profiles (e.g., Auger et al., 2010). While such profiles fit the image positions of lensed quasars and their lensed host galaxies well (e.g., Suyu et al., 2009), the flux ratios of the quasar images can be discrepant from the model predictions. These discrepancies can be explained by microlensing at optical

wavelengths or variability over the time delay, however multi-epoch follow-up at radio wavelengths overcomes these systematics implying flux-ratio discrepancies can only be attributed to unmodelled substructure in the lensing galaxy (or along the line-of-sight). This provides a powerful method to test ΛCDM predictions at galaxy scales, and such flux-ratio anomalies have been discovered in several systems (e.g., Mao and Schneider, 1998). The number of lenses with radio-loud sources currently hinders these studies with lensed quasars, and careful consideration of the multiple smooth mass components is fully required to probe substructure (Hsueh et al., 2017).

Image Separation Statistics

The number of lensed quasars across the sky as a function of image separation depends strongly on the cosmology, the lensing galaxy mass and magnification functions, and the quasar luminosity function. This dependence allows the underlying galaxy evolution parameters and cosmological parameters to be probed, but the selection function of the lensed quasars must be well accounted for. Such efforts have been made using the CLASS and SQLS surveys (see Section 1.3), demonstrating no strong evolution in the number density or mass function with redshift (e.g., Chae and Mao, 2003). Oguri et al. (2012) used the SQLS sample to show that lensed quasars alone confirm the acceleration of cosmic expansion.

1.3 Lensed Quasar Discovery Surveys

This thesis is concerned with discovering new lensed quasars across the whole sky, so it is prudent to consider the previous efforts on this front.

1.3.1 HST snapshot surveys

The first attempt to discover a statistical sample of lensed quasars was made using the *Hubble Space Telescope* (*HST*) imaging of bright quasars above a redshift of 1 (Maoz et al., 1992, 1993a,b). 498 bright quasars were observed in the hope that the bias from gravitational lensing magnification would populate such a sample with lensed quasars, but no new instances of gravitational lensing were confirmed. Four previously known lensed quasars were in their original sample. Recently, *HST* has been imaging known quasars above redshift 6 (McGreer et al., 2013), because again these objects represent the brightest in the population and thus might contain lenses, but selection effects might be biasing this sample from containing lenses (Fan et al., 2019; Pacucci and Loeb, 2019).

1.3.2 CLASS/JVAS

Even though radio-loud quasars make up approximately 10% of all quasars, the first successful campaigns to discover large samples of lenses were done at radio wavelengths. At such wavelengths, the data are uniform in sensitivity and resolution and are not affected by contamination from bright lensing galaxies or contaminant systems including stars. The Cosmic Lens All-Sky Survey (CLASS) imaged over 13,500 sources at a resolution of 0.2" with the Very Large Array (VLA) at 8.4 GHz (Myers et al., 2003). Together with the $\sim$2,400 images from the Jodrell Bank VLA Astrometic Survey (JVAS) (King et al., 1999), the sample was inspected for systems with multiple components, and promising candidates were followed-up for higher resolution imaging with the Multi-Element Radio Linked Interferometer Network (MERLIN), and possibly also the Very Long Baseline Array (VLBA), each at 5GHz.

These efforts led to the discovery of 22 new lenses and a statistical sample of 13 lenses. A similar investigation with the VLA in the Southern hemisphere uncovered 4 further radio-loud lensed quasars (e.g., Winn et al., 2002).

1.3.3 SQLS/BQLS

With the advent of large format CCD arrays, the Sloan Digital Sky Survey (SDSS) imaged over 14,500 square degrees of the Northern Sky using a 2.5m optical telescope from New Mexico, USA. A spectrograph on the same telescope has taken over 4 million spectra to-date, including 2,541,424 galaxy spectra, and 680,843 quasar spectra. This spectroscopic survey of quasars allowed a wide-area search for lensed quasars, called the SDSS Quasar Lens Search (SQLS), extending the sources beyond just radio-loud quasars. Furthermore, since the spectroscopic pre-selection was based on *ugriz* imaging, the selection effects could be accounted for, and hence represent a statistical sample of lensed quasars. SQLS targeted low-redshift ($0.6<z<2.2$) quasars brighter than i=19.1 from DR3, DR5, and DR7 (Oguri et al., 2006). Of the 50,836 quasars passing these criteria, deeper imaging and/or spectroscopic follow-up was given to objects passing a colour and/or morphological selection. The colour selection (340 candidates) required the SDSS pipeline to catalogue multiple components each with similar *ugriz* colours. The morphological selection (187 candidates) required a system to be inconsistent with a Point Spread Function (PSF), via the pipeline *star_L* parameter, followed by a fit of two PSF components to the SDSS images rejecting those with large flux ratios or small separations.

26 lensed quasars made up the final statistical sample, although other looser search criteria revealed a total of 62 lensed quasars within the SDSS spectroscopic quasar sample, including 13 previously known lenses. We note that colour selection of the original quasar

catalogue means that lensed quasars at high redshift, or those with bright lensing galaxies, are likely to have been missed by this search.

Since SDSS switched to only taking spectra after 2009, the number of higher redshift quasars rapidly increased, due to a targeted campaign by the Baryon Oscillation Spectroscopic Survey (BOSS). More et al. (2016) presented the first results from the BOSS quasar lens search (BQLS), using similar techniques to SQLS, discovering 13 new doubly imaged lensed quasars, after following up 55 of 250 candidates.

1.3.4 MUSCLES

By making use of the extra wavelength coverage due to the UKIRT Infrared Deep Sky Survey (UKIDSS) survey (Lawrence et al., 2007) and its typical image quality of 0.7", MUSCLES (Major UKIDSS-SDSS Cosmic Lens Survey) discovered 6 lensed quasars from the SDSS spectroscopic quasar catalogue (2 of which were also selected by SQLS, Jackson et al., 2008, 2009, 2012). The survey also showed that using a colour-separation diagnostic based on separation between multiple components against wavelength was an effective way to find lensed quasars since the red lensing galaxy often lies closer to one of the quasar images.

1.3.5 STRIDES

The STrong lensing Insights from the Dark Energy Survey (STRIDES) was set up to mine gravitational lenses from the 5,000 square degrees of deep, multi-band imaging in the Southern hemisphere, from the Dark Energy Survey (DES) (Treu et al., 2018). Given the lack of a large spectroscopic sample of quasars, and no u-band – a common diagnostic for identifying quasars – searches have relied heavily on other all-sky photometric datasets. Agnello et al. (2015a) discovered 2 doubles (with 1 also found by BQLS) using Artificial Neural Networks trained on DES catalogue magnitudes and morphology information, with initial cuts from WISE. Ostrovski et al. (2017) used Gaussian Mixture Models to classify quasars based on DES, VHS, and WISE magnitudes and selected extended objects from systems classified as quasars, discovering one double. Anguita et al. (2018) used the component-fitting techniques of Schechter et al. (2017) (see Section 1.3.6) to discover one quad and one double.

1.3.6 Other search techniques

Kochanek et al. (2006) was the first to suggest that variability could be used to discover lensed quasars, since difference imaging should reveal multiple nearby varying point sources,

which would not include the common contaminants including star-forming galaxies and stars. Lacki et al. (2009) tested this method on less than 1 square degree in the SDSS supernova field, recovering the one known lensed quasar with a false positive rate of $\sim$1/4000.

Ofek et al. (2007) used spectroscopic SDSS quasars with an infrared excess in the Two Micron All Sky Survey (2MASS), as a possible indication of a lensing galaxy, and discovered one new doubly imaged lensed quasar.

Jackson and Browne (2007) suggested that an offset between the optical and radio positions of a system could be used to find radio-loud lensed quasars since the optical position is centred on the lensing galaxy (for a faint optical counterpart to the source quasar), and the radio position is at the centroid of the quasar images. They discovered no new instances of gravitational lensing from a pilot study of 70 sources, but they note the efficiency of such a search would be improved significantly for reduced positional uncertainties on the optical galaxy catalogue.

Schechter et al. (2017) selected quasar candidates from WISE and modelled the pixels of VST ATLAS data as multiple quasi-Gaussians, identifying instances of similar colour objects. This revealed one quad and two doubles.

1.4 Wide-field Surveys

Recent optical all-sky data releases have opened up new areas of sky and have motivated our search for bright lensed quasars. This section describes the main wide-field surveys that will be used in this thesis. On occasion, candidates will lie in areas of sky with imaging from better seeing/deeper surveys, e.g. the Kilo-Degree Survey (KiDS, de Jong et al., 2013), or the Hyper Suprime Cam Survey (HSC, Aihara et al., 2018). Any other imaging presented in this thesis is from the CFHT science archive search[1] which includes CFHT, *HST*, NOAO, Subaru, and other telescopes' archival data.

1.4.1 Pan-STARRS

The Panoramic Survey Telescope and Rapid Response System (Pan-STARRS) consists of a 1.8m telescope in Hawaii, equipped with a 1.4 Gigapixel camera, imaging the sky in five broadband filters: *grizY* (see Figure 1.4).

The main time allocation of Pan-STARRS is for the 3π Steradian Survey (Chambers et al., 2016), a 30,000 square degree survey covering the whole sky above a declination of ≈ -30 degrees in *grizY*. Key characteristics of the survey are given in Table 1.1. The

[1] http://www.cadc-ccda.hia-iha.nrc-cnrc.gc.ca/en/search/

first data release provided stacked imaging for observations taken between June 2009 and February 2015 (Chambers et al., 2016), with single epoch, or warp, images being included in the second data release (Flewelling, 2018). For any analysis of Pan-STARRS data presented in this thesis, cutouts were obtained using the Pan-STARRS Image Cutout Server[2].

Due to the nature of the stacking pipeline, the exposure times and zeropoints on the downloaded FITS files are often unreliable, and so fluxes of nearby stars and reliable catalogued values are used for zeropointing these images.

Table 1.1 Summary of Pan-STARRS 3π survey details.

	g	r	i	z	Y
5σ stack depth	23.3	23.2	23.1	22.3	21.3
5σ single epoch depth	22.0	21.8	21.5	20.9	19.7
median seeing	1.31	1.19	1.11	1.07	1.02

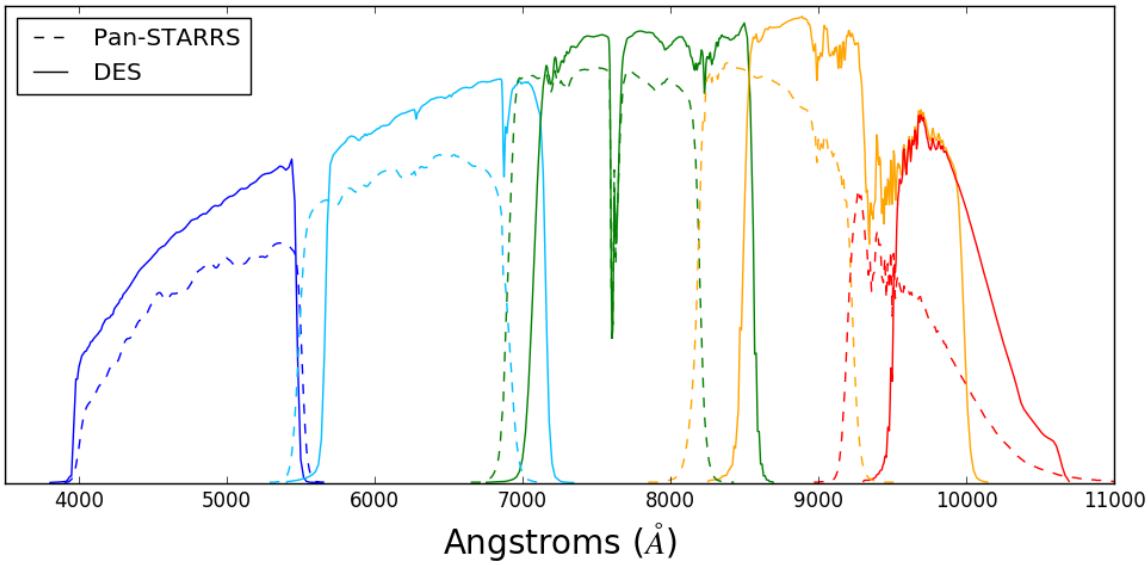

Fig. 1.4 Pan-STARRS and Dark Energy Survey *grizY* filters.

1.4.2 DES

The Dark Energy Survey (DES) has used the Dark Energy Camera (DECam) mounted on the 4-metre Victor M. Blanco Telescope in Cerro Tololo in Chile, to image over 5,000 square degrees of extragalactic sky in 5 bandpasses: *grizY* (see Figure 1.4). DECam is a 570

[2]https://ps1images.stsci.edu/cgi-bin/ps1cutouts

megapixel camera with a 2.2 degree diameter field of view, and 0.263" pixel size (Flaugher et al., 2015).

The footprint of the observations is shown in Figure 1.5 and was chosen to maximise overlap of the South Galactic cap, STRIPE 82 from SDSS (Abazajian et al., 2009), and the South Pole Telescope fields (Schaffer et al., 2011). DES began observing on 31 August 2013, and finished on 10 January 2019, with 758 nights of observations, leading to between 5 and 10 epochs in each band across the full footprint. The first public data release of DES contains data taken during the first three years of operation (Abbott et al., 2018).

The data used in this thesis primarily consist of the individual exposures. For this we use the “Final Cut" processing of single epoch images. See Morganson et al. (2018) for a full description of the data reduction. Table 1.2 describes the key characteristics of the survey in each band.

Table 1.2 Summary of DES data release 1 details. FWHM stands for Full-Width at Half Maximum.

	g	*r*	*i*	*z*	*Y*
Number of Exposures in Coadd	7626	7470	7470	7753	8531
Single-epoch PSF FWHM (arcsec)	1.12	0.96	0.88	0.84	0.90
Single-epoch depth (PSF, S/N=10)	23.57	23.34	22.78	22.10	20.69
Coadd depth (1.95" diameter, S/N = 10)	24.33	24.08	23.44	22.69	21.44

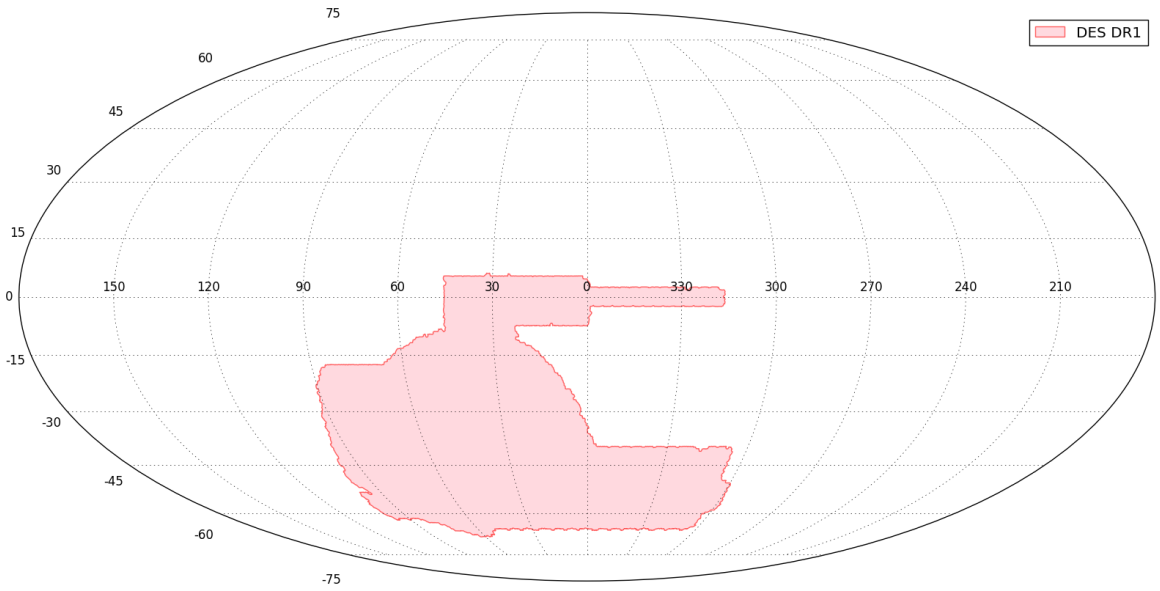

Fig. 1.5 Dark Energy Survey footprint on a Mollweide equal-area projection.

1.4.3 *Gaia*

Gaia is a space-based mission mapping the stars of the Milky Way with unprecedented astrometric precision (Gaia Collaboration et al., 2016b). It is a full-sky survey with resolving power at least 5 times better (measured FWHM of 0.1") than the best ground-based imaging, making it a powerful tool for lensed quasar searches. The data products released to the community do not include any raw data. They have released catalogues of detections with ancillary information on each detection. In this section we describe the basic *Gaia* mission and satellite details to explain the cataloguing in *Gaia*'s first and second data releases (hereafter GDR1 and GDR2).

Overview of the *Gaia* mission and satellite

The *Gaia* satellite (Gaia Collaboration et al., 2016a) was launched on 19 December 2013, with GDR1/GDR2 consisting of observations from the first 14/22 months (25 July 2014 to 16 September 2015/23 May 2016) of the nominal 60 month mission. *Gaia* consists of two identical telescopes, each with a rectangular aperture of 1.45m$\times$0.45m, that simultaneously point in directions separated by 106.5 degrees with beams folded to a common focal plane. As a result of the asymmetric focal plane with ratio 3:1, the PSF is also asymmetric with the same ratio and has a measured median FWHM of 103 mas (Fabricius et al., 2016) in the scanning axis direction. *Gaia* is located at L2 with a rotational sky-scanning orbit of period 6 hours and an orbital precession period of 63 days. Over the course of *Gaia*'s 5 year mission it will measure each source $\sim$ 70 times.

Gaia focal plane

The *Gaia* focal plane consists of 106 CCDs with 4500 pixels in the along-scan (AL) direction and 1966 pixels in the across-scan (AC) direction. Each pixel is rectangular in the ratio 1:3 similar to the PSF major and minor axes with size 10$\times$30 microns corresponding to 59$\times$177 mas on the sky, i.e. $\sim$ 2 pixels Nyquist sampling of the PSF FWHM. There are 14 sky-mapper (SM) CCDs and 62 astrometric field (AF) CCDs aligned in 7 rows in the AL direction and 9 columns in the AC direction with the middle CCD of the 9th AF column assigned to one of the two focus wave front sensors. The SM CCDs are in two columns (SM1 and SM2) with baffling such that each SM can only view a single *Gaia* telescope whereas the AF CCDs view the two fields simultaneously. The integration time per CCD is 4.42 seconds but it is not possible to download all the pixels to Earth and astrometric measurements are therefore made via windowed regions for sources detected in the SM CCDs.

For sources brighter than G=13, two dimensional (AF) windows of 12 AC pixels (2.12") and 18 AL pixels (1.06") are transmitted to ground (Carrasco et al., 2016). For all fainter sources (G>13) the windows are binned in the AC direction during readout to produce a 1D sample. For the faint sources brighter than G=16 (i.e. 13<G<16) there are 18 AL samples. For sources fainter than G=16 there are 12 AL samples with total length of 0.71". Figure 1.6 shows the 12×12 pixel 2D window for a faint source, for which a 1D data stream of 12 samples is downloaded with a sampling resolution of 0.059" in the AL direction and 2.12" in the AC direction.

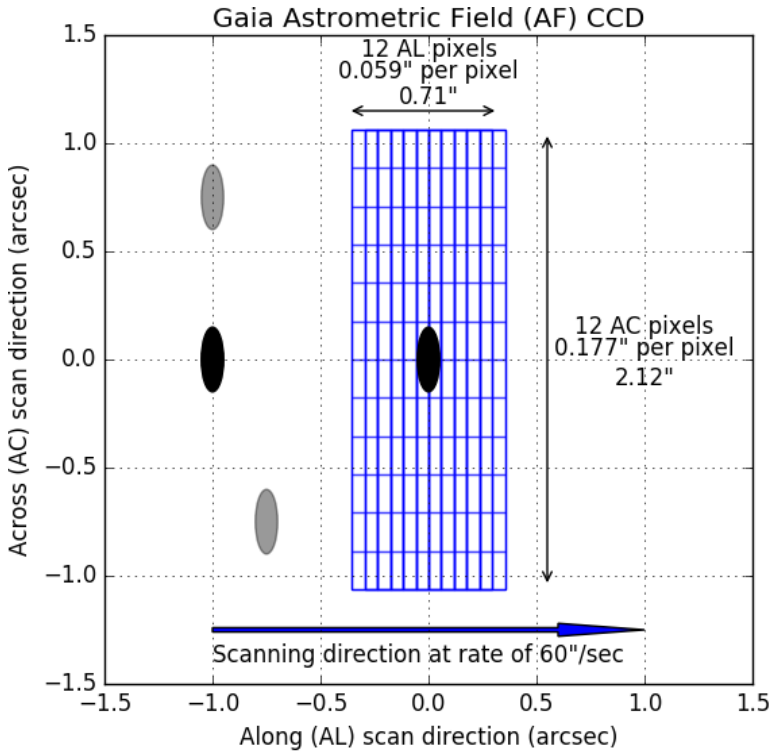

Fig. 1.6 A schematic of the sampling of a faint (G>16) source in a *Gaia* astrometric field CCD. The ellipses represent the images of point sources on the focal plane.

In principle, each component of a faint binary with separation greater than 2.12" will always be isolated in their window. Since each source will be observed multiple times with different scan directions during the 5 year *Gaia* mission, the 1D data can be used to create a 2D reconstruction (Harrison, 2011). At the current time the individual 1D scans have not been released by the *Gaia* team.

The AF fluxes are measured in a wide optical band (hereafter G-band) as shown in Figure 1.7. After the AF CCDs, there are two further rows of CCDs, the red photometer and blue photometer CCDs. The measured bandpasses are shown in Figure 1.7. GDR1 included only

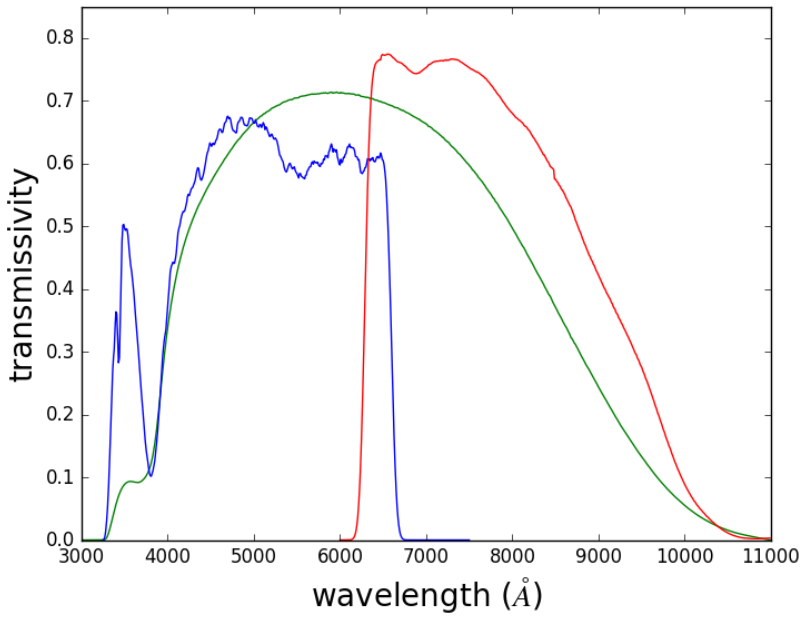

Fig. 1.7 The revised *Gaia* G, BP, and RP bandpasses based on GDR2 data, in green, blue, and red respectively.

G-band measurements, while GDR2 included BP and RP measurements for most bright sources, with less frequent measurements for fainter sources or objects with close neighbours.

Catalogue creation

Source measurements are based on modelling single point sources in these 2D windowed regions of pixels or 1D samples. When close pairs are encountered in the same windowed region, depending on the scanning direction and relative orientation of the pair, the fainter object is given a truncated window of pixels, which has not been processed for GDR1 or GDR2 (Fabricius et al., 2016)[3]. Due to the small number of scan directions, there is a significant lack of detections of the fainter companion in close binaries in GDR1, however this has improved for GDR2.

The main astrometric source catalogues for GDR1 and GDR2 contain over one billion sources (see Lindegren et al. (2016) and Gaia Collaboration et al. (2018) for details). Sources were removed from both data releases when they were separated from another source by less than 5 times the combined astrometric positional uncertainty. Often, this was due to the cataloguing of known objects against an initial *Gaia* source list, which catalogued many objects twice. Further objects were filtered if sources were observed fewer than 5 times (5 focal plane transits), or if their astrometric excess noise and positional standard uncertainty

[3]https://gea.esac.esa.int/archive/documentation/GDR2/Gaia_archive/chap_datamodel/

Table 1.3 Summary of WISE bandpasses. Magnitudes are given in the Vega system.

	W1	W2	W3	W4
central wavelength (μm)	3.4	4.6	12	22
PSF FWHM (")	6.08	6.84	7.36	11.99
Number of Detections	746,346,617	618,333,896	132,476,333	40,939,966
Magnitude for S/N $>$ 5	16.9	16.0	11.5	8.0

were greater than 20mas and 100mas respectively. Finally, sources were removed if they had fewer than 11 G-band measurements (CCD transits in the astrometric part of the focal plane). See Fabricius et al. (2016) for a full explanation of the data-processing and catalogue creation. The limiting magnitude of *Gaia* is $\sim$ 20.7 in the Vega magnitude system, but it is capable of detecting objects a magnitude fainter than this in sparse fields.

1.4.4 WISE

The Wide-Field Survey Explorer (WISE) was launched on 14 December 2009, and consists of a 40 cm diameter infrared telescope (Wright et al., 2010). WISE surveyed the sky in 4 bandpasses at 3.4, 4.6, 12, and 22 microns, hereafter W1, W2, W3, and W4. The primary mission with cryogenic coolant lasted 10 months. After this, the mission was extended as NEOWISE (Near-Earth Object WISE) until February 2011 as it could still use the W1 and W2 detectors without cryogen (Mainzer et al., 2011a,b). The satellite was then put into hibernation until September 2013, when its mission as NEOWISE was reactivated, and it continues to take data. Stern et al. (2012) showed that the W1$-$W2 colour is an efficient and pure metric to select quasars. Figure 1.8 shows a colour diagram making use of the W1$-$W2 colour, and G$-$W1, for a sample of spectroscopically confirmed quasars, stars, and galaxies. This clearly identifies quasars, due to the power-law-like continuum of quasars in the infrared (e.g., Glikman et al., 2006), whereas stars have blackbody distributions, whose infrared tails quickly drop through the WISE bandpasses.

One drawback to the WISE data is its much lower resolution than the previously described optical surveys. The native pixel size of WISE is 2.75 arcseconds per pixel. However, the ALLWISE data release which stacked data from before hibernation, blurred the stacked images by the PSF, and resampled the data onto 1.375 arcsecond pixels for optimal detection of point sources. Unblurred coadds have been created by the unWISE team (Lang, 2014), including data taken during the reactivation mission (Meisner et al., 2018; Schlafly et al., 2019). Table 1.3 lists the key characteristics of the WISE bandpasses. The PSF FWHM in the W1 and W2 bands are above 6 arcseconds, and hence the components of any galaxy-scale lensed quasar are blended in these data and catalogued as a single object.

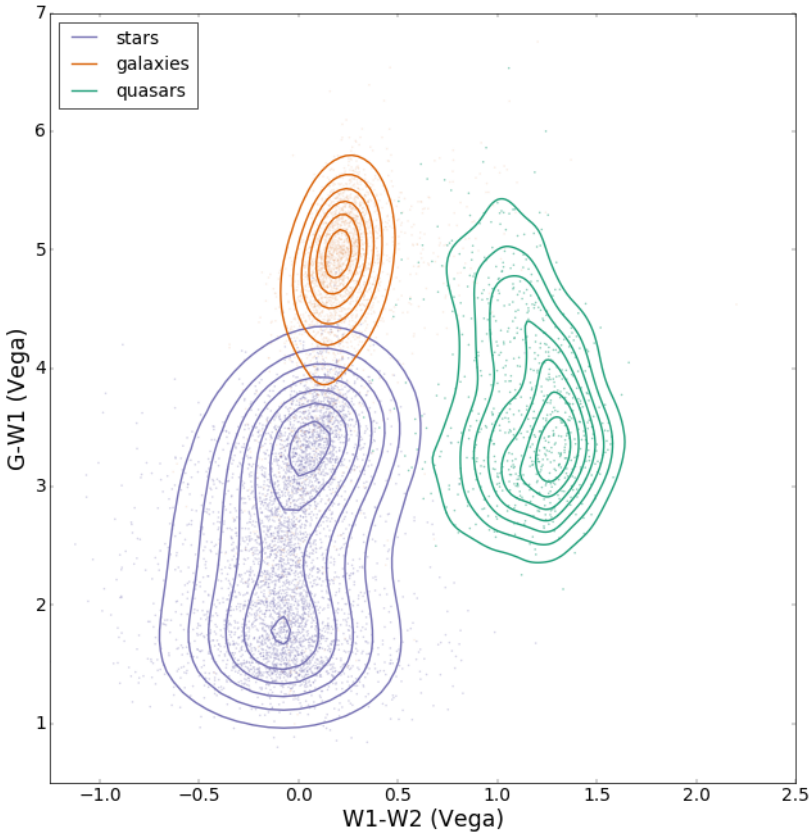

Fig. 1.8 *Gaia* G−W1 vs W1−W2 for a sample of spectroscopically confirmed galaxies, quasars, and stars.

1.5 Predictions

Before beginning a search for lensed quasars, we must first motivate how many new lensed quasars the dataset will contain, and what properties these lenses will have, by using a mock catalogue of lensed quasars. The luminosity function of source quasars, the mass function of the lensing galaxies, and their evolutions with redshift, must all be well-known to create such a catalogue (see, e.g., Turner et al., 1984). These parameters have been constrained by non-lensing studies (e.g., from SDSS galaxy spectra, Choi et al., 2007), and allowed Oguri and Marshall (2010) (hereafter OM10) to predict the lensing rates, image separations, and redshift distributions for lensed quasars across the whole sky (considering only elliptical galaxies as lenses). We note that Finet and Surdej (2016) predicted the number of lensed quasars expected from *Gaia* with results consistent with OM10.

The OM10 catalogue is based on the LSST footprint (∼20,000 square degrees), and is 5 times oversampled (i.e., represents the lensed quasars expected in 100,000 square degrees of sky). The catalogue only includes quasars lensed by single galaxies, and with image

Table 1.4 Predicted numbers of lensed quasars in *Gaia*, DES, and Pan-STARRS based on the OM10 catalogue. We note that *Gaia* is capable of resolving lensed quasars with image separations smaller than those given in the OM10 catalogue, though we only quote numbers based on this catalogue, and hence a minimum image separation of 0.5 arcseconds. We note that these numbers do not exclude any areas of significant stellar overdensities.

	Pan-STARRS 3π	DES DR1	*Gaia*
10σ detection limit	i<22.4	i<23.44	G<20.7
typical PSF FWHM (arcseconds)	1.11	0.88	0.1
survey area (sq. deg.)	30939	5230	41254
$N_{\rm quads}$	329 ± 35	103 ± 8	132 ± 24
$N_{\rm doubles}$	1825 ± 83	636 ± 19	567 ± 50

separations between 0.5 and 4 arcseconds. OM10 predicted the number of lenses in several wide-field optical surveys. For a lens to be detected by a survey, the second brightest image for doubles or third brightest for quads (hereafter $I_{2,3}$) must be brighter than the 10σ detection for point sources in the I-band, and the image separation for the system (twice the Einstein radius) greater than 2/3 the typical seeing FWHM of the survey. We recalculate the expected numbers of doubles and quads for Pan-STARRS and DES, based on measured detection depths and areas (see Tables 1.1 and 1.2), and list the results in Table 1.4. We also consider the number of expected lensed quasars using the *Gaia* detection threshold of G<20.7 in place of the 10σ detection threshold. However, to convert the OM10 *I*-band lensed image magnitudes to *Gaia G*-band magnitudes (see Figure 1.7), we use the SDSS spectroscopic quasar catalogue cross-matched to *Gaia*, so a $G-I$ relation is determined at each redshift. For each mock lens in the catalogue, a *Gaia G*-band magnitude is synthesised from the matched catalogue based on the source redshift. As there is scatter in the $G-I$ relation, the $G-I$ conversion is repeated for each mock lens 100 times and the G<20.7 threshold re-applied.

We now explore the distribution of three key lens parameters in each of these samples: the image separation (or Einstein radius), the brightness of the system, and the relative contributions of the lensing galaxy and quasar images to the light. To understand how the number of systems changes with image separation, we plot a cumulative histogram in decreasing image separation for the three surveys discussed above (Figure 1.9). As required, the final cumulative values match the totals given in Table 1.4. From *Gaia*, we expect 30 quads with image separations above 2 arcseconds (at least three images detected by *Gaia*), and 70 more with image separations between 0.5 and 2 arcseconds. The corresponding numbers for doubles are $\sim$150 and $\sim$400. The typical quad fraction at all image separations is $\sim$17% or 1 in 6.

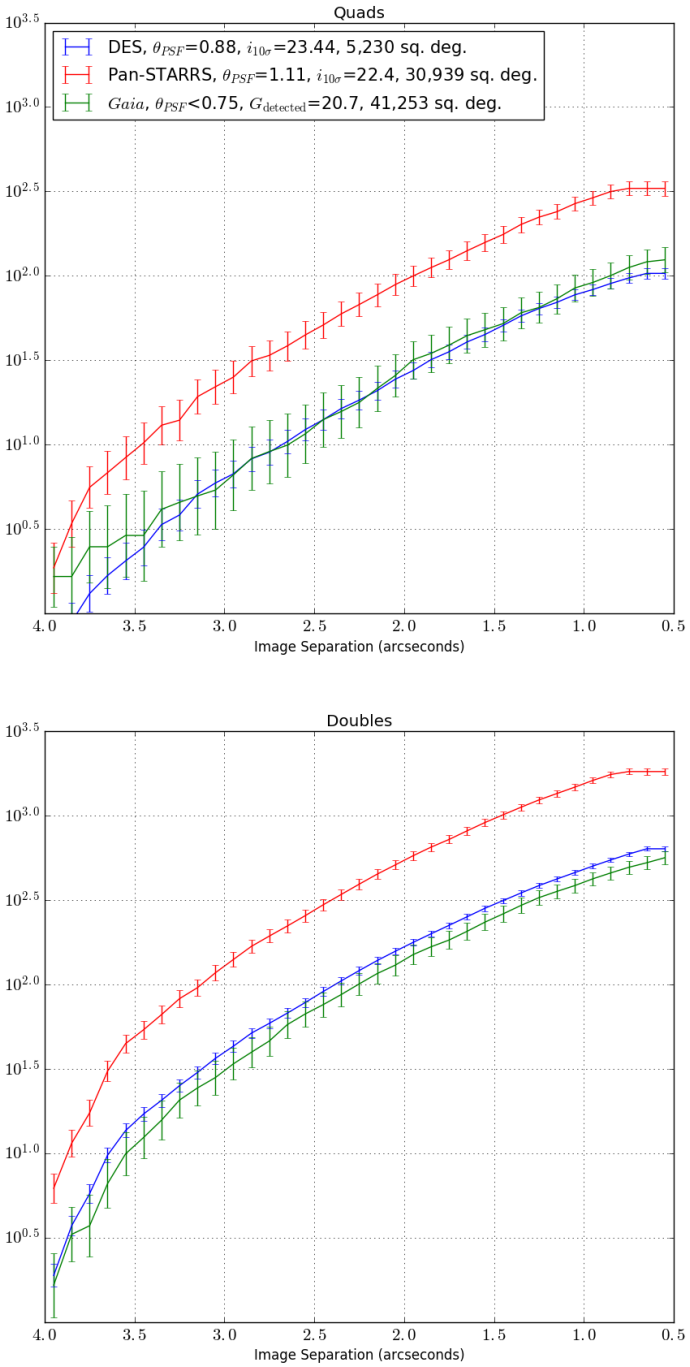

Fig. 1.9 Predicted numbers (cumulative) of lensed quasars against image separation (top: quads, bottom: doubles) in Pan-STARRS, DES, and *Gaia*, using the OM10 catalogue. For the *Gaia* predictions, a $G-I$ band conversion was applied using a sample of spectroscopic quasars, as described in the text. The uncertainties for each bin are from Poisson noise, and from spreads in the $G-I$ band conversion for the *Gaia* estimates.

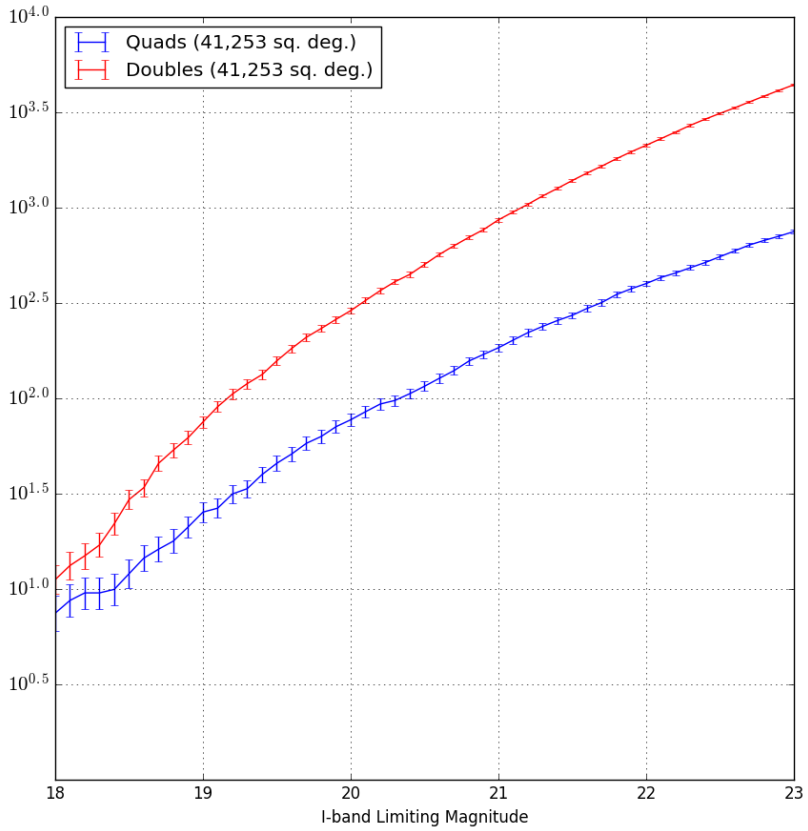

Fig. 1.10 Predicted numbers of lensed quasars against magnitude for the full sky. A mock is included if it is a double and both images are brighter than a given magnitude, or a quad and at least three images are brighter than that magnitude. The larger magnifications from quads causes a magnification bias at the bright end of the population.

Figure 1.10 repeats the above analysis but for varying survey magnitude limit (using all lensed quasars with image separations between 0.5 and 4 arcseconds). We note that beyond limiting magnitudes of I=23.3, the numbers become less trustworthy since all systems with $I_{2,3}$ below 23.3 have been removed from the catalogue. The plot clearly shows the magnification bias from quads at bright apparent magnitudes, as we expect a similar number of quads and doubles above a limiting magnitude of 18.

Finally we consider the relative contributions to the total brightness of a system from the lensing galaxy and the quasar images. The galaxy I-band magnitude is plotted against the combined quasar image magnitude in Figure 1.11. The widest area ground-based imaging we will use to check for possible lensing galaxies is Pan-STARRS. The 10σ I-band point source magnitude limit for this survey is 22.4, and we overlay this limit on the figure. 22.9% (16.9%) of lenses in OM10 (Gaia) have fainter lensing galaxies than this limit, and so we should not expect lens confirmation of these systems without deeper follow-up imaging. This

is a conservative estimate, as the lensing galaxy can be extended and thus not be as easily detected as a PSF, for which the detection magnitude is given.

1.6 Thesis Outline

The work presented in this thesis has mostly been performed in chronological order. Chapter 2 presents lensed quasar searches in Pan-STARRS and DES, using a combination of *Gaia* data release 1 and WISE, with spectroscopic follow-up and characterisation of 35 new lensed quasars. Chapter 3 presents a new method to discover small separation lensed quasars using flux deficits and astrometric offsets when comparing quasars in *Gaia* and ground-based imaging data. Chapter 4 presents lensed quasar searches based on Pan-STARRS, WISE, and *Gaia* data release 2, using a forced modelling of unWISE data, with spectroscopic follow-up and characterisation of 70 new lensed quasars. Chapter 5 describes a parametric modelling pipeline of DES single epoch images to extract variability information, with discussions on improving completeness and efficiency of future searches. Discussions and conclusions are given in Chapter 6.

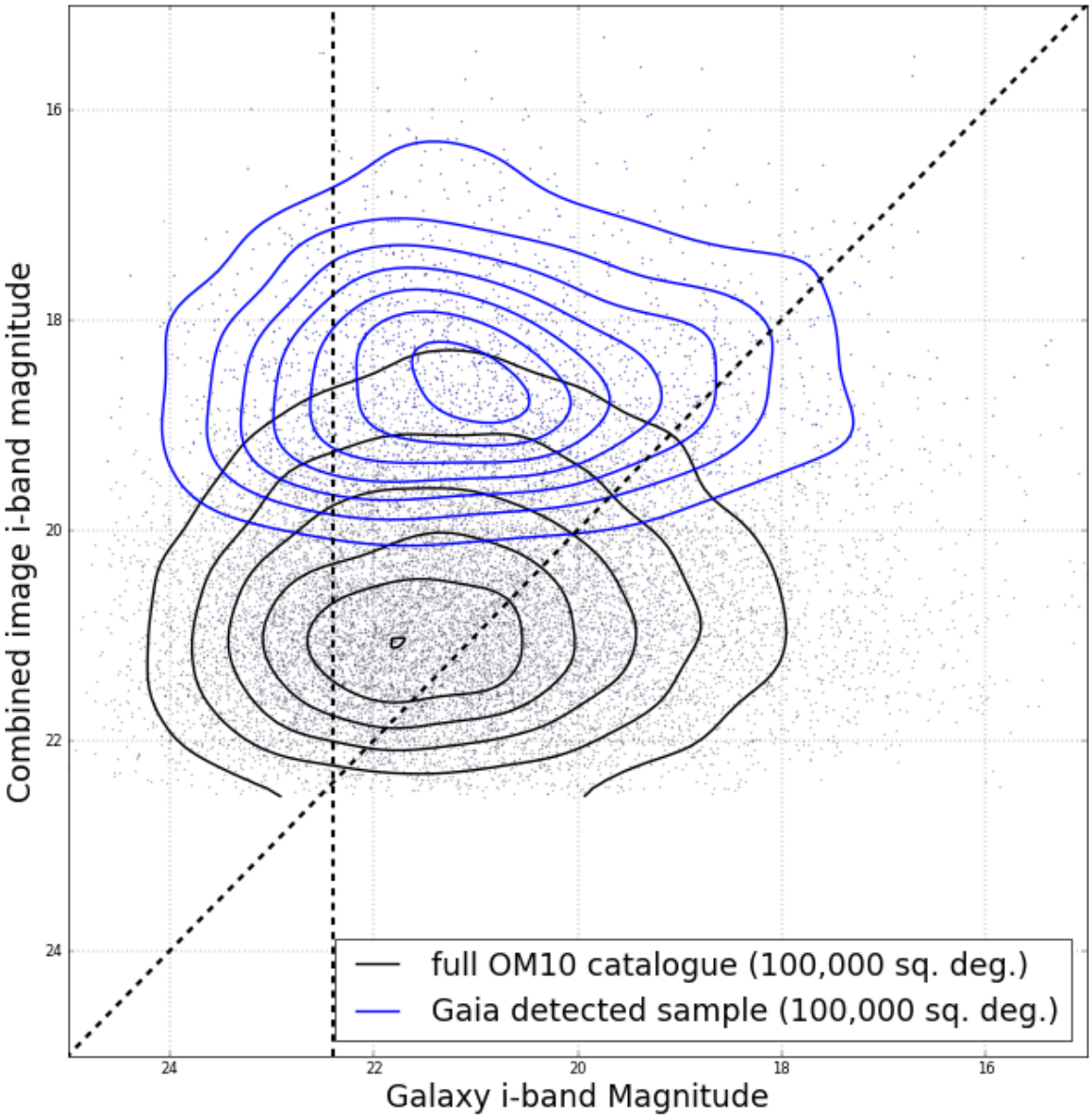

Fig. 1.11 Magnitude of the combined quasar images against magnitude of the lensing galaxy for the 15,088 mock lenses in OM10 (black) and those expected to be selected by *Gaia* (blue). The catalogue removes any systems not passing the criterion of $I_{2,3}$ <23.3, and so the catalogue becomes incomplete at combined magnitudes as early as $I \approx 21$. 39.9% of all lensed quasars in the catalogue have galaxies brighter than the quasar images in the i-band (i.e., fall below the diagonal line). For a *Gaia*-selected sample (which must require at least two detections of 20.7 and hence lie above $I \approx 20$), this fraction falls to 9.5%. The vertical dashed line represents a conservative detection threshold for Pan-STARRS, hence we do not expect to detect lensing galaxies for systems to the left of this line. In the full OM10 catalogue and *Gaia*-selected cases, this represents 22.9% and 16.9% of the total population.

Chapter 2

Lensed Quasars from *Gaia* Data Release 1

The main contaminants in photometric lensed quasar searches are single quasars projected near stars or galaxies, and compact star-forming galaxies (see, e.g., Treu et al., 2018). When viewed in ground-based imaging datasets, the PSF (typically FWHM around 1 arcsecond) blends the components of these contaminant systems, such that they resemble the blended images of a lensed quasar. Such a blend is often not segmented by the source extraction routine and hence is catalogued as a single object. Furthermore, the lack of resolution and depth from ground-based imaging often hides the lensing galaxy against the typically brighter quasar images, or makes compact galaxies appear consistent with single point sources. Space-based imaging overcomes many of these problems, as the multiple components become clearly resolved due to a diffraction-limited PSF (e.g., *HST* has a PSF FWHM of 0.1" at optical wavelengths) and galaxies appear extended. The *Gaia* mission offers a whole-sky detection of bright point sources, with the promise of good completeness at small separations. In this Chapter, we will use the catalogue from the first *Gaia* data release (GDR1) to look for photometric quasar candidates with multiple nearby *Gaia* detections, since these detections could be due to the multiple images of a lensed quasar. We also present a search based on just one point-source-like *Gaia* detection near extended objects. We present results based on 4 nights of spectroscopic follow-up at the WHT.

2.1 Known Lensed Quasars in GDR1

Before we apply crossmatches between *Gaia* and photometric quasar candidates, we investigate the cataloguing of the known lensed quasars in GDR1. Since *Gaia*'s effective resolution

can be as poor as 2.12" in the across scan direction, the variation in scanning angle and number of visits can strongly affect whether a point source is catalogued or not when it is in a locally crowded environment.

Table 2.1 shows the number of *Gaia* detections for the 204 currently published lensed quasars[1]. We note that we have manually corrected the number for SDSSJ2222+2745 since a star with a *Gaia* detection lies within the Einstein radius of the system.

Table 2.1 Summary of *Gaia* DR1 detections for known lensed quasars.

$N_{\text{detections}}$	Doubles	Quads	All
4	0	1	1
3	0	6	6
2	33	12	55
1	89	15	104
0	29	19	48

Only one quad has all images detected in GDR1: SDSSJ1004+4112, a quasar lensed by a cluster with an Einstein radius of 7" (Inada et al., 2003). While not all lensed quasars have bright optical images that we would expect *Gaia* to detect, there is a definite dearth of expected detections for many of the systems. About 20% of doubles have all images detected by *Gaia*, when we would expect that *Gaia*'s resolving capability would detect all images of $\sim$90% of these doubles (since only a handful of doubles have images separated by less than the 0.71" window size). This discrepancy is likely attributed to certain scan angles only providing the aforementioned 2.12" resolution (i.e., in the across direction), since truncated windows have not been processed by GDR1. Perpendicular scan angles do allow good detection and separation of the multiple images. However, based on the $\sim$16 scans from GDR1 (14 months), we expect that there are often fewer than 11 G-band measurements from these "good" scan angles, i.e. the required threshold for cataloguing.

In Chapter 3, we will investigate a new technique to infer the presence of multiple images when just one image has been catalogued by *Gaia*, but in the following we will only consider search techniques based on multiple *Gaia* detections or single *Gaia* detections near morphological galaxies. Our analysis and results are split into searches and follow-up of candidates from Pan-STARRS and those from DES, due to different selection conditions and different follow-up campaigns.

[1] https://www.ast.cam.ac.uk/ioa/research/lensedquasars/

2.2 Pan-STARRS

We must first define the area of sky in which we will carry out our search. The declination range was limited to $\gtrsim -30$ degrees, i.e. requiring *grizY* imaging from Pan-STARRS. For the majority of candidates we required the systems to lie outside the galactic plane, $|b| > 15$, however in some right ascension ranges (RA$\sim$80, along the galactic anti-centre) this was relaxed. Before a final sample was established, the local *Gaia* stellar density for each candidate was required to be less than 50,000 stars per square degree (calculated by counting *Gaia* sources within a 100" radius), in order to remove star clusters. For the $b >$15 degrees sky in Pan-STARRS, this only reduces the area by $\sim$90 square degrees.

Two quasar candidate catalogues are created, and two *Gaia*-based selection methods are applied to these catalogues to generate our final sample, as described in the following subsections.

2.2.1 Photometric quasar candidate catalogues

I. WISE mid-infrared colours

Stern et al. (2012) have shown that the W1 and W2 bands of WISE (Wright et al., 2010) can be used to select AGN by applying the colour criterion of W1$-$W2$\geq$0.8 (Vega). One advantage of this selection technique is its simplicity and effectiveness (Schechter et al., 2017; Wu et al., 2012), however a downside for our purposes is that lensed quasar photometry can be strongly affected by the lensing galaxy, leading to WISE colours bluer than those of isolated quasars.

To overcome this we apply a looser WISE criterion of W1$-$W2$\geq$0.5. With this limit we do not expect an unreasonable number of contaminants still meeting our *Gaia* detection criteria of Section 2.2.2. The main contaminant created by this lower limit is quasar+star projections.

We ensure that the WISE detections are robust in W1 and W2 by requiring catalogue ALLWISE uncertainties and a W1 value brighter than 15.5. After cross-matching to Pan-STARRS to the nearest object within 4" and keeping objects with *i*-band PSF magnitudes brighter than 21, our initial WISE-selected quasar candidate list has 1,298,877 objects with $|b| > 15$.

II. SDSS GMM photometric quasars

Recent papers (e.g. Agnello et al., 2018a; Williams et al., 2018, Ostrovski et. al. in prep.) have shown that the Sloan Digital Sky Survey (SDSS) imaging data still contain bright lensed

quasars, which had not been targeted for spectroscopy and hence were not targeted by the SDSS quasar lens searches.

Since the SDSS imaging dataset includes u-band data—which are particularly useful for selecting AGN—a complementary catalogue to our WISE quasar selection has been created by applying Gaussian mixture modelling (GMM) classification to SDSS objects as in Ostrovski et al. (2017). This is a morphology-independent selection based on $u-g$, $g-i$ and $i-$W1 colours. Classification is divided into four classes: stars, galaxies, and low- and high-redshift quasars ($z \lesssim 2.7$ and $z \gtrsim 2.7$ respectively). This classification is applied to all SDSS objects with $psfMag\_i < 21$. Our final GMM quasar candidate catalogue is composed of all objects that have a combined (low and high redshift) quasar probability > 0.5. This results in 1,158,557 quasar candidates.

2.2.2 Morphology Selection

Once a set of photometric quasar candidates is selected, we attempt to remove the objects that are not lensed quasars—mainly isolated quasars or misclassified star-forming galaxies. To this end we use *Gaia* data by searching our quasar candidate catalogues for objects in which multiple *Gaia* sources are detected, as would be expected for multiply imaged quasars. While this does not remove quasar+star projections from our candidates, it removes many star-forming galaxies and isolated quasars, since at most one *Gaia* detection is expected for these contaminants.

Since *Gaia* does not reliably detect all images of most lensed quasars, we also describe a simple morphology selection using just one *Gaia* detection. Even though this selection naturally removes fewer contaminants, it recovers 45 known lenses. The details of the two methods are described below. They are both applied to each of the quasar catalogues described in 2.2.1; Table 2.2 shows the number of candidates each technique and quasar catalogue produced, given the selection criteria. Note that the numbers are not exclusive.

I. Multiple *Gaia* detections

Our first selection technique is to find quasar candidates with multiple *Gaia* detections. We require at least two *Gaia* detections within 4" of each other. Lensed quasars with separations above this are rare (e.g. Oguri and Marshall, 2010) and the number of contaminant systems is proportional to the square of the maximum image separation allowed in a search. Furthermore *Gaia* is most useful at combating the blending of smaller-separation systems in ground-based optical survey data, in which lenses with images separated by more than 4" should already be deblended. This technique is applied in a two-step process: firstly all quasar candidates

are matched to *Gaia* within 2" of the Pan-STARRS or SDSS detection and secondly this is matched to *Gaia* again within 4" of the initial *Gaia* position. We choose the first matching distance to be only 2" since this retains all known lenses with two *Gaia* detections while removing many single quasar candidates projected near stars with *Gaia* detections.

II. *Gaia* detection near morphological galaxy

Only 1 in 5 small-separation lensed quasars have all quasar images detected by *Gaia*, even when all images should be detected (see Chapter 3 for a full discussion). Though this fraction increases with separation (one third at the largest separations; Agnello, 2017), requiring multiple *Gaia* detections will miss the majority of lenses. One way to find some of these "missing" lenses is to perform a search depending on only one *Gaia* detection. We do this by requiring a morphological galaxy within 4" of the quasar candidate, removing contamination from wider-separation star+quasar projections. If the single *Gaia* detection is indeed a quasar, a bright galaxy within 4" is a strong candidate for acting as a foreground lens. We crossmatch our quasar candidates to *Gaia* within 4" and then back to Pan-STARRS within 4" of the single *Gaia* detection but requiring the criterion of $r_{PSF} - r_{KRON} > 0.2$ for the new match. This extended object can be the original quasar candidate.

2.2.3 Final Lens Candidate Catalogue

After applying the *Gaia* multiple and single detection techniques to the two quasar candidate catalogues, we apply two further filters. The first is requiring the astrometric excess noise (AEN, Lindegren et al., 2016, 2012) for each *Gaia* detection to be less than 10 mas. The AEN is a useful indicator for point source/galaxy separation (Belokurov et al., 2016; Koposov et al., 2017) which holds for known lensed quasars (described further in Chapter 3). Therefore we can remove many star-forming galaxies from our search by applying the simple cut AEN$<$ 10 mas. The second filter is the local *Gaia* stellar density cut of 50,000 stars per square degree.

The catalogues are then stacked and duplicates from the two quasar candidate selection techniques are removed, leaving 109,941 *Gaia* singles and 31,486 *Gaia* pairs. After selecting $\sim$200 of the most promising candidates through visual inspection, the Pan-STARRS *grizY* images are modelled simultaneously as described in Section 2.2.6. This is to ensure the postulated quasar images have similar colours and to prioritise systems with residual features consistent with a lensing galaxy.

Table 2.2 Candidate numbers for the two quasar catalogues and the two *Gaia* morphological selection methods.

	WISE quasars (W1−W2>0.5)	1,298,877
MULTIPLES	*Gaia* matches < 2"	416,990
	2 *Gaia* matches within 4" of each other	9,125
	Gaia AEN < 10mas	8,889
	Stellar density < 50,000 / sq. degree	**8,447**
SINGLES	*Gaia* matches <4"	428,559
	Gaia singles with $r_{PSF} - r_{KRON} > 0.2$	120,817
	Gaia AEN < 10mas	80,595
	Stellar density < 50,000 / sq. degree	**80,206**
	SDSS GMM quasars	1,158,557
MULTIPLES	*Gaia* matches < 2"	686,311
	2 *Gaia* matches within 4" of each other	24,851
	Gaia AEN < 10mas	24,765
	Stellar density < 50,000 / sq. degree	**24,749**
SINGLES	*Gaia* matches < 4"	710,052
	Gaia singles with $r_{PSF} - r_{KRON} > 0.2$	54,352
	Gaia AEN < 10mas	50,491
	Stellar density < 50,000 / sq. degree	**50,488**

2.2.4 Observations

Spectra of 60 candidates were taken with the Intermediate dispersion Spectrograph and Imaging System (ISIS) on the 4.2-m William Herschel Telescope (WHT) on the nights of 31 March, 1 April, 12 and 13 September 2017. Since we only needed to identify broad emission line features, we used the low resolution gratings, R158 (121 Åmm^{-1}/ 1.81 Åpixel^{-1}) for the red arm and B300 (64 Åmm^{-1}/ 0.86 Åpixel^{-1}) for the blue arm to maximise wavelength coverage. Each lens candidate was positioned along a 1"-wide slit to capture both quasar images. Multiple position angles were used for one quad candidate, J1721+8842.

After masking cosmic rays and subtracting the sky background, the spectra were visually inspected for broad emission lines in the separated traces and 1D spectra were extracted using Gaussian apertures with 0.5" width.

2.2.5 Results

Table 2.3 shows a summary of the observations with sky positions, candidate selection method, outcome of the observation and *Gaia* magnitudes.

We have classified 24 objects as lensed quasars since the spectra reveal the presence of (at least) two quasars at the same redshift and the pixel modelling of the Pan-STARRS images reveals a lensing galaxy. Figure 2.1 shows Pan-STARRS *gri* cutouts of the confirmed lens systems with *Gaia* detections overlaid. Figure 2.2 shows the component spectra for each lens. We are able to establish the lens galaxy redshift for 4 lenses.

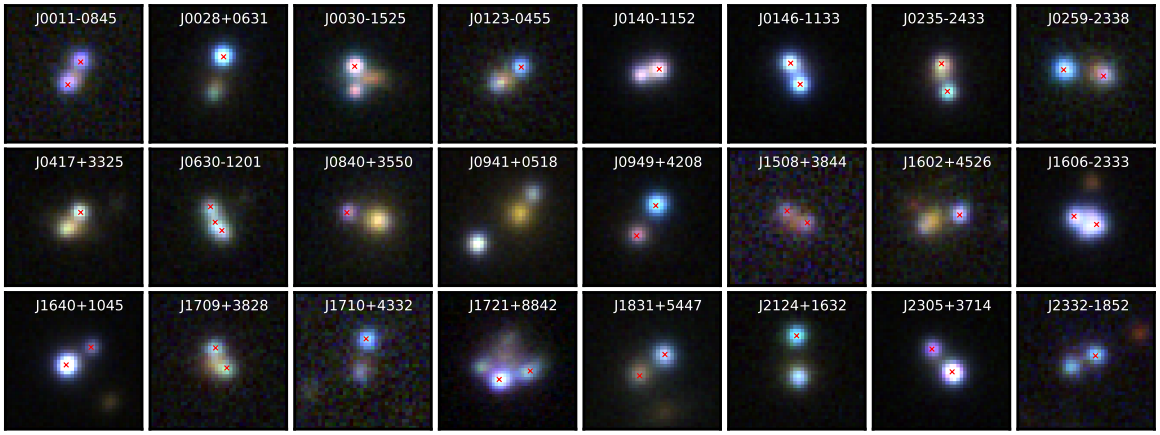

Fig. 2.1 Pan-STARRS *gri* colour images of the confirmed lenses with *Gaia* detections overlaid with red crosses. Cutouts are 10" on the side.

We further discover 10 systems consisting of pairs of quasars at the same redshift, shown in Figure 2.3. Their spectra are shown in Figure 2.4. However in these systems, the residuals

after PSF subtraction do not convincingly demonstrate a lens, or the spectral features rule out the lensing hypothesis. Follow-up imaging of one quasar pair, PSJ0140+4107, with NIRC2 on Keck, reveals a lensing galaxy. See section 2.4 for details on individual systems.

2.2.6 Pan-STARRS Modelling

I. Pixel modelling

In this section we model the Pan-STARRS *grizY* imaging data for each lens system to derive simple component shapes, positions, and colours. In the next section we use the image and galaxy positions and flux measurements to fit simple lens models to each system.

The PSF is derived by fitting a Moffat profile (Moffat, 1969) to a nearby star. The *grizY* Pan-STARRS images are modelled simultaneously with each quasar image fit with a PSF, and galaxies fit with Sérsic profiles (Sérsic, 1963) convolved with the PSF. In all lens systems, the presence of a lens galaxy is apparent from the colour image, except for J0630-1201 and J1606-2333. The free parameters for the pixel modelling are the positions of the quasar images and the lensing galaxy, as well as the flattening, size and Sérsic index of the galaxy, all of which we assume to be the same across bands. The log likelihood is sampled using the EMCEE package (Foreman-Mackey et al., 2013) to determine statistical uncertainties. Finally the fitting is repeated with a different PSF star to determine the systematic error from a possible PSF mismatch.

Figure 2.5 shows the Pan-STARRS *gri* images and the residuals after modelling each system as the relevant sum of quasars and galaxies. Astrometry and photometry for all available bands are given in Appendix A.

II. Mass modelling

We fit all the systems with singular isothermal ellipsoids (SIE) using our own Python-based image-plane modelling code, which has been checked for consistency with LENSMODEL (Keeton, 2001). We use the two-step process of modelling the pixels to find positions and fluxes, and then deriving a lens model. This is to ensure that, if the system is not well-described by a singular isothermal ellipsoid, it does not affect the PSF subtraction. Furthermore, we can quantify the χ^2 contributions from positions and flux ratios robustly. For all the doubly imaged lenses, we start from two image positions and a galaxy position (6 parameters). However to constrain a singular isothermal ellipsoid (galaxy position, mass, ellipticity, position angle, and source position; 7 parameters), we require one further observable. For this we use the image flux ratio. We take the median flux ratio from the *griz* bands and include a 20% uncertainty on the input fluxes since optical flux ratios depend

Table 2.3 Summary of Pan-STARRS-selected candidate observations. NIQ=nearly identical quasar. Selection shows the quasar catalogue and *Gaia* technique with which the candidate was selected: S=single, D=double, T=triple. All dates are in 2017. See Lemon et al. (2018) for WISE magnitudes, and colours of each system.

Name	RA	DEC	Selection	*Gaia* G	Date, Exp. Time	Outcome
J0003+4555	0.96401	45.92215	D+WISE	17.61, 18.97	12 Sep, 600s	quasar+star
J0011– 0845	2.83435	-8.76407	D+GMM/WISE	20.31, 20.35	12 Sep, 1200s	**lens**, z=1.70
J0028+0631	7.09369	6.53195	S+GMM/WISE	18.95	12 Sep, 1200s	**lens**, z=1.06
J0030– 1525	7.56378	-15.41752	S+WISE	19.30	13 Sep, 1200s	**quad lens**, z=3.36
J0123– 0455	20.84084	-4.93266	S+GMM/WISE	20.29	12 Sep, 2100s	**lens**, z=1.38
J0127– 1441	21.78539	-14.68861	D+WISE	20.15, 20.50	12 Sep, 1200s	NIQ, z=1.76
J0139+3526	24.88888	35.43658	D+WISE	19.46, 19.65	12 Sep, 600s	NIQ, z=0.65
J0140– 1152	25.01231	-11.872	S+WISE	18.41	12 Sep, 1800s	**lens**, z=1.80
J0140+4107	25.20420	41.13331	S+WISE	17.54	12 Sep, 1200s	NIQ, z=2.50
J0146– 1133	26.63691	-11.56113	D+WISE	18.39, 18.66	12 Sep, 1800s	**lens**, z=1.44
J0232– 2429	38.06565	-24.49433	S+WISE	17.99	13 Sep, 600s	quasar+star
J0235– 2433	38.86431	-24.55356	D+WISE	18.12, 18.85	12 Sep, 1800s	**lens**, z=1.44
J0259– 2338	44.88961	-23.63388	D+WISE	19.23, 20.34	12 Sep, 2400s	**lens**, z=1.19
J0322+5024	50.71298	50.41402	D+WISE	18.82, 19.11	12 Sep, 600s	stars
J0417+3325	64.49682	33.41700	S+WISE	19.22	13 Sep, 1200s	**lens**, z=1.41
J0511– 0351	77.91098	-3.85049	D+WISE	19.25, 19.99	13 Sep, 600s	quasar+other
J0515+0652	78.75772	6.86855	S+WISE	18.98	13 Sep, 1200s	quasar+other
J0616+4912	94.13678	49.20712	S+WISE	18.33	12 Sep, 600s	star+quasar
J0630– 1201	97.53796	-12.02223	T+GMM	19.61, 19.76, 19.95	01 Apr, 1200s	**5-image lens**, $z = 3.34$
J0659+5217	104.92159	52.28907	D+WISE	18.60, 19.63	12 Sep, 600s	stars
J0723+4739	110.93660	47.65259	S+WISE	19.60	12 Sep, 1200s	inconclusive
J0740+2926	115.05603	29.44677	D+GMM/WISE	18.20, 19.64	12 Sep, 1200s	NIQ, z=0.98
J0812+3349	123.22844	33.83062	S+GMM	19.75	13 Sep, 1500s	NIQ, z=1.49
J0822+6659	125.57509	66.99985	D+GMM/WISE	18.77, 19.20	31 Mar, 900s	stars
J0823+4929	125.87600	49.48748	D+GMM/WISE	19.41, 19.99	01 Apr, 600s	quasar pair, $z = 0.52, 0.86$
J0826+7002	126.53489	70.04488	S+WISE	17.50	13 Sep, 600s	inconclusive, quasar(+star?)
J0840+3550	130.13842	35.83334	S+GMM/WISE	19.95	31 Mar, 1200s	**lens**, $z = 1.77$, z_{lens}=0.26
J0941+0518	145.34378	5.30664	SDSS spectra	—	31 Mar, 1200s	**lens**, $z = 1.54$, z_{lens}=0.34
J0949+4208	147.47830	42.13381	D+GMM/WISE	18.94, 19.81	31 Mar, 1200s	**lens**, $z = 1.27$, $z_{lens} = 0.51$
J1139+4143	174.94610	41.73088	D+GMM/WISE	19.46, 19.62	01 Apr, 1200s	NIQ, $z = 2.23$
J1147+3634	176.89300	36.57819	D+GMM	19.16, 20.23	31 Mar, 600s	quasar + star
J1239– 2216	189.83645	-22.27778	S+GMM/WISE	18.28	01 Apr, 750s	quasar + galaxy
J1440+3736	220.20396	37.61107	S+WISE	19.27	01 Apr, 600s	galaxy + star
J1508+3844	227.18253	38.73934	D+GMM/WISE	20.21, 20.92	31 Mar, 2700s	**lens**, $z = 1.68$
J1536+3629	234.01479	36.49226	S+GMM	20.51	01 Apr, 600s	galaxy at $z = 0.111$
J1540+4445	235.10759	44.75457	D+GMM/WISE	19.73, 20.37	01 Apr, 600s	NIQ, $z = 0.61$
J1551+3157	237.77584	31.95027	S+GMM/WISE	20.48	31 Mar, 1200s	inconclusive, ($z = 2.27$?)
J1554+2616	238.54871	26.27657	D+GMM/WISE	18.95, 20.03	31 Mar, 600s	quasar + star
J1602+4526	240.70535	45.43528	S+GMM	20.17	31 Mar, 2700s	**lens**, $z = 2.16$, $z_{lens} = 0.43$
J1606– 2333	241.50074	-23.55612	D+WISE	18.74, 18.88	31 Mar, 2400s	**quad lens**, $z = 1.69$
J1611+5756	242.98266	57.93872	S+GMM/WISE	20.24	31 Mar, 600s	galaxies at $z = 0.257$
J1617– 2146	244.25462	-21.76683	D+WISE	19.75, 20.39	01 Apr, 1500s	inconclusive, likely stars
J1617– 2305	244.34009	-23.09620	D+WISE	18.95, 19.23	13 Sep, 1200s	quasar+star
J1640+1045	250.07549	10.75175	D+GMM/WISE	18.12, 19.87	31 Mar, 3000s	**lens**, $z = 1.7$
J1709+3828	257.36966	38.46700	D+WISE	20.07, 20.33	31 Mar, 2650s	**lens**, $z = 1.38$
J1710+4332	257.74257	43.54287	S+GMM	20.49	31 Mar, 2100s	**lens**, $z = 3.08$
J1721+8842	260.45419	88.70621	D+WISE	17.97, 18.24	13 Sep, 4800s	**quad lens**, $z = 2.37$
J1821+6005	275.37642	60.09062	S+WISE	19.96	13 Sep, 1800s	NIQ, z=2.05
J1831+5447	277.86360	54.79965	D+WISE	18.79, 19.86	12 Sep, 1200s	**lens**, z=1.07
J2018– 3015	304.73256	-30.26574	T+WISE	18.26, 18.52, 19.72	12 Sep, 900s	stars+galaxy
J2032– 2358	308.15741	-23.97291	D+WISE	19.04, 19.17	13 Sep, 1200s	NIQ, z=1.64
J2057+0217	314.46696	2.29683	D+GMM/WISE	20.06, 20.10	12 Sep, 1200s	NIQ, z=1.52
J2058– 0744	314.53051	-7.74705	D+WISE	19.72, 19.75	13 Sep, 600s	quasar+star
J2111+1349	317.80707	13.82978	S+WISE	19.74	13 Sep, 600s	quasar+star
J2124+1632	321.07029	16.53841	S+GMM/WISE	19.11	12 Sep, 1200s	**lens**, z=1.28
J2302– 2813	345.74028	-28.22055	S+WISE	18.40	12 Sep, 600s	quasar+star
J2305+3714	346.48273	37.23932	D+WISE	17.55, 18.71	12 Sep, 1200s	**lens**, z=1.78
J2327+2238	351.75343	22.63698	D+GMM/WISE	20.68, 20.75	13 Sep, 600s	quasar pair, z=0.53, 0.55
J2332– 1852	353.08034	-18.86853	S+WISE	19.48	12 Sep, 1200s	**lens**, z=1.49
J2350– 1930	357.58645	-19.51585	D+WISE	19.49, 20.71	13 Sep, 600s	quasar+star

Fig. 2.2 Spectra of lensed quasars from Pan-STARRS+*Gaia*-DR1 selection. The fluxes of the brighter components (red) have been shifted.

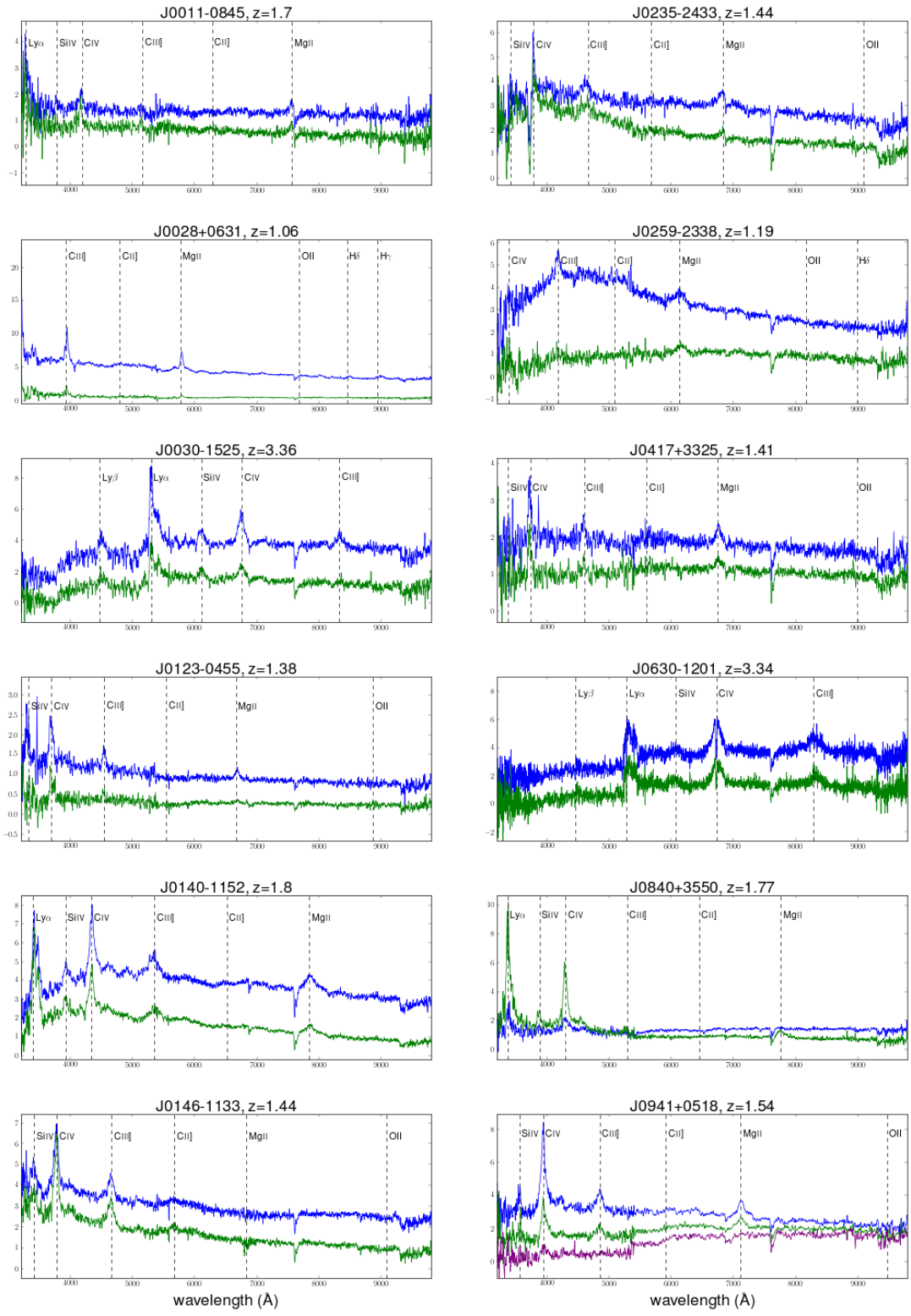

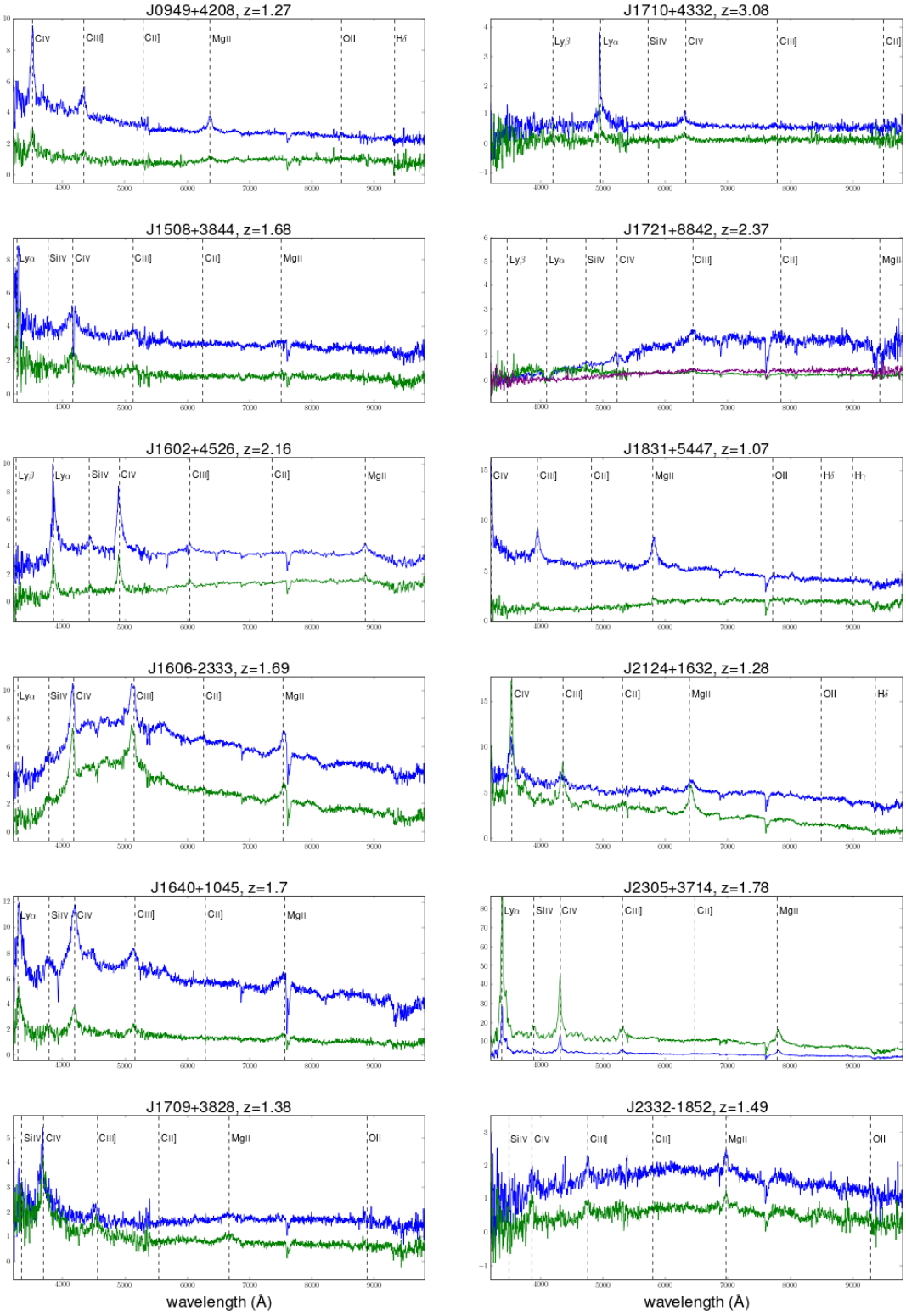
J0949+4208, z=1.27
CIV
CIII]
CII]
MgII
OII
Hδ
J1710+4332, z=3.08
Lyβ
Lyα
SiIV
CIV
CIII]
CII]
J1508+3844, z=1.68
Lyα
SiIV
CIV
CIII]
CII]
MgII
J1721+8842, z=2.37
Lyβ
Lyα
SiIV
CIV
CIII]
CII]
MgII
J1602+4526, z=2.16
Lyβ
Lyα
SiIV
CIV
CIII]
CII]
MgII
J1831+5447, z=1.07
CIV
CIII]
CII]
MgII
OII
Hδ
Hγ
J1606-2333, z=1.69
Lyα
SiIV
CIV
CIII]
CII]
MgII
J2124+1632, z=1.28
CIV
CIII]
CII]
MgII
OII
Hδ
J1640+1045, z=1.7
Lyα
SiIV
CIV
CIII]
CII]
MgII
J2305+3714, z=1.78
Lyα
SiIV
CIV
CIII]
CII]
MgII
J1709+3828, z=1.38
SiIV
CIV
CIII]
CII]
MgII
OII
J2332-1852, z=1.49
SiIV
CIV
CIII]
CII]
MgII
OII
wavelength (Å)
wavelength (Å)

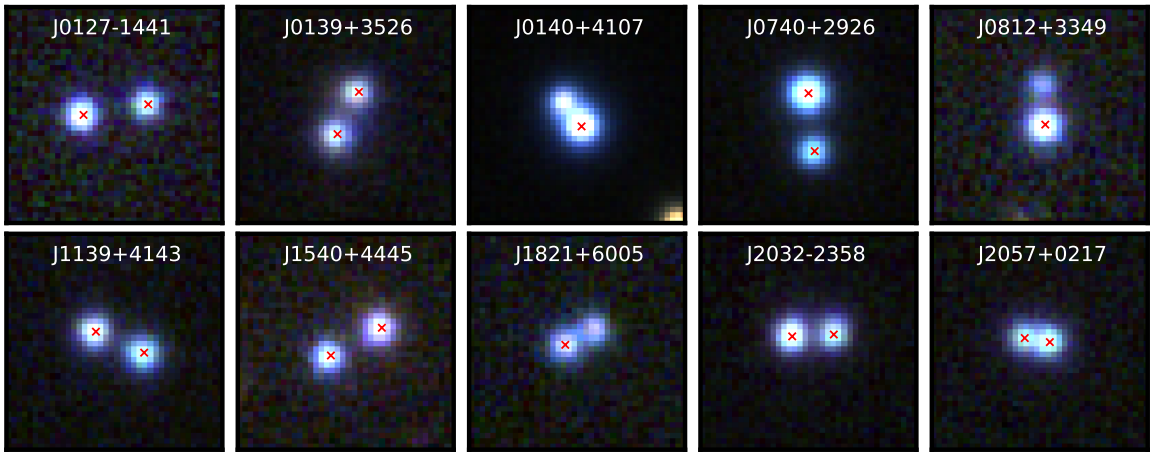

Fig. 2.3 Pan-STARRS *gri* colour images of the nearly identical quasars. Cutouts are 10". PSJ0140+4107 has since been upgraded to a lensed quasar, since NIRC2 data reveal a lensing galaxy between the quasars.

not only on the lens potential but also on extinction, quasar variability over the time delay, microlensing, etc. Using these pixel-based measurements and their uncertainties, the lens parameters are sampled by comparing model image positions in the image plane. Given the extra information in quads, we are able to use more realistic models with more parameters. We use SIE+shear models for these systems.

The lens model parameters (medians with 68% confidence intervals) and χ^2 contributions are listed in Table 2.4. For the three quadruply imaged lensed quasars we include a 50% uncertainty on the input fluxes for the two saddle point images in each system, in accordance with their increased susceptibility to microlensing (Schechter and Wambsganss, 2002).

Systems with significantly elliptical SIE fits and a large image-position χ^2 are indicative of a strong external shear if the lens is not elliptical in the photometry.

2.3 DES

While there is significant overlap between the DES and Pan-STARRS footprints, the DES imaging extends further South, and has deeper imaging, allowing detection of faint lensing galaxies. The repeated imaging nature of DES also provides ancillary data for any lens found within the footprint (see Chapter 5).

Table 2.4 Median parameter values with 1σ uncertainties for mass models and light profiles. b=Einstein radius, PA= position angle (north of west), q=axis ratio, μ=total source magnification. † The mass model and galaxy light profile for J0030-1525 are based on better seeing VST-ATLAS data (Shanks et al., 2015) as described in Section 2.4.

name	b (")	PA_{SIE}	q_{SIE}	PA_{light}	q_{light}	${\chi^2}_{gal}$	${\chi^2}_{images}$	${\chi^2}_{flux}$	μ
J0011–0845	$0.96^{0.01}_{0.01}$	176^{1}_{2}	$0.70^{0.03}_{0.02}$	99^{32}_{44}	$0.86^{0.12}_{0.13}$	0.07	0.19	0.03	$5.0^{0.3}_{0.5}$
J0028+0631	$1.43^{0.01}_{0.01}$	55^{3}_{4}	$0.81^{0.02}_{0.02}$	58^{4}_{4}	$0.86^{0.02}_{0.02}$	0.07	0.19	0.02	$4.2^{0.2}_{0.1}$
J0030–1525†	$1.08^{0.07}_{0.03}$	170^{12}_{5}	$0.82^{0.13}_{0.49}$	55^{2}_{4}	$0.81^{0.02}_{0.02}$	0.97	13.0	13.1	71^{17}_{42}
J0123–0455	$0.96^{0.01}_{0.01}$	136^{4}_{2}	$0.72^{0.03}_{0.04}$	6^{4}_{5}	$0.84^{0.02}_{0.02}$	0.04	0.09	0.01	$3.5^{0.2}_{0.1}$
J0140–1152	$0.72^{0.01}_{0.01}$	127^{22}_{7}	$0.56^{0.01}_{0.02}$	101^{12}_{7}	$0.92^{0.03}_{0.03}$	0.07	0.18	0.01	$10.3^{1.1}_{1.0}$
J0146–1133	$0.83^{0.01}_{0.01}$	$4.5^{0.9}_{1.1}$	$0.52^{0.06}_{0.07}$	175^{1}_{1}	$0.43^{0.02}_{0.02}$	0.03	0.11	0.01	$3.9^{0.1}_{0.1}$
J0235–2433	$1.04^{0.01}_{0.01}$	44^{1}_{3}	$0.74^{0.01}_{0.01}$	68^{2}_{3}	$0.89^{0.02}_{0.01}$	0.06	0.19	0.02	$5.4^{0.1}_{0.1}$
J0259–2338	$1.41^{0.01}_{0.01}$	99^{2}_{2}	$0.67^{0.03}_{0.02}$	86^{62}_{58}	$0.98^{0.02}_{0.02}$	0.06	0.17	0.04	$3.1^{0.1}_{0.1}$
J0417+3325	$0.82^{0.01}_{0.01}$	173^{2}_{2}	$0.65^{0.03}_{0.01}$	177^{1}_{1}	$0.48^{0.01}_{0.02}$	0.06	0.19	0.01	$4.0^{0.1}_{0.1}$
J0840+3550	$1.43^{0.02}_{0.04}$	164^{2}_{4}	$0.83^{0.05}_{0.04}$	89^{4}_{4}	$0.88^{0.02}_{0.01}$	0.12	0.72	0.39	$4.5^{0.4}_{0.4}$
J0941+0518	$2.72^{0.01}_{0.05}$	97^{12}_{4}	$0.81^{0.01}_{0.04}$	66^{2}_{2}	$0.88^{0.01}_{0.01}$	0.02	0.12	0.01	$5.2^{0.1}_{0.1}$
J0949+4208	$1.23^{0.07}_{0.02}$	155^{2}_{3}	$0.68^{0.08}_{0.06}$	137^{12}_{18}	$0.96^{0.02}_{0.02}$	0.08	0.12	0.02	$3.1^{0.1}_{0.2}$
J1508+3844	$0.92^{0.01}_{0.02}$	103^{4}_{3}	$0.91^{0.02}_{0.03}$	173^{19}_{29}	$0.88^{0.08}_{0.09}$	0.10	0.25	0.03	19^{6}_{4}
J1602+4526	$1.41^{0.03}_{0.01}$	78^{2}_{3}	$0.59^{0.02}_{0.02}$	143^{2}_{3}	$0.74^{0.01}_{0.02}$	0.12	0.19	0.05	$3.4^{0.1}_{0.1}$
J1606–2333	$0.60^{0.01}_{0.01}$	95^{20}_{8}	$0.77^{0.05}_{0.08}$	130^{43}_{26}	$0.67^{0.28}_{0.16}$	0.21	9.9	0.54	$9.4^{1.3}_{0.9}$
J1640+1045	$1.04^{0.01}_{0.01}$	122^{1}_{4}	$0.31^{0.04}_{0.01}$	119^{5}_{5}	$0.88^{0.02}_{0.02}$	0.05	0.07	0.01	$7.6^{0.6}_{2.0}$
J1709+3828	$0.96^{0.01}_{0.01}$	170^{1}_{3}	$0.81^{0.02}_{0.02}$	175^{6}_{5}	$0.81^{0.03}_{0.03}$	0.05	0.06	0.01	$10.7^{1.2}_{0.9}$
J1710+4332	$1.21^{0.02}_{0.01}$	62^{67}_{39}	$0.95^{0.03}_{0.02}$	17^{23}_{32}	$0.85^{0.11}_{0.13}$	0.03	0.07	0.02	$5.2^{0.9}_{0.6}$
J1721+8842	$1.99^{0.01}_{0.01}$	169^{4}_{23}	$0.87^{0.09}_{0.05}$	136^{3}_{3}	$0.87^{0.01}_{0.01}$	2.55	0.64	1.2	27^{6}_{4}
J1831+5447	$1.10^{0.01}_{0.01}$	126^{4}_{4}	$0.75^{0.04}_{0.04}$	44^{4}_{3}	$0.87^{0.03}_{0.02}$	0.06	0.18	0.02	$3.1^{0.1}_{0.1}$
J2124+1632	$1.41^{0.01}_{0.01}$	176^{1}_{3}	$0.39^{0.11}_{0.05}$	148^{5}_{3}	$0.75^{0.03}_{0.02}$	0.07	0.11	0.01	$2.7^{0.1}_{0.1}$
J2305+3714	$1.10^{0.01}_{0.01}$	59^{3}_{3}	$0.62^{0.05}_{0.02}$	91^{7}_{6}	$0.88^{0.02}_{0.03}$	0.05	0.07	0.01	$8.6^{1.0}_{0.4}$
J2332–1852	$0.96^{0.01}_{0.01}$	99^{2}_{3}	$0.63^{0.04}_{0.04}$	75^{3}_{3}	$0.51^{0.04}_{0.04}$	0.05	0.13	0.01	$4.5^{0.4}_{0.2}$

Table 2.5 Summary of new Pan-STARRS lensed quasars (image separations are the largest ones for quads). † Lens redshift from Agnello et al. (2018c).

name	z_{source}	z_{lens}	sep. (")	i_{images}, i_{lens}
J0011–0845	1.70	-	1.92	20.09, 20.32
J0028+0631	1.06	-	2.78	18.81, 18.44
J0030–1525	3.36	-	1.78	18.60, 18.88
J0123–0455	1.38	-	2.00	19.42, 18.15
J0140–1152	1.80	0.28†	1.45	18.25, 18.53
J0146–1133	1.44	-	1.69	18.09, 18.70
J0235–2433	1.44	-	2.05	18.74, 18.10
J0259–2338	1.19	-	2.92	19.17, 18.72
J0417+3325	1.41	-	1.59	18.89, 18.54
J0630–1201	3.34	-	1.90	18.30, —
J0840+3550	1.77	0.26	2.46	19.74, 18.03
J0941+0518	1.54	0.34	5.40	18.30, 17.51
J0949+4208	1.27	0.51	2.57	18.88, 19.19
J1508+3844	1.68	-	1.69	20.67, 20.04
J1602+4526	2.16	0.43	2.70	19.81, 18.67
J1606–2333	1.69	-	1.74	17.58, 20.85
J1640+1045	1.70	-	2.22	18.24, 18.67
J1709+3828	1.38	-	1.70	19.90, 19.36
J1710+4332	3.08	-	2.43	20.95, 20.60
J1721+8842	2.37	-	4.03	18.36, 18.02
J1831+5447	1.07	-	2.32	18.80, 18.17
J2124+1632	1.28	-	3.02	18.11, 18.40
J2305+3714	1.78	-	2.20	17.03, 18.32
J2332–1852	1.49	-	1.97	18.76, 18.93

Table 2.6 Summary of nearly identical quasars and binaries.

name	z_{source}	sep. (")	i_{mag}
J0127– 1441	1.76	2.96	19.30
J0139+3526	0.65	2.22	18.49
J0140+4107	2.50	1.44	16.94
J0740+2926	0.98	2.59	18.23
J0812+3349	1.49	1.99	19.12
J1139+4143	2.23	2.30	18.86
J1540+4445	0.61	2.74	19.21
J1821+6005	2.05	1.48	19.34
J2032– 2358	1.64	1.91	18.40
J2057+0217	1.52	1.06	18.96

Fig. 2.4 Spectra of the nearly identical quasars and binaries.

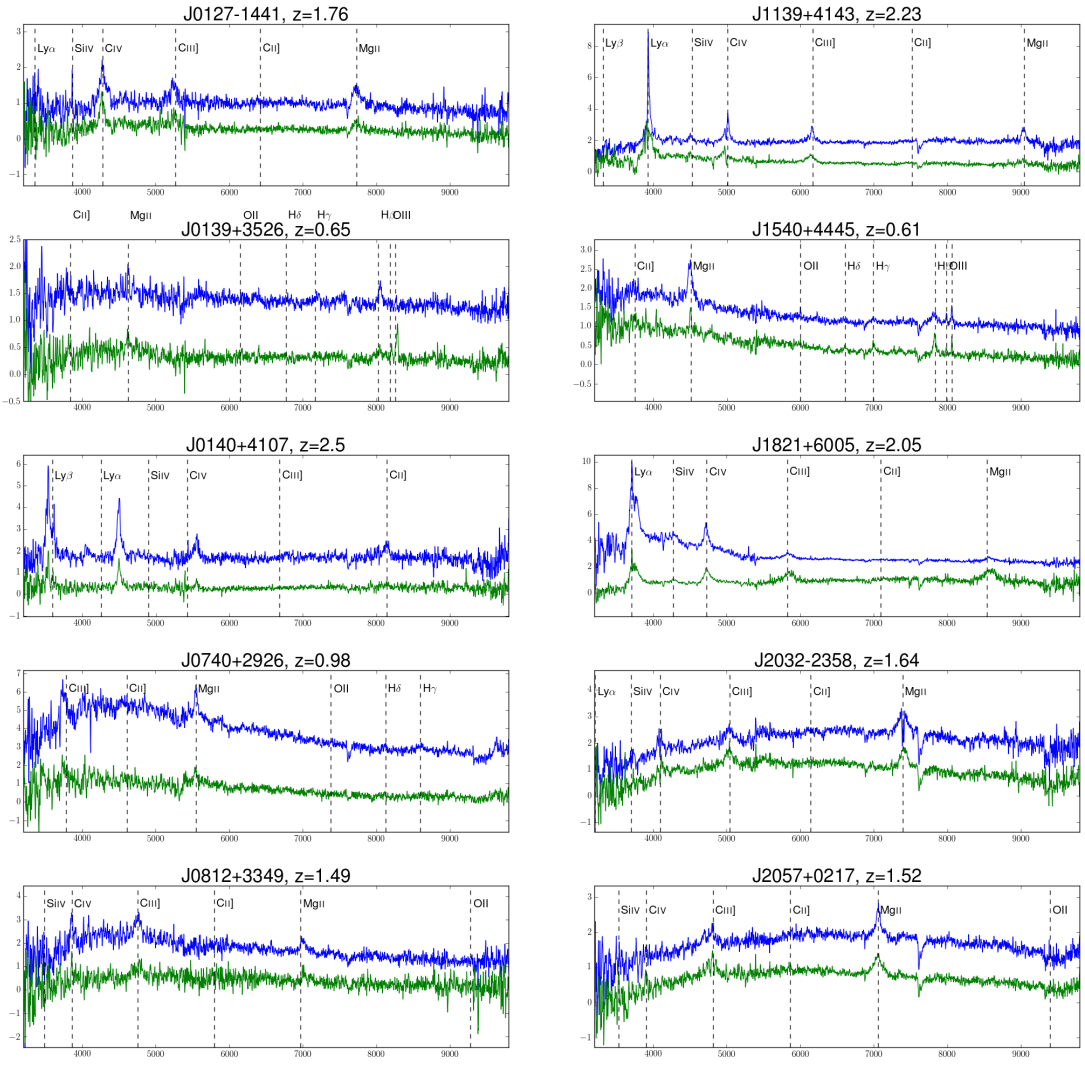

2.3.1 Selection

This selection method is the same as for the Pan-STARRS search, relying on multiple *Gaia* detections near WISE-selected candidate quasars, or single *Gaia* detections corresponding to extended DES objects. The input catalogue for both searches is ALLWISE detections with W1−W2>0.5, W1<15.5, and catalogued uncertainties in W1 and W2. The multiple *Gaia* detection search required at least 2 *Gaia* detections within 4" of the WISE source, and within 5" of each other. The single *Gaia* detection search required one *Gaia* detection within 4" of an extended DES object ($MAG\_PSF\_I - MAG\_AUTO\_I > 0.2$, $MAG\_AUTO\_I < 20.5$). A stellar density cut of < 50,000 *Gaia* detections per square degree was applied to both techniques, resulting in 5,996 and 43,128 candidates, respectively. Candidates were visually

Fig. 2.5 Pixel modelling of the confirmed Pan-STARRS lenses. Left to right: *gri* data, model, *gri* PSF-subtracted, and r-band residuals. Blue crosses indicate the positions of quasar images and red pluses mark the locations of lensing galaxies.

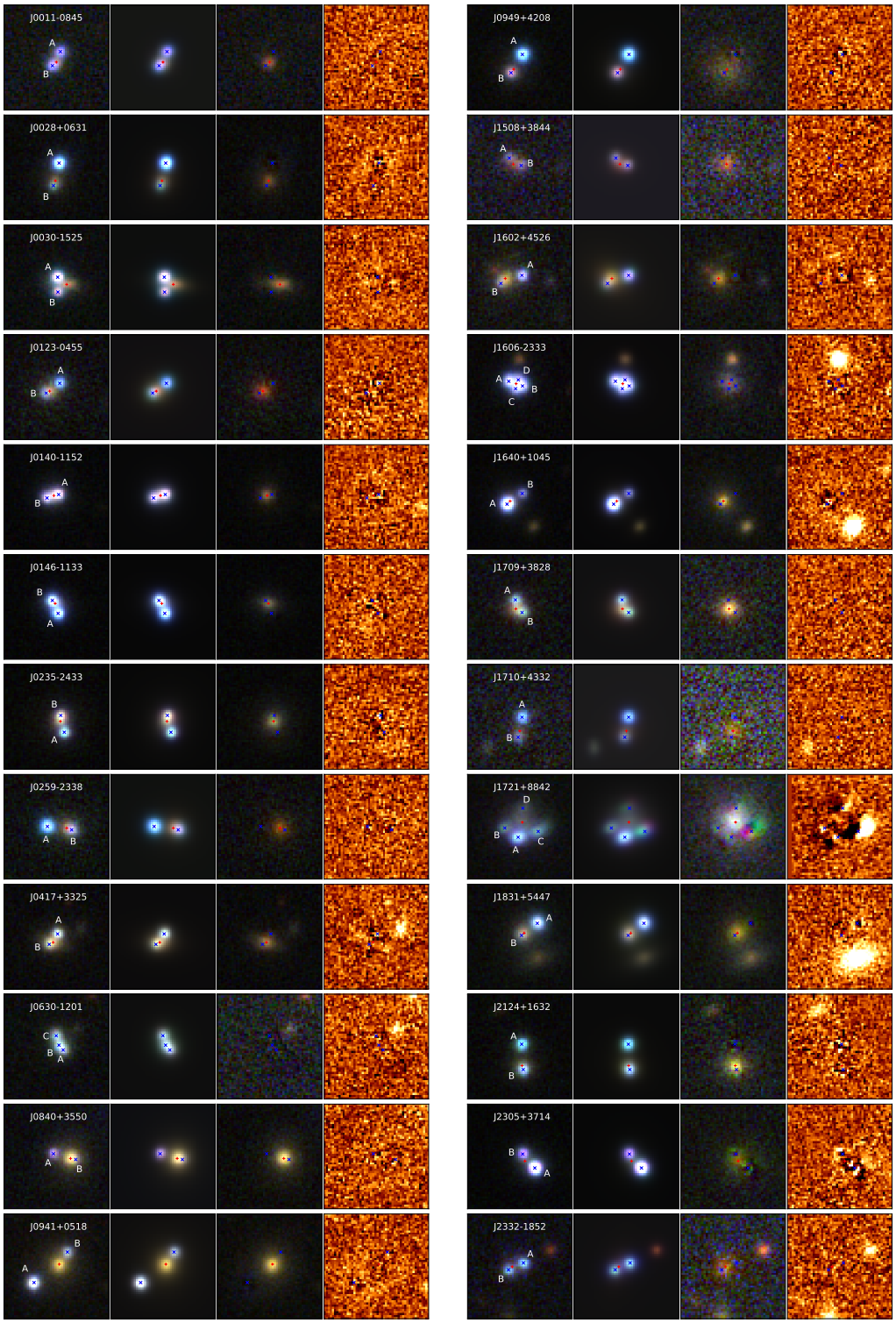

Table 2.7 Confirmed DES-selected lensed quasars. † DESJ0246-1845 was recovered by our search, however it was not proposed by us as a lensed quasar. Instead this system was selected by other members of STRIDES, and we are including our analysis of the system here.

Name	R.A.	Dec.	spectrum	imaging	outcome
DESJ0053-2012	13.4353	-20.2092	EFOSC2	SOAR	**quad**, z≈3.80
DESJ0112-1650	18.1412	-16.8410	ESI	-	**double**, z=0.54 and z=0.99
DESJ0150-4041	27.7369	-40.6956	EFOSC2	SOAR	**double**, z=1.85
DESJ0245-0556	41.3565	-5.9501	EFOSC	SOAR/NIRC2	**double**, z=1.54
DESJ0246-1845	41.55083	-18.7514	EFOSC2	SOAR/NIRC2	**double**, z=1.86
DESJ0340-2545	55.0351	-25.7610	EFOSC2	SOAR/NIRC2	**triple**, z=1.68
DESJ0407-1931	61.9741	-19.5225	EFOSC2	SOAR	**double**, z=0.288 and z=2.26
DESJ0501-4118	75.4413	-41.3003	EFOSC2	SOAR	**double**, z=2.10
DESJ0600-4649	90.1242	-46.8168	EFOSC2	SOAR	**double**, z=2.21
DESJ2349-4518	357.4924	-45.3147	EFOSC2	-	**double**, z=2.90

inspected and graded as in the Pan-STARRS-selected sample. Inconclusive and contaminant systems are listed in their entirety in Appendix 2.

2.3.2 Spectroscopy

Spectroscopic follow-up was performed using grism #13 on the ESO Faint Object Spectrograph and Camera 2 (EFOSC2) on the NTT over the nights of 21-23 October 2017 and 7-9 January 2018, as well as the Echellette Spectrograph and Imager (ESI) on Keck 2 on the nights of 17-18 November 2017. ESI was used in the default Echellette mode.

All 2D spectra were visually inspected to confirm broad emission lines (or lack thereof) in the multiple spatially resolved components, and 1D spectra were extracted using Gaussian apertures of widths dependent on the seeing. Spectra of confirmed lensed quasars are shown in Figure 2.6 (with their DES *gri* colour cutouts shown in Figure 2.7), and spectra of quasar pairs in Figure 2.8.

2.3.3 High resolution imaging

3 systems were observed using the Near InfraRed Camera 2 (NIRC2) on Keck-2, and 16 observed using the Southern Astrophysical Research Telescope (SOAR) Adaptive optics Module Imager (SAMI), as listed in Tables 2.7 and 2.8. The data reduction and modelling for the two datasets are described as follows.

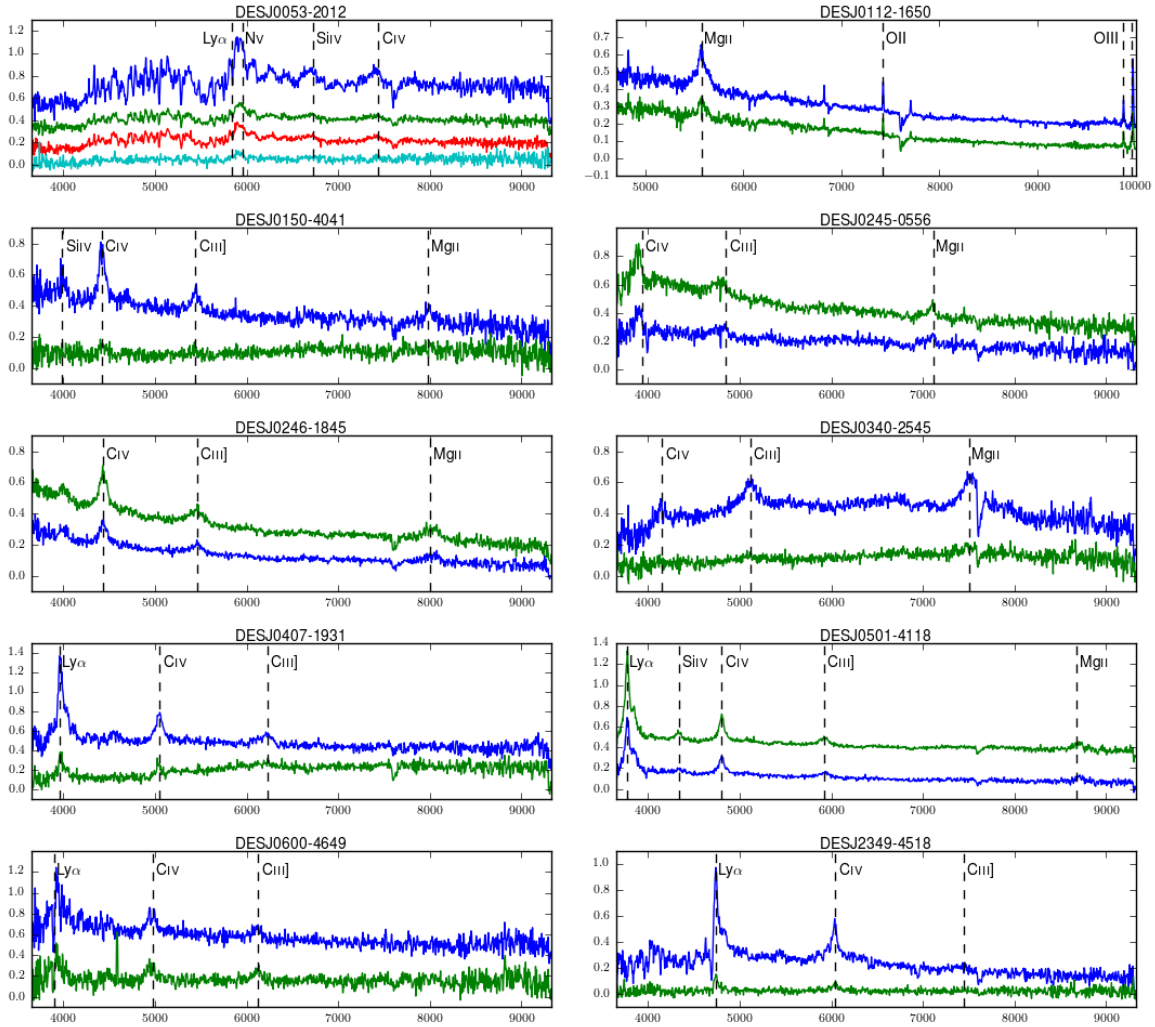

Fig. 2.6 Spatially resolved spectra of quasar images of the confirmed lensed quasars from DES. The flux is in arbitary units and in some cases the spectra have been offset to aid comparison of the spectra.

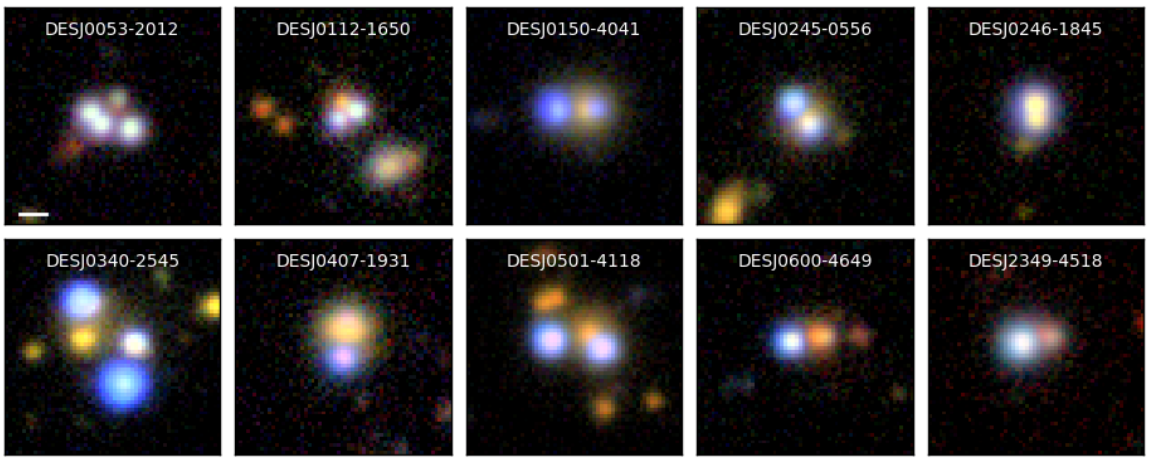

Fig. 2.7 DES *gri* colour images of the confirmed lensed quasars. Cutouts are 16.2" on the side. The white scale bar in the first panel is 2".

NIRC2

DESJ0245-0556, DESJ0246-1845, and DESJ0340-2545 were observed with the NIRC2 narrow camera, giving a 10×10 arcsecond field of view and 10 mas pixels. Observations were taken in the K′ band in order to maximise the effect of the AO correction. Since there are no other PSFs in the field of the narrow camera, we reconstruct the PSF based on the data. While this can lead to fitting real structures such as host galaxy light, particularly degenerate for doubles, using analytical profiles often leaves significant residuals at the cores of PSFs where we would expect the lensed host galaxy to be brightest (Chen et al., 2016; Rusu et al., 2016). The PSF reconstruction is performed for each set of position and galaxy parameters, for a square PSF grid (with pixel sizes the same as the data) and linear interpolation. The reconstructed PSF from the best-fit model is used for convolution with the Sersic galaxy profiles. Since this PSF might not represent the true PSF, and due to atmospheric variations between frames, we include a positional uncertainty of 5mas (half a pixel) in quadrature on our sampled statistical uncertainty. All three candidates observed by NIRC2 are lensed quasars, with their data, PSF subtractions, and model subtractions shown in Figure 2.9.

SOAR

16 candidates were observed with the SAMI instrument with its AO system SAM (Tokovinin et al., 2016). Imaging was carried out in the z-band to maximise AO correction and optimise the contrast between quasar images and possible lensing galaxies. The pixel scale was 0.09 arcsec per pixel (2×2 binning of 0.045 arcsec per pix) and the typical exposure times were 3×180s.

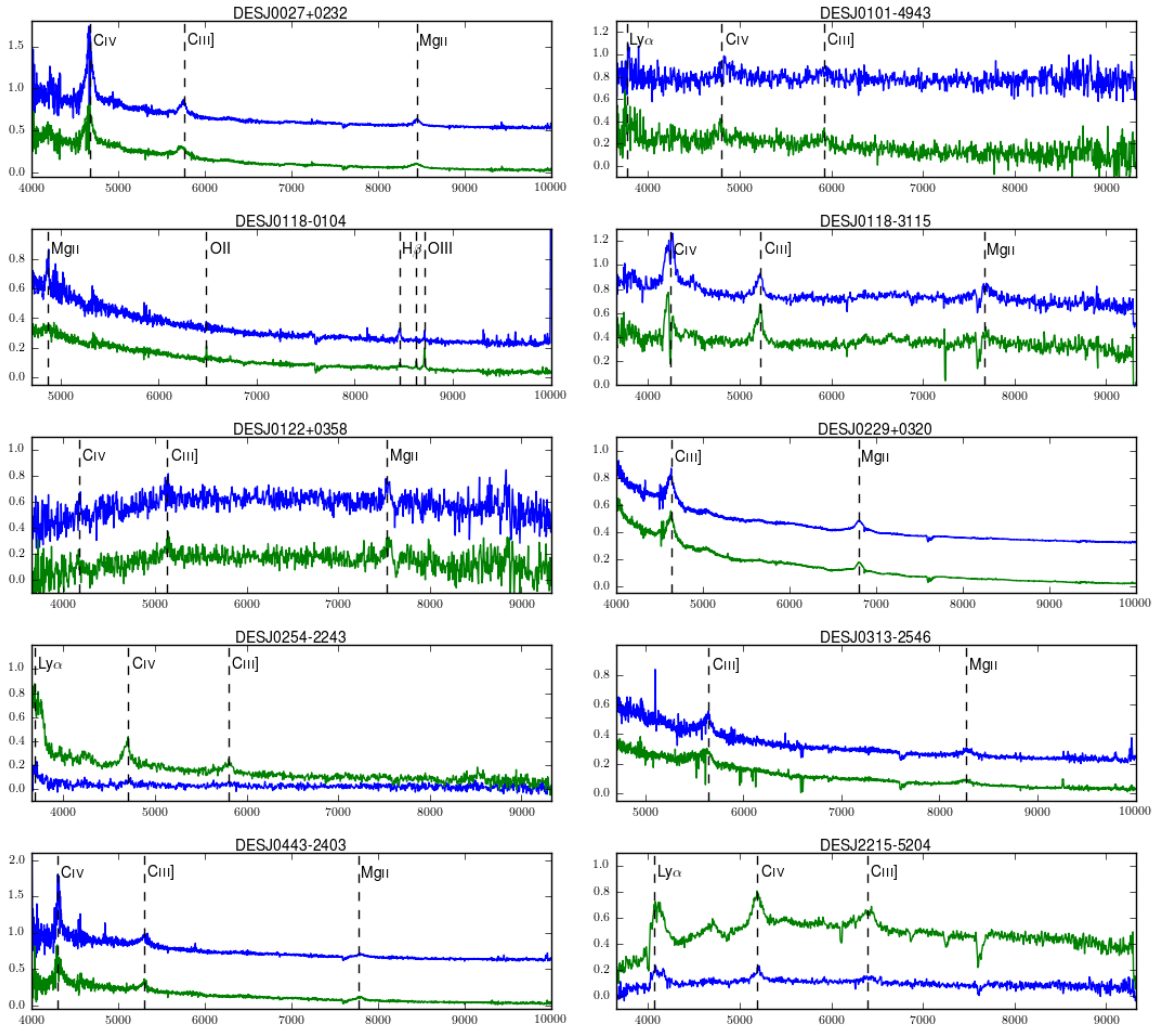

Fig. 2.8 Spatially resolved spectra of pairs of quasars at similar (or possibly the same) redshifts discovered in the DES sample. The flux is in arbitrary units and in some cases the spectra have been offset to aid comparison of the spectra. DESJ0118-3115 and DESJ0229+0320 were not selected with our technique, but by other STRIDES members. We include our analysis and reduced spectra here.

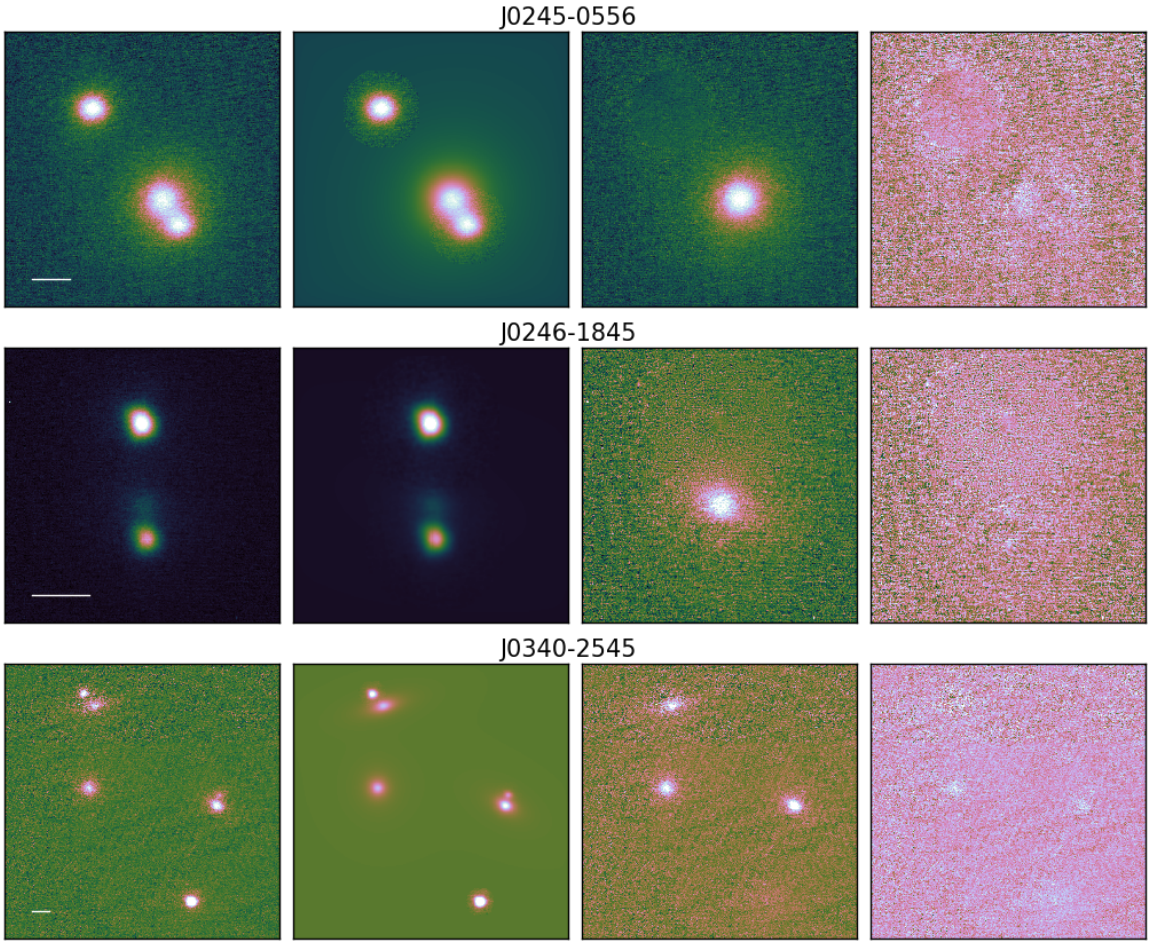

Fig. 2.9 NIRC2 AO data for confirmed lensed quasars. From left to right: data, model, PSFs subtracted, and PSFs and galaxy subtracted. The white scale bar is 0.5". Flux is displayed using the cubehelix colour scheme (Green, 2011a).

Given the large field of view (3×3 arcminutes), nearby stars were used to fit Moffat profiles. When a good fit was achieved the Moffat parameters were used for the PSF model of the candidate system. If this PSF did not fit the system well, the Moffat parameters were included as part of the modelling of the system and simultaneously inferred with the galaxy and image parameters. If this was still a poor description for the system's PSF, a nearby star was used, and pixel shifts were computed via a spline interpolation. All quasar pairs and inconclusive candidates, as listed in Tables 2.8 and Appendix B respectively, were consistent with 2 PSFs when modelling the SOAR data. The data, PSF subtractions, and model subtractions for lenses without NIRC2 data are shown in Figure 2.10.

2.3.4 DES Modelling

As described in Section 2.2.6, we are able to construct simple SIE mass models for our confirmed lenses. NIRC2 and SOAR positions are used for all lenses except for DESJ0112-1650 and DESJ2349-4518, which lack high resolution imaging. For these systems we use the DES data, which is modelled as in Chapter 5. For the triply imaged system, DESJ0340-2545, and the quad, DESJ0053-2012, we explore more complex mass models as described in Section 2.4. Table 2.9 summarises the model parameters of the lens systems.

Table 2.8 Quasar Pairs. NIQ stands for nearly identical quasar pair

Name	R.A.	Dec.	spectrum	imaging	outcome
DESJ0027+0232	6.7619	2.5375	ESI	-	z=2.02 NIQ
DESJ0101-4943	15.3366	-49.7234	EFOSC2	-	z=2.10 NIQ
DESJ0118-0104	19.5501	-1.0785	ESI	-	z=0.74 NIQ
DESJ0122+0358	20.5990	3.9771	EFOSC2	SOAR	z=1.69 NIQ
DESJ0254-2243	43.5720	-22.7315	EFOSC2	SOAR	z=2.04 NIQ
DESJ0313-2546	48.4088	-25.7751	ESI	SOAR	z=1.955 NIQ
DESJ0330-4413	52.5070	-44.2266	EFOSC2	SOAR	projected QSOs, z=0.52, 1.25
DESJ0443-2403	70.9802	-24.0572	ESI	SOAR	z=1.78 NIQ
DESJ2215-5204	333.9171	-52.0679	EFOSC2	-	z=2.35 NIQ

2.4 Notes on individual systems

PSJ0030–1525

The Pan-STARRS *gri* image for this object shows two bright PSFs and a galaxy significantly offset from where it should lie to create a double-image system. However a better seeing VST *r*-band image, Figure 2.11, resolves four objects including a faint blue PSF next to an

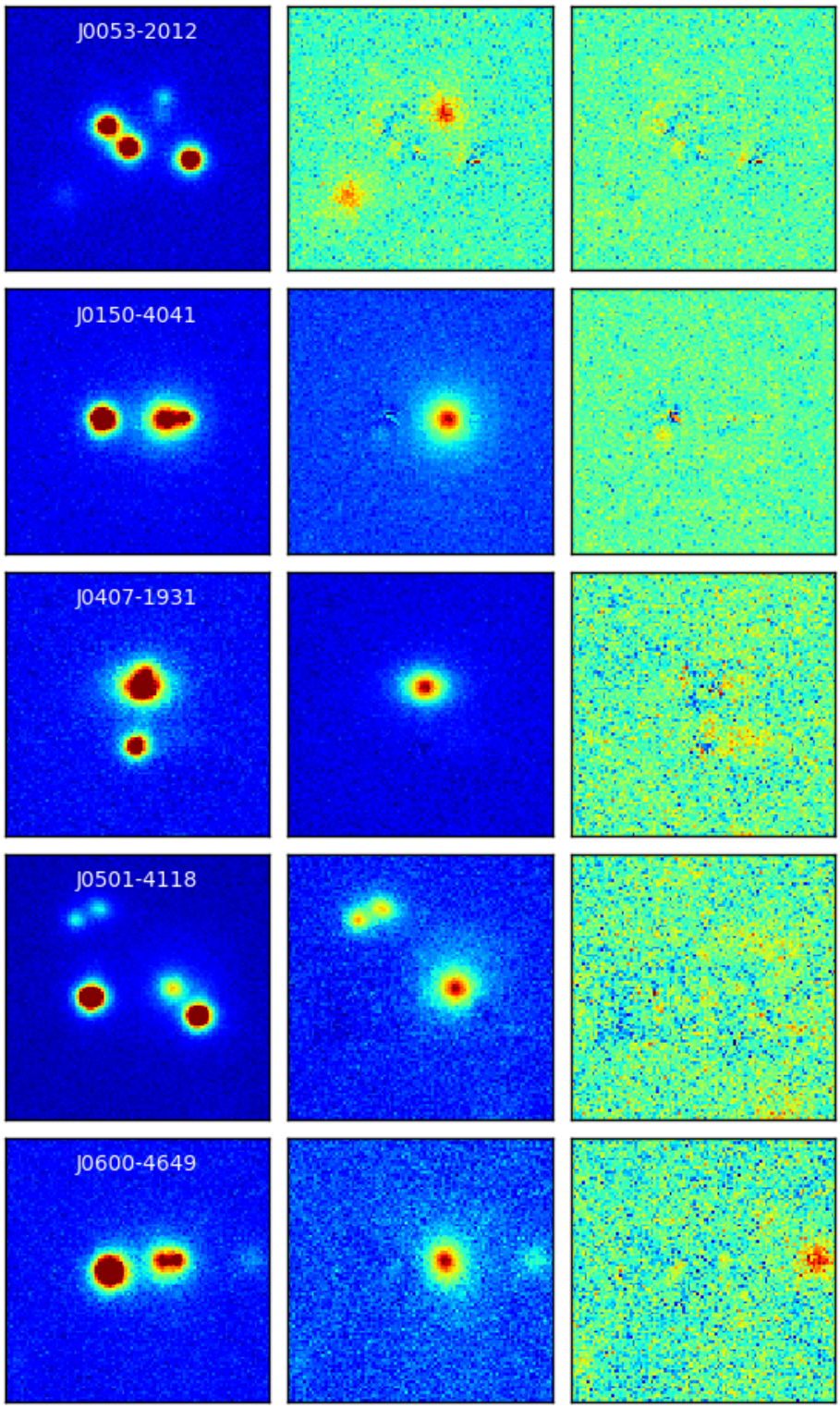

Fig. 2.10 Left: SOAR z-band cutouts for confirmed lensed quasars; middle: PSF subtracted images; right: PSF and galaxies subtracted. Cutouts are 9" on the side.

Table 2.9 Median parameter values with 1σ uncertainties for mass model and galaxy light profiles of confirmed lensed quasars. b=Einstein radius, PA= position angle (East of North), q = axis ratio, and μ = total source magnification. Given the group lensing DESJ0340-2545, more detailed mass models are described in the text and Table 2.13 for this system. The model we use for DESJ0053-2012 is a 2 SIE model. For this model, we expect a good fit to have $\chi^2 \approx 3$.

name	b (")	PA_{SIE}	q_{SIE}	PA_{phot}	q_{phot}	$\chi^2{}_{gal.,images,flux}$	μ
DESJ0053-2012	$1.17^{0.01}_{0.01}$	78^{2}_{3}	$0.56^{0.04}_{0.03}$	111^{10}_{9}	$0.67^{0.11}_{0.09}$	0.19, 0.03, 2.21	$17.3^{0.5}_{0.7}$
DESJ0112-1650	$0.77^{0.01}_{0.01}$	75^{6}_{5}	$0.69^{0.01}_{0.02}$	84^{1}_{2}	$0.77^{0.01}_{0.02}$	0.00, 0.00, 0.00	$5.68^{0.14}_{0.04}$
DESJ0150-4041	$1.44^{0.02}_{0.02}$	14^{6}_{4}	$0.86^{0.04}_{0.05}$	0^{13}_{14}	$0.96^{0.02}_{0.02}$	0.00, 0.00, 0.00	$4.47^{0.02}_{0.02}$
DESJ0245-0556	$0.90^{0.02}_{0.01}$	41^{3}_{2}	$0.67^{0.11}_{0.10}$	67^{3}_{3}	$0.947^{0.005}_{0.005}$	0.00, 0.00, 0.00	$3.16^{0.03}_{0.04}$
DESJ0246-1845	$0.49^{0.01}_{0.01}$	-21^{12}_{26}	$0.92^{0.03}_{0.06}$	168^{1}_{1}	$0.44^{0.02}_{0.03}$	0.00, 0.00, 0.00	$4.56^{0.07}_{0.07}$
DESJ0407-1931	$1.30^{0.02}_{0.01}$	44^{20}_{20}	$0.92^{0.02}_{0.03}$	177^{1}_{1}	$0.70^{0.02}_{0.02}$	0.00, 0.00, 0.00	$3.61^{0.03}_{0.02}$
DESJ0501-4118	$1.97^{0.03}_{0.03}$	-76^{3}_{3}	$0.43^{0.02}_{0.02}$	131^{7}_{7}	$0.90^{0.03}_{0.02}$	0.00, 0.00, 0.02	$3.35^{0.22}_{0.19}$
DESJ0600-4649	$1.22^{0.02}_{0.02}$	-3^{5}_{8}	$0.85^{0.05}_{0.07}$	12^{6}_{6}	$0.85^{0.04}_{0.04}$	0.00, 0.00, 0.00	$4.27^{0.04}_{0.04}$
DESJ2349-4518	$1.24^{0.02}_{0.02}$	-21^{2}_{3}	$0.59^{0.03}_{0.03}$	-33^{9}_{11}	$0.73^{0.06}_{0.06}$	0.26, 0.01, 0.98	$4.84^{0.59}_{0.50}$

extended red object. This is consistent with a flux-ratio anomaly fold-configuration quad with the faint PSF being the counterimage. We model the Pan-STARRS data for photometry of A+B, C and D+G, given in Appendix A. However for the mass model we use the VST r-band data given its excellent seeing and resolution of the counterimage. The PSF is inferred from the data due to the lack of a nearby star. We find that the data are fit by models with the merging pair consisting of a bright image north-west of a faint image or vice versa. The former is much more plausible given that saddle points are more commonly demagnified than maxima and minima (Schechter and Wambsganss, 2002) and so this is the mass model we report in Table 2.4. The best fit mass model gives flux ratios of $\sim$ 7:7:3:1 while the measured flux ratios are $\sim$ 7:0.5:4:1, i.e., a 14$\times$ decrease for image B.

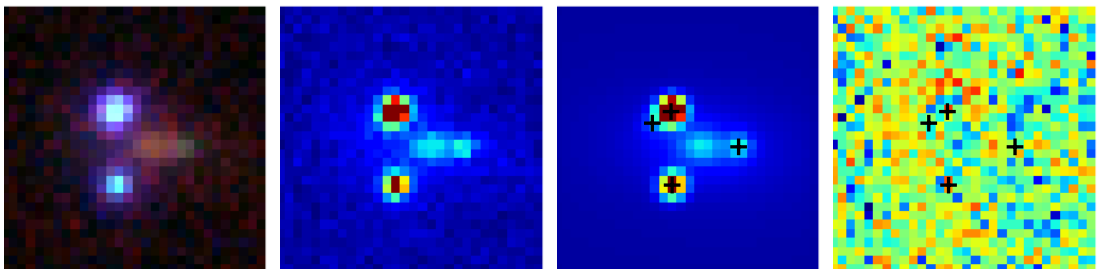

Fig. 2.11 From the left: PSJ0030-1525 VST *grz* colour image; 0.42"-seeing r-band VST image; 4PSFs+galaxy model with PSF positions overlaid; residuals after model subtraction.

PSJ0127–1441

DECaLS data reveal two faint red objects between the two PSFs that could be lensing galaxies. These are only detected in the z-band data and each has a magnitude of ~ 24. Comparing to mock lenses from OM10 with similar source redshift and image separation, the faintest i-band lens magnitudes are ~ 22. While the multiple component nature of this putative lens complicates the comparison, the faintness and large separation suggests either a binary quasar or high-redshift group lens. Deeper data will help secure the magnitudes of these objects.

PSJ0139+3526

While this was a promising candidate given the similar SEDs and residuals consistent with a lensing galaxy, the redshift of the quasars is low ($z = 0.65$) and the [OIII] emission lines are significantly different. There is no discernible redshift difference from the spectra, so this system is likely a quasar merger in which we are seeing the onset of AGN activity. The residuals are probably associated with the quasar host galaxies interacting. A nearby bright star makes this system ideal for adaptive optics follow-up.

PSJ0140–1152

This lens has been independently identified in the VST-ATLAS survey by Agnello et al. (2018c), who report a lens redshift of 0.277. It is a highly magnified (~ 10 times) double. The elliptical mass model suggests a strong external shear given the relatively circular light profile of the galaxy.

PSJ0140+4107

This system was originally reported as a quasar pair, with similar spectra at z=2.50. Follow-up imaging with NIRC2 on Keck reveals two point sources with a galaxy in between, shown in Figure 2.12, confirming this system as a lensed quasar. The images are bright (G=17.62, 18.50) and separated by 1.33".

PSJ0235–2433

Agnello et al. (2018b) have independently selected this object as a candidate gravitational lens from the Dark Energy Survey (DES) footprint (The Dark Energy Survey Collaboration,

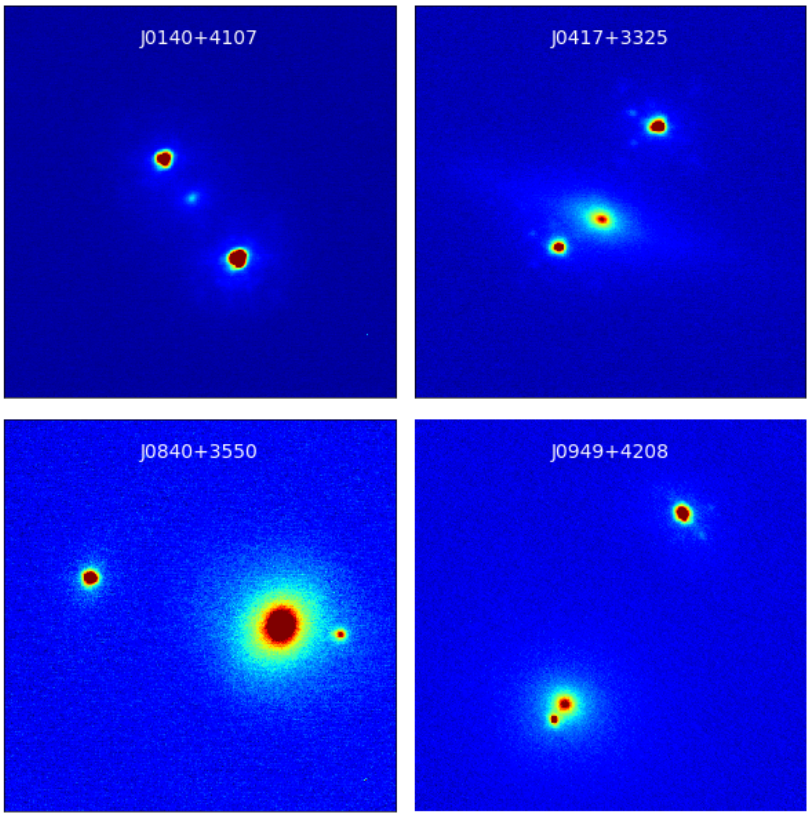

Fig. 2.12 NIRC2 imaging of four gravitationally lensed quasars identified in Pan-STARRS, via the presence of multiple or single *Gaia* detections.

2005). We confirm the PSFs to be quasars at a redshift of z=1.44. The DES data displayed in Agnello et al. (2018b) show that the image closest to the lens galaxy is brighter than the other, while the opposite is true in the Pan-STARRS data. This change by approximately one magnitude within less than a few years (mean epoch for the Pan-STARRS detection is 56475, and ∼57350 for DES (Abbott et al., 2018)) is likely attributed to a microlensing event rather than quasar variability. Indeed in the *Gaia* data, the closest and furthest images have magnitudes of G=18.12 and G=18.85 respectively. Since both images are detected by *Gaia*, they will have well-sampled lightcurves over 5 years. When released, these lightcurves will clearly distinguish a microlensing event in one image from quasar variability which would be seen in both images but separated by the time delay. Support for the microlensing interpretation from the DES lightcurves is presented in Chapter 5.3.2.

PSJ0417+3325

This double has an elliptical lens galaxy ($q = 0.48$) and the SIE lens model is aligned along the same position angle but less elliptical ($q = 0.65$). It was originally detected by Colla et al.

(1970) at 408MHz with a flux of 290 mJy, and subsequently at 5GHz by Davis (1971) and Altschuler (1986) with detections of 60 mJy and 39 mJy respectively. It is also detected in NVSS (Condon et al., 1998) at 1.4GHz with a flux density of 109mJy. Archival 8GHz VLA data show two point sources in the same positions as the optical quasar point sources with a hint of a third source south of image A. There is an extended radio source 3" west of the system, lacking any optical detection in Pan-STARRS. The A to B flux ratio at 8GHz is 1.2, while the g-band ratio—the magnitudes least affected by the presence of the lens galaxy—is 2.0, a discrepancy that could be explained by a number of effects including microlensing or extinction. The presence of a radio source is promising for using resolved source structure and radio flux ratios to precisely constrain lens models.

PSJ0630–1201

This system was identified in a Pan-STARRS+WISE photometric quasar catalogue as explained in Ostrovski et al. (2017). After the spectroscopic confirmation of multiple quasars, the system was observed on April 11 2017 UT with the NIRC2 camera mounted on Keck 2. Four 180s exposures were obtained with the K' filter. These data clearly resolve the three quasars observed with WHT spectroscopy (A, B, and C in Figure 2.13), and also reveal two additional point-like objects (D and E) and two extended objects (G1 and G2). Note that most of the structure around the bright images is an artefact ("waffling") due to AO correction problems with the low-bandwidth wavefront sensor.

The PSF of image C appears to have a structure extending down from the core of the PSF that is not seen in images A or B but could be consistent with a lensed arc. We therefore produced a pixellated model of the PSF around the images ABC to remove it and increase the dynamic range of the image. In the first iteration of this procedure an arc between images B and C was clearly visible, and we therefore re-fitted for the PSF excluding pixels that contain arc flux. The residuals of this fit are shown in the middle and right panels of Figure 2.13.

The AO imaging data show that PS J0630-1201 is a lensed quasar in a 'cusp' configuration, with two lensing galaxies. The presence of a fifth point source, E in Figure 2.13, is intriguing as it is located approximately where the fifth (demagnified) image would be expected to appear. To understand the nature of E as a possible fifth quasar image, we initially create a mass model using the positions of the brighter quasar images (A to D) and the two lensing galaxies, and use this model to predict the location of any additional images. We first determine the position of each point source by modelling them with Gaussian or Moffat profiles, and we fit Sersic profiles to G1 and G2. We also perform moment-based centroiding in a range of apertures, and use the spread of all of our measurements to estimate the uncertainties on the positions; these are typically $\sim$1 mas for the point sources and $\sim$10

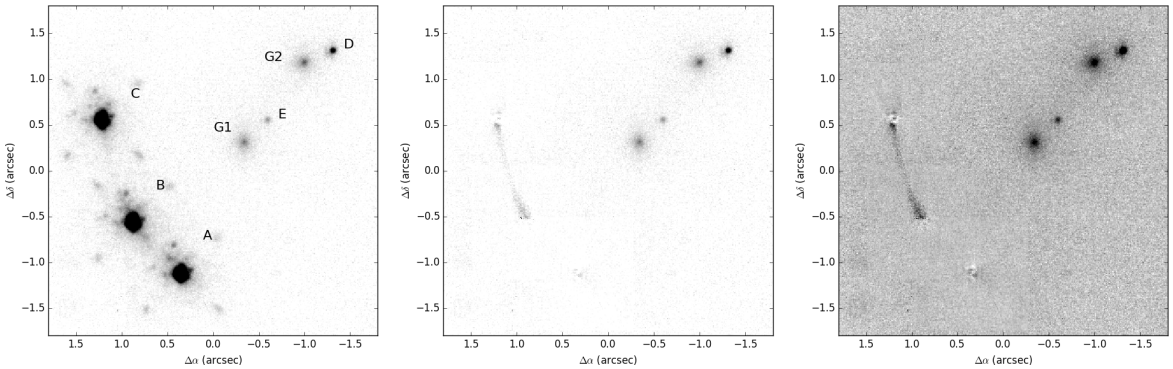

Fig. 2.13 (Left) NIRC2 K' AO imaging of PS J0630-1201. The four images ABCD are in a canonical 'cusp' configuration, but note the presence of two galaxies, G1 and G2, as well as the additional point source E. The additional structure around the images A, B, and C is due to poor wavefront correction. (Middle) The same as the left panel, but with a model for the AO PSF subtracted from the three brightest images, revealing the presence of a faint arc. (Right) Same as the middle but with enhanced contrast to better show the lensed quasar host galaxy.

to 20 mas for the galaxies. However, we also find that the relative positions of the quasar images change from exposure to exposure, presumably due to atmospheric fluctuations, and we therefore impose a 5 mas minimum uncertainty on each position.

We use the positions of the galaxies and point sources to constrain a lensing mass model. The two galaxies are initially modelled as singular isothermal spheres and we use the positions of the four brighter images to infer their Einstein radii. The best-fit lens model predicts a fifth image near the location of image E with a flux approximately half of image D, comparable to the observed flux ratio. We consequently use the position of E to constrain a more realistic lens model, allowing the two galaxies to have some ellipticity, and we include an external shear. This model has five free parameters for each galaxy (two position parameters, an Einstein radius, and an ellipticity with its orientation) and two additional parameters each for the position of the source and the external shear, i.e., there are 14 total parameters. We likewise have 14 constraints from the observed positions of the five quasar images and the two lensing galaxies.

We model the system as described in Section 2.2.6, with two SIE components. Both mass components are inferred to be coincident with the light, with Einstein radii for G1 and G2 of 1.01 ± 0.01" and 0.58 ± 0.01", respectively. Both masses are also mildly flattened, but we find that the light and mass *orientations*, given in Table 2.10, are significantly misaligned. We also note that the shear is well constrained ($\gamma = 0.14 \pm 0.01$ with PA$=-76$) and is particularly

large, though there is no nearby galaxy along the shear direction. The total magnification for the system is $\sim$53.

Table 2.10 Light and mass shape parameters for the lens galaxies. Position angles are East of North.

	PA (light)	q (light)	PA (mass)	q (mass)
G1	-9 $\pm$ 4	0.81 $\pm$ 0.03	-21 $\pm$ 6	0.81 $\pm$ 0.02
G2	-69 $\pm$ 4	0.79 $\pm$ 0.03	-2 $\pm$ 7	0.83 $\pm$ 0.04

We recover flux ratios to within 30% with discrepancies likely caused by microlensing and/or differential extinction and reddening, as evidenced by the strongly varying flux ratio between images B and C from optical to near-infrared wavelengths. The mass-light orientation misalignment and large shear could be the result of an additional mass component, e.g., a dark matter halo that is not coincident with either galaxy (e.g., Shu et al., 2016). In that case, the weak demagnification of the fifth image might indicate that the dark matter halo is not cuspy (e.g., Collett et al., 2017), although constraints from the quasar image positions alone are not sufficient to test this. Deeper imaging of the arc of the lensed host galaxy and observations at radio wavelengths, where extinction and the effects of microlensing are no longer important, will help to constrain a more complex model for the mass distribution.

The relatively bright fifth image of PSJ0630-1201 also presents the possibility of obtaining four new time delay measurements, for a total of ten time delays. Based upon our current best lens model, these delays should range between 1 and 245 days for lens redshifts between z=0.5 and z=1 (Table 2.11). Because of the overall compactness of the system and the presence of the two lensing galaxies, it would be difficult to obtain time delays from the fifth image with conventional seeing-limited monitoring programmes. However, if such a campaign observed a sudden brightening (or dimming) event in one of the brighter images, dedicated monitoring with a high-resolution facility (e.g., Robo-AO; Baranec et al., 2014) could yield an observation of the delayed brightening of the fifth image.

PSJ0740+2926

This is an SDSS quasar that was subsequently found to be followed up as part of the SDSS quasar lens search, which also confirm this as a quasar pair at z=0.98 (Inada et al., 2010).

PSJ0812+3349

While we have classified this as a nearly identical quasar (NIQ), there is support for this object being a lens since a faint red object is seen upon subtracting the PSFs. Because of the

Table 2.11 Predicted time delays between the image pairs in PSJ0630-1201. All values are in days. The values in the top right (bottom left) are for a lens redshift of 1 (0.5). Light arrives in the images in the following order: CABED.

	A	B	C	D	E
A	-	0.9	1.8	243	208
B	0.4	-	2.7	242	207
C	0.7	1.1	-	245	210
D	97.8	97.4	98.5	-	35
E	83.7	83.3	84.4	14.1	-

lack of any imaging data sets other than Pan-STARRS we cannot confirm this detection since this faint residual is only seen in the *i*-band at $i \sim 23$. The quasars' proximity could mean lens galaxy light is being fit or appearing due to poor PSF subtraction. Therefore deeper and/or higher-resolution imaging of this system is required.

PSJ0941+0518

We note that this system was concurrently discovered by Williams et al. (2018). Deep CFHT data reveals an Einstein ring of the quasar host galaxy in the *u*, *g* and *r* bands, as shown in Figure 2.14. We calculate the velocity dispersion of our SIE model to be 365 km s^{-1} and compare this to the measured velocity dispersion of the galaxy from an SDSS spectrum of 313 ± 18 km s^{-1}. This discrepancy can be accounted for by a shallower than isothermal density profile of $\gamma \sim 1.8$ (see Figure 4 of Auger et al., 2010). However, this lens is embedded within a galaxy group and so close companions would suggest a steeper profile (Auger, 2008; Dobke et al., 2007). Since a quasar emission line from the closer, fainter quasar image is present in the galaxy spectrum, the SDSS velocity dispersion might not be trustworthy. A deeper spectrum and deeper optical imaging of the Einstein ring will help constrain the mass model. We calculate the time delay for this system as B lagging A by $\sim$270 days.

PSJ0949+4208

This lens has a radio counterpart detected in NVSS and FIRST, however FIRST clearly associates the emission with the lensing galaxy. The lensing galaxy is likely a radio galaxy, however we cannot rule out the fainter optical image being much brighter in the radio. It was targetted for a BOSS spectrum which shows quasar emission lines at $z = 1.27$ and a galaxy at $z = 0.507$, in agreement with the absorption lines seen in our WHT spectrum.

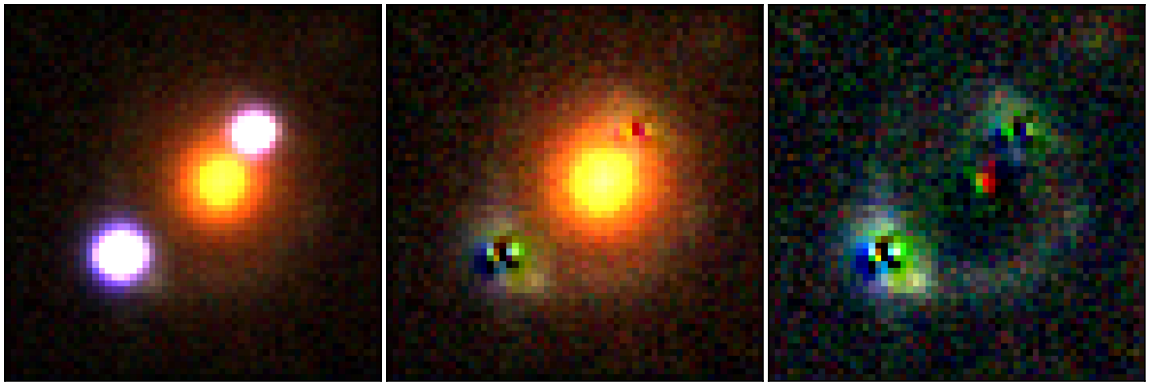

Fig. 2.14 From left to right: J0941+0518 stacked CFHT *ugr* data, PSF-subtraction, and PSF and galaxy subtraction.

PSJ1540+4445

This NIQ is at low redshift ($z = 0.61$) and shows variation in the emission line profiles between the two components. Furthermore it appears to be associated with a galaxy cluster. Two BOSS spectra of galaxies in the field place them at the same redshift as the NIQ.

PSJ1606–2333

This system was identified as a *Gaia* double. Though the seeing for the WHT spectrum was poor, quasar emission lines are visible across the broad trace. The two-component decomposition is made the same distance as that between the *Gaia* detections, and a narrow uniform aperture is used for the spectral extraction. An archival, shallow *Chandra* image shows extended emission at the positions of the two *Gaia* detections and also near image C, as labelled in Figure 2.5. Recent HST imaging (proposal 15320, PI: Treu) clearly resolves four quasar images and a lens galaxy. The mass model suggests a shear of 0.15 and an image position χ^2 of $\sim$10. The majority of this is attributed to a poorly fitting position of image D. The best-fit models consistently place D 0.02-0.04" more northern than the measured value. This discrepancy could be explained by an astrometric perturbation from an unresolved galaxy near image D.

PSJ1640+1045

This double system appears to be a flux-ratio anomaly double with the closest image 1.5 magnitudes brighter than the further image (0.52" and 1.71" from the galaxy respectively). The fit of an SIE is possible to explain this flux ratio but requires a highly elliptical (q $\sim$ 0.3) mass model, while the light profile is reasonably circular (q $\sim$ 0.9). Therefore if this flux

ratio is to be explained by a mass model it is much more likely to be due to a strong external shear in the same direction as the inferred mass position angle. A singular isothermal sphere + shear model for this system is also a good fit ($\chi^2 \sim 0.25$), with a shear of 0.32 at 122 degrees North of East. This position angle is well-aligned with a nearby galaxy less than 4" from the main lensing galaxy at a position angle of 133 degrees North of East. Furthermore, SDSS, Pan-STARRS, *Gaia* and DECaLS data all show that this lens maintains the measured flux ratio implying this flux ratio is unchanging over 15 years. While microlensing events cannot be ruled out, it is more likely that this apparent flux-ratio anomaly is explained by a strong external shear. Since both quasar images are detected by *Gaia*, their lightcurves will become useful data for breaking the microlensing/shear degeneracy for this system.

PSJ1721+8842

The "polar quad" shows strong signs of line-of-sight absorption systems in all 4 images. The Pan-STARRS imaging data have highly distorted PSFs in some bands, so the mass model is based on flux ratios measured only in the *r*-band. The residuals after subtracting PSFs show flux to the west of image C, perhaps associated with a second lensing galaxy or an arc from the quasar host galaxy. Given its high declination, the position and airmass of this system is essentially unchanged year-round, providing an excellent opportunity to efficiently measure time delays without any seasonal gaps. We note that the mass model is well-fit to the data, with a χ^2 of $\sim$4.4 (the number of degrees of freedom for the quad models is 13-9=4). Most of the flux χ^2 contribution comes from image A being too bright.

PSJ1831+5447

This is an NVSS radio source with a flux of 23.5mJy at 1.4GHz.

PSJ2032–2358

MgII absorption is seen in just one of the quasar spectra, with similar emission line profiles. The MgII absorption system is at z=1.642, consistent with the source's systemic redshift based on the CIII and CIV lines and the other quasar's MgII emission line. This could be a lens with magnesium absorption in the host quasar along the line-of-sight of just one image. If deeper imaging reveals a lens galaxy or a lensed host galaxy, then this system could be used to constrain the covering fraction of MgII.

DESJ0053–2012

This system is the only confirmed quad from the DES follow-up campaign. It was selected by the *Gaia* multiple selection as a *Gaia* DR1 double (G=19.21, 19.43) corresponding to a red WISE detection (W1−W2=0.55). It is the highest redshift four-image lensed quasar discovered, making it a valuable object for extending source and intergalactic medium studies to higher redshifts.

A SIE+shear model is insufficient to reproduce the positions and flux ratios, providing a best-fit $\chi^2 \approx 30$ for 4 degrees of freedom. The model requires a strong shear of 0.22, 159 degrees East of North, while the companion galaxy G2 is 4.3" 131 degrees East of North. We choose to explicitly model G2 as an SIE with shape fixed to that of the light (as measured in the z-band SOAR data), and leave the Einstein radius as a free parameter. This new model provides a best-fit $\chi^2 = 2.43$ for 3 degrees of freedom, now requiring a smaller shear of 0.13, 20 degrees East of North. The caustics and critical curves of this model are shown in Figure 2.15. The main contribution to the χ^2 is due to the flux ratios, with B being 25% fainter than predicted. This is consistent with the expectations of microlensing suppression since this image is a saddle point (Schechter and Wambsganss, 2002). Finally, we note that, assuming a lens redshift of $z \sim 0.7$, expected time delays are 22, 26, and 137 days, in the image ordering ACBD.

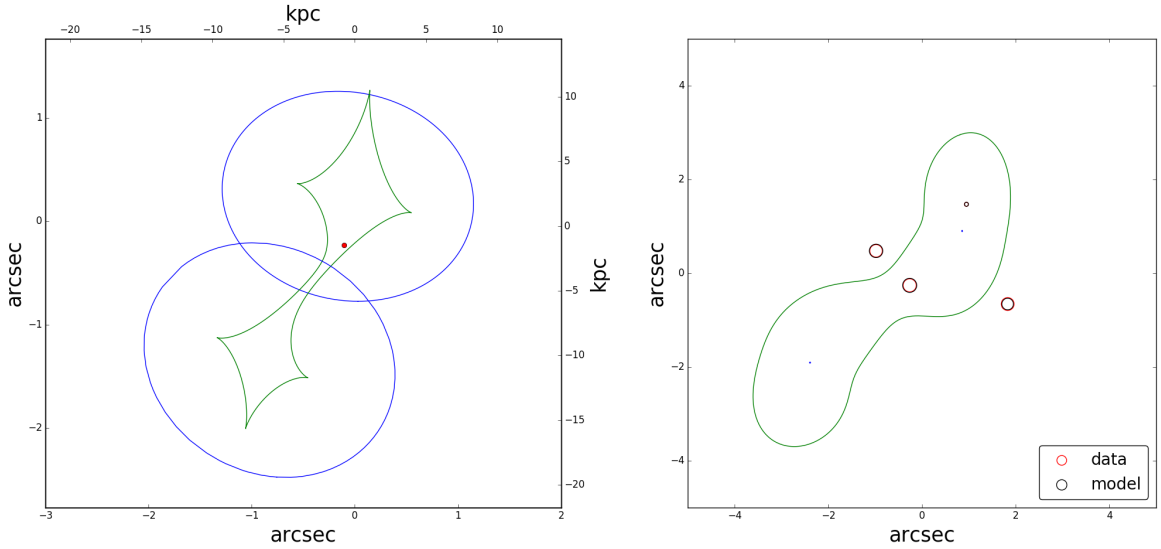

Fig. 2.15 Best-fit mass model for DESJ0053-2012. Left: source plane caustics with source position overlaid in red. Right: image plane critical curves with measured image positions, and best-fit model image positions overlaid, with area representing flux.

DESJ0112–1650

Resolved ESI spectra show two quasars with very similar spectra at z=0.99. There is absorption due to a massive galaxy seen in both quasar images at z=0.52 (from Ca H and K, G-band, and Na at 6063, 6116, 6635, and 9084Å respectively), which is a promising sign of a lensing galaxy. While we lack high-resolution imaging of this system, the DES data clearly show a redder object offset from the line joining the two blue PSFs. This is often seen with fold quad configurations, where the faint counterimage is either highly reddened or the data are not deep enough, while one of the observed PSFs is a pair of close images, as was observed in the cases of PSJ0030-1525 (Figure 2.11) or SDSSJ1330+1810 (Oguri et al., 2008a). We model the system as two PSFs, and subsequently as three PSFs, which shows an extended galaxy in the residuals. Therefore we adopt three PSFs and a galaxy as the fiducial pixel model for this system, as this fits the data to the noise (Figure 2.16). We currently cannot determine whether the third PSF, C, is a highly reddened quasar image, a foreground star, or structure due to the lensing galaxy. Our mass model given in Table 2.9 assumes only A and B are quasar images, with G being the only lensing galaxy. High-resolution imaging is required to fully understand this system.

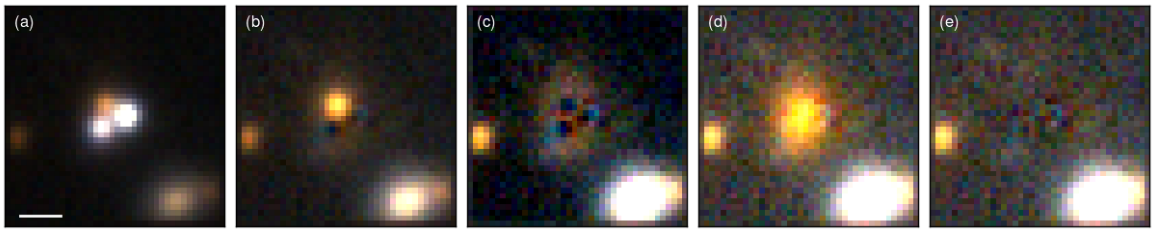

Fig. 2.16 DESJ0112-1650 *gri* DES images; (a) data, (b) three PSF model subtracting the two blue PSFs, (c) three PSF model subtracting all PSFs, which clearly shows an extended component in the residuals, (d) three PSF and galaxy model subtracting the three PSFs, and (e) three PSF and galaxy model subtracting all components. The white scale bar is 2".

DESJ0229+0320

This system consists of two quasars at a redshift of 1.43, separated by 2.13". The spectra are similar, and multi-band single-epoch modelling (Chapter 5) shows similar long term variability. Furthermore, the apparent brightness of these quasars (*Gaia* magnitudes of 18.15 and 18.79) places them at the bright end of the luminosity function for quasars. These characteristics are all in accordance with strong gravitational lensing — similar variations, similar spectra, and large apparent brightness due to magnification — however no lensing galaxy is seen in the deep DES images. To investigate how faint a lens galaxy can be for such

a system, we find the I-band magnitudes of a subset of the OM10 mocks, namely those with similar redshift sources (z=1.43±0.2) and similar image separations 2.13±0.2". Of the 192 systems satisfying theses criteria, the faintest lensing galaxy magnitude is 20.8 ($z_{\rm lens}$ ∼0.9; expected once in 100,000 square degrees of sky). This magnitude is reached in a single-epoch image (for a S/N of 10 for a PSF Abbott et al., 2018); however, if it lies close to one of the quasar images, or is particularly extended, then it might not be apparent after PSF subtraction. We believe this is a binary quasar, but high-resolution imaging is required to fully rule out the lensing hypothesis.

DESJ0340–2545

This system was found through a *Gaia* and WISE selection following Section 2.3.1. A slit positioned at 27 degrees East of North confirms two quasar images separated by 6.8", each at z=1.68 (see Figure 2.7). NIRC2 imaging of the system clearly shows three lensing galaxies, two quasar images, and one further object, north of G1. Overlaying the *Gaia* detections for the system on the NIRC2 data reveals that this further object is exactly centred on a *Gaia* optical detection, and the DES colour image reveals a blue object blended with G1. We investigate whether this object could be the third image of the system, as these faint central images are often observed in lenses with multiple galaxies, resulting in an image slightly offset from one of the lensing galaxy centres, for example, PSJ0630-1201 (Figure 2.13). To investigate whether C is another quasar image, we create lens models based only on the confirmed quasar images, and see whether the best-fitting lens models naturally predict another image near C. However, we are severely underconstrained given the complex mass distribution of the galaxy group and only two quasar positions and their, often untrustworthy, flux ratio. Given that our model will require a source position, we are left with only three degrees of freedom for our lens model. We choose to model the mass contributions of the three galaxies, G1, G2, and G3, set as singular isothermal ellipsoids, with their flattening parameters set to those of the light (Table 2.12), and pinned to the measured light positions. Their Einstein radii are all modelled by 1 parameter, b, assuming a constant mass-to-light ratio amongst the galaxies, i.e. using the galaxy flux ratios to set the Einstein radii ratios ($L \propto M \propto b^{0.5}$ assuming the Faber-Jackson relation $L \propto \sigma^4$). We also choose to include an external shear so we have no degrees of freedom remaining, and expect a good fit to have $\chi^2 \approx 0$. This model reproduces the two bright confirmed quasar images and their flux ratio well. It also predicts a third image 0.22" away from the postulated image C, and with a flux 15% that of A, while C has a measured flux of 10% of A. This prediction is enough for us to consider C as a third quasar image without its spectroscopic confirmation. Further evidence for C being a quasar image comes from the remarkably similar flux ratios of the

point sources in *Gaia* and in the NIRC2 K-band data (as given in Table 2.12), suggesting they have similar SEDs. We can use the three extra constraints this image provides to consider more complex lens models. Considering the same model as before, but now including C as a required quasar image to be reproduced, produces a poor best-fit with $\chi^2 = 676$, given 3 degrees of freedom. We consider two further lens models. Firstly, we allow the mass-to-light ratio to vary between the lensing galaxies, i.e. fit for the Einstein radius of each galaxy. This results in a good fit to the astrometry, but image A is predicted to be about as bright as B, while it is in fact measured to be 2.7 times brighter. This model might describe the system well, considering there could be large variability over the time delay, so later DES and LSST observations will help exclude this possible model. Our final model fixes the Einstein radii as in our initial models, but now includes an SIS, representing a dark matter halo shared by the lensing galaxies. Its best-fit position is Δx, $\Delta y = 0.75"$, $0.60"$ from from A (as given in Appendix A), and the χ^2 for this model is 0.43, given 0 degrees of freedom. Since the true mass distribution within this group is likely very complicated, these models should only serve to aid discussion of the possible probes this system could offer, in particular if deeper high-resolution imaging is pursued to reveal the multiply imaged host galaxy arcs.

DESJ0340-2545 has a detection by the VLA Sky Survey (VLASS) of $\sim$1mJy at 3GHz (Lacy and VLASS Survey Team, 2018) and a 2.6mJy detection in NVSS at 1.4GHz (Condon et al., 1998). Given the 2.5 arcsecond resolution of VLASS, and the large separation of this system, we are able to determine whether the radio emission is due to the quasar images. Figure 2.17 shows the VLASS 3GHz cutout with *Gaia* detections overlaid. The emission is consistent with coming from one or two of the lensing galaxies, G2 and G3 as labelled in Figure 2.17.

This system is, to our knowledge, the fourth known triply imaged lensed quasar, after APM08279+5255 (Irwin et al., 1998), SDSSJ1029+2623 (Inada et al., 2006; Oguri et al., 2008b), and SDSSJ0909+4449 (Shu et al., 2018).

Table 2.12 DESJ0340–2545 parameters based on NIRC2 data.

Component	q	PA	K'(*Gaia* G) flux ratio
A	—	—	9.59 (9.55)
B	—	—	3.49 (3.50)
C	—	—	1.00 (1.00)
G1	0.54 ± 0.01	150 ± 1	1.00 (—)
G2	0.92 ± 0.02	96 ± 7	0.95 (—)
G3	0.344 ± 0.008	15.5 ± 0.5	0.97 (—)

Table 2.13 DESJ0340–2545 mass models.

Model	Fit C as an image?	Constraints	Model Parameters	χ^2 astrometry/flux	total χ^2	μ
1	No	5: XY_{AB}, f_{AB}	5: XY_S, b, γ, θ_γ	0.00, 0.00	0.00	4.40
2	Yes	8: XY_{ABC}, f_{ABC}	5: XY_S, b, γ, θ_γ	670.6, 5.3	675.9	4.53
3	Yes	8: XY_{ABC}, f_{ABC}	7: XY_S, b_1, b_2, b_3, γ, θ_γ	0.02, 9.51	9.53	5.25
4	Yes	8: XY_{ABC}, f_{ABC}	8: XY_S, b, γ, θ_γ, XY_{HALO}, b_{HALO}	0.01, 0.42	0.43	11.6

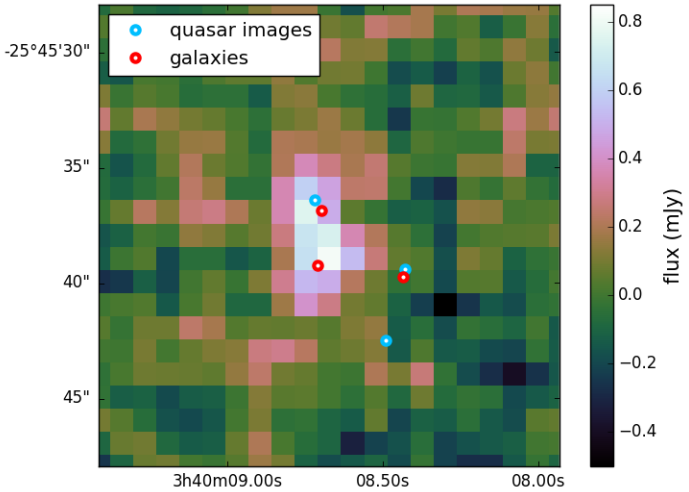

Fig. 2.17 VLASS 3GHz image of DESJ0340–2545 with quasar and galaxy positions overlaid, as measured from the NIRC2 data and shifted to the *Gaia* DR2 frame.

DESJ0407–1931

The fainter image of this double is significantly blended with the lensing galaxy, but it is clearly detected in the DES stacked data and the SOAR imaging. By subtracting off the scaled NTT spectrum of A from B, we are able to see clear signs of the lensing galaxy absorption lines at z=0.288 as shown in Figure 2.18. The stacked modelled residuals show an excess to the East and West of the brighter image, potentially caused by the lensed host galaxy.

DESJ2349–4518

This system is a high-flux-ratio double (7.5 to 1), with a SUMSS detection of 13.6mJy at 843 MHz (Mauch et al., 2003). This lens system lacks SOAR or NIRC2 data, so we show DES *gri* colour images with the brighter PSF and both PSFs subtracted in Figure 2.19.

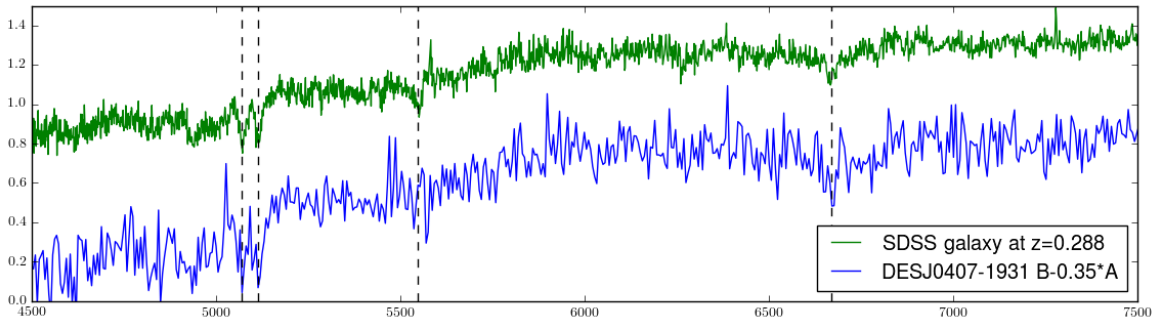

Fig. 2.18 NTT spectrum of the lensing galaxy of DESJ0407-1931, created by subtracting a scaled spectrum of image A from the B+G blended spectrum. A high signal-to-noise spectrum from SDSS of a galaxy at z=0.288 is plotted for comparison, highlighting the Ca H, K, and Mg lines at 5070, 5115, and 6670Å respectively.

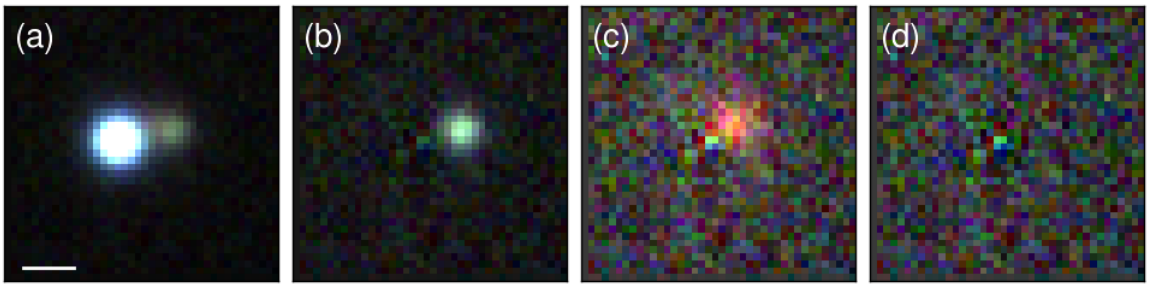

Fig. 2.19 DES *gri* stacked model for DESJ2349-4518; (a) data, (b) subtraction of image A and lensing galaxy, (c) subtraction of both quasar images, and (d) subtraction of all components. The white scale bar is 2".

2.5 Discussion

To understand the limitations of our selection method, we have compiled a list of 147 lensed quasars known before *Gaia* DR1, against which we can test our selection. While we report 34 new lensed quasars, our selection criteria also selected 59 previously known lensed quasars in the Pan-STARRS footprint, as described in Table 2.14.

2.5.1 Recovering Known Lenses

Performing an analysis of the 181 known lensed quasars before *Gaia* DR1 (including our sample, i.e. 147+34=181), 5 lenses have 3 *Gaia* detections, 46 have 2 detections, 92 have 1 detection and 38 have no detections. Only 2 of the non-detections have bright enough images that should have been detected by *Gaia*—J0941+0518 and WFI2026-4536—with the rest being optically faint mainly due to radio selection. The non-uniformity of the scanning law is the case for these non-detections, rather than any processing problems.

Applying our Pan-STARRS-based selection criteria, we recover 82 lenses (37 *Gaia* multiples and 45 *Gaia* singles). 23 of these lenses are quadruply imaged (quad fraction of 28%), while of all known lenses the quad fraction is 44/181 (24%). The lenses that we fail to select fall into three categories: separation $>$ 4", separation $<$1.5", or high-flux-ratio doubles. We do not recover the very rare large-separation lenses because of our 4" *Gaia* multiple separation cut. The small-separation lenses are missed because of lack of multiple *Gaia* detections. Our single *Gaia* detection search does not recover these because the systems are not extended enough and do not pass our morphological classifier. This latter failure also explains the high-flux-ratio doubles being missed, since the majority of the flux is in one PSF.

Table 2.14 *Gaia* selection of lenses with WISE or GMM colour techniques. Numbers shown in brackets are for lenses in the Pan-STARRS footprint. 82 lenses are selected in Pan-STARRS, 25 of which are new lenses presented in this Chapter and the remaining 57 are known lenses. †One of these 43 lenses, SBS1520+530, has one of its two detections due to a nearby star. We keep this in our sample since it would still be selected via this method.

Known lensed quasars (in PS)	181 (158)
3 *Gaia* detections (in PS)	5 (5)
2 *Gaia* detections † (in PS)	45 (35)
1 *Gaia* detections (in PS)	92 (83)
0 *Gaia* detections (in PS)	38 (35)
Multiples selected by WISE or GMM in PS	37
Singles selected by WISE or GMM in PS	45

2.5.2 Comparison to Simulated Lenses

Our search techniques failed to recover 33 known lenses with *Gaia* detections. We understand this as the extremes of small- and high-separation images and high-flux-ratio doubles. We can verify this and infer which lenses our search is missing by comparing the selected lenses to a simulated sample.

In particular we compare to the OM10 simulations which have readily listed image configurations, lensing galaxy parameters, source parameters, etc., for 15,658 mock systems. We limit the entire OM10 sample to those lenses we would expect to be able to find with images brighter than the *Gaia* threshold, as detailed in Section 1.5.

Figures 2.20 and 2.21 show histograms of source redshifts and separations respectively for our 35 *Gaia* lens sample and the reduced OM10 sample. The first plot demonstrates the lack of selected lenses with source redshifts above $z \simeq 2.2$. Two reasons for this are: (i) there is an anti-correlation between lens galaxy brightness and source redshift, since low redshift sources tend to have lower redshift lenses (ii) the u-band dropout for quasars above $z = 2.7$ makes them more difficult to classify, and at higher redshifts WISE colours tend to become bluer for quasars (as in Figure 2.22). Figure 2.21 shows that small-separation lenses are not being selected. This is expected since these are the hardest to identify in imaging data and to target for follow-up spectroscopy.

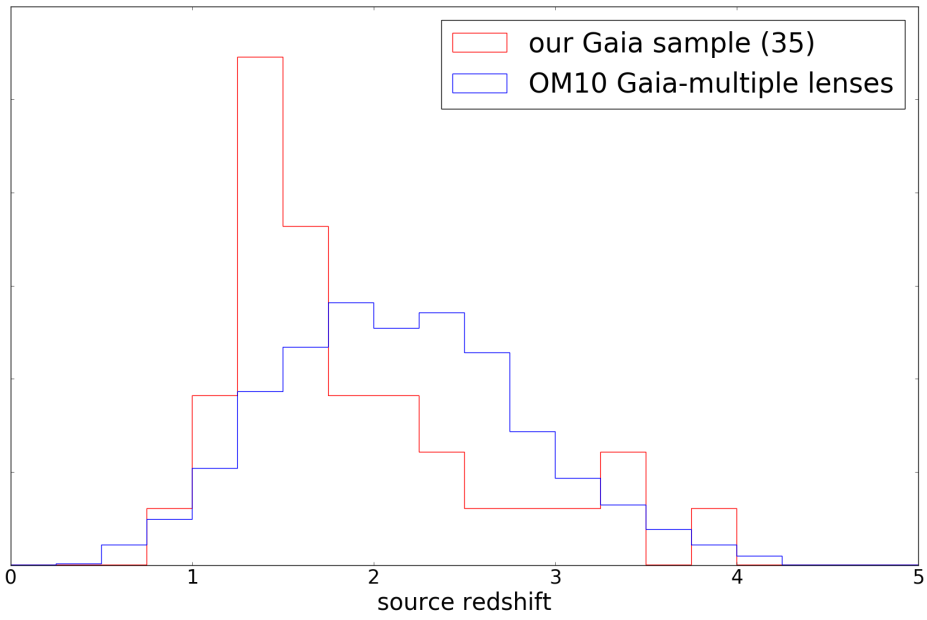

Fig. 2.20 Source redshift distributions for our *Gaia*-selected sample and OM10 mock lenses with predicted multiple *Gaia* detections.

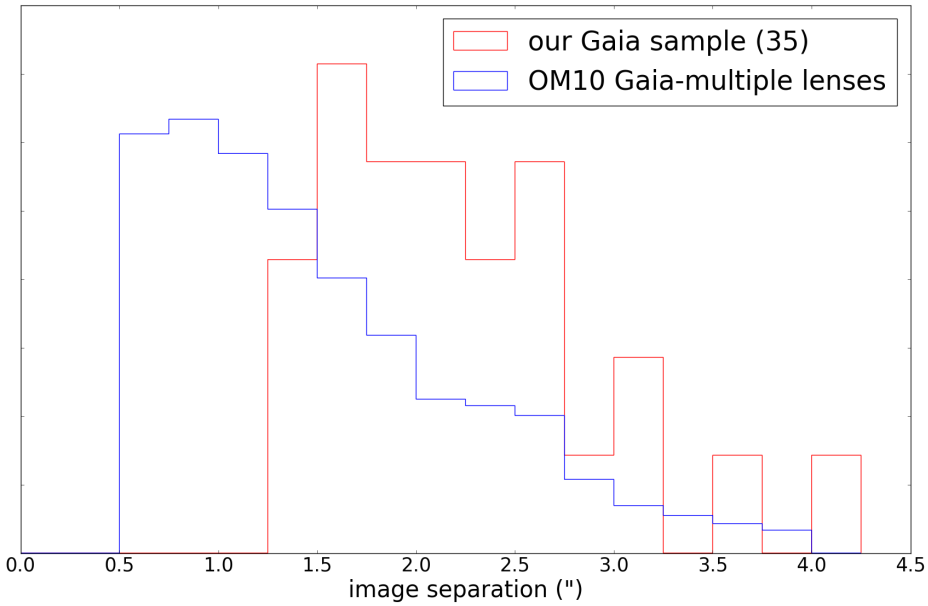

Fig. 2.21 Image separation distributions for our *Gaia* sample, and OM10 mock lenses with predicted multiple *Gaia* detections. OM10 used a lower limit of 0.5" for the image separation of their mocks and 4" as an upper limit.

We note that the quad fraction of the mocks is 18%, compared to 25% for all known lenses, demonstrating current and previous search biases towards quads—they are more magnified and hence are over-represented in the current magnitude-limited samples, they are more identifiable once visually inspected, and they are more likely to be caught by search algorithms (e.g. a higher likelihood of multiple *Gaia* detections).

Figure 2.23 shows the fainter image magnitude against galaxy magnitude in the *i*-band for our *Gaia* lens sample. Overlaid are the same values for the entire OM10 mock catalogue. Figure 2.24 repeats the same plot but for combined image magnitudes. Naturally we are still discovering lenses with bright images, but we note that there should be many more lenses with bright images with faint galaxies, and faint images with bright galaxies (the top left and bottom right respectively). The 17 NIQs identified here can make up the former of these two classes of lens, but require deeper imaging to reveal the lens galaxy. The latter will be missed by searches requiring quasar colour selection. These lenses could be discovered by starting from photometric galaxies and requiring multiple *Gaia* detections, as Lucey et al. (2017) have successfully applied to the Pan-STARRS dataset.

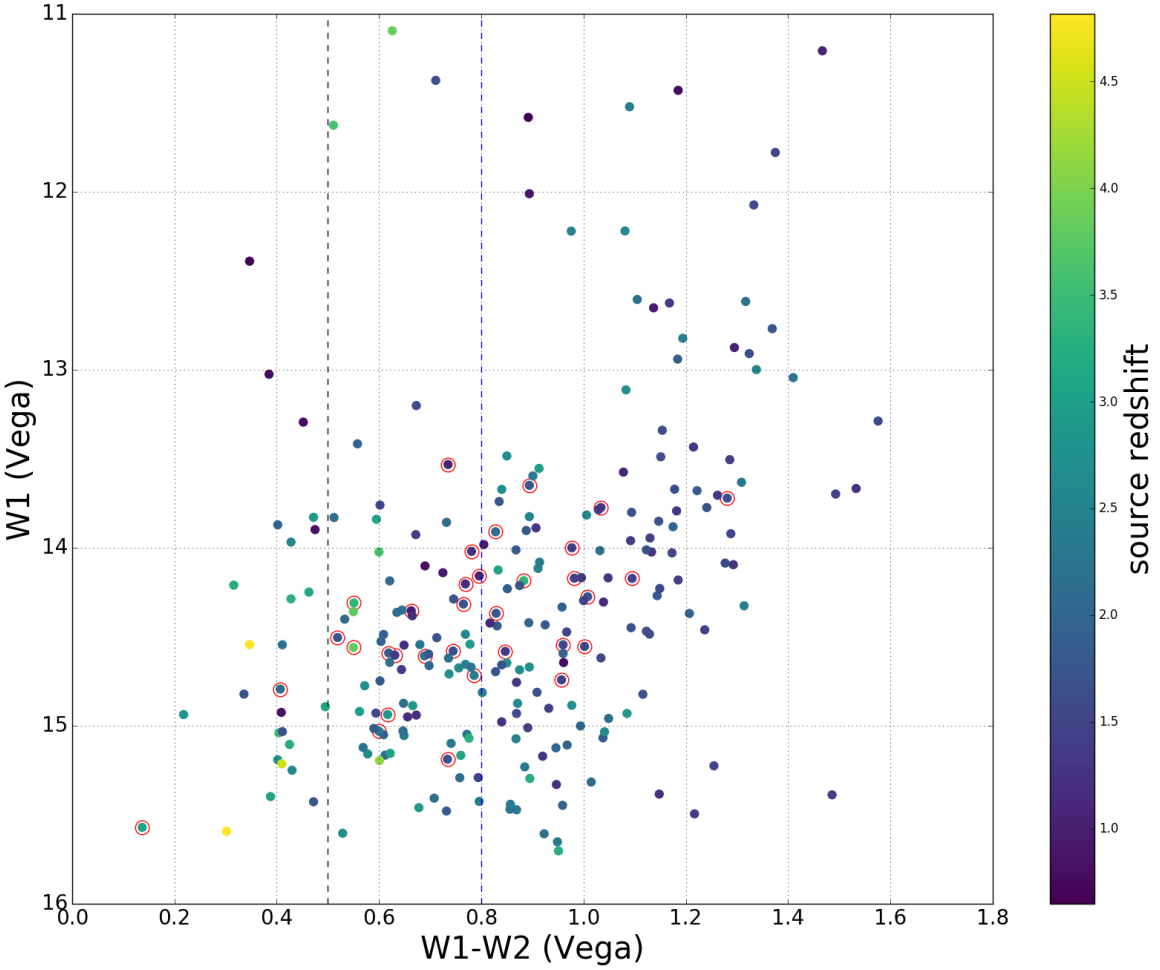

Fig. 2.22 W1 against W1−W2 for all known lenses with at least one *Gaia* detection and robust WISE photometry, coloured by source redshift. Lenses from our *Gaia* sample are circled. Lenses circled to the left of the W1−W2=0.5 black dashed line were selected with the GMM method only. The blue dashed line shows the quasar selection criterion of Stern et al. (2012).

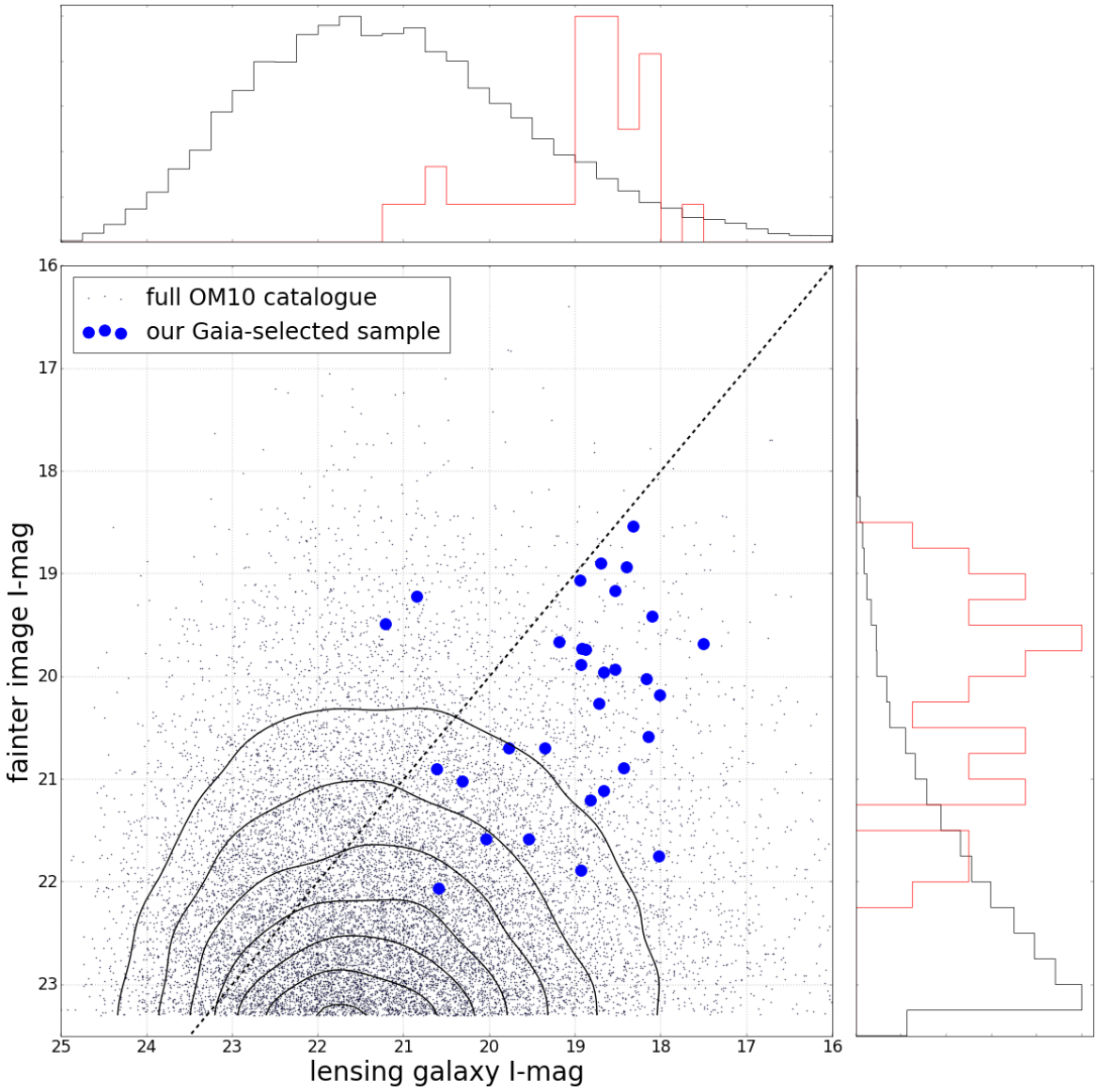

Fig. 2.23 Fainter image magnitude (second faintest for quads) against lensing galaxy magnitude in the *I*-band. The contours and black dots represent the entire OM10 sample, while our *Gaia*-selected lenses are overlaid in blue.

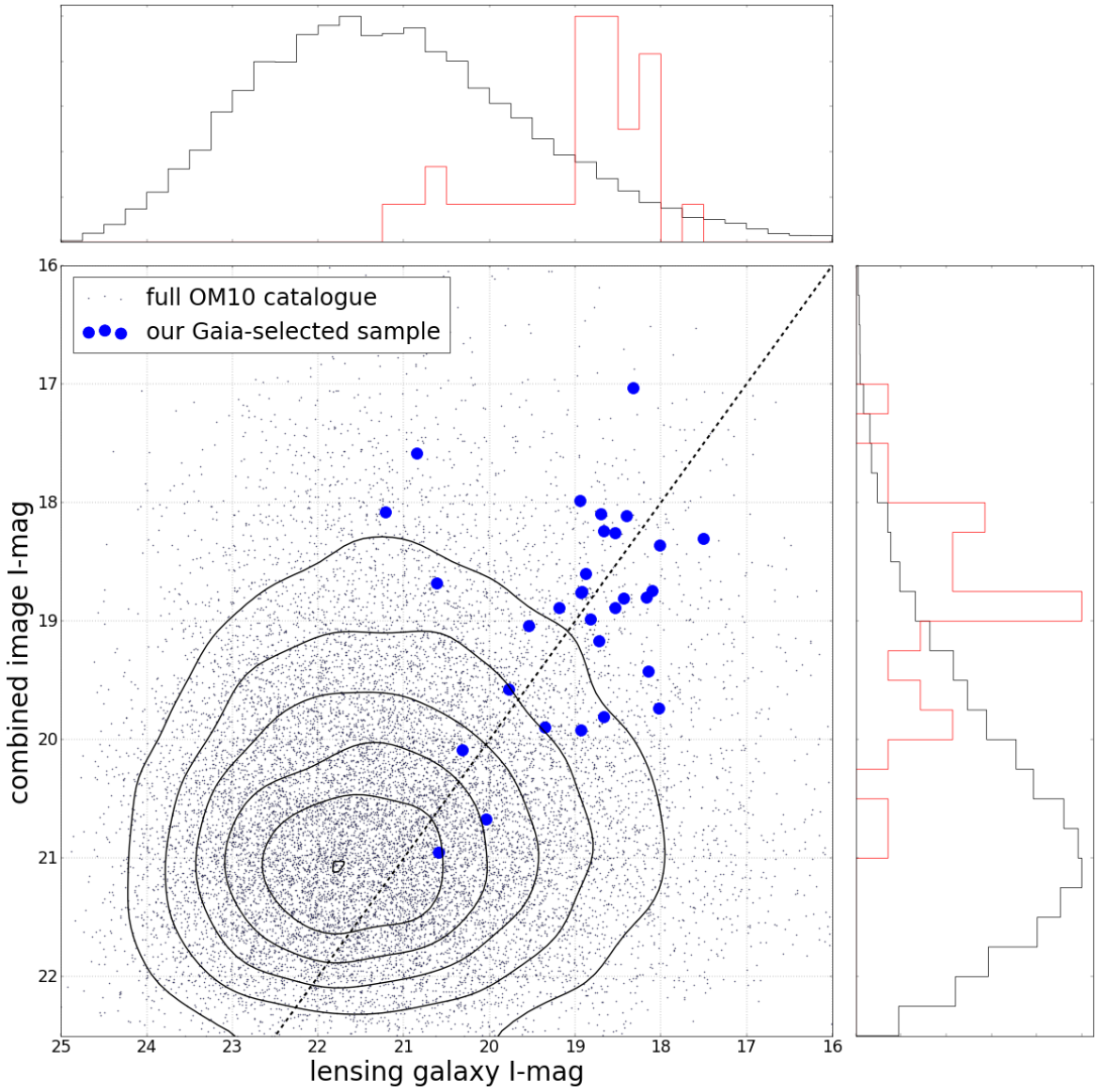

Fig. 2.24 Combined image magnitude against lensing galaxy magnitude in the *I*-band. The contours and black dots represent the entire OM10 sample, while our *Gaia*-selected lenses are overlaid in blue.

2.6 Conclusions

We have presented the discovery of 34 new gravitationally lensed quasars selected using *Gaia* DR1. 25 were discovered in Pan-STARRS imaging data, while 9 were discovered in DES. We also identified 17 quasar pairs, 9 from Pan-STARRS and 8 from DES, which could represent lensed quasars with lensing galaxies not bright enough to be identified in existing imaging datasets. At spectroscopic follow-up, our success rates are between 43% and 58% for Pan-STARRS follow-up, and 32% and 71% in DES. Overall, the success rate is between 40% and 63%. The upper bounds include inconclusive and quasar-pair systems as potential lensed quasars. These percentages are typically better than previous spectroscopic searches; e.g., SQLS had a success rate between 10% and 25% (including imaging follow-up). However, we do not believe this is due to a better selection technique. Rather, it is because of the very large number of objects that were visually inspected, with new areas of imaging data, and many easily identifiable lensed quasars, i.e. those with bright lensing galaxies.

17 are discovered by having multiple *Gaia* components, 16 as *Gaia* detections near morphological galaxies and 1 from an emission line identification in an SDSS galaxy spectrum. All of these systems have well-resolved images in ground-based imaging and are bright, lending themselves to monitoring and subsequent time delay cosmography studies (Treu and Marshall, 2016). Our sample includes 5 quads, 1 triply imaged system, and one double lens which shows a blue Einstein ring in deep CFHT data. One quad, J0030-1525, requires high resolution imaging to verify our understanding that one image is highly demagnified, by a factor of ~ 14.

Comparing our sample of lensed quasars to simulations, we show that we are not sensitive to arcsecond-separation lenses and those at high redshift. This is due to colour selection and the bias from visually inspecting a large number of candidates. This biases our sample towards systems with bright lensing galaxies (and hence lower redshift sources) and quads, and away from small-separation lenses and bright doubles that are often confused for stars.

Oguri and Marshall (2010) predict several thousand lensed quasars to be detectable using LSST (Large Synoptic Survey Telescope), however to confirm such large numbers of lenses to become useful astrophysical and cosmological tools, we must ensure we select lenses efficiently and in a complete manner. We have demonstrated that combining *Gaia*, WISE, SDSS, Pan-STARRS, and DES data with pixel-based modelling can efficiently select new lenses, however such visual inspection is unsustainable and incomplete. The new lensed quasars presented here will provide a useful check for other search techniques, and represent a significant increase in the number of systems available for lensed quasar studies.

Chapter 3

Resolving Small-separation Lensed Quasars

Our investigations into discovering new lensed quasars with *Gaia* showed we are not selecting lensed quasars with small separation. This is largely attributed to wider-separation systems having more massive, and hence brighter, lensing galaxies, and so visual inspection prioritises these systems for spectroscopic follow-up. Furthermore, small-separation systems require good seeing to obtain spatially resolved spectra, and are further biased against during spectroscopic follow-up. In this Chapter we show that *Gaia* data release 1 is also biased against resolving such small-separation lensed quasars, often cataloguing just one quasar image. We present a new technique, making use of ground-based imaging data from SDSS, in synergy with *Gaia*, to infer the presence of extra quasar images by looking for flux differences and positional differences between the two datasets. Such small-separation lensed quasars are interesting since they probe a different parameter space of the lensing world: high-redshift and/or low-mass lenses.

3.1 Close pairs in *Gaia*

Where *Gaia* can provide the most use for lensed-quasar searches is in determining whether a source is composed of multiple stellar objects. In ground-based optical imaging surveys, the typically much larger FWHM causes many contaminant systems to resemble lensed quasars. These contaminants include single quasars with bright host galaxies, quasars or stars blended with galaxies, projected systems, and starburst galaxies with quasar-like colours. Because of the truncated windows given to fainter companions around brighter neighbours by *Gaia*, there is a limitation in *Gaia*'s handling of close pairs (Arenou et al., 2017). We demonstrate

how this issue affects lensed quasars in Figure 3.1. The blue histogram shows the distribution of separations of detected *Gaia* pairs in a sparse field out of the galactic plane ($l \sim 173$ degrees, $b \sim 67$ degrees), i.e. a field in which *Gaia* is able to read out all objects within the magnitude threshold. The green line is the expected distribution from randomly positioned sources on the sky matched to a large-separation asymptote. We expect an overdensity of close-separation objects relative to this line associated with stellar binaries, bright star-forming mergers, and even lensed quasars, however the *Gaia* catalogue significantly lacks the detection of the second object of such pairs below 2.2". The pairs with very small *Gaia* separations are possibly duplicate sources that could not be filtered from GDR1 (Arenou et al., 2017). We also show the numbers of lensed quasars OM10 predicted across the whole sky with either the brightest object detectable by *Gaia* (approximately equal to an *i*-band magnitude < 20.7) or with at least two images detectable by *Gaia*, in bins of 0.1" separation. The OM10 catalogue is truncated at an image separation of 0.5". This cut was made due to difficulty in detection and characterisation of lenses at lower image separations, however *Gaia* will likely be able to push past this limit in detection. Finet and Surdej (2016) discuss the detection of smaller image separation lensed quasars in *Gaia*, however currently we use the full OM10 catalogue for predicted numbers of lenses since we are interested in those that can be characterised in ground-based imaging data. The area under the magenta curve of Figure 3.1 shows that later *Gaia* catalogues, which will include secondary source detections in close binaries, should detect the multiple images of ~ 600 lensed quasars, including ~ 140 quadruply-imaged systems. This value is in agreement with other estimates based on *Gaia*'s expected pre-launch capabilities (Finet and Surdej, 2016; Surdej et al., 2002). The number of lensed quasars expected with only one image detected by *Gaia* is ~ 1400, only ~ 50 of which are quads. This very low quad fraction is due to the brightest two images of quads often having similarly magnified fluxes.

3.2 A sample of small-separation lensed quasars

At separations larger than 2", the images of lensed quasars are deblended in ground-based surveys and *Gaia* cannot provide much further information; nevertheless it is still useful in some cases, for example in detecting quasar images around bright lensing galaxies, where the system might remain blended in ground-based data.

To investigate how *Gaia* catalogues known small-separation lensed quasars, we compile a set of 49 lensed quasars in the SDSS footprint with image separations less than 2" and which are typically blended in SDSS. All lenses in the sample have at least one *Gaia* detection, but only 8 have multiple detections in GDR1, whereas $\sim$43 are expected to have further

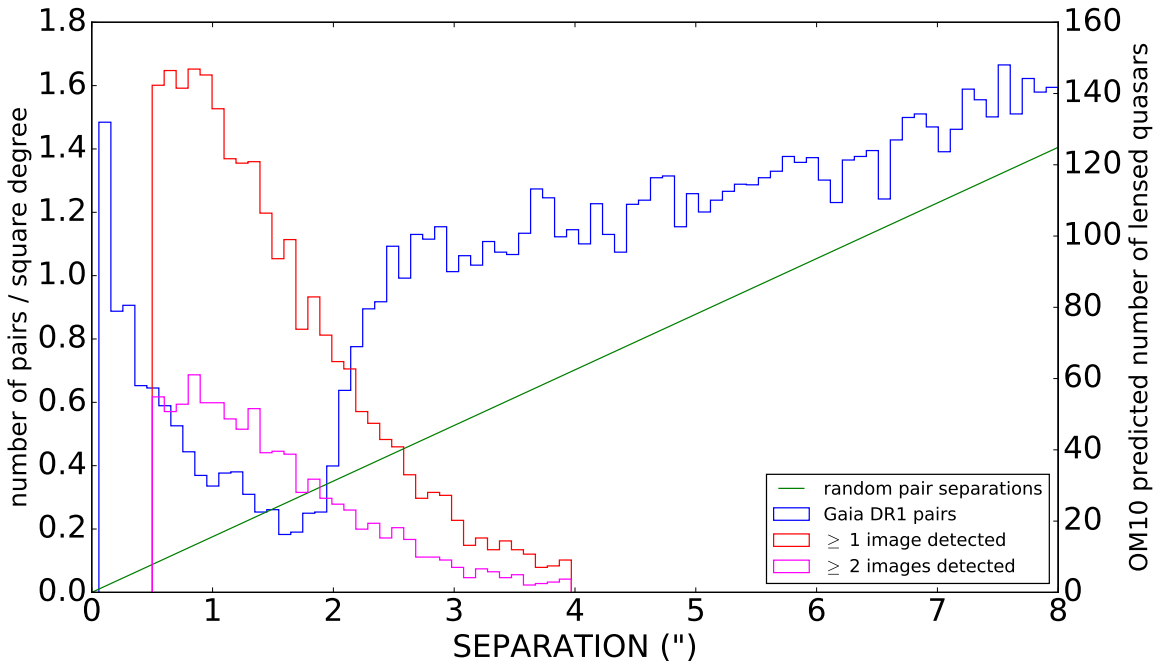

Fig. 3.1 Expected numbers of lensed quasars as a function of image separation in 0.1" bins. The plot shows expected numbers for at least two images to be detected by *Gaia* (magenta) and just one image to be detected by *Gaia* (red). The blue histogram is the *Gaia* distribution of source pairs against separation, which shows a distinct dropout around the typical separations of lensed quasars. The green line is the distribution expected from a field of randomly-positioned sources.

images brighter than the *Gaia* detection limit. Only one lens, PG1115+080, is detected as three separate images (though we note this is one of the larger-separation systems) and is deblended into 2 components in SDSS. These 8 systems are shown in Figure 3.2 with *Gaia* detections overlaid on SDSS *gri* colour images.

Since many objects were removed as possible duplicates in GDR1, we check for duplicate removal of the non-catalogued images through the *duplicated_source* flag. Approximately 5% of objects in GDR1 have this flag. For the lensed quasars with single *Gaia* detections where multiple detections are expected, only 4 of 35 are flagged as duplicated sources, indicating the further missing detection(s) in *Gaia* may be due to truncated windows being given to the missing images in certain scan directions. Since these windows have not yet been processed, not all quasar images have enough G-band measurements to be included in GDR1 (Fabricius et al., 2016).

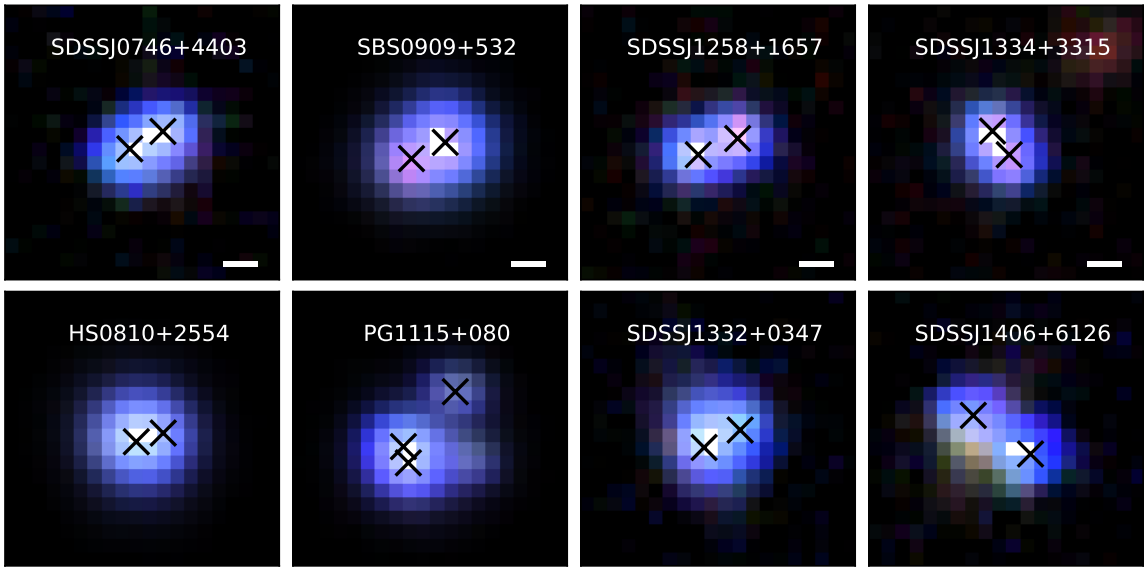

Fig. 3.2 The 8 small-separation lensed quasars that have multiple detections in the *Gaia* catalogue with positions overlaid on an SDSS *gri* colour image. These lenses are: SDSSJ0746+4403 (Inada et al., 2007), HS0810+2554 (Reimers et al., 2002), SBS0909+532 (Kochanek et al., 1997), PG1115+080 (Weymann et al., 1980), SDSSJ1258+1657 (Inada et al., 2009), SDSSJ1332+0347 (Morokuma et al., 2007), SDSSJ1334+3315 (Rusu et al., 2011) and SDSSJ1406+6126 (Inada et al., 2007). The scale bars are 1".

Table 3.1 Details of small-separation lensed quasars with multiple *Gaia* detections (source redshift, image separation and *Gaia* magnitudes). [a]Values for PG1115+080 are for the close-separation merging pair.

Name	z	sep (")	G	G1-G2
SDSSJ0746+4403	2.00	1.08	19.39, 19.47	0.07
HS0810+2554	1.50	0.81	15.94, 16.99	1.05
SBS0909+532	1.38	1.09	16.25, 16.73	0.48
PG1115+080[a]	1.72	0.48	17.08, 17.20	0.12
SDSSJ1258+1657	2.70	1.25	19.19, 19.50	0.31
SDSSJ1332+0347	1.45	1.15	19.61, 19.64	0.02
SDSSJ1334+3315	2.43	0.84	19.58, 19.80	0.22
SDSSJ1406+6126	2.13	1.99	19.77, 19.97	0.20

3.3 Finding quasar lenses in *Gaia*

Since small-separation lenses are much more common than the easily deblended larger-separation lenses (Figure 3.1), we now explore several ways that GDR1 can help identify these small-separation lensed quasars by considering our sample of known lenses. Firstly we consider multiple *Gaia* detections corresponding to the multiple images of a small-separation lensed quasar (as opposed to the wider-separation systems targeted in Chapter 2.3.1). In the case of single *Gaia* detections, we investigate the *Gaia* catalogue parameter of astrometric excess noise which might hint at the presence of a lensing galaxy or further quasar images. Finally we compare *Gaia* fluxes and positions to other datasets that blend lensed quasars into single objects, which will naturally measure larger fluxes and different centroids from those given in the *Gaia* catalogue.

For the following analysis we use spectroscopically confirmed objects from the *SpecObjAll* table from the twelfth data release of SDSS (Alam et al., 2015), in which most spectroscopically confirmed quasars are from SDSS-III BOSS, but also includes spectra from all previous SDSS data releases.

3.3.1 Multiple *Gaia* detections

Our sample of small-separation lensed quasars shows that several objects are still separated into multiple components by *Gaia*. Arenou et al. (2017) have shown that the detection of both components of close pairs is more likely when they are of similar magnitude since the primary object can be either of the pair in different focal plane transits, leading to both objects being catalogued in GDR1. We see this in the 7 of the 8 lensed quasars with multiple detections in our sample (see Table 3.1). For the case of HS0810+2554, a particularly bright secondary image might be the cause of its cataloguing. Therefore even in GDR1 it is possible to use *Gaia*'s resolution to deblend potential small-separation quasar lens candidates into multiple objects immediately. A common limitation to finding lensed quasars in ground-based imaging surveys is the lensing galaxy causing a possible contamination to the colour of the object, meaning conventional quasar colour classification will miss these objects (see Ostrovski et al., 2017 for a full discussion). However, the prior that two point sources must be present means *Gaia* can help detect these bright-lens-galaxy systems, relying less on constraints from quasar colour-selection techniques.

3.3.2 Single *Gaia* detections

As discussed in Section 3.1, most bright lensed quasars will have one detection in GDR1. However, even when *Gaia* detects a single image of a lensed quasar, it provides useful information in its catalogue values of astrometric excess noise, position, and flux for each detection. The latter two measurements are useful because we are able to search for systems with missing flux and/or a different centroid relative to that of a dataset capturing all the flux, e.g. from proper imaging, where the difference would be caused by *Gaia* not cataloguing all sources. That is, GDR1 effectively resolves out the flux from single images of lensed quasars. For a given object, a potential close-separation quasar lens or perhaps just a single quasar, we outline how to derive a synthesised *Gaia* magnitude from ground-based broad-band survey photometry, with which one can compare the *Gaia* magnitude. In the case of a large discrepancy, this could be accounted for by the presence of extra quasar images and a lensing galaxy, which the ground-based imaging has blended with the original *Gaia* detection. To determine the centroid difference we use SDSS positions, which have been recalibrated as in Deason et al. (2017). The detection of only one image of a lensed quasar in *Gaia* will not be limited to the first *Gaia* data release. Indeed $\sim$ 1400 lenses (Section 3.1) will have just one component bright enough to be detected by *Gaia* but have other images fainter than the magnitude threshold, as can be seen by the difference between the two lensed quasar population histograms in Figure 3.1.

I. Astrometric Excess Noise

We initially consider the catalogue value of *astrometric excess noise* (hereafter AEN). This parameter represents the scatter in the astrometric model for a single object (Lindegren et al., 2016, 2012). A large AEN might indicate the presence of uncatalogued nearby images in lenses or perhaps a bright lensing galaxy. We match *Gaia* observations to the SDSS spectroscopic catalogues for stars, galaxies, and quasars within 0.5". We further require no flags from the spectral classification and recover 534,172 stars, 286,488 galaxies and 218,980 quasars. We plot their magnitude and AEN distributions in Figure 3.3, splitting the quasar sample into those above and below redshift 0.3. This plot reflects the method to separate galaxies from stars using AEN, as used in Belokurov et al. (2016) and Koposov et al. (2017). From the overlaid positions corresponding to lensed quasars, AEN alone cannot sufficiently identify most lensed quasars, however it is a useful parameter to consider for the brightest candidates. Therefore we turn our attention to using other datasets and *Gaia* catalogue parameters to indicate missing components from the catalogue.

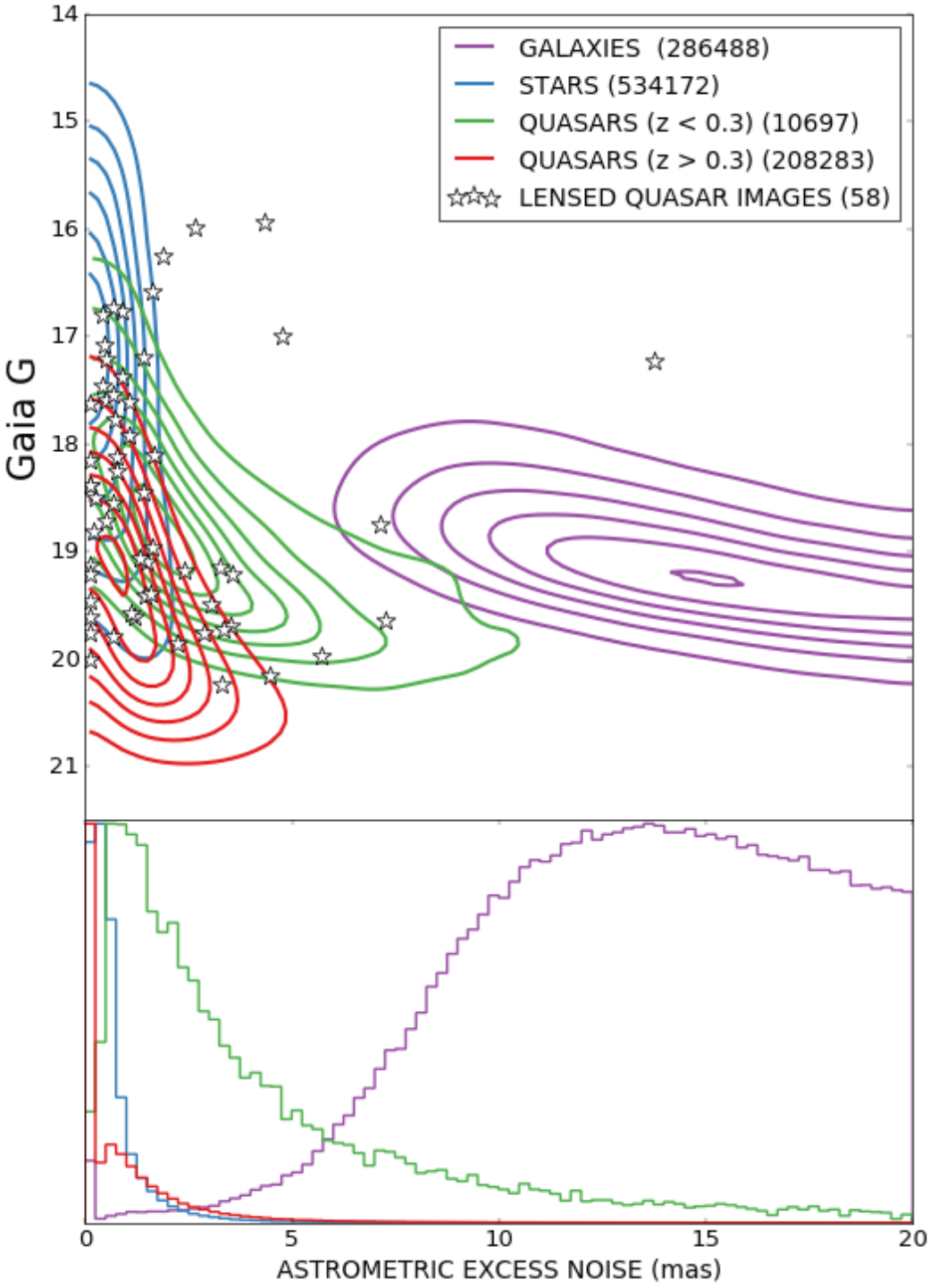

Fig. 3.3 Distributions of astrometric excess noise and *Gaia* magnitudes for spectroscopically confirmed galaxies, quasars, and stars matched to *Gaia* with all lensed quasar images from our small separation sample overlaid.

II. Flux deficit

Gaia's 0.1" FWHM PSF means that it can completely resolve the images of any useful lensed quasar (those that have large enough image separation to be spectroscopically confirmed from the ground). Therefore the *Gaia* flux measurement is truly an indication of the magnitude of a single image of the system. Comparing this value to a ground-based flux measurement of the entire blended system may allow the detection of the presence of further components in the system. Firstly we must determine a relationship between the *Gaia* G-band and ground-based photometric magnitudes.

To derive an empirical G-band fit for quasars, we need an isolated sample of quasars with *Gaia* detections. We use the extensive spectroscopically confirmed quasar catalogues from SDSS, which we match to the *Gaia* secondary source catalogue. On attempting to fit an empirical relation between the SDSS *ugriz* magnitudes and *Gaia*, the variability over the $\sim$ 10 year mean epoch difference is apparent (2015 for *Gaia* and 2003 for SDSS). Therefore we use the much better matched mean epoch of Pan-STARRS, 2013 (Chambers et al., 2016).

For the photometric fit we use the Pan-STARRS PSF magnitudes to ensure that we are comparing to the flux from just the quasar, since this is what *Gaia* is measuring. We apply the following cuts to the combined spectroscopic and photometric catalogues:

1. spectroscopic class = QSO
2. z < 5
3. zerr < 0.05
4. zwarning = 0
5. no *Gaia*, SDSS or Pan-STARRS neighbours within 5"
6. type = 6 (PSF morphology in SDSS)
7. Pan-STARRS $r_{\rm PSF}$-$r_{\rm kron}$ < 0.05
8. *Gaia*-SDSS centroid distance < 0.1"
9. *Gaia*-SDSS proper motion < 5mas yr^{-1}

Though the SDSS PSF morphology removes the majority of objects with bright hosts or nearby neighbours, we also apply an $r_{\rm PSF}$-$r_{\rm kron}$ magnitude cut to the deeper Pan-STARRS data to remove further extended objects. Finally, once an empirical fit to the G-band photometry is made, we remove those with the most inconsistent flux when compared to *Gaia* (5σ

outliers in a given magnitude bin) and repeat the fit. We are left with a catalogue of 117,599 *Gaia*-matched isolated quasars.

We are now able to fit an empirical G-band magnitude from the Pan-STARRS photometry, via a simple linear combination of g, r, i and z:

$$\mathrm{G_{synth}} = \alpha + \mathrm{r} + \beta(\mathrm{g}-\mathrm{r}) + \gamma(\mathrm{r}-\mathrm{i}) + \delta(\mathrm{i}-\mathrm{z}) \tag{3.1}$$

$$\sigma^2 = {\sigma_{int}}^2 + {\sigma_G}^2 + {\sigma_{Gsynth}}^2 \tag{3.2}$$

$$\mathrm{logP} = -\frac{\left(\mathrm{G}-\mathrm{G_{synth}}\right)^2}{2\sigma^2} - \frac{\log(2\pi\sigma^2)}{2} \tag{3.3}$$

This is well-motivated since the nominal *Gaia* bandpass roughly overlaps these optical filters, as shown in Figure 1.7. To include the high-redshift quasars in the sample we allow for their g-band dropout by fitting for two separate formulae at some $g-r$ cut. We optimise using the log likelihood of equation 3.3, determining the parameters $\alpha, \beta, \gamma, \delta, \sigma_{int}$ and the $g-r$ cutoff.

On applying this method to SDSS DR9 photometry we find an intrinsic dispersion of 0.263 mag. The fit to Pan-STARRS gives an improved intrinsic dispersion of 0.151 mag, reflecting the increased brightness variation of quasars over the larger SDSS timescales. The best fit formulae using Pan-STARRS photometry[1] are:

$$\mathrm{g}-\mathrm{r} < 0.11 : \mathrm{G} = -0.033 + \mathrm{r} + 0.131(\mathrm{g}-\mathrm{r}) - 0.660(\mathrm{r}-\mathrm{i}) - 0.162(\mathrm{i}-\mathrm{z})$$

$$\mathrm{g}-\mathrm{r} > 0.11 : \mathrm{G} = -0.061 + \mathrm{r} + 0.217(\mathrm{g}-\mathrm{r}) - 0.548(\mathrm{r}-\mathrm{i}) - 0.013(\mathrm{i}-\mathrm{z})$$

Figure 3.4 shows the residual magnitudes against redshift. The non-uniform redshift distribution of the quasar sample does not significantly bias the fit given the very similar dispersion at all redshifts. Furthermore the residuals are essentially Gaussian-distributed

[1]The best fit formulae using SDSS photometry are:

$$\mathrm{g}-\mathrm{r} < 0.24 : \mathrm{G} = 0.029 + \mathrm{r} + 0.139(\mathrm{g}-\mathrm{r}) - 0.641(\mathrm{r}-\mathrm{i}) - 0.496(\mathrm{i}-\mathrm{z})$$
$$\mathrm{g}-\mathrm{r} > 0.24 : \mathrm{G} = -0.038 + \mathrm{r} + 0.138(\mathrm{g}-\mathrm{r}) - 0.400(\mathrm{r}-\mathrm{i}) - 0.163(\mathrm{i}-\mathrm{z})$$

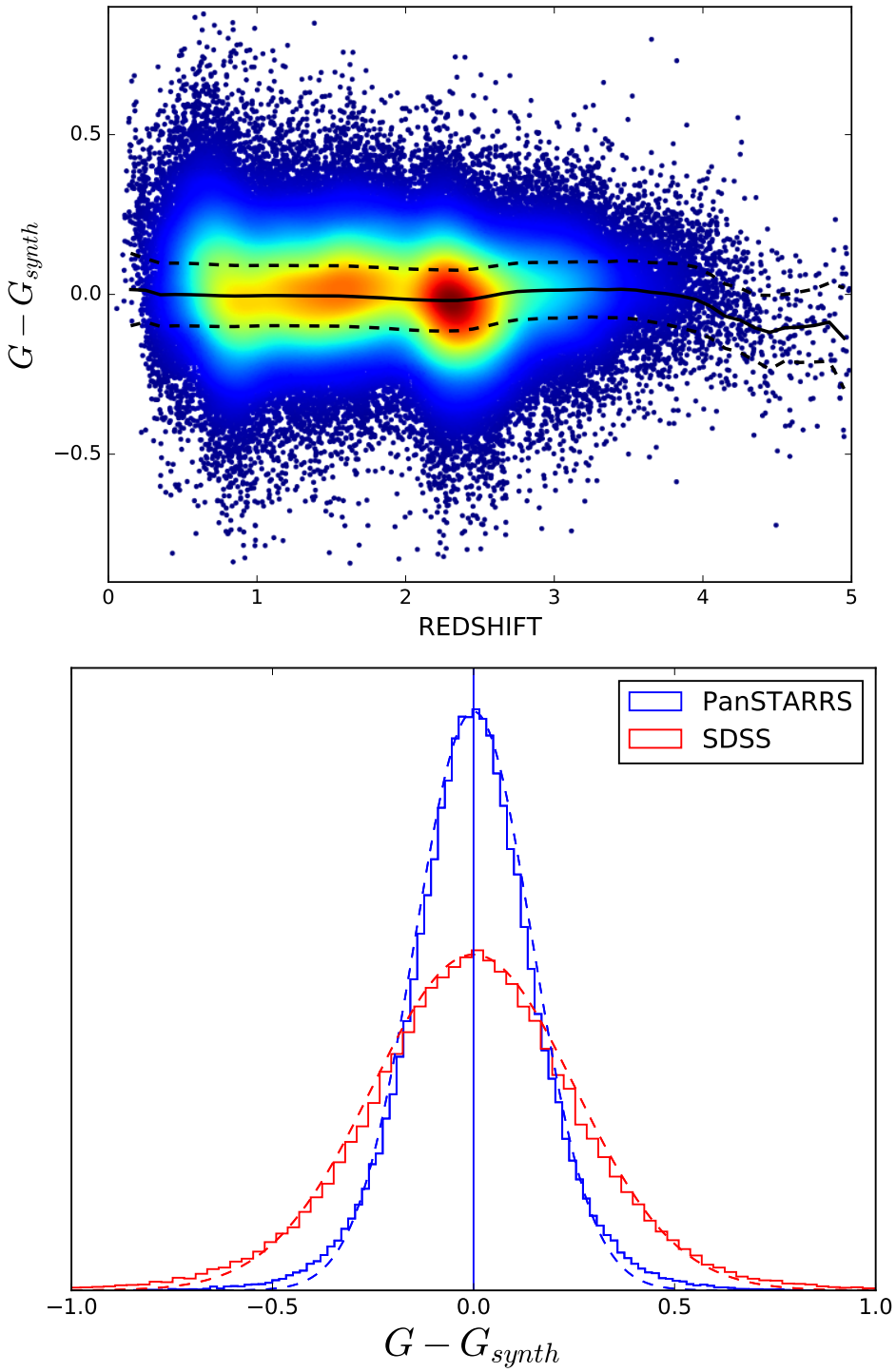

Fig. 3.4 The top plot shows synthesised *Gaia* G-band residuals against redshift for our sample of 117,599 isolated quasars. The overdensities are due to the non-uniform redshift distribution. The median and median absolute deviations are plotted at each redshift (black solid and dotted lines respectively). The bottom plot compares the fit to SDSS and Pan-STARRS data and equivalent Gaussians from the median absolute deviation are overlaid.

about zero (Figure 3.4). Estimates of median variability for this sample between *Gaia* and Pan-STARRS or SDSS are $\sim$0.1 or $\sim$0.15 respectively (Hook et al., 1994; MacLeod et al., 2012). Our dispersions (0.15 and 0.26 respectively) are larger than these estimates because of the error from the simple model fit to all quasar spectral shapes and redshifts.

We apply these empirical G-band fits to the sample of lensed quasars and compare them to *Gaia* measurements in Section 3.4.

III. Positional Offsets

Quasar lenses are often discovered by looking for extended quasar candidates. This is done by performing a cut in a PSF magnitude minus a model magnitude (i.e., a fit to a galaxy profile), where it is expected that a PSF magnitude will not capture all the flux of an extended object. However, this technique may fail to find all lensed quasars, especially those with small separations. To determine the limitations of this method, we match all *Gaia* pairs (two catalogue detections) between 0.5" and 1.0" separation to SDSS and compute $r_{\rm PSF}$-$r_{\rm model}$ (in this case we use the SDSS PSF and CMODEL magnitudes in the *r*-band Stoughton et al., 2002). We keep all pairs with brightness differences within 1 magnitude (based on their *Gaia* G-band magnitudes) as is typical for lensed quasar image fluxes, and remove objects obviously made up from non-point sources. We find a spread in $r_{\rm PSF}$-$r_{\rm model}$ of 0.076 ± 0.049 for objects with image separation 0.5-0.6" and 0.215 ± 0.117 for those with image separation 0.9-1.0". To understand these values we compare to single PSF objects (isolated *Gaia* detections) and find a value of 0.003 ± 0.042. Therefore, given the overlap in the $r_{\rm PSF}$-$r_{\rm model}$ values for single stars and pairs at separations of 0.5", the $r_{\rm PSF}$-$r_{\rm model}$ magnitude comparison for classification of extended/point source objects will often not be able to distinguish between relatively close binaries and single stellar objects. Furthermore, the sample of pairs we have used here is highly biased to objects of similar magnitude (as explained in Arenou et al., 2017 and due to our magnitude difference cut) whereas objects with large flux ratios will tend to appear even more PSF-like, implying a conservative upper bound on our $r_{\rm PSF}$-$r_{\rm model}$ values for pairs.

Given this discussion, it is clear that the PSF classification of SDSS ($r_{\rm PSF}$-$r_{\rm model} < 0.145$) will class many binaries and small separation lensed quasars as PSFs. This is perhaps less likely for quad lensed quasars in which there are four images; however, the image separations of the brightest components can often be much smaller than the Einstein radius, leading to a more PSF-like appearance.

Therefore we again turn to *Gaia*'s excellent resolution to define a parameter indicative of systems with multiple components. When a system is composed of two close stellar components, *Gaia* will catalogue the centroid of one of the two components with high

precision and accuracy. However, the same system in ground-based imaging will be blended and the catalogued centroid will lie between the two objects, offset from the *Gaia* centroid. This offset can easily be calculated and should be large for crowded systems like lensed quasars. Jackson and Browne (2007) suggest searching for an offset between optical and radio positions for identifying lensed quasars in radio surveys. Our method is similar, but we rely on both the galaxy and uncatalogued quasar images to cause the offset and only require optical data. While this offset might not be significant for doubles with large flux ratios, we always expect it to be apparent for quadruply-lensed quasars, since flux ratios between the two brightest images are approximately unity.

To robustly compare the difference in *Gaia* and SDSS positions, we must understand the minimum uncertainty expected from fitting a single PSF. Using a Gaussian PSF defined only by the FWHM and assuming at least critical sampling, any unbiased estimator is limited to a centroid positional error of $\sim$ (FWHM)/(signal to noise) (Mendez et al., 2013). The FWHM, signal and noise are inferred from the SDSS catalogues in the *r*-band since the standard SDSS positions are derived from the *r*-band. In order to look for sub-pixel offsets we must have very accurate SDSS astrometry. We therefore use the *Gaia*-based calibration of SDSS positions explained in Deason et al. (2017). Using this catalogue, the median *Gaia*-SDSS offset for quasars brighter than r=19 is 0.02". We use these recalibrated SDSS positions to define an offset parameter (OP):

$$\mathrm{OP} = \frac{\text{distance between } \textit{Gaia} \text{ and SDSS centroids}}{\text{SDSS PSF centroid uncertainty}} \tag{3.4}$$

The spread of this offset parameter in combination with the flux deficit from Section 3.3.2 can be seen for lenses and SDSS spectroscopically confirmed quasars in Figure 3.5 (see Section 3.4.2 for details).

This plot confirms the intuition that lensed quasars should have centroid and flux differences between *Gaia* and ground-based survey measurements. We use this plot in the next section to search for new lens candidates.

3.4 Lens candidate selection

GDR1 gives several clues to a source's nature, but cannot be used to distinguish between quasars and stars alone. Therefore we must start from a quasar candidate catalogue to find lensed quasars. Chapter 2.3.1 presented the results of a search for lensed quasars using *Gaia* detections in a variety of photometric quasar catalogues. However, to better understand the limitations of our methods, we will only consider the spectroscopically confirmed quasars of

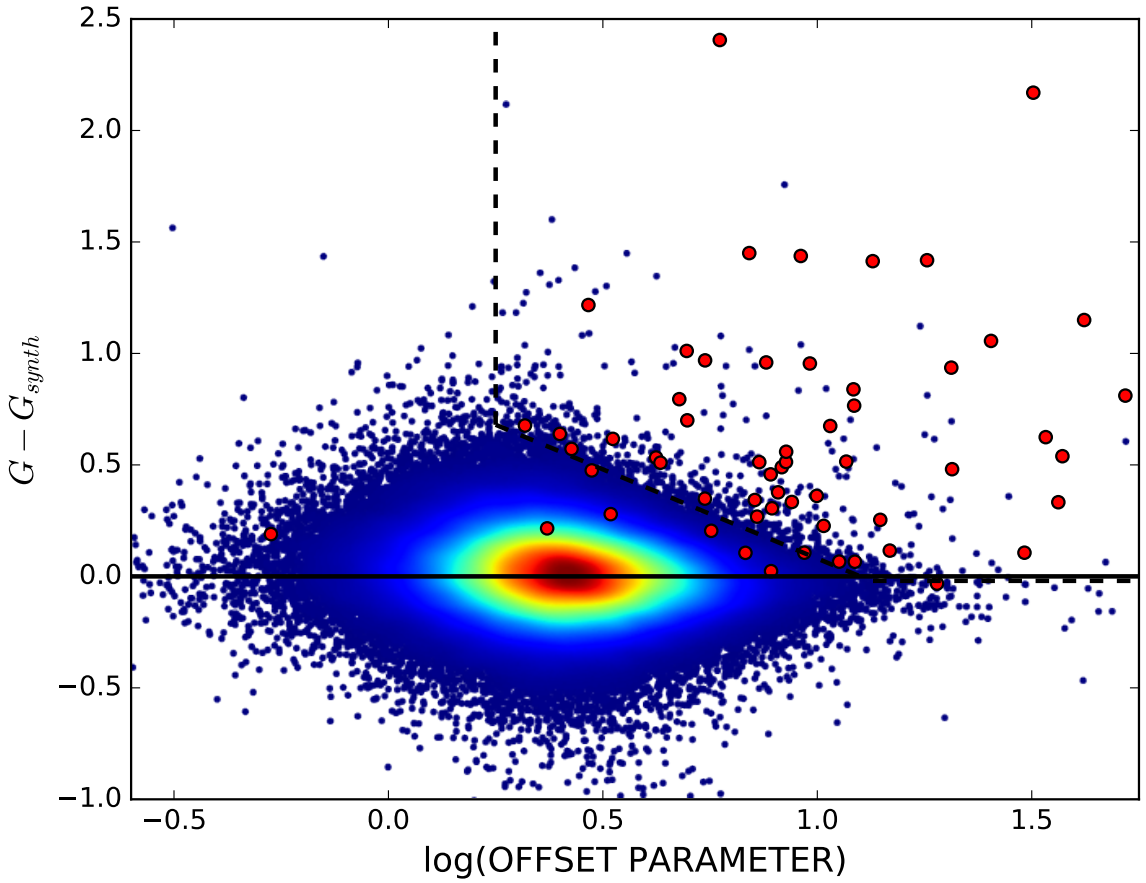

Fig. 3.5 Spectroscopically confirmed quasars (blue) and known lensed quasars (red) plotted in the parameter space described in the text. The upper-right region indicates an area of centroid and flux disagreement between *Gaia* and ground-based optical data that contains a large number of lensed quasars and few single quasars.

SDSS as a starting catalogue. The extra information from the spectra allows us to identify contaminant systems.

Many of the SDSS spectroscopically confirmed quasars have already been targeted by extensive lens follow-up programmes, as described in Section 1.3. However these campaigns focused on lenses with larger image separations than 1", so we expect lenses still exist in this catalogue at smaller separations. We restrict the redshift range of the SDSS quasars to $0.6 < z < 5$ to avoid low-redshift host galaxies creating outliers in positional and flux offsets and incorrectly identified objects as high-redshift quasars. Upon matching this set of quasars to *Gaia* detections within 3", we find 199,376 objects which we take as our catalogue for the following searches.

3.4.1 Multiple detections

We search the quasar catalogue for multiple *Gaia* detections within 1.5" to target the lenses that might have been missed by previous searches. We find that only 74 systems from our quasar catalogue have multiple detections in *Gaia* up to 1.5" and visually inspect their Pan-STARRS images. 7 of the 74 systems are the lensed quasars in our original sample (Section 3.2). Another 7 objects were falsely classified as high-redshift quasars. Approximately half of these 74 systems have very small separations (< 0.25") and appear as single PSFs in Pan-STARRS. Of the remaining higher-separation candidates, they are either obvious quasar and star pairs (indicated by large colour differences or stellar spectral features in the quasar spectra) or have already been followed up by SQLS and identified to be binary quasars or potential small-separation lenses.

3.4.2 Single detections

We calculate the flux deficit and offset parameter for our quasar catalogue and lens sample. The Pan-STARRS magnitudes are used to calculate a synthetic G-band magnitude as described in 3.3.2. However, since we want the total flux from the ground-based survey instead of the PSF magnitudes we used to fit the relation, we use the KRON magnitudes. The parameter values are plotted in Figure 3.5 for both the quasar and lensed quasar samples. As expected the lenses populate the area in which *Gaia* and SDSS have disagreeing centroids, and where *Gaia* is missing flux relative to Pan-STARRS. We note that the outlier with the smallest offset is SDSSJ0737+4825 (More et al., 2016). This system is a faint double with a large flux ratio (*i*-band magnitudes of 18.28 and 20.58, a flux ratio of ~ 8.5). Therefore, as we expected, it does not have a large statistical offset to the *Gaia* detection. Furthermore the other lenses that lie towards the bottom left of the plot are doubles. All quadruply-imaged

lenses are well-separated from the single quasars since the extra images cause larger flux deficits and more robust offsets, as already predicted in Section 3.3.2.

Based on the offset parameters (OP) and flux deficits (FD=$G - G_{synth}$) of our lens sample, we search for possible new lenses in our quasar catalogue by inspecting quasars with similar parameter values to the known lenses. We define a region in Figure 3.5 which clearly retains the majority of lenses while including very few of the main spectroscopic sample. The region is defined as log(OP) > 0.25, FD > -0.05 and FD+0.86log(OP) > 0.914, and contains 362 objects in the quasar catalogue (from the original sample of 199,376). We find about 10% of these objects are associated with blue stars with featureless spectra that the SDSS pipeline has classified as quasars without any spectrum-based warning. These objects have large OP and FD values perhaps due to proper motions and the empirical G-band values being based on a fit to quasars. After removing these from our sample by requiring a WISE detection (Wright et al., 2010), we find 319 possibly-extended candidates, of which 63 have Canada France Hawaii Telescope (CFHT) archival data or Hyper Suprime Cam (HSC, Aihara et al., 2018) Survey data, which we inspect. Many do not show distinct components either due to being outliers from the single quasar population (i.e., highly-variable quasars becoming fainter between Pan-STARRS and *Gaia* measurements) or having component separations small enough to become blended in the ground-based imaging.

We find 4 objects with clearly resolved components that have similar colours and do not show obvious contaminant spectral features (e.g., stellar absorption lines). These are shown in Figure 3.6 and several properties for the systems are listed in Table 3.2. Examples of the contaminant systems that can be distinguished through their spectra or colour images are shown in Figure 3.7 and their properties are also included in Table 3.2. Each of these systems was classed as a contaminant because of a strong colour gradient and, in the case of J0112+1512, the presence of an extended source. While we might be seeing lensing galaxies, no other quasar image is apparent and such large colour differences are unlikely between quasar images. These detections further demonstrate the effectiveness of our method in selecting close-separation pairs.

After KiDS data release 4 on 28 February 2019 (Kuijken et al., 2019), 6 further objects of our original 319 candidates had high-resolution imaging. One of these objects, J1359+0128, shows an extended nature in the KiDS data. In the *r*-band data, two PSFs are apparent, and subtraction shows an extended galaxy. Figure 3.8 shows PSF and galaxy subtractions. The separation of the two components is 1.00". The SDSS spectrum shows clear quasar emission lines at z=1.10, and a possible galaxy redshift of 0.21 based on a 4000Å break feature, and possible Ca H and K features.

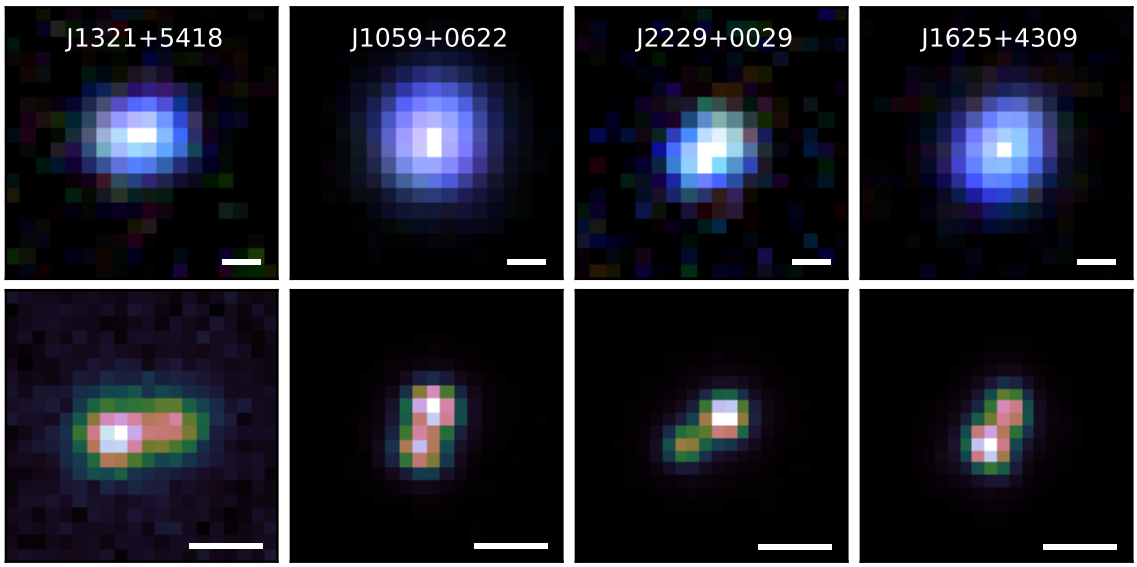

Fig. 3.6 New SDSS lensed quasar candidates. The top images show SDSS *gri* cutouts and bottom are either CFHT *r*-band cutouts (J1321+5418, J1059+6200) or HSC *i*-band cutouts (J2229+0029, J1625+4309) in a cubehelix colour scheme (Green, 2011b). The white bar is scaled to 1". Details for these systems can be found in Table 3.2.

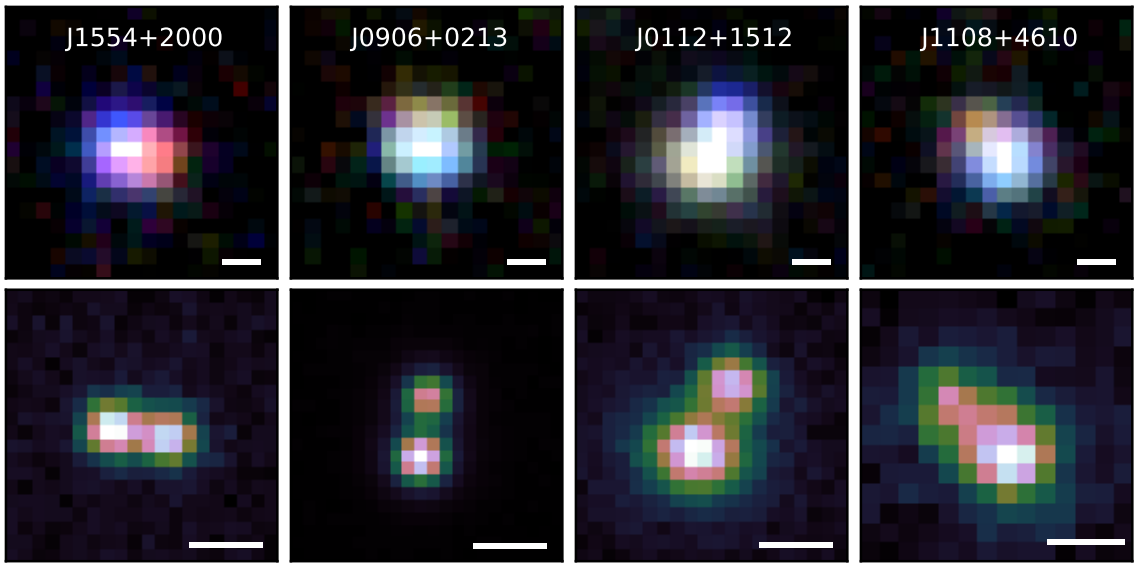

Fig. 3.7 SDSS quasar contaminant systems. The top images show SDSS *gri* cutouts and bottom are either CFHT *r*-band (J1554+2000, J0112+1512), HSC *i*-band (J0906+0213) or Pan-STARRS *z*-band (J1108+4610). The white bar is scaled to 1". Details for these systems can be found in Table 3.2.

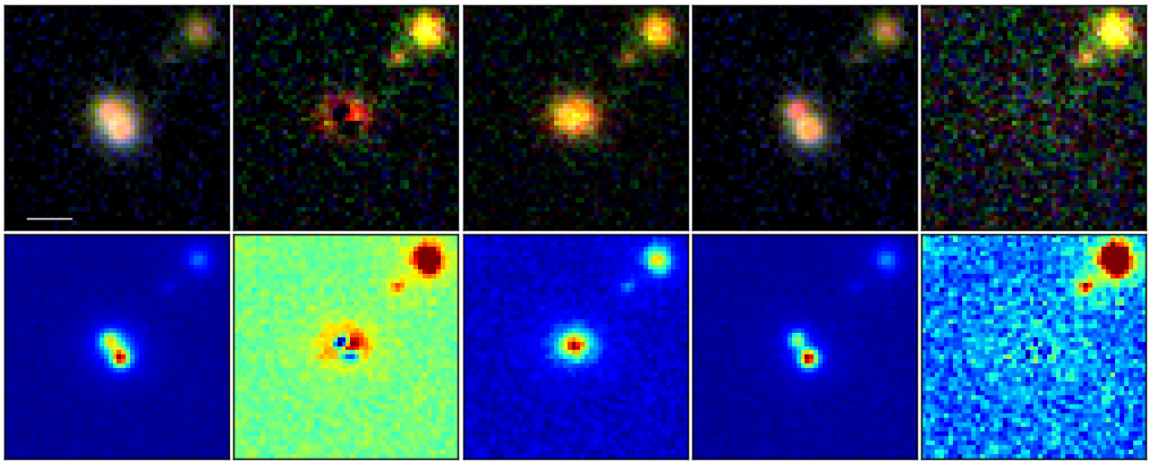

Fig. 3.8 KiDS data for J1359+0128. Top row shows *ugr* colour images of data, data subtracting two PSF fit, 2 PSF + galaxy fit with PSFs removed, the same as before but with PSFs removed, and finally all components removed. The bottom row shows the same panels but for just the *r*-band data. The white scale bar in the first panel is 2".

Table 3.2 Details of new candidate lensed quasars (LC) and contaminant systems (CS).

Name	outcome	RA	DEC	redshift	sep.(")	G	FD	centroid offset(")	log(OP)
J1359+0128	LC	209.9342	1.4693	1.10	1.00	20.30	0.517	0.365	1.12
J1321+5418	LC	200.3694	54.3154	2.26	0.81	20.24	0.429	0.226	0.74
J1059+0622	LC	164.8602	6.3742	2.19	0.59	17.48	0.337	0.253	1.31
J2229+0029	LC	337.4285	0.4984	2.14	0.64	20.48	0.523	0.244	0.70
J1625+4309	LC	246.2583	43.1587	1.65	0.53	19.27	0.345	0.231	0.94
J1554+2000	CS	238.5814	20.0025	2.25	0.73	20.38	0.499	0.426	0.84
J0906+0213	CS	136.7272	2.2209	2.01	0.82	20.35	0.769	0.060	0.42
J0112+1512	CS	18.1225	15.2041	1.96	0.99	19.80	0.479	0.712	1.07
J1108+4610	CS	167.1878	46.1766	1.84	0.97	19.99	0.494	0.117	0.64

3.5 Conclusions

Given the sky coverage, depth and excellent resolution of *Gaia*'s first data release, it is a prime dataset to use for lensed quasar searches. However, GDR1 has often catalogued only one component of lensed quasars, in particular for systems with small image separations (Arenou et al., 2017). It is at these separations that we would benefit most from *Gaia*, since ground-based imaging is unable to resolve the separate images of a lensed quasar. Therefore we have developed a method to exploit a single *Gaia* detection to find the population of small-separation lensed quasars. This method relies on *Gaia* effectively resolving out the flux from just one image of a lensed quasar, whereas ground-based observations (from SDSS and Pan-STARRS) blend the components together. For a sample of 49 known small-separation lensed quasars, we demonstrate that the Pan-STARRS flux is larger than the *Gaia* flux, verifying the idea that *Gaia* is only measuring a single image. We also show that the offset between *Gaia* and SDSS positions for our sample of lensed quasars is significant, because the *Gaia* centroid lies on top of the detected image, whereas in SDSS it is at the luminosity-weighted centroid of the system.

By performing the same flux and centroid difference measurements on spectroscopically confirmed SDSS quasars, we are able to search for new lensed quasars. Inspecting better-seeing data of the systems with the largest flux and centroid offsets, we find 5 new sub-arcsecond lensed quasar candidates with resolved components in HSC, CFHT, or KiDS data. At such small separations, projected systems (e.g. quasar+star) are less common, and so lensed quasars selected in this way are less contaminated.

As future *Gaia* data releases improve the completeness of secondary source detection in close pairs, multiple *Gaia* detections will become an easily-implemented method to find lensed quasar candidates. However, our method of using single *Gaia* detections will still be a useful tool to discover lensed quasars that have only one image bright enough to be detected by *Gaia*. This will include $\sim$1400 lensed quasars. Furthermore, as wide-field optical surveys become deeper, the centroid offset will become a more robust statistic for differentiating between single quasars and lensed quasars. The task will then be to remove contaminant systems such as quasar and star alignments. *Gaia*'s long temporal baseline and repeated measurements will help select systems with similar component variability and its blue and red photometer instruments can ensure components have a similar colour.

Finally we note that these methods are not restricted to lensed quasar searches, but should be useful for searches for stellar binary companions, or to remove contaminants from samples of isolated quasars. These techniques demonstrate how *Gaia*'s excellent resolution provides an important complement to future deep ground-based optical surveys.

Chapter 4

Lensed Quasars from *Gaia* Data Release 2

The second *Gaia* data release (GDR2) from 25 April 2018 contains data from the first 22 months of the nominal 60 month *Gaia* mission. Table 4.1 shows the numbers of detections and measured ancillary information for the first and second data releases[1]. In this Chapter we will review the state of lensed quasars in GDR2, showing a significant improvement in the detection of lensed quasar images. We detail how the modelling of unblurred WISE pixels based on *Gaia* positions is a particularly useful way to remove quasar+star contaminants, while retaining nearly all lensed quasars. Applying this modelling alongside simple cuts from proper motions and astrometric excess noise, we carry out a variety of lensed quasar searches in photometric and spectroscopic quasar and galaxy catalogues. We present results based on 4 nights of spectroscopic follow-up at the WHT.

Table 4.1 Summary of detections in GDR1 and GDR2. 5-parameter sources include proper motion and parallax information, while 2-parameter sources only include position information.

	sources in *Gaia*DR2	sources in *Gaia*DR1
Total number of sources	1,692,919,135	1,142,679,769
Number of 5-parameter sources	1,331,909,727	2,057,050
Number of 2-parameter sources	361,009,408	1,140,622,719
Sources with mean G magnitude	1,692,919,135	1,142,679,769
Sources with mean BP photometry	1,381,964,755	-
Sources with mean RP photometry	1,383,551,713	-

[1]Replicated from https://www.cosmos.esa.int/web/gaia/dr2

4.1 *Gaia* DR2 data

Before searching the *Gaia* DR2 catalogue for lensed quasars, we investigate how the *Gaia* parameters can be used to remove common contaminants. As part of this investigation and to aid future lens searches, we have compiled a list of all published, spectroscopically followed-up lensed quasar candidates. This is readily accessible on our online database[2], and is intended to both prevent repeated observations and to allow tests of future lens-finding techniques' selection purity.

4.1.1 Detection Rate

Table 4.2 shows the number of images detected by *Gaia* for the known lensed quasars in *Gaia* DR1 and DR2. We split the sample into doubles and quads, with the latter including all systems with more than 2 images. There is a dramatic improvement for lensed quasar image detection in DR2, with 3 times more doubles having both images detected. The 24 doubles that have only one image detected are due to the fainter image not meeting the detection threshold. Of the doubles and triples with all images bright enough for *Gaia* to detect, only one system, APM08279+5255, has just one Gaia detection (Irwin et al., 1998). This is likely due to the small separation of the system—0.38". The improved completeness generally applies to the quads as well. The small number of quads with only one image detected in DR2 demonstrates not only how most quads have at least two bright images of similar flux (either in folds, crosses, or cusp configurations), but also *Gaia*'s increased detection rate in crowded regions with DR2.

Table 4.2 Number of lensed quasars with N *Gaia* detections in *Gaia* DR1 and DR2, from a total sample of 206 lenses—52 quads, 2 triples, and 152 doubles. We include triply imaged systems in the quads column.

	Gaia DR1			*Gaia* DR2		
	All	Quads	Doubles	All	Quads	Doubles
N=0	45	19	26	32	14	18
N=1	105	14	91	27	3	24
N=2	50	13	37	122	10	112
N=3	5	5	—	12	12	—
$N \geq 4$	1	1	—	13	13	—

Figure 4.1 replicates the analysis from Chapter 2.3.1, in which separations between all point sources in a sparse field showed that *Gaia* DR1 did not catalogue companions separated

[2]https://www.ast.cam.ac.uk/ioa/research/lensedquasars/

by less than 2.1". For the same field of sky, the number of detections has increased by 31%, and the effective resolution has decreased to 0.7", with a strict cut at 0.4".

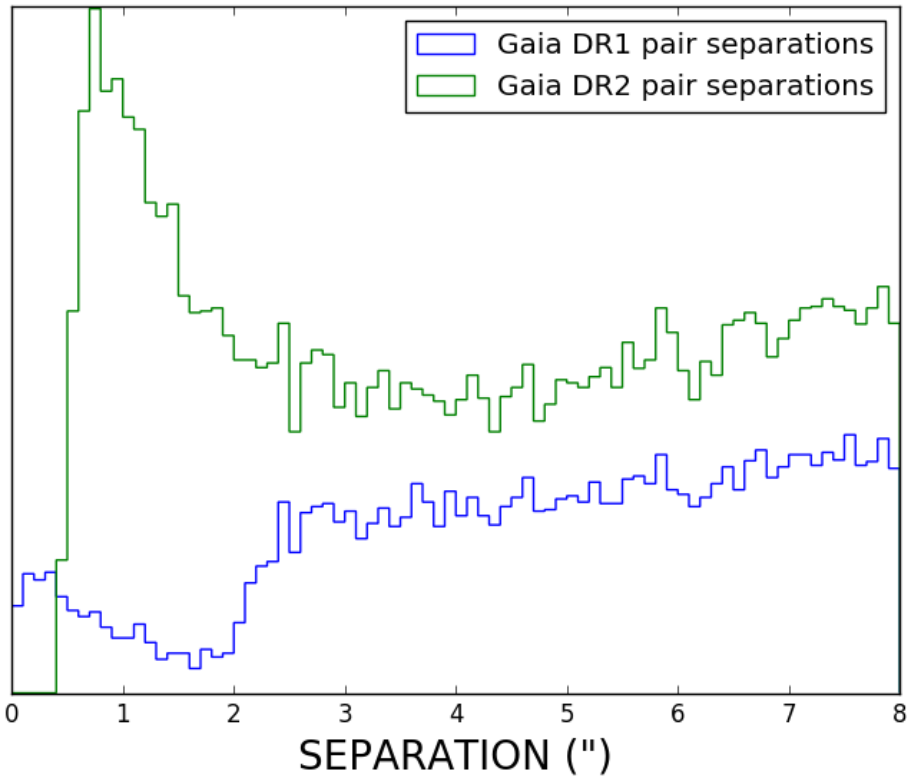

Fig. 4.1 Histogram of pair separations in the sparse extragalactic field around $l \sim 173$ degrees, $b \sim 67$ degrees. While *Gaia* DR1 had an effective resolution of ∼2.1", this is improved to ∼0.7" in *Gaia* DR2, with >30% more sources detected in this field.

4.1.2 Proper Motions

Gaia's precise, multi-epoch photometry also enables proper motions to be measured, and these can be very effective at removing stellar contaminants. Cross-matching SDSS spectroscopic quasars and stars to *Gaia*, all bright (G<20) isolated quasars and stars have catalogued proper motions, while only 84 % of lensed quasar images, also with G<20, have proper motions. This must be due to the crowding of nearby detections and overlapping windows not yet being processed (Riello et al., 2018). For all fainter objects (G>20) this percentage quickly drops to around 50 %.

Proper motions alone do not help without taking their uncertainties into account. We therefore define the proper motion significance (PMSIG) as:

$$\mathrm{PMSIG} = \left[\left(\frac{\mathrm{pmra}}{\mathrm{pmra\_error}} \right)^2 + \left(\frac{\mathrm{pmdec}}{\mathrm{pmdec\_error}} \right)^2 \right]^{1/2} \tag{4.1}$$

where pmra, pmra_error, pmdec, and pmdec_error are obtained from the *Gaia* DR2 catalogue. The distributions of PMSIG for lensed quasar images, isolated quasars, and stars, are shown in Figure 4.2. There are 4 lensed quasar images with a PMSIG value above 10: QJ0158-4325 (Morgan et al., 1999), DESJ0405-3308 (Anguita et al., 2018), RXJ0911+0551 (Bade et al., 1997), and SDSSJ1330+1810 (Oguri et al., 2008b). The latter three cases are compact quads with nearby collections of quasar images, perhaps leading to *Gaia* mis-assigning the images at each epoch due to the required binning of a 2.1"-wide window perpendicular to the scan direction. However, for the doubly imaged lens, QJ0158-4325, the brighter image (G=17.60) has a PMSIG of 13.8 and a small astrometric excess noise of 0.7mas (see Section 4.1.3), with the other image also being detected by *Gaia* 1.22" away. It is unclear what has caused this image's large PMSIG.

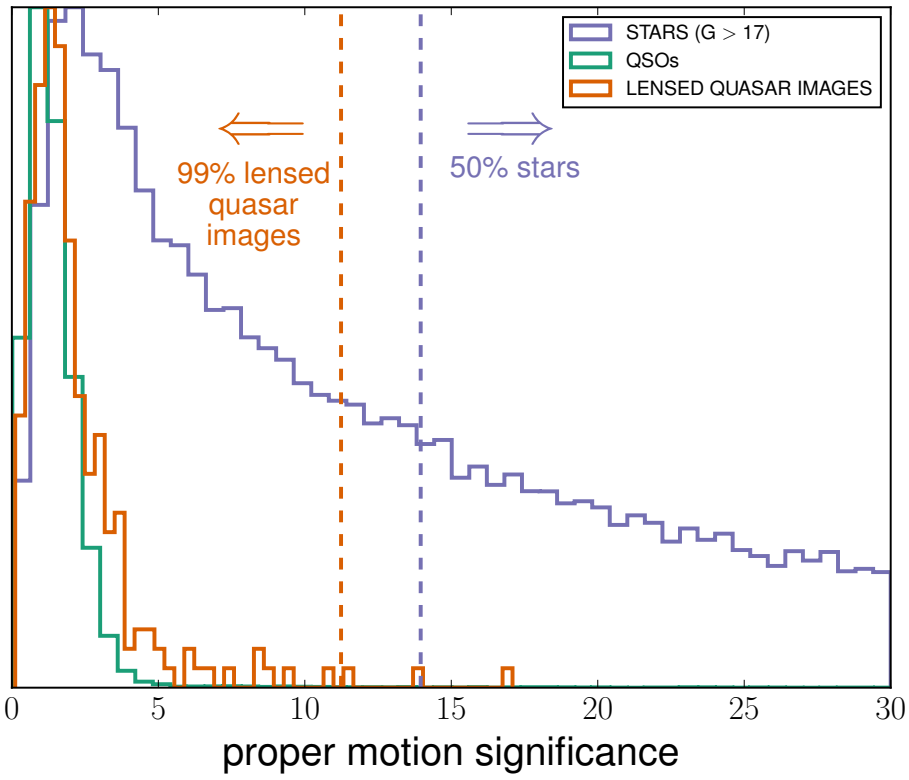

Fig. 4.2 A histogram of proper motion significances for spectroscopic stars fainter than $G = 17$, spectroscopic quasars, and lensed quasar images. The histograms are scaled to the same peak values.

4.1.3 Astrometric Excess Noise

A major contaminant for lens searches relying on photometric quasar selection is compact star-forming galaxies (e.g. Treu et al., 2018). Upon inspection of ground-based data, a pair of star-forming galaxies can appear consistent with PSFs and worthy of spectroscopic follow-up. *Gaia* provides a way to remove such systems, through the astrometric excess noise (hereafter AEN) parameter (e.g. Belokurov et al., 2016; Koposov et al., 2017). *Gaia* DR1 showed that the AEN could separate intermediate-to-high redshift quasars from star-forming galaxies via a simple cut. In essentially all cases this also kept all lensed quasar images (see Chapter 3).

We repeat the *Gaia* DR1 AEN comparison from Chapter 3 for *Gaia* DR2. From our list of known lensed quasars, there are 321 lensed quasar images with *Gaia* detections. Figure 4.3 shows *Gaia* magnitude against AEN for each of these images, and also SDSS spectroscopic quasars, galaxies, and stars. All lensed quasar images clearly avoid the galaxy locus in the *Gaia* *G*-AEN plane. When only considering AEN, several lens images have galaxy-like AEN values.

The 7 quasar images with AEN>10 fall into three categories: 1. PSJ0840+3550 (Lemon et al., 2018) and WGD2038-4008 (Agnello et al., 2018b) have their large AEN image very close to a bright extended galaxy; 2. WFI2026 (a 0.33" separation pair, Morgan et al., 2004) and SDSSJ1640+1932 (a 0.72" separation pair, with both images catalogued by *Gaia* and each with AEN>10, Wang et al., 2017) have very small separation image pairs; and 3. H1413+117 (Magain et al., 1988) and DESJ0405-3308 (Anguita et al., 2018) are compact quads. The first two examples are likely to remain with a large AEN after subsequent *Gaia* data releases, though the remainder may improve as further scans at different angles are able to pin down each image. Surprisingly, the two detections in the Einstein cross, Q2237+030, have AENs of 2.2 and 3.0 in spite of all four images being embedded in the centre of the bulge of a relatively local ($z = 0.04$) galaxy.

A search using an AEN cut based on separation would help recover the compact quad systems and still remove wider-separation galaxy pairs. We however only use the AEN to prioritise candidates for most of our searches. Indeed, *Gaia* detections could be due to the lensing galaxy, for which a high AEN is expected (see Section 4.3.2 for examples).

4.1.4 Removing crowded regions

All-sky lens searches must perform a cut to remove very high density regions on the sky. This is usually done by some cut on galactic latitude (e.g. Krone-Martins et al., 2018) around $|b|$>15 or higher. While this effectively removes the galactic centre, it does not remove star clusters, extended star-forming regions, or the Magellanic clouds, and treats differently

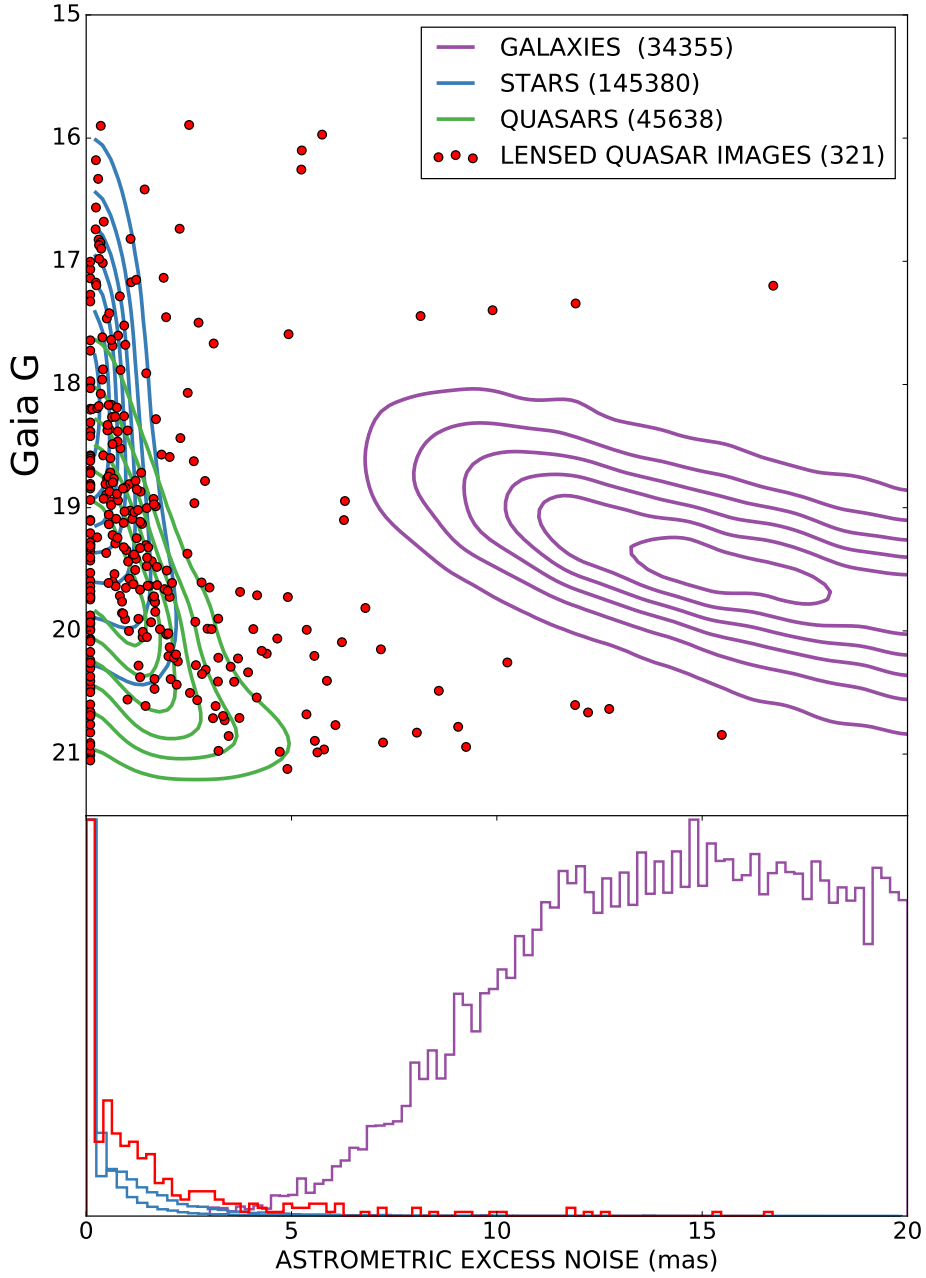

Fig. 4.3 *Gaia G* against AEN for SDSS DR12 spectroscopically confirmed stars, galaxies, and quasars. 321 lensed quasar images detected by *Gaia* are also overlaid as red dots. They are clearly separated from the galaxy locus.

crowded areas of sky equally. *Gaia* by default allows us to remove regions where the concentration of contaminants (stars near quasars) becomes unmanageable. We do this following Chapter 2.3.1 by defining the local *Gaia* detection density per square degree within 100" of a particular target. A search-dependent cut is then placed on this density. For the Pan-STARRS footprint ($\sim$30,832 square degrees), after a density cut of 20,000 detections per square degree, the area drops to 22,094 (i.e. 72%). For density cuts of 30,000, 50,000, and 100,000 detections per square degrees, the remaining areas are 24,336 (79%), 26,939 (87%), and 28,995 square degrees (94%) respectively.

4.2 Lens Selection

In this section, we present three searches for lensed quasars. For each search we use different cuts on number of *Gaia* detections, PMSIG, local *Gaia* density, and AEN.

4.2.1 Multiple *Gaia* detections around quasar catalogues

I. WISE

The Wide-Field Infrared Survey Explorer (WISE, Wright et al., 2010) provided a full-sky survey at wavelengths of 3.4, 4.6, 12, and 22 microns (W1, W2, W3 and W4). This photometry has since been used as an efficient way to identify pure samples of quasars (e.g. DiPompeo et al., 2015). Figure 4.4 shows the ALLWISE detection rate of $|b|$>20 Milliquas quasars (Flesch, 2015) against Pan-STARRS *i*-band magnitude. The Pan-STARRS-to-ALLWISE crossmatch was made within 4". At optical magnitudes brighter than 19.5– roughly the faintest magnitude we expect for the sum of quasar images each detected by *Gaia*, and a lensing galaxy detected in Pan-STARRS–nearly all quasars are detected. Such a catalogue is ideal for searching for lensed quasars with multiple *Gaia* detections; however, we note that a small percentage of bright quasars are not detected due to blending with nearby bright galaxies or PSF spikes.

We repeat the search from Chapter 2.3.1 for multiple *Gaia* detections around red ALLWISE detections (Mainzer et al., 2011a). We visually inspect all sets of 2, 3, and 4 *Gaia* detections separated by less than 4.5" and all within 4.5" of an ALLWISE source satisfying W1$-$W2>0.2, 0.3, and 0.4 respectively, and W1<15.5. Constraints on PMSIG and local stellar density are varied for each selection and summarised in Table 4.3. These cuts are as loose as possible while still keeping the number of systems inspected manageable.

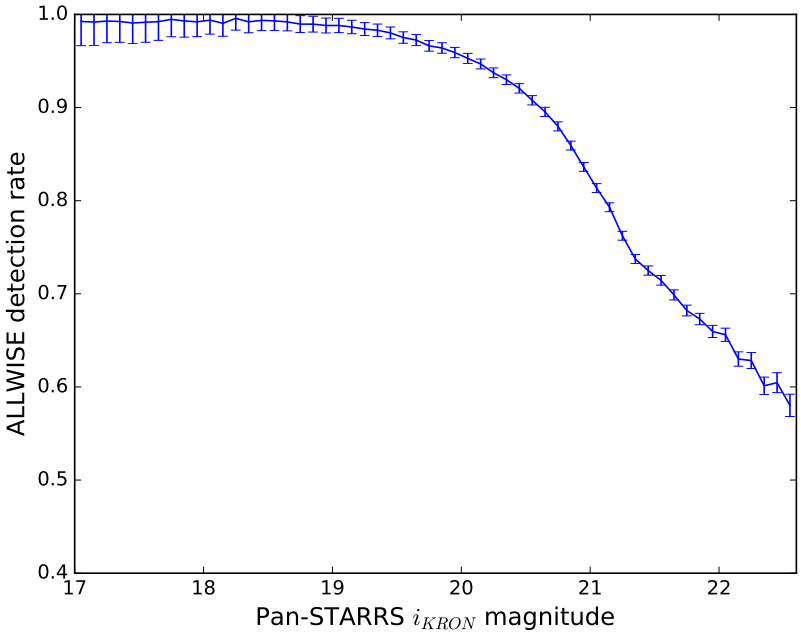

Fig. 4.4 ALLWISE catalogue detection rate of Milliquas quasars ($|b|$>20), as a function of Pan-STARRS i_{KRON} magnitude. Lensed quasars with two or more *Gaia* detections (G<20.7) will have a total G-band (and approximately i-band) magnitude less than 19.5.

II. Milliquas

The quasar catalogue from Flesch (2015) contains nearly 2 million high-confidence quasars[3]. While this catalogue has a large overlap with the WISE colour-selected sample, it includes quasars detected in the X-ray and radio. At these wavelengths a lensed quasar with a bright lensing galaxy will still be selected, whereas in optical- and infrared-selected photometric quasar catalogues, the galaxy can shift the system away from the quasar locus and hence remove it from the selection. We search this catalogue for lensed quasars by requiring 2 *Gaia* detections both within 4.5" of the catalogue position and separated from each other by less than 4.5". This yields 14,046 candidates after a density cut of 20,000 and PMSIG less than 12.

4.2.2 Modelling unWISE pixels

The FWHM of the WISE PSF in the W1 and W2 bands is $\sim$ 6". While a quasar and star separated by a few arcseconds will be blended and catalogued as one object, the WISE pixels can be modelled if the PSF and positions of the components are known, as has been demonstrated with SDSS data (Lang et al., 2016) using a set of unblurred WISE coadds

[3]http://quasars.org/milliquas.htm

(unWISE, Lang, 2014). We apply this technique, using the *Gaia* positions and ALLWISE catalogue positions, to the most up-to-date unWISE coadds and PSFs (Meisner et al., 2017a,b, 2018). The data are very well calibrated astrometrically, allowing us to use the *Gaia* positions to model the pixels directly without needing to infer a registration between the two datasets. Any modelled cutouts must be large enough to include PSF spikes from nearby stars, but also small enough for the relative component fit to be computationally fast. Therefore, we divide the sky through an equal area HealPix tiling (Górski et al., 2005), resulting in 50,331,648 70"$\times$70" tiles across the whole sky. Each tile overlaps neighbouring tiles by 5" in order to ensure that lens candidates at the edges of these tiles are not missed. Applying the following process to each of these cutouts resulted in 25,129 candidates:

1. The *Gaia* density (as defined in Section 4.1.4) is calculated at the tile centre, and the modelling proceeds if this is below 20,000 per square degree.

2. If any close pair of *Gaia* detections exists on the cutout separated by 5" and any PMSIG values are less than 10, the modelling proceeds.

3. For both the W1 and W2 bands, a model is built by placing unWISE PSFs at the positions of all *Gaia* detections, and at ALLWISE catalogue detections which are more than 2" from a *Gaia* detection. A uniform background is added to this model.

4. The fluxes of each PSF and background level are inferred through a non-negative least squares fit to the data weighted by the uncertainty maps. These are then converted into best fit W1 and W2 Vega magnitudes.

5. If for each component of the close pairs, W1<15.5 and either W1$-$W2>0.4 or G$-$W1>3.75, a Pan-STARRS cutout is visually inspected. See Figure 4.5 for these colour cuts.

To test this technique's efficiency at recovering known lenses, we extracted W1 and W2 magnitudes for all 147 known lensed quasars with 2 or more *Gaia* detections. The *Gaia G*, W1, W2 colour plot for the reddest two components of all 147 systems is shown in Figure 4.5 (without cuts on separation or PMSIG). From the list of previously followed-up systems (Section 4.1), we compiled a list of 127 spectroscopically confirmed quasar+star systems that were identified as potential lensed quasar systems in previous lens searches (Hennawi et al., 2006; Inada et al., 2008, 2010, 2012; Lemon et al., 2018; More et al., 2016; Williams et al., 2018). 52 of these systems have two *Gaia* detections. We plot their modelled WISE+*Gaia* colours in Figure 4.5, separating the stellar and quasar components.

Only two lens systems have a component with no modelled W1 or W2 flux, both with *Gaia* detections separated by less than 1": SDSSJ1640+1932 (Wang et al., 2017) and SDSSJ0248+1913 (Ostrovski et al. in prep., Delchambre et al., 2018). However, 21 such examples exist in the quasar+star sample. Using the previously mentioned colour cuts, we are able to remove 41 of the 52 contaminants, while keeping 145 of the 147 lensed quasars. The contaminant systems are already biased to those systems which most resemble lensed quasars, as the search teams thought they merit spectroscopic follow-up. The 11 contaminant systems which evade our colour cut removal are all 1" or less separation.

On application, about 1 in 20 tiles from steps (1) and (2) are subject to unWISE model fitting, while approximately 1 in 300 of these contain systems passing the remaining colour criteria. The main contaminants are galaxy pairs and pairs of *Gaia* sources on bright WISE star streaks. Since there is no required cut on the W1−W2 colour of each component, any source for which *Gaia* is not capturing all the flux—for example, PSFs with nearby galaxies—will lead to an inflated G−W1 colour, bringing the system into our inspected sample. Figure 4.5 shows that our selection efficiency can be improved by applying a strict cut of W1−W2>0, without any change to the completeness.

Figure 4.6 shows the unWISE modelling and pixel model subtractions for PSJ0028+0631, PSJ2145+6345, and ULASJ2343-0050 (Jackson et al., 2008).

4.2.3 LRGs with *Gaia* detections

Quasar-colour-selected lensed quasar searches will be biased away from discovering systems with bright lensing galaxies (see Lucey et al., 2018). We therefore aim to complement our quasar-colour-selected search with a search for *Gaia* detections around bright galaxies. Firstly, we use the SDSS DR12 spectroscopic galaxy sample (i.e., any spectra with CLASS="GALAXY"). For each galaxy we require two detections separated by less than 4.5", and each within 4.5" of the SDSS position. A second search is also performed requiring just one *Gaia* detection between 1" and 3.5" from the galaxy. After a cut on the PMSIG of 8 and AEN of 5, the two searches yielded 3,056 and 11,201 candidates respectively.

Thirdly, we perform a search for bright morphological Pan-STARRS galaxies satisfying $i_{PSF} - i_{KRON} > 0.7$, $i_{KRON} < 19$, and with at least one *Gaia* detection between 1" and 3" away. We apply further cuts of PMSIG < 5 and an AEN < 5 on the nearest *Gaia* detection, yielding 22,156 candidates. These search criteria recover previous lenses with bright lensing galaxies and only one *Gaia* detection, i.e. SDSSJ0819+5356 (Inada et al., 2009), PSJ0123-0455, and PSJ1602+4526 (Lemon et al., 2018).

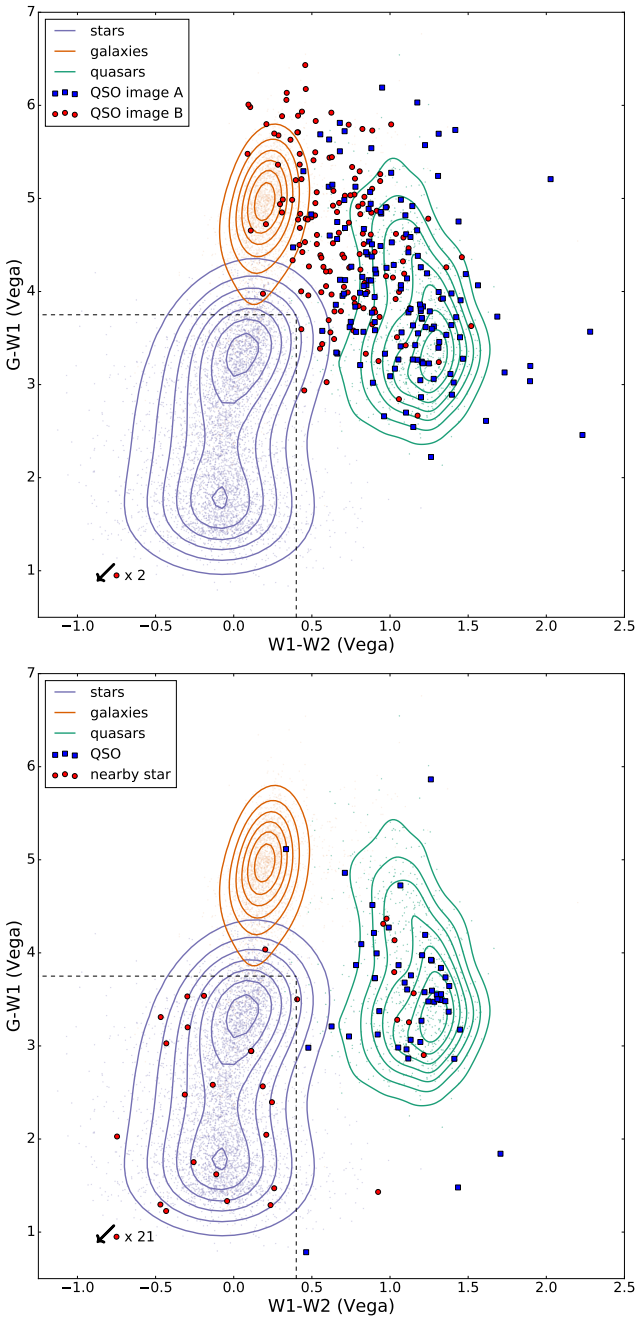

Fig. 4.5 *Gaia*-WISE colour plots. *Top*: modelled unWISE W1,W2 and *Gaia G* colours for all 147 known lensed quasars with two or more *Gaia* detections. When more than two images are present, the two with the reddest W1−W2 points are plotted. Red circles show the less red component of this pair, i.e. W1−W2(A)>W1−W2(B). *Bottom*: Modelled unWISE W1,W2 and *Gaia G* colours for 52 spectroscopically confirmed quasar+star contaminant systems. The stellar components' colours are plotted as red circles. A cut of W1−W2<0.4 and G−W1<3.75 removed 41/52 contaminant systems, while keeping 145/147 lensed quasars.

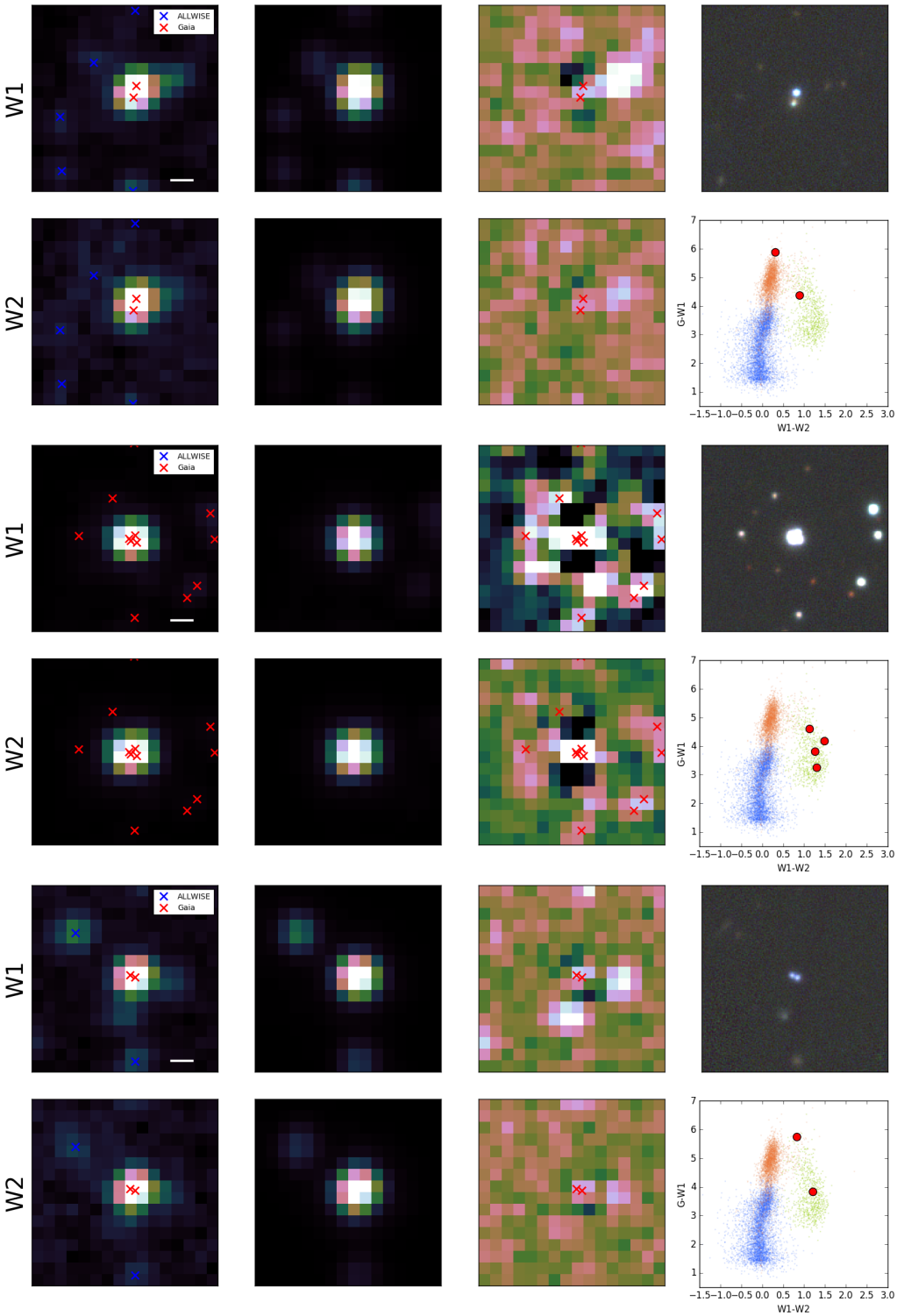

Fig. 4.6 unWISE pixel modelling for PSJ0028+0631, PSJ2145+6345, and ULASJ2343-0050. The first three columns are data, model, and data-model, with modelled *Gaia* and ALLWISE detections overlaid. The upper right panel shows the Pan-STARRS *gri* colour image for the same field. The white scale bars are 5".

4.2.4 Multiple *Chandra* detections

Using the recently updated source catalogue from *Chandra* (Evans et al., 2010), we performed a search for close pairs of sources within this catalogue, since *Chandra*'s PSF FWHM is $\sim$0.5". This search is aimed at looking for lensed quasars with bright lensing galaxies, which might be missed by our other quasar-colour-selected catalogues. The catalogue has 315,875 detections. We performed a self-crossmatch within 5" for declinations above -30 degrees. This returned 8,513 objects, for which Pan-STARRS cutouts were then visually inspected.

Table 4.3 Summary of lens selection techniques. For each method, the number of required *Gaia* detections, density cut, and PMSIG cut is given. All *Gaia* searches also include a *Gaia* magnitude threshold of G>15. We note the candidates are not mutually exclusive.

quasar selection	N_{Gaia}	density	PMSIG	N
W1−W2> 0.2	4	<100000	<18	2895
W1−W2> 0.3	3	<50000	<15	10274
W1−W2> 0.4	2	<30000	<10	13397
unWISE model	2	<20000	<12	25129
Milliquas	2	<20000	<12	14046
Spec. Gals	1/2	<20000	<12	11201/3056
Morph. Gals	1	<20000	<5	22156
Chandra double	–	–	–	8513

4.2.5 Final candidate selection

The total number of candidates selected by each technique is shown in Table 4.3. For each candidate, a Pan-STARRS *gri* colour image is inspected. The majority of candidates are discarded since they are obvious contaminants—they have components with different colours, or the *Gaia* detections correspond to extended galaxies. The most promising candidates, showing nearby PSFs of similar colours, are graded between 1 and 10. The most promising quad candidates with similar unWISE model colours are given a grade of 10. Doubles showing putative lensing galaxies are graded 7-9 depending on component colours, proper motion values, and astrometric excess noise value, while pairs without lensing galaxies were graded 1-6 depending on the same information.

For any WISE-selected candidates, the W1 and W2 images are checked for contamination from nearby stars/galaxies. Finally, the model $G-$W1 and W1$-$W2 colours are inspected for all remaining candidates, and their grades adjusted according to their relative position to the quasar locus (see Figure 4.5). The candidates with the highest grades were prioritised for follow-up.

4.3 Results

Spectra of 87 candidates were taken using ISIS on the William Herschel Telescope in two observing periods. 33 candidates were observed on 11 and 12 July 2018 in variable seeing and cloud cover conditions, while 55 were observed on 11 and 12 February 2019 in sub-arcsecond seeing with partial clouds. The R158R and R300B gratings were used on the red and blue arms respectively, along with the standard 5300Å dichroic and GG495 second order cut filter in the red arm. This provided a dispersion of 1.81Åpixel^{-1} and 0.86Åpixel^{-1} for the red and blue arms. The component spectra were extracted using a Python-based pipeline which accounts for the CCD+grating response and trace variation based on the standard stars Hz 44 and BD+21 0607. The final spectra, shown in Figure 4.7, were extracted using a Gaussian aperture of varying width centred on each component. The 2D-spectra were also visually inspected to confirm that the spectral features were spatially resolved. Table 4.4 provides a summary of all WHT observations, including selection method, *Gaia* magnitudes, and proper motion significances. Figure 4.8 shows colour images of all observed systems, with *Gaia* DR2 detections overlaid.

In total, we confirmed 70 new lensed quasars (of which 8 are quads), 1 probable lens, 4 nearly identical quasar pairs, 4 inconclusive systems, and 8 contaminant systems. This represents a success rate between 81% and 90% at spectroscopic follow-up.

4.3.1 Modelling

The *grizY* Pan-STARRS images are modelled as in Chapter 2.3.1. The astrometry and photometry for all systems are provided in Appendix A. Figure 4.9 shows *gri* colour images of each system, with galaxy and PSF positions overlaid, alongside model galaxy-subtracted and model PSF-subtracted *gri* images.

For each lens we constrain a singular isothermal ellipsoid (SIE) mass model using the inferred galaxy and image positions and their uncertainties. These positions provide 6 constraints for doubles and 10 for quads (excepting quads for which no lensing galaxy is detected in the Pan-STARRS data). The model requires a source position, galaxy mass position, and SIE Einstein radius, axis ratio, and position angle, i.e. 7 parameters. We also use the median flux ratios in the *griz* bands, with a 20% uncertainty included to mitigate against microlensing or variations arising from the different light paths. For the quads, flux ratios are also used as constraints, with the uncertainty set at 50% for saddle points, since microlensing is more likely to suppress them (Schechter and Wambsganss, 2002). An external shear is included for the quad mass models. We expect $\chi^2 \sim 0$ for the double systems, and $\chi^2 \sim 4$ for the quads ($\chi^2 \sim 2$ for quads without lens positions). The best-fit mass model parameters,

Fig. 4.7 Spectra of lensed quasars and quasar pairs from *Gaia* DR2 selection. The fluxes of the brighter components have been shifted.

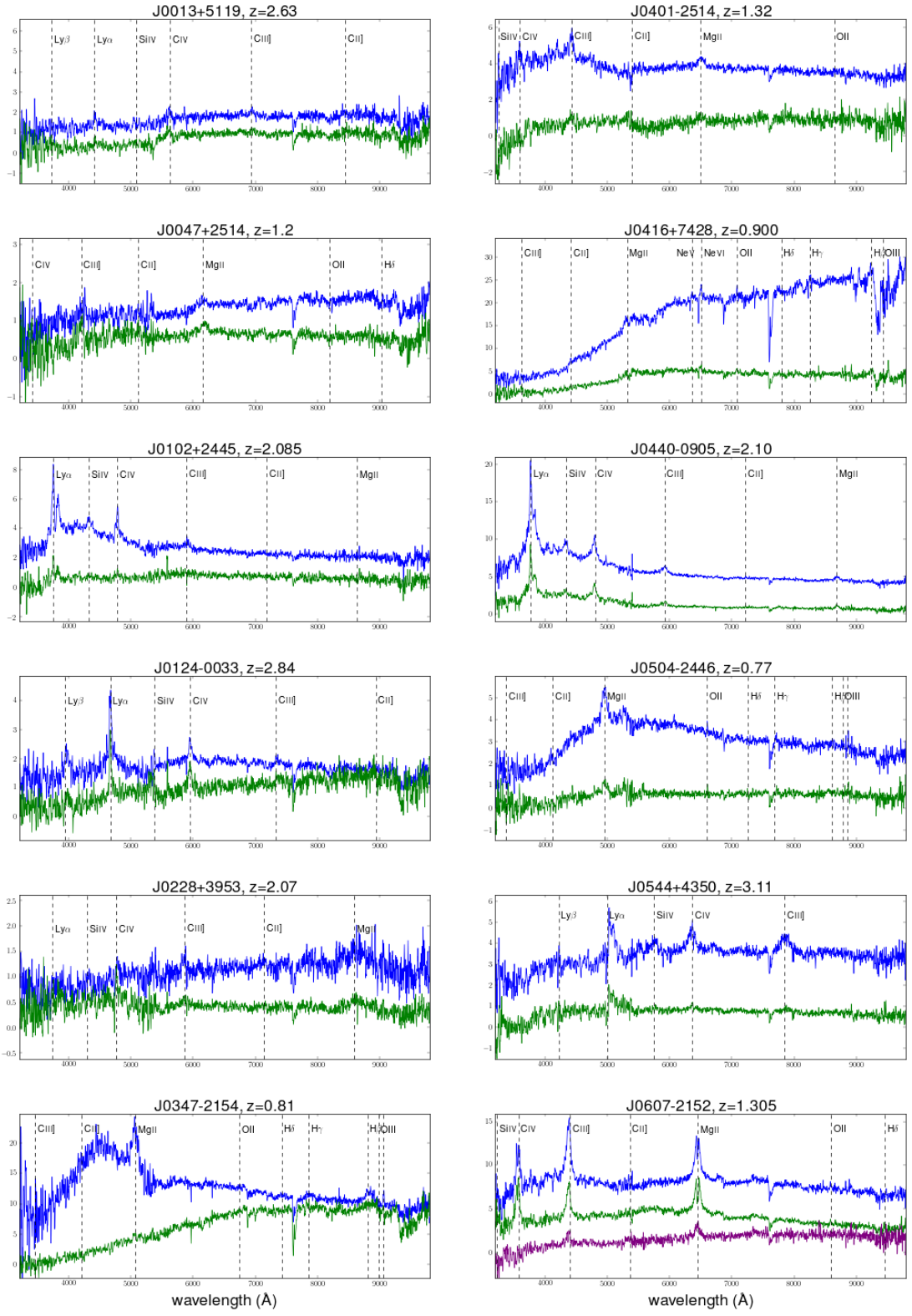

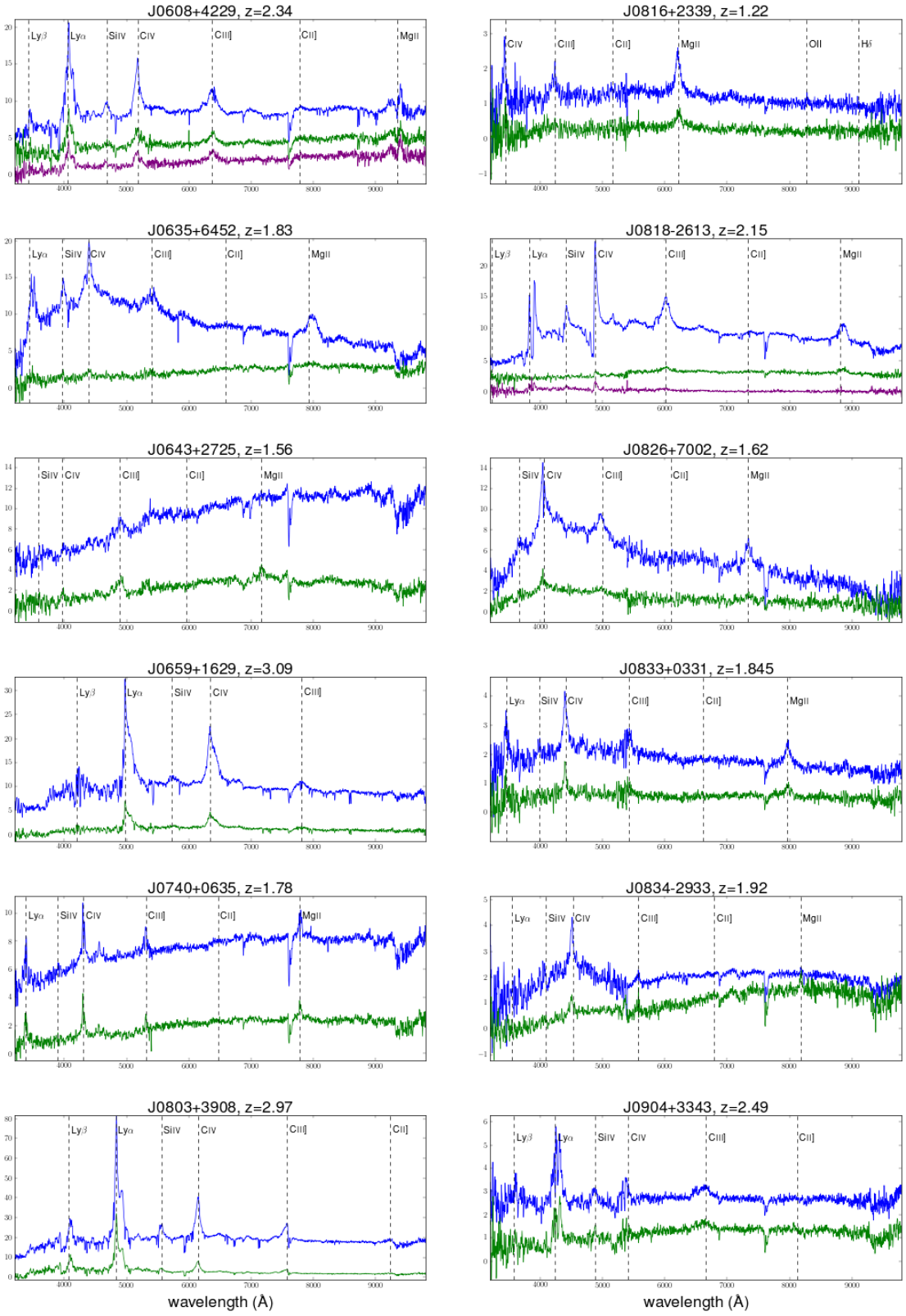
J0608+4229, z=2.34
Lyβ
Lyα
SiIV
CIV
CIII]
CII]
MgII
J0816+2339, z=1.22
CIV
CIII]
CII]
MgII
OII
Hδ
J0635+6452, z=1.83
Lyα
SiIV
CIV
CIII]
CII]
MgII
J0818-2613, z=2.15
Lyβ
Lyα
SiIV
CIV
CIII]
CII]
MgII
J0643+2725, z=1.56
SiIV
CIV
CIII]
CII]
MgII
J0826+7002, z=1.62
SiIV
CIV
CIII]
CII]
MgII
J0659+1629, z=3.09
Lyβ
Lyα
SiIV
CIV
CIII]
J0833+0331, z=1.845
Lyα
SiIV
CIV
CIII]
CII]
MgII
J0740+0635, z=1.78
Lyα
SiIV
CIV
CIII]
CII]
MgII
J0834-2933, z=1.92
Lyα
SiIV
CIV
CIII]
CII]
MgII
J0803+3908, z=2.97
Lyβ
Lyα
SiIV
CIV
CIII]
CII]
wavelength (Å)
J0904+3343, z=2.49
Lyβ
Lyα
SiIV
CIV
CIII]
CII]
wavelength (Å)

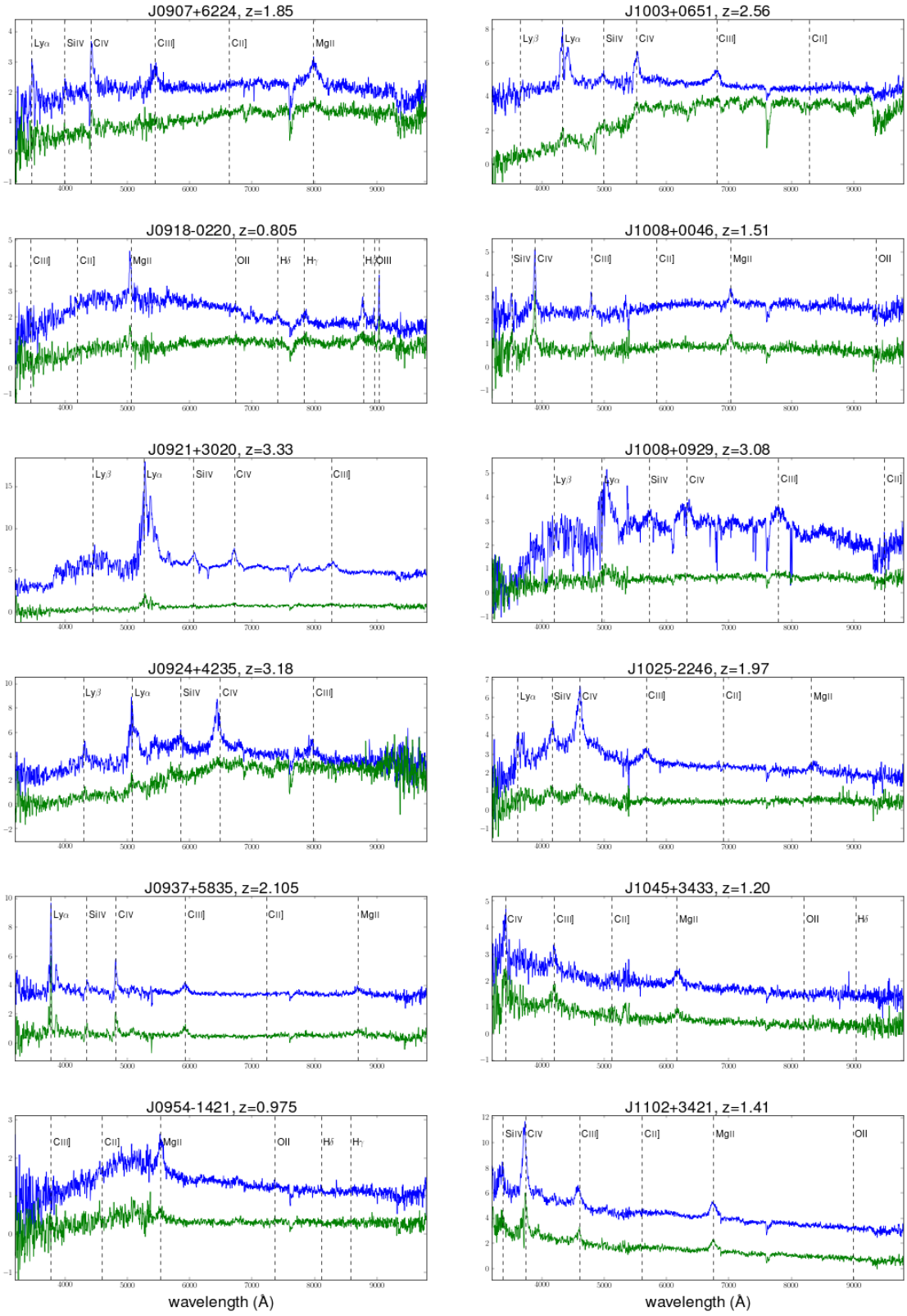
J0907+6224, z=1.85
Lyα SiIV CIV CIII] CII] MgII
J1003+0651, z=2.56
Lyβ Lyα SiIV CIV CIII] CII]
J0918-0220, z=0.805
CIII] CII] MgII OII Hδ Hγ H/OIII
J1008+0046, z=1.51
SiIV CIV CIII] CII] MgII OII
J0921+3020, z=3.33
Lyβ Lyα SiIV CIV CIII]
J1008+0929, z=3.08
Lyβ Lyα SiIV CIV CIII] CII]
J0924+4235, z=3.18
Lyβ Lyα SiIV CIV CIII]
J1025-2246, z=1.97
Lyα SiIV CIV CIII] CII] MgII
J0937+5835, z=2.105
Lyα SiIV CIV CIII] CII] MgII
J1045+3433, z=1.20
CIV CIII] CII] MgII OII Hδ
J0954-1421, z=0.975
CIII] CII] MgII OII Hδ Hγ
J1102+3421, z=1.41
SiIV CIV CIII] CII] MgII OII
wavelength (Å)
wavelength (Å)

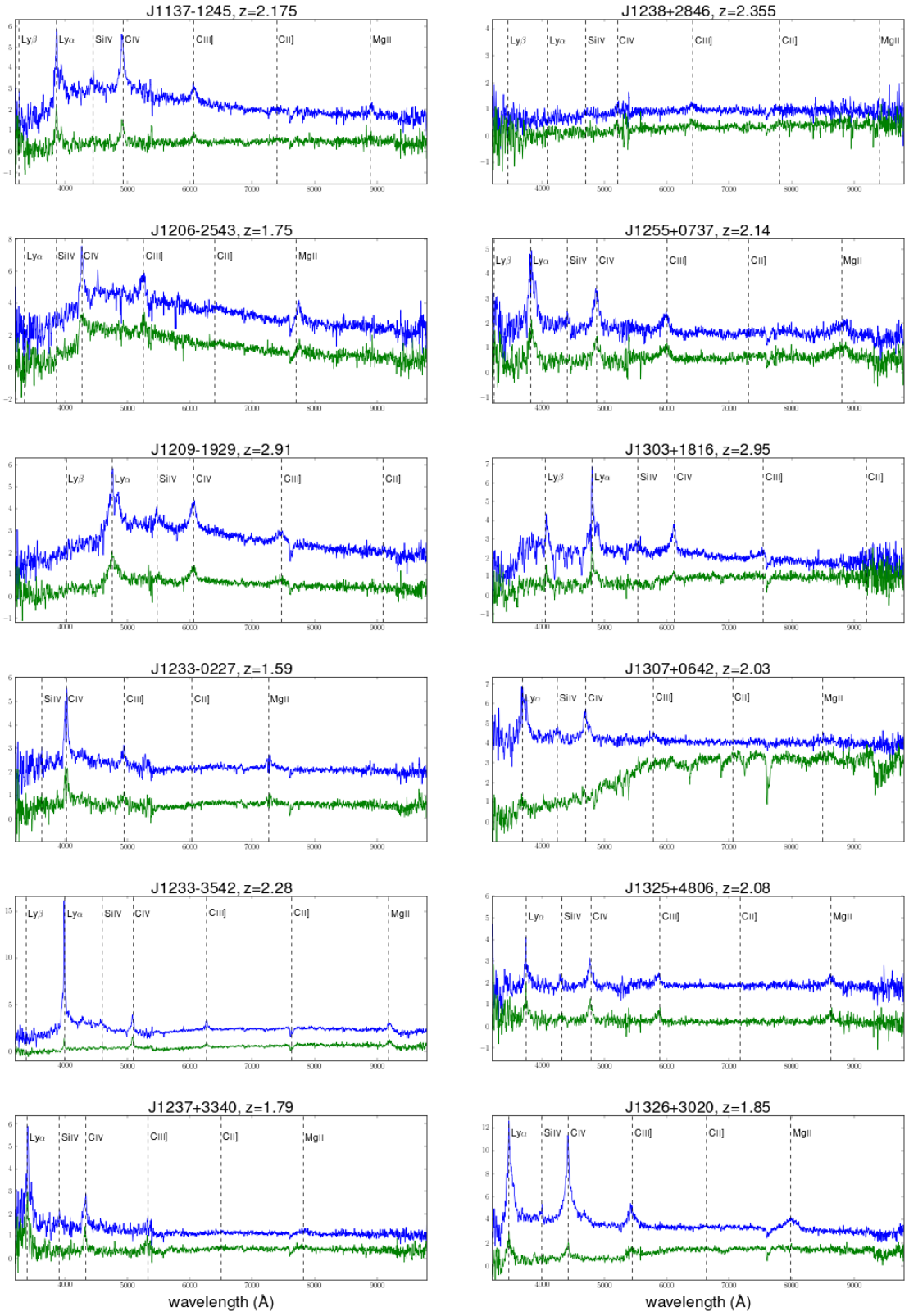
J1137-1245, z=2.175
J1238+2846, z=2.355
J1206-2543, z=1.75
J1255+0737, z=2.14
J1209-1929, z=2.91
J1303+1816, z=2.95
J1233-0227, z=1.59
J1307+0642, z=2.03
J1233-3542, z=2.28
J1325+4806, z=2.08
J1237+3340, z=1.79
J1326+3020, z=1.85
Lyβ
Lyα
SiIV
CIV
CIII]
CII]
MgII
wavelength (Å)

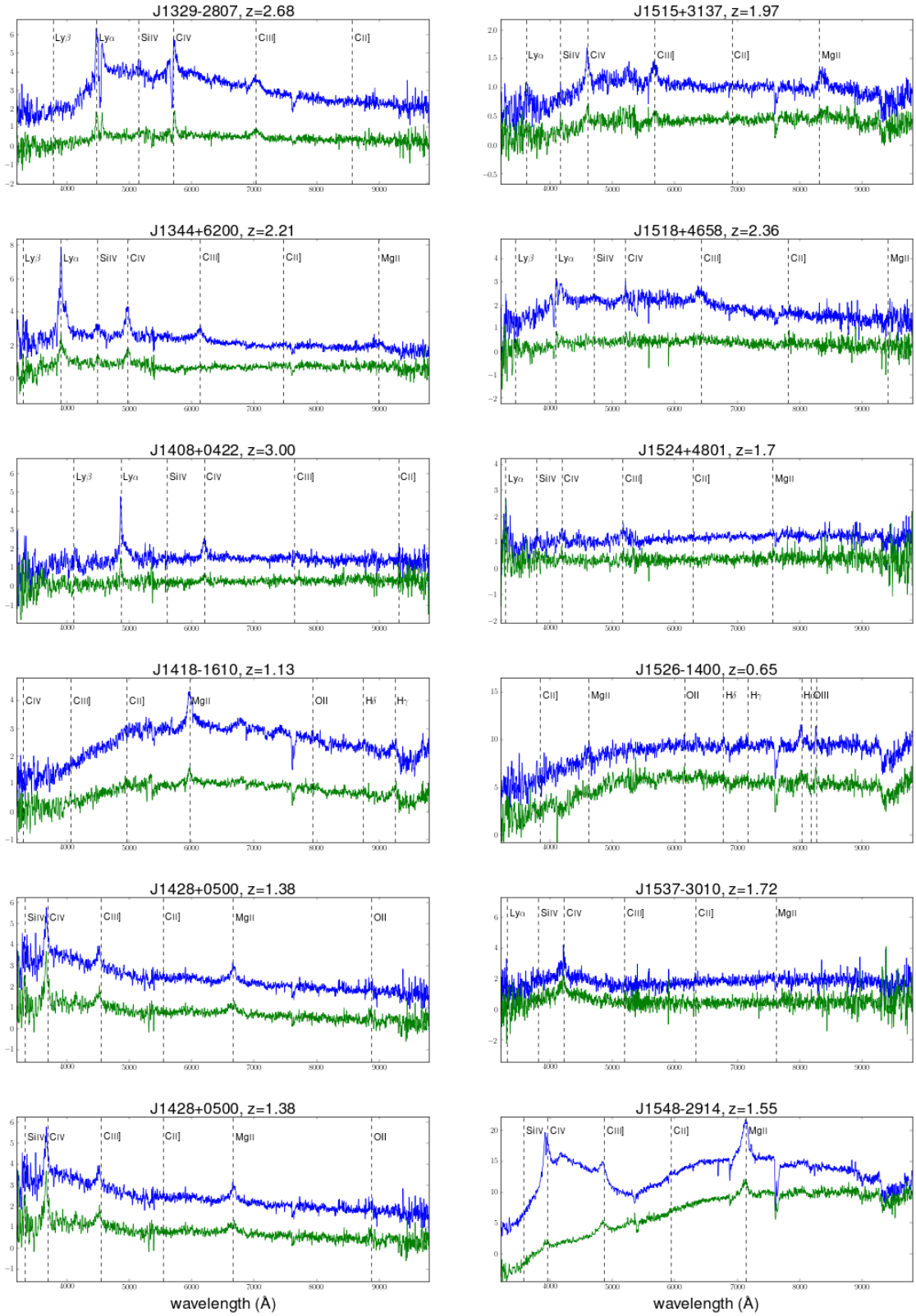
J1329-2807, z=2.68
Lyβ Lyα SiIV CIV CIII] CII]
J1515+3137, z=1.97
Lyα SiIV CIV CIII] CII] MgII
J1344+6200, z=2.21
Lyβ Lyα SiIV CIV CIII] CII] MgII
J1518+4658, z=2.36
Lyβ Lyα SiIV CIV CIII] CII] MgII
J1408+0422, z=3.00
Lyβ Lyα SiIV CIV CIII] CII]
J1524+4801, z=1.7
Lyα SiIV CIV CIII] CII] MgII
J1418-1610, z=1.13
CIV CIII] CII] MgII OII Hδ Hγ
J1526-1400, z=0.65
CII] MgII OII Hδ Hγ HδOIII
J1428+0500, z=1.38
SiIV CIV CIII] CII] MgII OII
J1537-3010, z=1.72
Lyα SiIV CIV CIII] CII] MgII
J1428+0500, z=1.38
SiIV CIV CIII] CII] MgII OII
J1548-2914, z=1.55
SiIV CIV CIII] CII] MgII
wavelength (Å)
wavelength (Å)

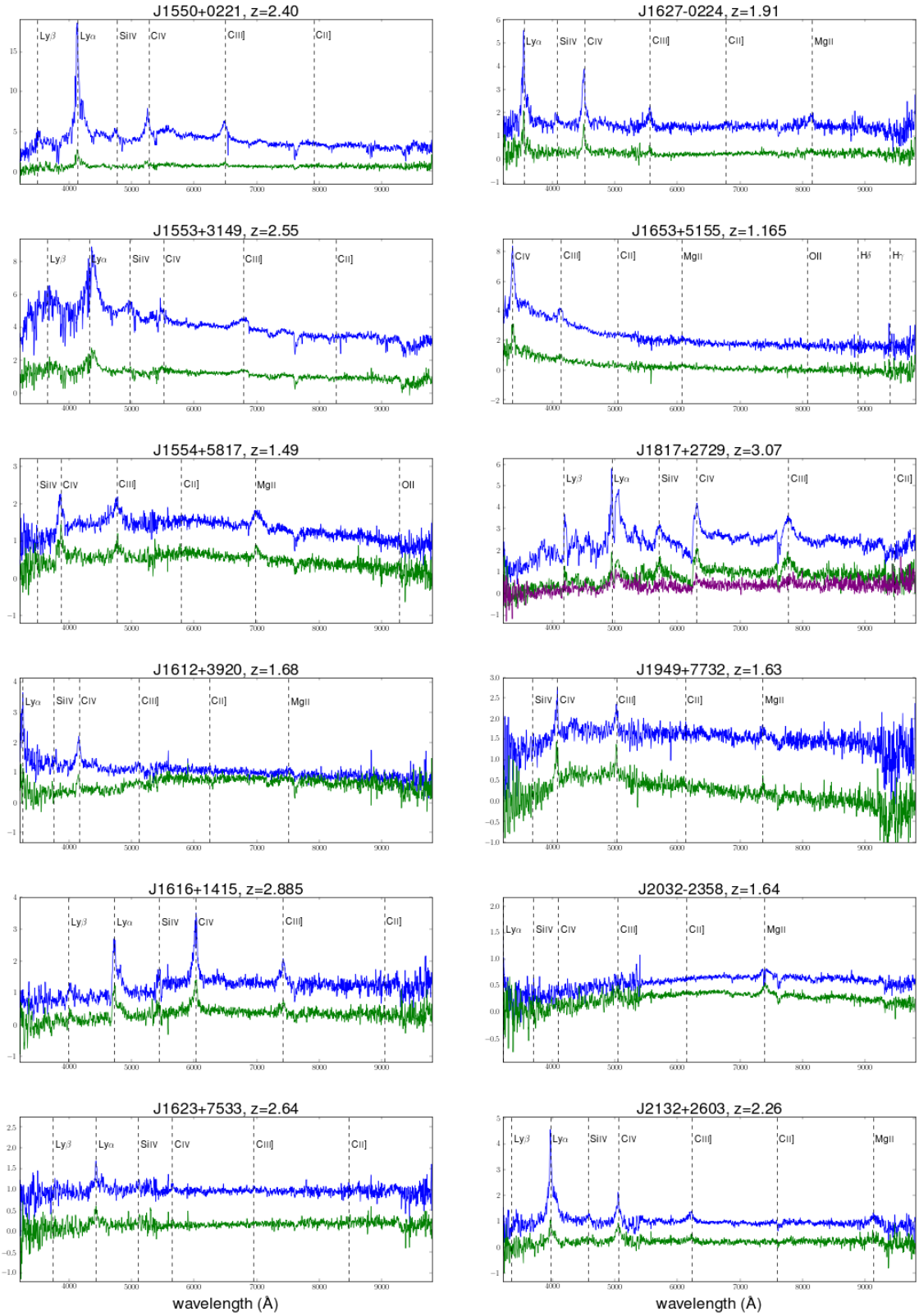
J1550+0221, z=2.40
Lyβ
Lyα
SiIV
CIV
CIII]
CII]
J1627-0224, z=1.91
Lyα
SiIV
CIV
CIII]
CII]
MgII
J1553+3149, z=2.55
Lyβ
Lyα
SiIV
CIV
CIII]
CII]
J1653+5155, z=1.165
CIV
CIII]
CII]
MgII
OII
Hδ
Hγ
J1554+5817, z=1.49
SiIV
CIV
CIII]
CII]
MgII
OII
J1817+2729, z=3.07
Lyβ
Lyα
SiIV
CIV
CIII]
CII]
J1612+3920, z=1.68
Lyα
SiIV
CIV
CIII]
CII]
MgII
J1949+7732, z=1.63
SiIV
CIV
CIII]
CII]
MgII
J1616+1415, z=2.885
Lyβ
Lyα
SiIV
CIV
CIII]
CII]
J2032-2358, z=1.64
Lyα
SiIV
CIV
CIII]
CII]
MgII
J1623+7533, z=2.64
Lyβ
Lyα
SiIV
CIV
CIII]
CII]
J2132+2603, z=2.26
Lyβ
Lyα
SiIV
CIV
CIII]
CII]
MgII
wavelength (Å)
wavelength (Å)

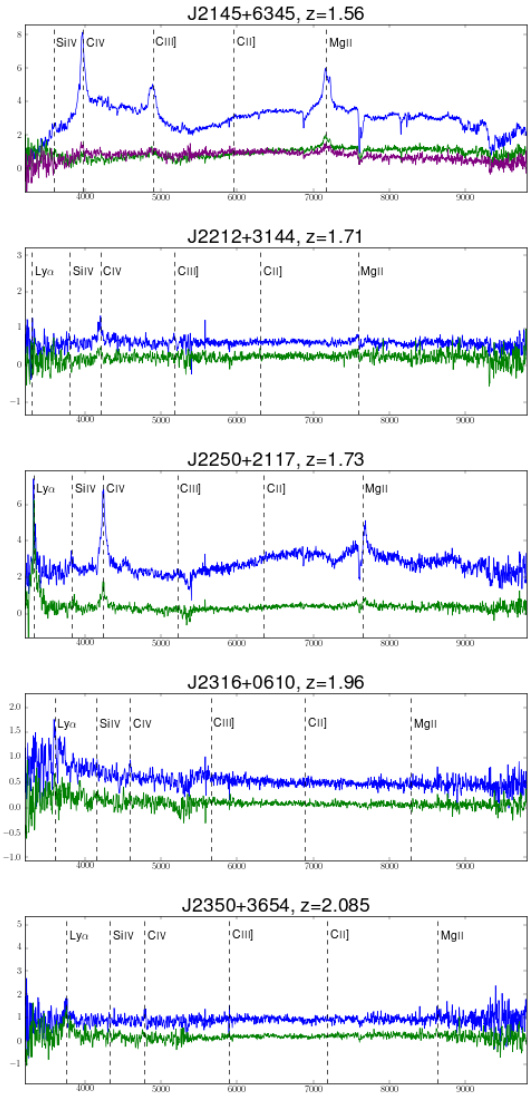
J2145+6345, z=1.56
SiIV
CIV
CIII]
CII]
MgII
J2212+3144, z=1.71
Lyα
SiIV
CIV
CIII]
CII]
MgII
J2250+2117, z=1.73
Lyα
SiIV
CIV
CIII]
CII]
MgII
J2316+0610, z=1.96
Lyα
SiIV
CIV
CIII]
CII]
MgII
J2350+3654, z=2.085
Lyα
SiIV
CIV
CIII]
CII]
MgII

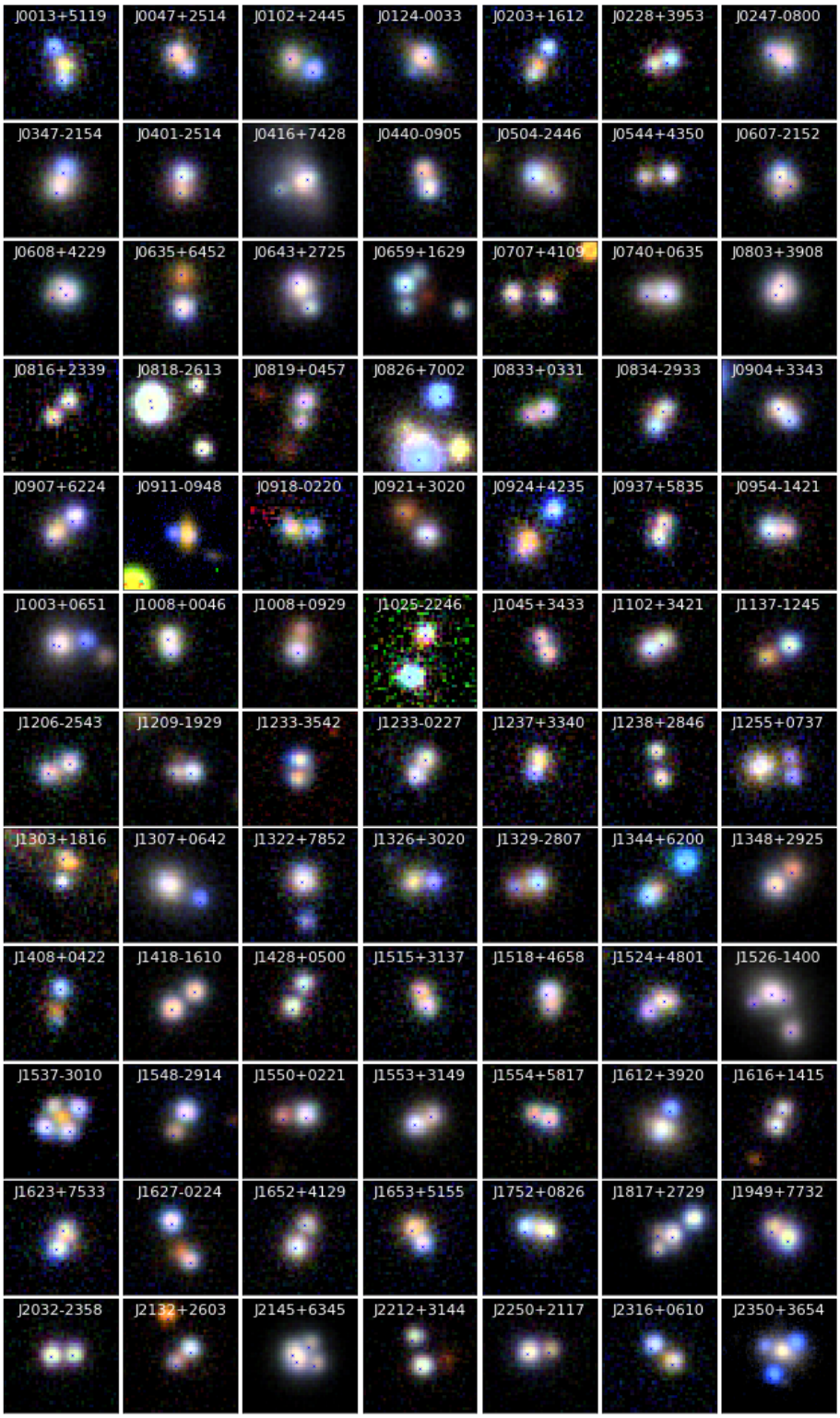

Fig. 4.8 Pan-STARRS *gri* colour images of observed candidates, except for J1537-3010 (DECam *grz*) and J2350+3654 (HSC *gi*). *Gaia* detections are overlaid in blue. Cutouts are 10×10". 3 contaminant systems are not shown.

Table 4.4 Summary of WHT observations. NIQ=nearly identical quasar, assigned to systems of quasars at the same redshift but without photometric detection of a lensing galaxy. The selection method is given for each candidate: WD, WT, WQ = ALLWISE double, triple, quad; uW = unWISE model fitting; MQ = Milliquas; SG1=spectroscopic galaxy with one *Gaia* detection; MG1 = morphological galaxy with one *Gaia* detection.

Name	RA	Dec.	Selection	*Gaia* G	*Gaia* PMSIG	Exp. Time	Outcome
J0013+5119	3.3481	51.3182	WD	20.65, 20.87	2.72, 0.73	1800s	**lens** z=2.63
J0047+2514	11.9466	25.2409	WD,uW	20.58, 20.69	2.01, -	1800s	**lens** z=1.20
J0102+2445	15.6965	24.7543	MQ,WD,uW	19.34, 20.22	0.76, -	1200s	**lens** z=2.085
J0124-0033	21.2394	-0.5533	MG1	20.67	1.05	2400s	**lens** z=2.84
J0203+1612	30.9977	16.2021	SG1	20.76	-	1200s	probable **lens**, z=0.488, 2.18
J0228+3953	37.0462	39.8854	MQ,WD,uW	20.37, 20.93	-, -	1600s	**lens** z=2.07
J0247-0800	41.956	-8.015	WD,uW	20.55, 20.70	-, -	1500s	inconclusive z=1.73?
J0347-2154	56.7689	-21.9094	WD,uW	19.46, 20.01	2.38, -	1200s	**lens** z=0.81
J0401-2514	60.4504	-25.2438	MQ,WD,uW	19.03, 20.22	1.67, 1.60	600s	**lens** z=1.32
J0416+7428	64.1972	74.4827	WD,uW	19.01, 19.74	3.57, 1.96	2400s	**lens** z=0.90
J0440-0905	70.0483	-9.0911	MQ,WD,uW	19.19, 19.92	2.15, 2.38	600s	**lens** z=2.10
J0504-2446	76.1616	-24.7751	WD,uW	19.22, 20.50	5.44, 1.48	2100s	**lens** z=0.77
J0544+4350	86.1447	43.8386	WD	19.64, 20.25	0.40, 1.09	600s	**lens** z=3.11
J0607-2152	91.7954	-21.8715	WT,uW	19.32, 20.86, 20.90	2.05, -, -	1800s	**quad** z=1.305
J0608+4229	92.1725	42.4935	WT	18.23, 19.86, 20.13	3.94, -, -	2400s	**quad** z=2.34
J0635+6452	98.9863	64.8711	MQ,WD,uW	18.96, 20.86	0.55, -	1800s	**lens** z=1.83
J0643+2725	100.9258	27.4275	WD	19.48, 19.82	0.88, 1.64	1200s	**lens** z=1.56
J0659+1629	104.7669	16.4859	WT	18.59, 19.94, 20.05	1.73, 1.96, 0.77	600s	**quad** z=3.09
J0707+4109	106.9468	41.164	MQ,WD,uW	20.47, 20.53	1.30, 1.57	600s	QSO pair z=0.516
J0740+0635	115.0907	6.5938	WD,uW	18.32, 19.56	1.84, 1.55	600s	**lens** z=1.78
J0803+3908	120.9905	39.1397	MQ,WD,uW	18.14, 18.88	-, 0.76	600s	**quad** z=2.97
J0816+2339	124.1427	23.663	MQ,WD,uW	20.32, 20.94	1.33, -	800s	**lens** z=1.22
J0818-2613	124.6183	-26.2234	WQ	17.52, 17.58, 19.94	-, -, 2.01	1200s	**quad** z=2.15
J0819+0457	124.8685	4.9522	WD,uW	20.58, 20.85	0.74, -	800s	z=0.46 QSO + other
J0826+7002	126.5347	70.045	MG1,uW	17.46	1.06	600s	**lens** z=1.62
J0833+0331	128.3368	3.5247	WD,uW	20.08, 21.10	1.16, -	600s	**lens** z=1.845
J0834-2933	128.641	-29.5505	WD,uW	19.91, 20.17	2.96, 2.11	1800s	**lens** z=1.92
J0904+3343	136.1713	33.7291	WD,uW	19.93, 20.13	1.19, 4.06	600s	**lens** z=2.49
J0907+6224	136.9658	62.4116	MQ,WD,uW	19.27, 20.06	0.54, 1.45	600s	**lens** z=1.85
J0911-0948	137.7843	-9.8055	MG1	20.84	-	900s	inconclusive z=1.48?
J0918-0220	139.6805	-2.3354	MG1	20.43	3.10	900s	**lens** z=0.86
J0921+3020	140.2683	30.3419	MQ,WD,uW	18.66, 20.85	1.40, -	600s	**lens** z=3.33
J0924+4235	141.124	42.5948	MQ,WD,uW	19.77, 20.70	0.90, -	1200s	**lens** z=3.18
J0937+5835	144.3832	58.5906	WD,uW	20.45, 20.93	1.42, -	900s	**lens** z=2.105
J0954-1421	148.7078	-14.3527	MQ,WD,uW	19.80, 20.58	1.79, -	600s	**lens** z=0.975
J1003+0651	150.7887	6.85	WT,SG2,uW	19.80, 19.85, 20.20	-, 0.84, -	900s	**lens** z=2.56
J1008+0046	152.1929	0.7723	MQ,WD,uW	20.60, 20.60	-, -	900s	**lens** z=1.51
J1008+0929	152.2041	9.4877	MG1	19.01	0.85	900s	**lens** z=3.08
J1025-2246	156.3566	-22.7689	WD,uW	19.94, 21.31	0.20, -	1800s	**lens** z=1.97
J1045+3433	161.4977	34.5658	MQ,WD,uW	20.38, 20.93	1.86, -	900s	**lens** z=1.21
J1102+3421	165.5266	34.3624	MQ,WD,uW	19.28, 19.63	2.28, 0.17	600s	**lens** z=1.41
J1137-1245	174.3127	-12.7506	WD,uW	19.55, 20.78	0.52, 0.99	900s	**lens** z=2.175
J1206-2543	181.7447	-25.7253	MQ,WD,uW	19.97, 20.40	1.27, 3.58	1800s	**lens** z=1.75
J1209-1929	182.3615	-19.4879	WD,uW	19.55, 20.66	0.89, -	900s	**lens** z=2.91
J1233-3542	188.326	-35.7159	WD,uW	18.54, 19.56	1.27, 0.66	600s	**lens** z=2.29
J1233-0227	188.4218	-2.4604	WD,uW	19.74, 19.98	3.03, 2.91	600s	**lens** z=1.59
J1237+3340	189.2536	33.6819	MG1	20.90	2.12	900s	**lens** z=1.79
J1238+2846	189.6778	28.7830	MQ,WD,uW	20.75, 20.88	0.52, -	2400s	**lens** z=2.355
J1255+0737	193.9326	7.6296	WD,uW	20.40, 21.03	0.70, -	1107s	**lens** z=2.14
J1303+1816	195.7765	18.2778	WD,uW	20.20, 21.12	4.18, -	900s	**lens** z=2.95
J1307+0642	196.9294	6.7037	SG1	20.16	2.44	1200s	**lens** z=2.03
J1322+7852	200.7302	78.8791	WD,uW	20.15, 20.20	0.46, -	900s	z=0.35 QSO + galaxy
J1326+3020	201.7409	30.34	MG1	20.24	1.87	900s	**lens** z=1.85
J1329-2807	202.4531	-28.1279	MQ,WD,uW	19.23, 20.57	1.26, -	800s	**lens** z=2.68
J1344+6200	206.2042	62.0118	MQ,WD,uW	20.14, 20.68	1.48, 0.65	600s	**lens** z=2.21
J1348+2925	207.206	29.4195	MQ,WD,SG2,uW	18.43, 20.31	2.63, -	800s	QSO pair z=0.29
J1408+0422	212.1405	4.3747	MG1	20.61	0.98	1800s	**lens** z=3.00
J1418-1610	214.5737	-16.1690	MQ,WD,uW	18.46, 19.33	1.34, 2.50	1200s	NIQ z=1.13

Name	RA	Dec.	Selection	*Gaia* G	*Gaia* PMSIG	Exp. Time	Outcome
J1428+0500	217.2308	5.0057	MQ,WD,uW	19.89, 19.96	1.50, 2.26	600s	NIQ z=1.38
J1515+3137	228.9160	31.6278	MQ,WD,uW	19.97, 20.83	1.14, -	700s	**lens** z=1.97
J1518+4658	229.5129	46.9711	WD,uW	19.82, 21.04	2.83, -	900s	**lens**? z=2.36
J1524+4801	231.1243	48.0206	WD,uW	20.29, 20.60	1.84, -	1500s	**lens** z=1.70
J1526-1400	231.6889	-14.0032	uW	18.51, 19.29, 19.35, 19.44	-, 1.00, -, -	1200s	**lens** z=0.65
J1537-3010	234.3556	-30.1713	WT	20.22, 20.32, 20.45	-, -, -	2500s	**quad** z=1.72
J1548-2914	237.1733	-29.2351	WD,uW	18.17, 20.07, 21.22	0.70, 1.49, -	1500s	**lens** z=1.55
J1550+0221	237.7385	2.3629	MQ,WD,uW	18.44, 20.34	1.83, 0.42	600s	**lens** z=2.40
J1553+3149	238.4092	31.8254	WD,uW	18.38, 19.43	1.42, 2.55	600s	**lens** z=2.55
J1554+5817	238.5769	58.2964	MQ,WD,uW	19.17, 20.01	1.13, 1.09	450s	NIQ z=1.49
J1612+3920	243.0514	39.3463	MG1	20.08	0.26	900s	**lens** z=1.68
J1616+1415	244.1934	14.2621	WD,uW	19.89, 20.48	2.60, 0.51	600s	**lens** z=2.88
J1623+7533	245.8205	75.5551	WD,uW	19.47, 20.01	0.30, 2.68	1500s	**lens** z=2.64
J1627-0224	246.9594	-2.4036	WD,uW	19.25, 20.08	0.99, 0.55	600s	**lens** z=1.91
J1641+1002	250.3552	10.0484	MQ,WD,uW	18.82, 20.95	1.48, -	1200s	z=1.72 quasar + other
J1652+4129	253.1934	41.4934	WD,uW	20.09, 20.72	1.81, -	600s	QSO pair z=0.22
J1653+5155	253.4387	51.9180	WD,uW	19.94, 20.91	1.97, -	750s	**lens** z=1.165
J1724+0807	261.0767	8.1231	WD,uW	18.82, 20.26, 20.44	9.71, -, -	600s	stars+galaxy
J1752+0826	268.1778	8.4339	WD,uW	20.44, 20.54	4.55, 3.80	2800s	inconclusive z=0.78 QSO
J1817+2729	274.3786	27.4945	WQ	18.93, 20.07, 20.72	3.05, 2.56, 0.75	1050s	**quad** z=3.07
J1949+7732	297.4012	77.5442	MQ,WD,uW	18.71, 19.51	1.22, 2.68	600s	**lens** z=1.63
J2014-3024	303.7258	-30.4146	WT	18.76, 19.09, 19.24	4.51, 5.00, -	450s	z=2.35 quasar+star
J2032-2358	308.1572	-23.9729	MQ,WD,uW	19.12, 19.26	1.23, 0.67	800s	NIQ z=1.64
J2132+2603	323.0079	26.0517	WT	19.76, 20.89	0.91, -	600s	**lens** z=2.26
J2145+6345	326.2716	63.7615	WQ	16.86, 17.26, 18.34, 18.56	4.39, 2.86, 1.87, 1.10	900s	**quad** z=1.56
J2212+3144	333.0336	31.7379	MQ,WD,uW	19.28, 19.97	1.39, 1.58	1200s	**lens** z=1.71
J2250+2117	342.6440	21.2899	MQ,WD,uW	18.62, 20.27	1.93, -	600s	**lens** z=1.73
J2316+0610	349.1335	6.1804	MQ,WD,uW	20.05, 20.75	1.18, -	1900s	inconclusive (lens z=1.96?)
J2350+3654	357.5314	36.9096	MG1	21.12	-	3300s	**lens** z=2.085

galaxy light flattenings, and lens model magnifications for lenses confirmed during the first observing run are given in Table 4.5. The χ^2 contributions from the image positions, lens mass-light misalignment, and flux ratios are also given for each system's best-fit model.

4.3.2 Notes on Individual Systems

J0203+1612

This system was selected as a single *Gaia* detection near a spectroscopic galaxy. The 1 hour BOSS spectrum reveals a LRG spectrum at $z = 0.488$ with obvious quasar emission lines at z=2.18 (Dawson et al., 2013). Figure 4.10 shows the original BOSS spectrum, best-fit galaxy model spectrum, and the residuals. Four quasar emission lines have been identified at $z = 2.18$, with potential broad absorption blueward of the CIV line. We targetted J0203+1612 with the WHT for 1200s however the spectrum (Figure 4.7) reveals no broad lines, perhaps due to high airmass observations coupled with variable weather conditions. Given the definite presence of a low-redshift galaxy and a high-redshift quasar within the BOSS 2" fibre diameter, as well as the imaging showing two point sources either side of the massive galaxy, it is a strong lens candidate. To test this we compare the stellar mass from a composite stellar population synthesis model based on the galaxy's colours and redshift with the lensing mass within the Einstein radius under the assumption of strong

Fig. 4.9 Pan-STARRS modelled pixels. *Left: gri* colour image; *middle:* model galaxy subtracted, *right:* model quasar PSFs subtracted. PSF and galaxy positions are overlaid with blue and red crosses respectively. In the case of J1653+5155, the MzLS+BASS DR6 *grz* pixels are used. For J1238+2846 and J1616+1415, the colour images are *grz* and *izY* to show the lensing galaxy more clearly.

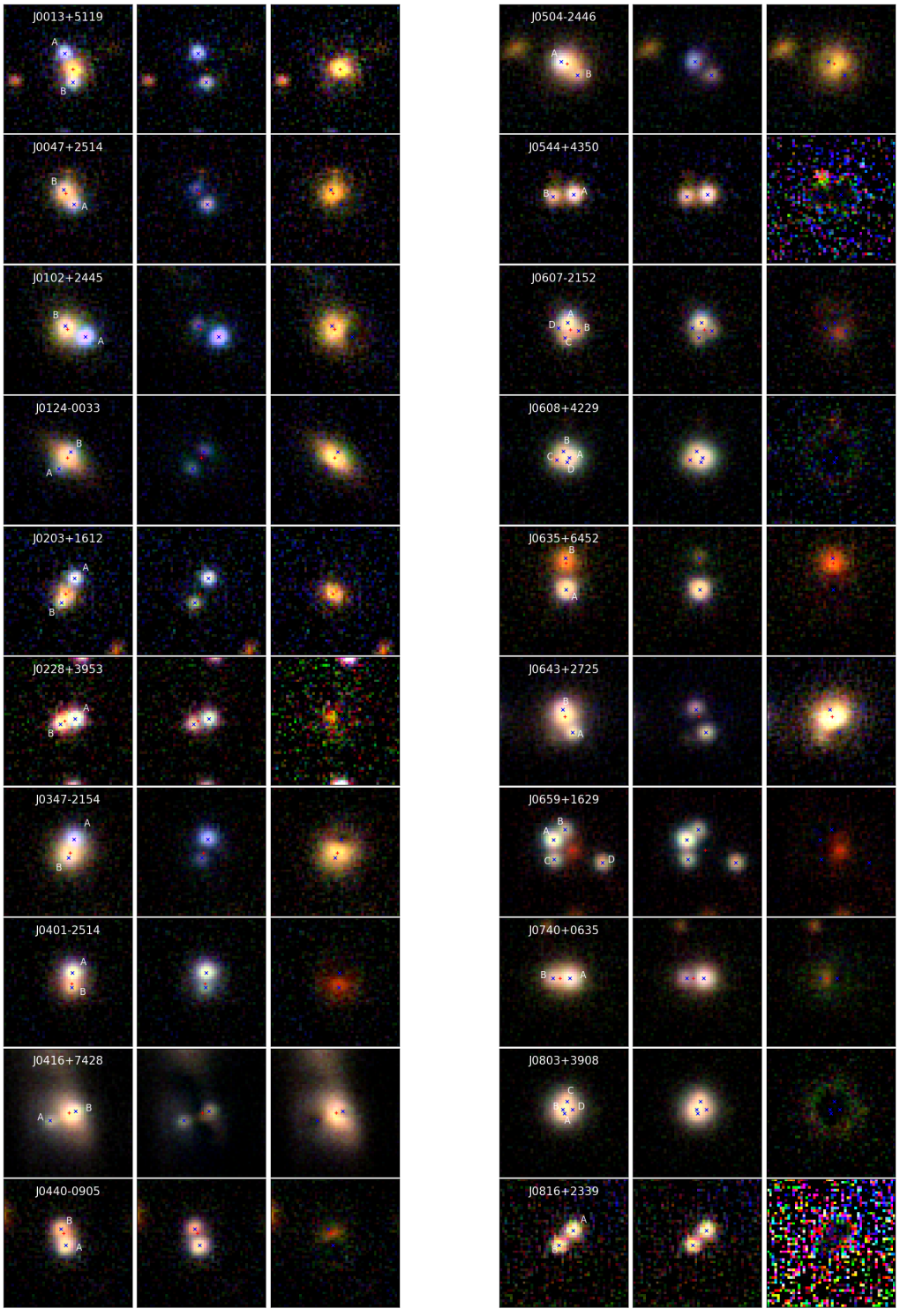

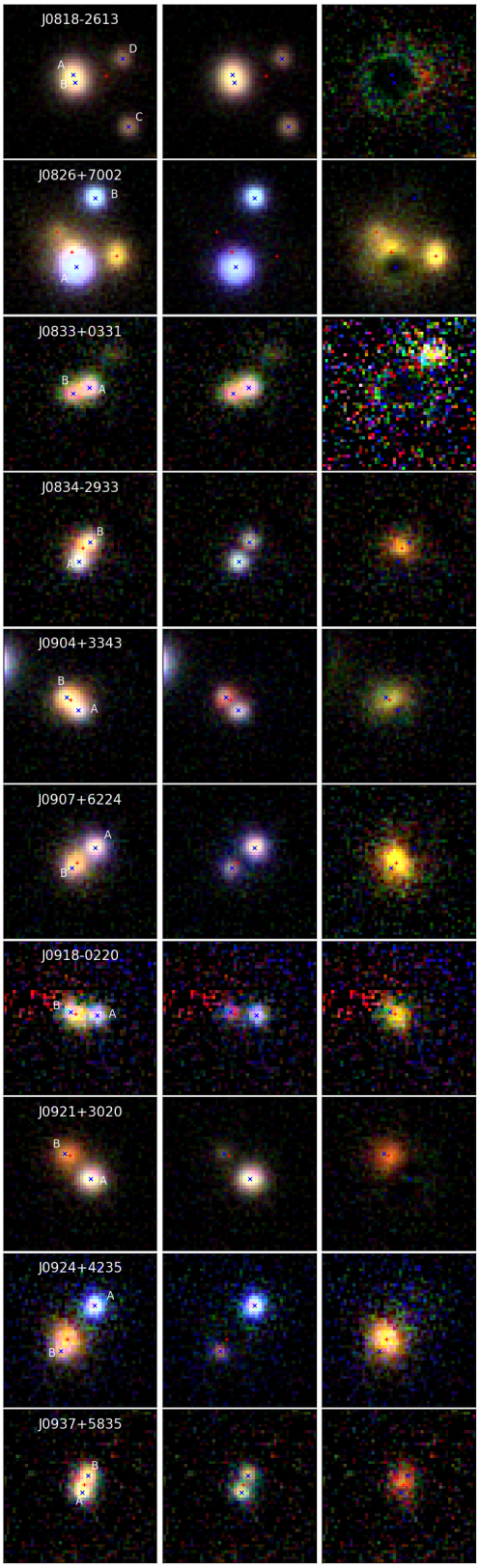
J0818-2613
J0826+7002
J0833+0331
J0834-2933
J0904+3343
J0907+6224
J0918-0220
J0921+3020
J0924+4235
J0937+5835

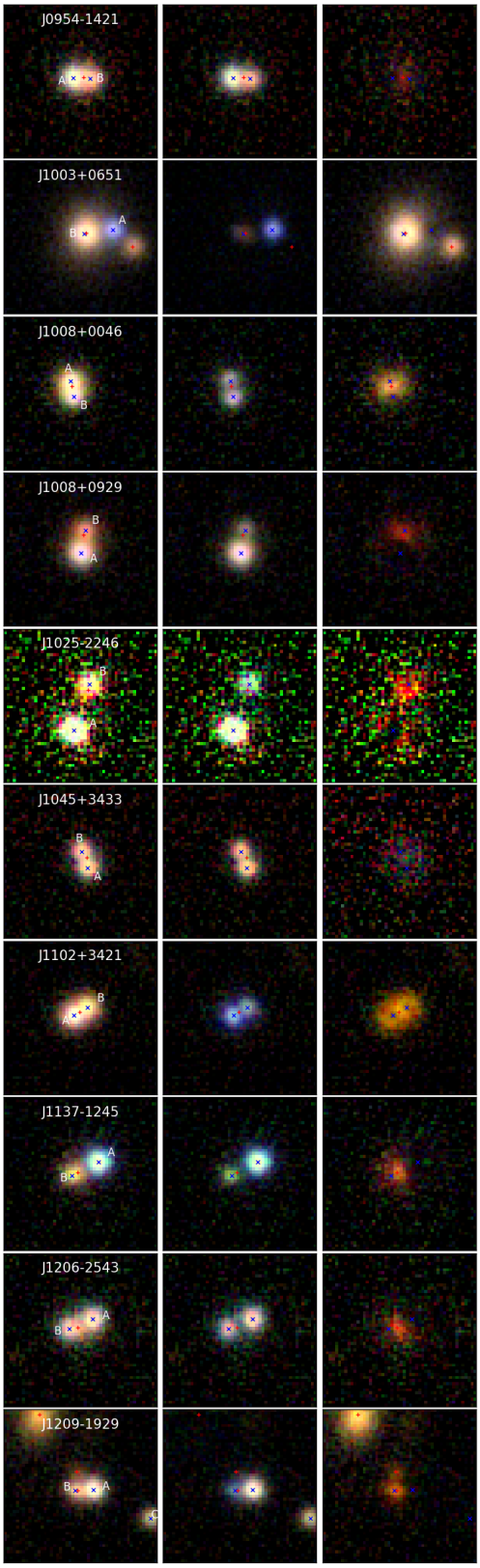
J0954-1421
J1003+0651
J1008+0046
J1008+0929
J1025-2246
J1045+3433
J1102+3421
J1137-1245
J1206-2543
J1209-1929

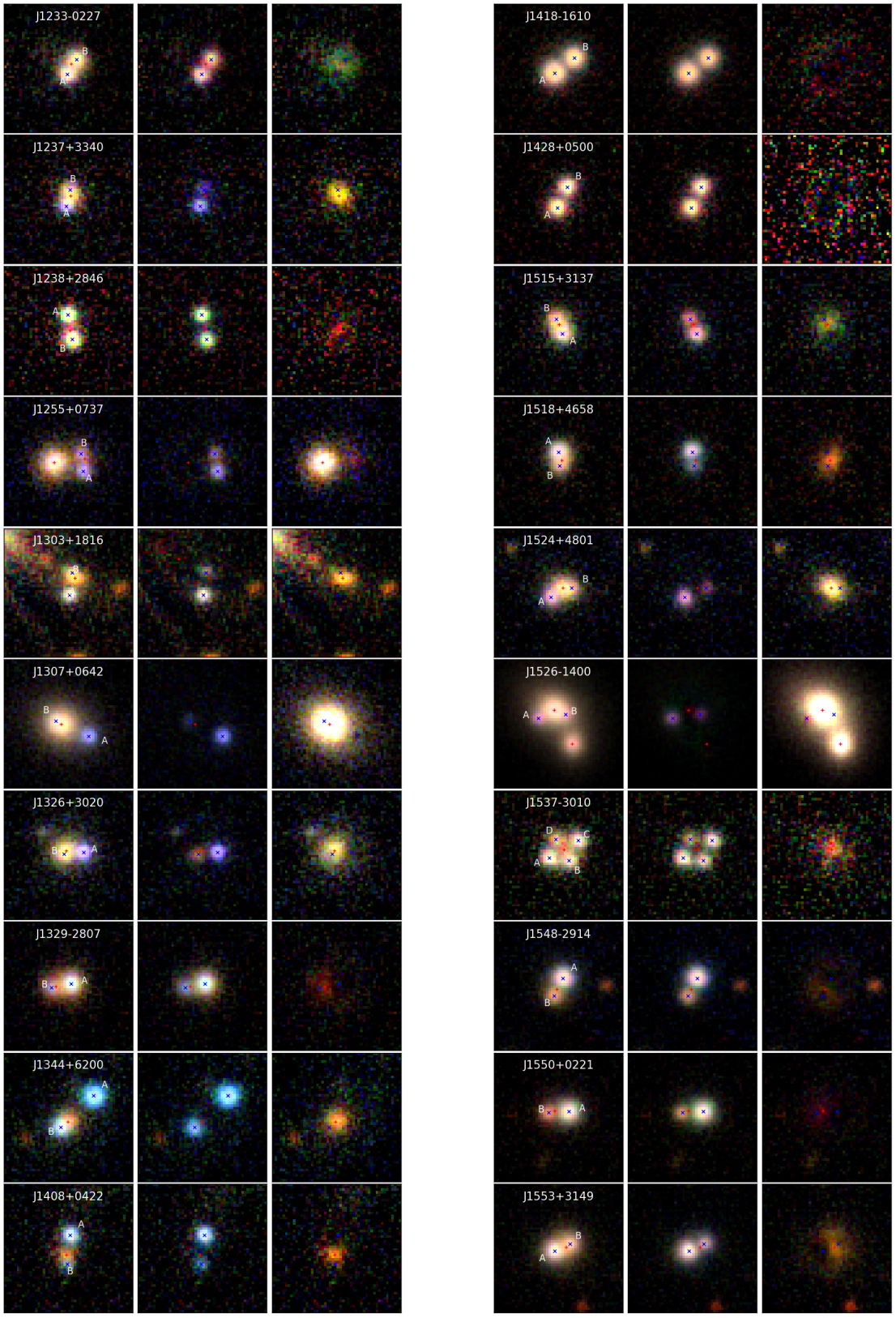
J1233-0227
J1237+3340
J1238+2846
J1255+0737
J1303+1816
J1307+0642
J1326+3020
J1329-2807
J1344+6200
J1408+0422
J1418-1610
J1428+0500
J1515+3137
J1518+4658
J1524+4801
J1526-1400
J1537-3010
J1548-2914
J1550+0221
J1553+3149

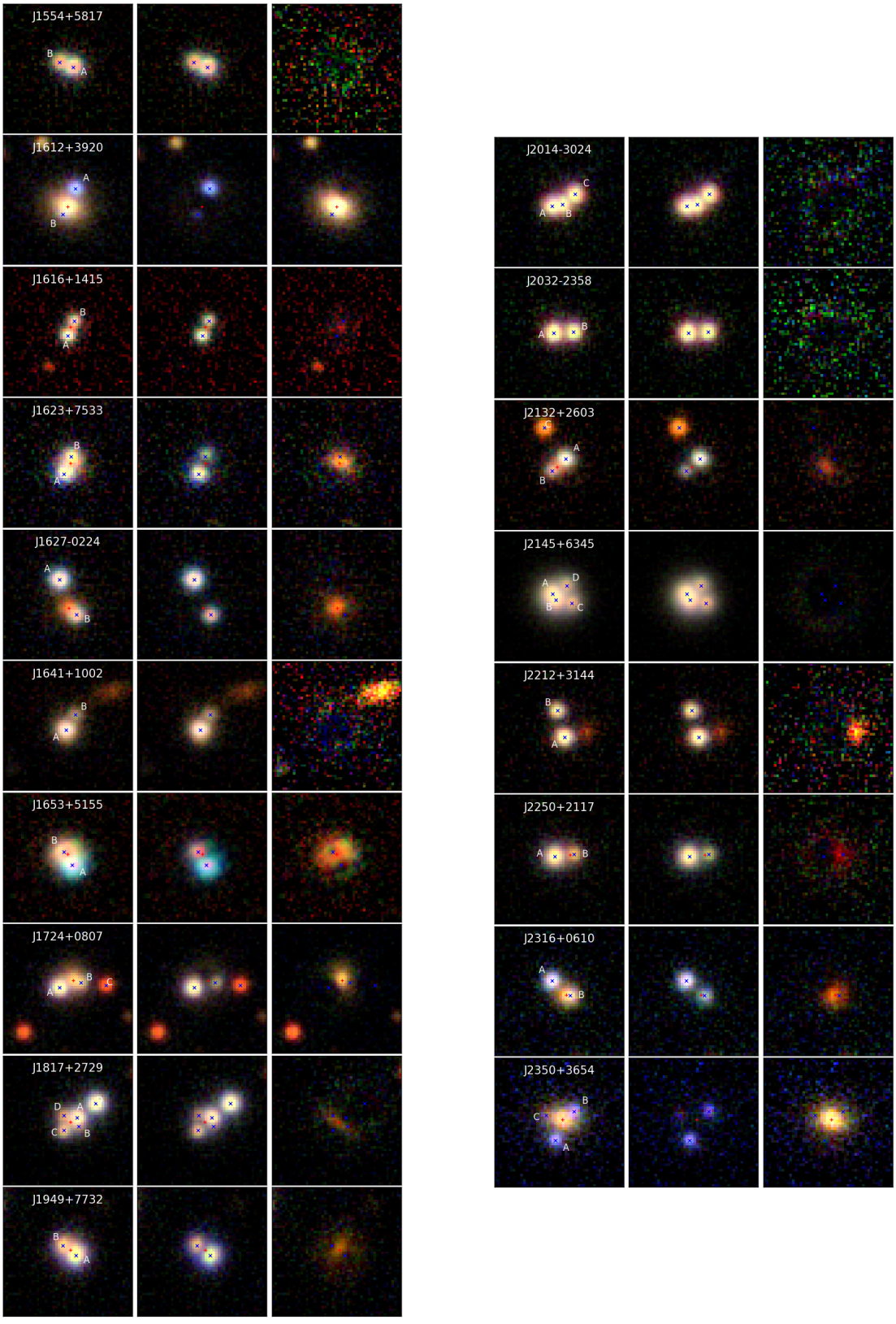
J1554+5817
J1612+3920
J1616+1415
J1623+7533
J1627-0224
J1641+1002
J1653+5155
J1724+0807
J1817+2729
J1949+7732
J2014-3024
J2032-2358
J2132+2603
J2145+6345
J2212+3144
J2250+2117
J2316+0610
J2350+3654

Table 4.5 Median parameter values with 1σ uncertainties for mass models of all systems from the first observing run with a lensing configuration. b=Einstein radius, PA= position angle (East of North), q = axis ratio, and μ = total source magnification.

name	b (")	PA_{SIE}	q_{SIE}	PA_{phot}	q_{phot}	$\chi^2_{gal.,images,flux}$	μ
J0013+5119	$1.51^{0.03}_{0.02}$	$142.5^{7.4}_{7.4}$	$0.87^{0.01}_{0.02}$	$112.1^{4.1}_{4.0}$	$0.79^{0.03}_{0.03}$	0.01, 0.04, 0.00	$10.7^{0.8}_{0.8}$
J0047+2514	$0.86^{0.05}_{0.03}$	$138.3^{19.9}_{13.0}$	$0.86^{0.09}_{0.13}$	$171.3^{9.2}_{9.7}$	$0.89^{0.03}_{0.03}$	0.00, 0.07, 0.00	$3.9^{0.4}_{0.3}$
J0102+2445	$1.14^{0.06}_{0.03}$	$1.6^{6.3}_{6.6}$	$0.50^{0.04}_{0.05}$	$20.9^{1.1}_{1.1}$	$0.75^{0.01}_{0.01}$	0.00, 0.08, 0.04	$2.4^{0.1}_{0.1}$
J0124-0033	$0.95^{0.04}_{0.02}$	$47.3^{2.5}_{3.3}$	$0.70^{0.07}_{0.08}$	$47.9^{0.4}_{0.4}$	$0.37^{0.01}_{0.01}$	0.04, 0.01, 0.00	$5.8^{0.8}_{0.5}$
J0203+1612	$1.36^{0.04}_{0.02}$	$70.4^{83.1}_{36.8}$	$0.98^{0.02}_{0.03}$	$56.1^{3.4}_{3.5}$	$0.66^{0.05}_{0.04}$	0.02, 0.06, 0.00	$7.0^{0.8}_{0.5}$
J0228+3953	$0.79^{0.03}_{0.01}$	$162.5^{8.5}_{8.6}$	$0.80^{0.05}_{0.06}$	$177.1^{3.2}_{3.7}$	$0.17^{0.08}_{0.06}$	0.03, 0.04, 0.00	$5.6^{0.9}_{0.9}$
J1238+2846	$1.19^{0.04}_{0.02}$	$91.4^{7.0}_{7.8}$	$0.86^{0.06}_{0.07}$	$133.5^{11.3}_{10.5}$	$0.53^{0.16}_{0.15}$	0.04, 0.02, 2.21	$7.0^{2.1}_{1.1}$
J1515+3137	$0.76^{0.03}_{0.01}$	$77.0^{18.0}_{20.7}$	$0.91^{0.05}_{0.08}$	$146.8^{10.5}_{11.6}$	$0.81^{0.06}_{0.06}$	0.03, 0.04, 0.00	$6.6^{3.3}_{1.4}$
J1518+4658	$0.74^{0.03}_{0.01}$	$152.8^{4.4}_{7.5}$	$0.76^{0.05}_{0.05}$	$161.7^{2.7}_{2.7}$	$0.50^{0.04}_{0.04}$	0.06, 0.03, 0.00	$8.0^{2.8}_{1.1}$
J1524+4801	$1.19^{0.06}_{0.03}$	$70.5^{6.5}_{9.1}$	$0.71^{0.03}_{0.03}$	$63.5^{2.0}_{1.8}$	$0.53^{0.02}_{0.03}$	0.03, 0.01, 0.02	$5.4^{0.7}_{0.5}$
J1537-3010	$1.48^{0.11}_{0.06}$	$31.8^{1.2}_{1.9}$	$0.50^{0.35}_{0.09}$	$33.1^{7.1}_{7.2}$	$0.74^{0.07}_{0.06}$	1.56, 0.41, 2.96	$7.8^{10.3}_{0.1}$
J1553+3149	$0.82^{0.02}_{0.01}$	$157.4^{9.7}_{9.7}$	$0.80^{0.03}_{0.03}$	$4.1^{2.2}_{2.2}$	$0.71^{0.04}_{0.03}$	0.05, 0.07, 0.00	$4.6^{0.3}_{0.4}$
J1612+3920	$1.37^{0.08}_{0.04}$	$104.1^{34.5}_{30.4}$	$0.87^{0.04}_{0.12}$	$64.2^{0.7}_{0.7}$	$0.73^{0.01}_{0.01}$	0.04, 0.03, 0.00	$5.2^{0.8}_{0.3}$
J1616+1415	$0.79^{0.04}_{0.01}$	$108.8^{27.1}_{28.4}$	$0.88^{0.08}_{0.10}$	$160.6^{15.8}_{16.7}$	$0.77^{0.14}_{0.11}$	0.02, 0.05, 2.41	$8.7^{7.5}_{1.9}$
J1623+7533	$0.94^{0.04}_{0.02}$	$29.9^{9.0}_{7.7}$	$0.76^{0.03}_{0.03}$	$51.6^{4.4}_{4.4}$	$0.69^{0.04}_{0.04}$	0.03, 0.07, 0.00	$5.1^{0.4}_{0.4}$
J1627-0224	$1.91^{0.06}_{0.03}$	$85.8^{5.3}_{5.1}$	$0.62^{0.02}_{0.03}$	$60.6^{13.8}_{20.1}$	$0.92^{0.04}_{0.04}$	0.02, 0.04, 0.00	$3.3^{0.1}_{0.1}$
J1653+5155	$0.80^{0.05}_{0.02}$	$88.4^{8.8}_{7.7}$	$0.60^{0.04}_{0.05}$	$93.5^{2.8}_{2.3}$	$0.81^{0.02}_{0.02}$	0.04, 0.01, 0.00	$3.7^{0.3}_{0.2}$
J1817+2729	$1.07^{0.04}_{0.03}$	$54.7^{1.5}_{1.5}$	$0.22^{0.03}_{0.02}$	$56.1^{1.9}_{1.4}$	$0.10^{0.05}_{0.05}$	0.21, 0.53, 15.9	$14.2^{1.9}_{0.9}$
J1949+7732	$0.80^{0.02}_{0.01}$	$161.5^{9.2}_{5.6}$	$0.93^{0.03}_{0.03}$	$23.8^{44.5}_{66.9}$	$0.95^{0.03}_{0.05}$	0.05, 0.04, 0.00	$18.2^{6.8}_{3.1}$
J2132+2603	$0.89^{0.02}_{0.01}$	$117.4^{18.8}_{27.8}$	$0.92^{0.05}_{0.04}$	$20.0^{17.6}_{21.2}$	$0.82^{0.10}_{0.09}$	0.04, 0.06, 0.00	$7.1^{1.5}_{1.5}$
J2145+6345	$1.02^{0.04}_{0.00}$	$166.4^{7.2}_{14.1}$	$0.86^{0.04}_{0.32}$	—	—	—, 0.61, 4.67	$21.0^{0.4}_{0.9}$
J2250+2117	$0.93^{0.03}_{0.01}$	$89.9^{61.5}_{56.4}$	$0.93^{0.05}_{0.07}$	$72.1^{12.7}_{53.6}$	$0.88^{0.08}_{0.09}$	0.03, 0.06, 0.05	$3.3^{0.4}_{0.5}$
J2316+0610	$1.13^{0.03}_{0.02}$	$126.9^{2.1}_{2.5}$	$0.29^{0.06}_{0.05}$	$131.9^{4.8}_{5.1}$	$0.71^{0.05}_{0.04}$	0.03, 0.02, 0.00	$2.3^{0.2}_{0.1}$
J2350+3654	$1.73^{0.05}_{0.02}$	$92.2^{5.7}_{6.2}$	$0.78^{0.02}_{0.02}$	$160.3^{15.5}_{13.7}$	$0.76^{0.13}_{0.10}$	0.01, 0.05, 0.04	$7.1^{0.8}_{0.4}$

gravitational lensing. For the former we used the median colours derived from the pixel modelling (Appendix A), along with the galaxy's spectroscopic redshift. Using the Bayesian stellar population analysis code of Auger et al. (2009), we derive a *total* stellar mass of $\log_{10}(M/M_{\odot}) = 11.66 \pm 0.05$ (11.42 ± 0.05) for a Salpeter (Chabrier) IMF. In contrast our SIE lens model implies the Einstein mass within the Einstein radius is $\log_{10}(M/M_{\odot}) \approx 11.64$. This lensing mass to stellar mass ratio is typical for samples of strong lenses (e.g. Auger et al., 2010), and is on the more conservative side of the gravitational lensing regime since the predicted Einstein radius from the stellar mass is marginally larger than the mass model predicts. On balance, we expect that this is a gravitationally lensed quasar.

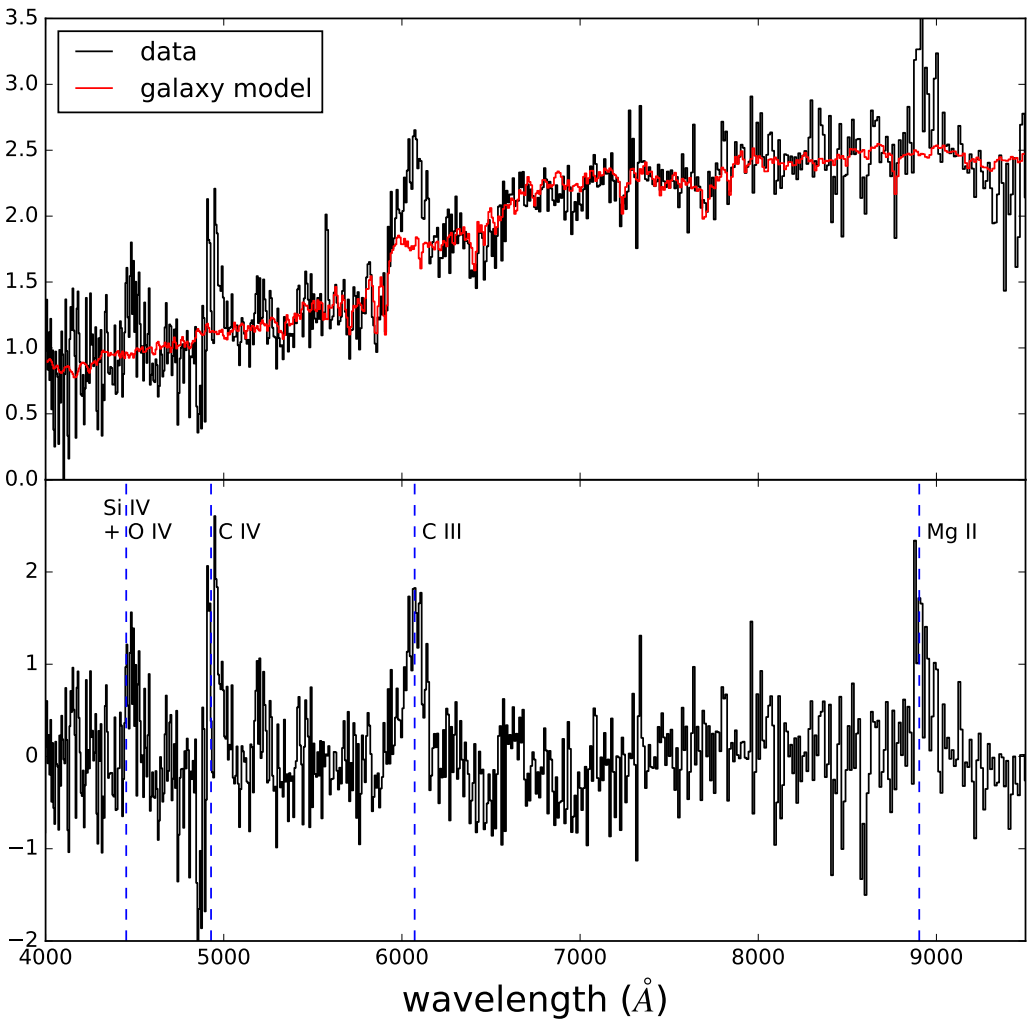

Fig. 4.10 *Top*: BOSS spectrum of J0203+1612, classified as a galaxy with pipeline galaxy model overlaid. *Bottom*: galaxy model subtracted from the data (residual signal-to-noise) clearly showing several quasar emission lines at $z = 2.18$.

J0416+7428

This double has a particularly bright lensing galaxy, with i=16.22, and is at a redshift of z=0.098. Ne V and Ne VI are seen spatially resolved at a background redshift of 0.9, with broad Hβ, confirming this as a lensed quasar. The *Gaia* detections associated with each image also suggest this must be a quasar. The low redshift lensing galaxy is rare amongst lensed quasars, with the only known lensed quasar with a redshift lower than this being the Einstein cross (Huchra et al., 1985). Another double in our sample, J1526-1400, has a low-redshift, bright lensing galaxy, so we investigate the expected number of lenses as a function of lensing galaxy brightness after describing J1526-1400.

J0607-2152

Spectra at two position angles were taken for this system, to confirm that the three *Gaia* detections are quasar images at z=1.305. Spectra of each image are similar, however there are slight variations in the line profiles. In particular, the two bright images have strong narrow absorption in Mg and C IV at the same redshift as the quasar emission lines, neither of which is seen in the fainter image. This system could allow measurements of the spatial extent of the narrow absorption system in the quasar host galaxy.

Figure 4.11 shows the presence of 2 further objects between and to the East of the 3 *Gaia* detections. Fitting a galaxy and a PSF respectively to these features models the system to the noise, so we expect that these are the lensing galaxy and fourth quasar image. Using these 5 positions, we are not able to fit a SIE+shear model to the data ($\chi^2 \sim$100), suggesting a more complex lensing model is required, or the fourth image is much closer to A (Figure 4.12).

J0608+4229

This system has three *Gaia* detections with G=18.22, 19.86, 20.12. The compact nature of the system and high flux ratio led to blending of the spectra. However, the broad emission lines are clearly extended in the 2D spectra. Modelling the system as three PSFs, reveals residual flux just south of the brightest image, and modelling the systems as 4 PSFs fit the Pan-STARRS data to the noise, as shown in Figure 4.13. We note, however, that no lensing galaxy is seen upon PSF subtraction, but this is often expected to be the case for higher redshift sources (here, z=2.34). A SIE+shear lens model shows A is observed brighter than the model, and D is observed fainter (Figure 4.14). Since D is a saddle point in this model, we should expect microlensing to be playing a part in its brightness suppression (Schechter and Wambsganss, 2002).

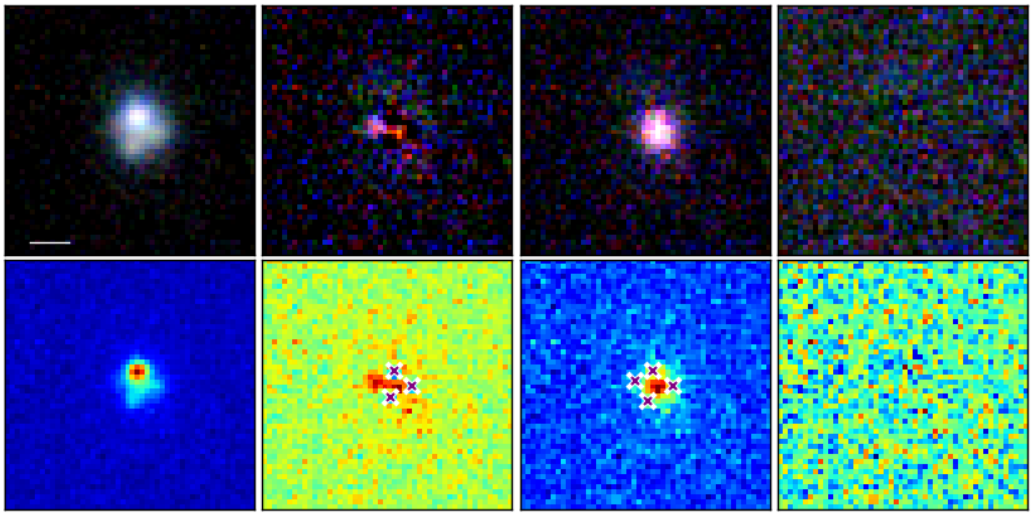

Fig. 4.11 Pan-STARRS modelling of J0607-2152. Top row is *riz* of data, 3 PSF model subtraction, 4 PSF+galaxy model subtraction with PSFs subtracted, 4 PSF+galaxy model subtraction. Bottom row is the same but just for *z*-band data, with modelled PSF positions overlaid.

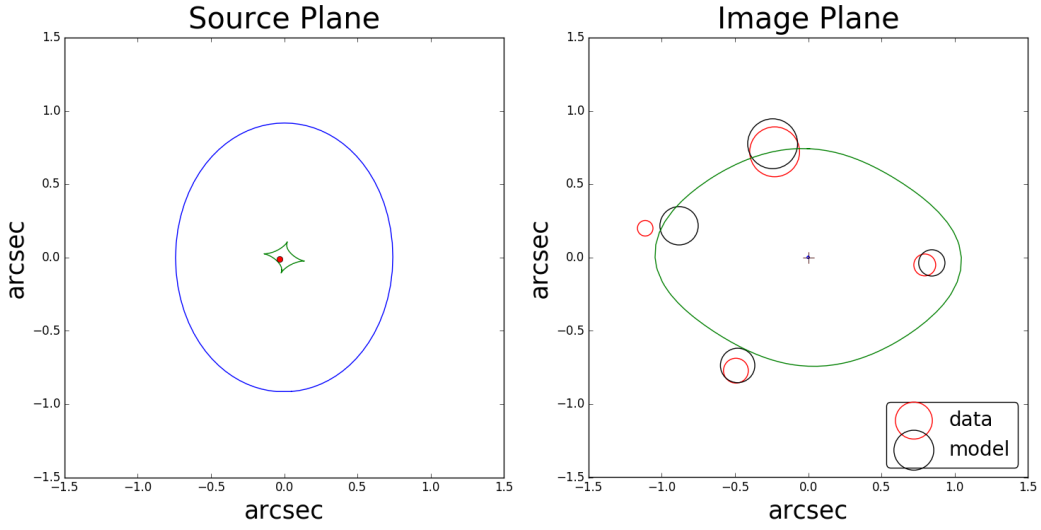

Fig. 4.12 SIE+shear model for J0607–2152, based only on the 4 PSF positions and galaxy position. The position of the Eastern image is not reproducible with a SIE+shear model.

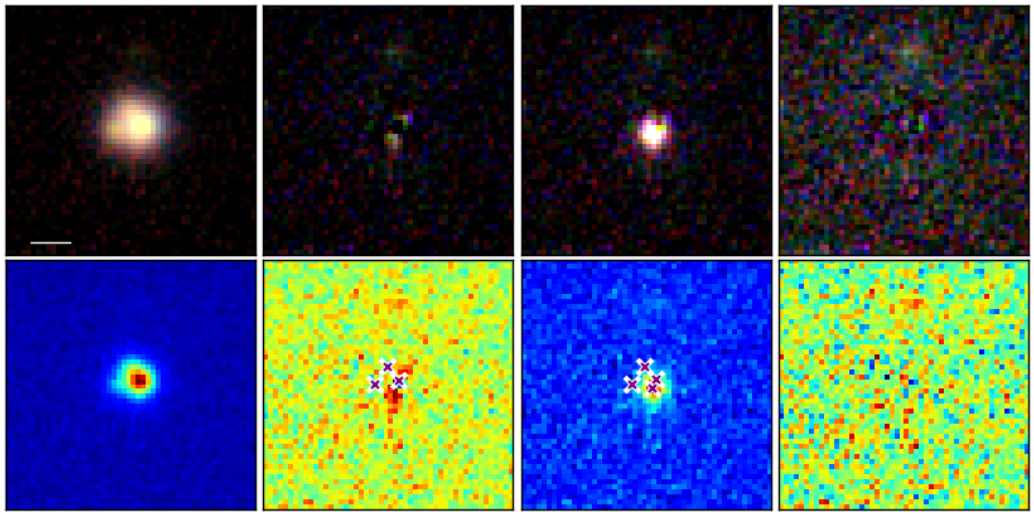

Fig. 4.13 Pan-STARRS modelling of J0608+4229. Top row is *riz* of data, 3 PSF model subtraction, 4 PSF model subtraction with D unsubtracted, 4 PSF model subtraction. Bottom row is the same but just for z-band data, with modelled PSF positions overlaid.

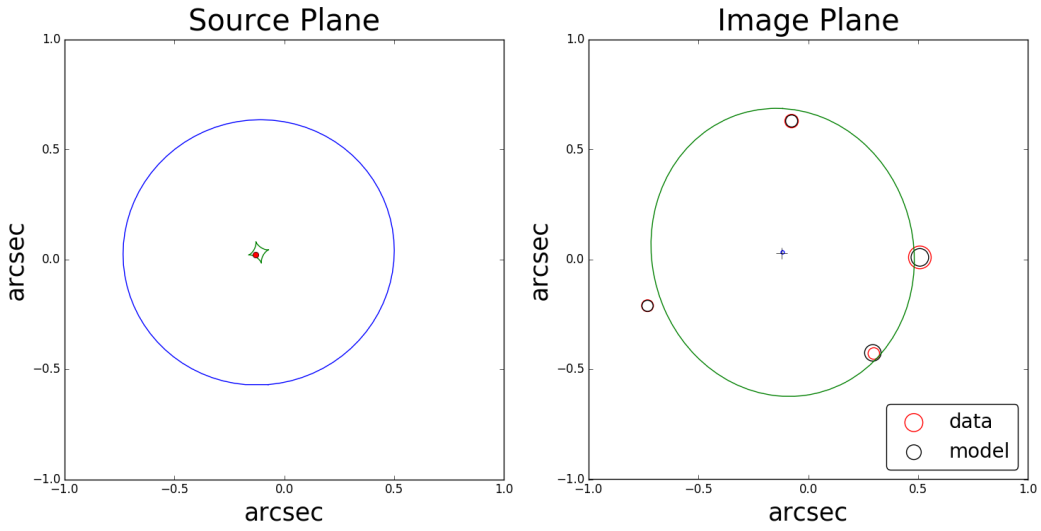

Fig. 4.14 SIE+shear model for J0608+4229, based only on the 4 PSF positions and their flux ratios. The discrepancy between brightnesses from the model and observations for images A and D is likely attributed to microlensing.

J0635+5452

This is a large flux-ratio, 3.06"-separation double. The PS *gri* data appear consistent with only a PSF+galaxy, however a *Gaia* detection associated with the galaxy suggested the presence of a counterimage, which our WHT spectrum confirms. The fainter image has dropped from G=20.57 to G=20.86 between GDR1 and GDR2.

J0643+2725

This double has a bright lensing galaxy at z=0.185. The image next to the lensing galaxy is brighter than the further one (and is likely resolved since the AEN is small, ≈2.57), which is either due to a microlensing event/sudden dimming of the source quasar (since this image arrives last), or a strong external shear.

J0659+1629

This lens is a short axis quad, with a large Einstein radius (2.3"). We obtained spectra of the two brightest images, confirming the source at z=3.09. The modelled shear is modest at 0.06, and the best fit SIE+shear model has a magnification of 25. The model predicts image D to be 60% fainter than observed. Since this system has a large time delay between image D, we expect that variability over the time delay can explain this discrepancy. This sytem was also independently selected by Delchambre et al. (2018) as a lens candidate.

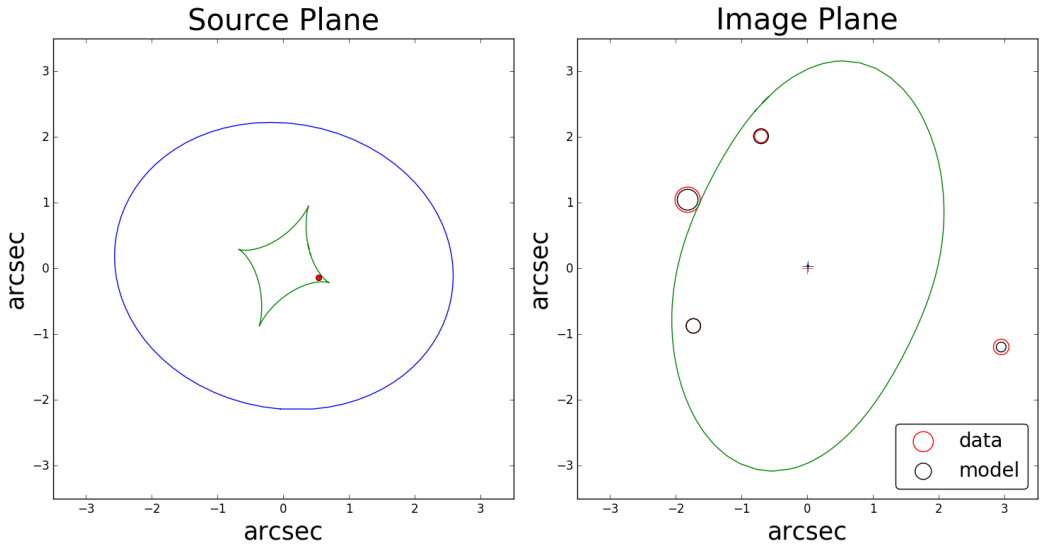

Fig. 4.15 SIE+shear model for J0659+1629, based on the 4 PSF positions, flux ratios, and lensing galaxy position.

J0803+3908

This system was originally selected with the unWISE modelling technique, given it has two *Gaia* detections separated by 0.91". Better seeing CFHT *r*-band reveal a possible fold configuration quad. Figure 4.16 shows these data, with a 4 PSF fit and subtraction, showing faint extended residuals likely due to a lensing galaxy. Very good seeing conditions allowed spatially resolved spectra between the bright pair and the Northern image, confirming the source to be at z=2.97.

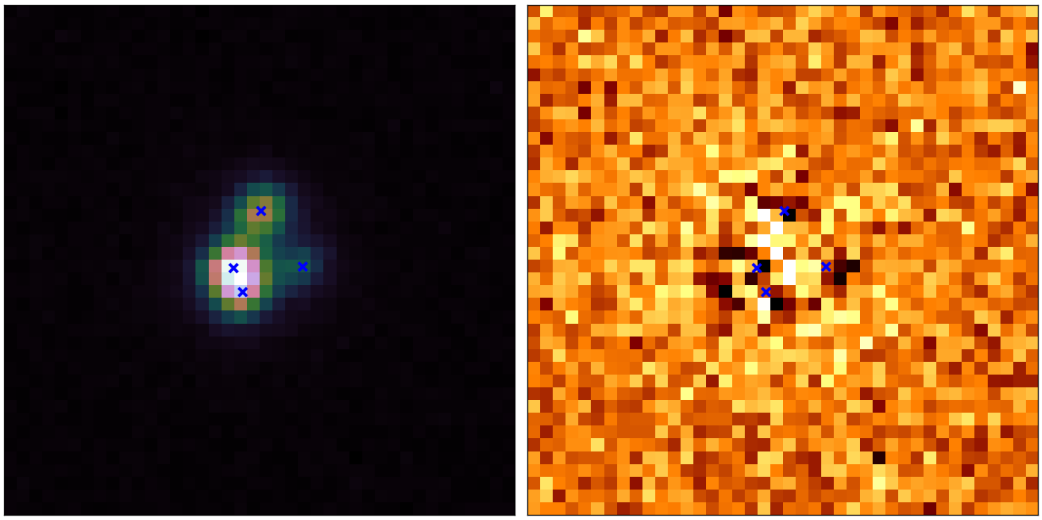

Fig. 4.16 CFHT *r*-band data of J0803+3908, with 4 PSF subtraction, showing residuals possibly due to the lensing galaxy.

J0818-2613

This quad lies in a high stellar density field, at a galactic latitude of b=5.4. It was discovered as four *Gaia* detections associated with a red ALLWISE detection. However at such high densities, quasar+star projections are common, or even contaminants from young stellar objects with red WISE colours due to dust. This configuration of images is peculiar for a quad, but it is similar in nature to WFI2033-4723. The *Gaia* magnitudes are 17.51, 17.58, 19.73, and 19.94, and the system has 3 ROSAT counts within 25". The system was targetted for spectroscopic follow-up despite the high stellar density and odd configuration, since the SEDs from optical to infrared wavelengths for all images are similar, and a faint lensing galaxy is seen upon subtraction of the PSFs (see Figure 4.17). When fitting a SIE+shear model to the 4 image positions and relative fluxes, the lensing galaxy position is recovered to within 0.5" (see Figure 4.18). A model using the galaxy position provides a total magnification of

58, a galaxy mass ellipticity of 0.61, and position angle 34 degrees East of North, with a strong shear of 0.38 at a position angle 126 degrees East of North. This model seems highly unphysical with such a large shear and orthogonal mass and shear axis directions, and is perhaps indicative of the lensing potential not being simple. Indeed the large Einstein radius of 2.96" is suggestive of a galaxy group or cluster acting as the lens.

Spectra at two position angles were taken, in order to get spectra from A+B and C, and A+B and D. The spectra shows a Broad Absorption Line quasar at z=2.15 with multiple velocity outflows (e.g. Korista et al., 1993).

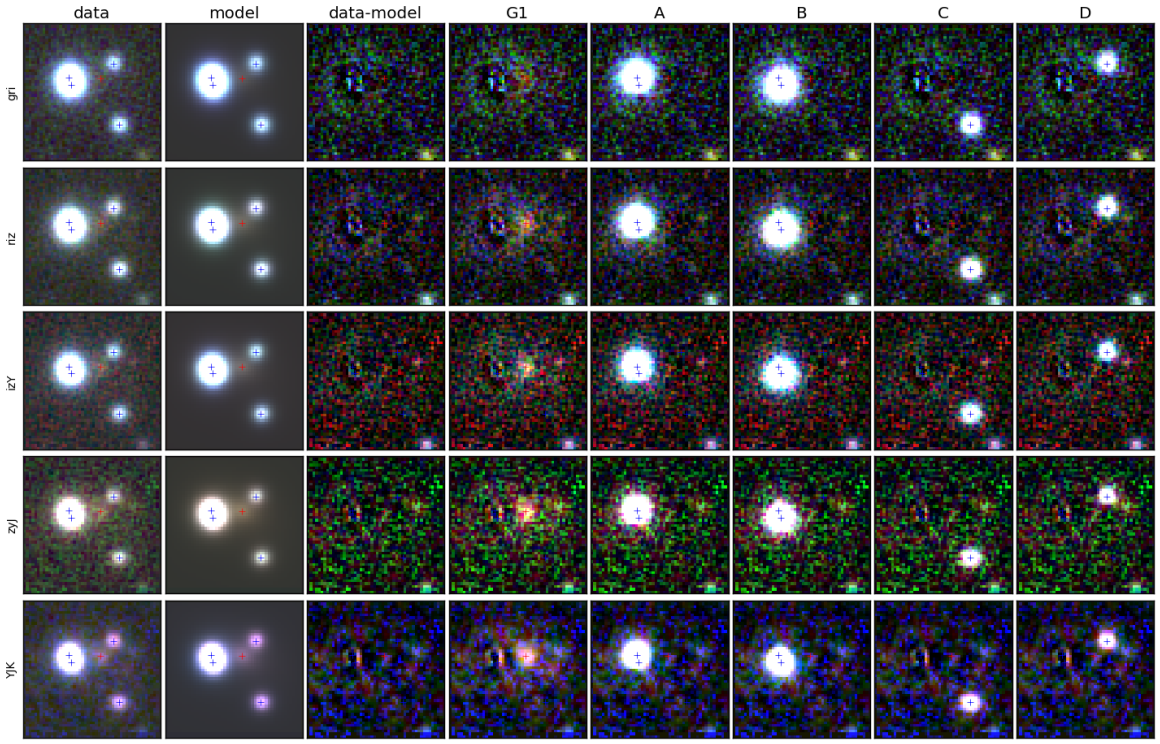

Fig. 4.17 Pan-STARRS and VHS simultaneous modelling of J0818–2613. The four point sources have similar SEDs from ∼4500Å to 4.6 microns.

J0826+7002

This system was targetted from our GDR1 search (Chapter 2.3.1), as it was selected as a *Gaia* singlet near a morphological Pan-STARRS galaxy, however the WHT spectra were not deep enough to confirm the fainter object as a quasar. It was targetted again after it was recovered by the same search technique in GDR2, and better seeing conditions and lower airmass observations reveal both *Gaia* detections to be quasars at z=1.62. Both images are detected in GDR1 and GDR2, but the separation is 5.82" and hence the system was not

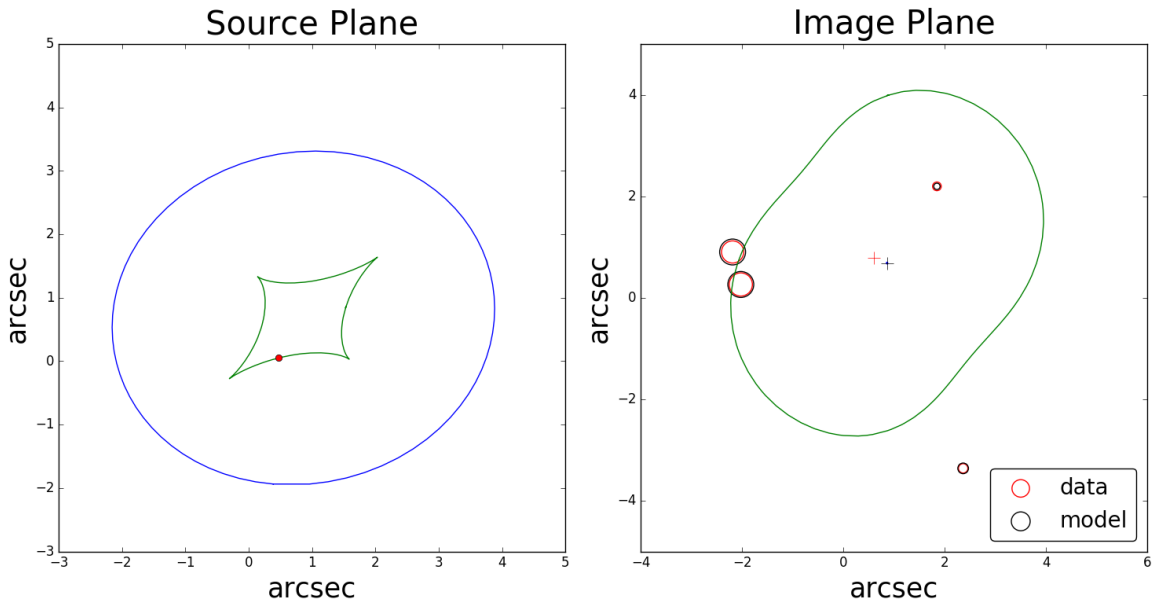

Fig. 4.18 Best-fit SIE+shear model for J0818-2613, based only on image positions and flux ratios. *Left*: Source plane caustics with source position overlaid; *right*: image plane critical curves with best-fit image positions, and observed image positions overlaid. The lens model reproduces the position of the lensing galaxy based only on image positions and relative fluxes.

discovered by the unWISE modelling or WISE-*Gaia* doublet selection. Pixel modelling shows three lensing galaxies lying closer to the brighter image.

J0907+6224

This double has SDSS (from the seventh data release) and BOSS spectra. It has a redshift of z=1.87 and a separation of 2.48". It has two narrow absorption features in the C IV line based on the BOSS spectrum. The different continuum between the BOSS and SDSS spectra is likely attributed to the different fibre apertures (2 and 3" respectively), and hence contribution from the lensing galaxy.

The SDSS pipeline catalogues this as two objects, with an i-band magnitude of 18.93 for the Northern component, allowing a colour selection from SQLS to select this as a potential lens. The likely reason this was not selected was due to a colour difference in $g-r$ between the two components: 0.54 and 1.01 for the quasar and companion respectively (Oguri et al., 2006).

J0921+3020

This 2.93"-separation double has a source redshift of z=3.33, with one bright image (G=18.66 with SDSS and BOSS spectra), and one faint image (G=20.86) blended with a galaxy. The system lies in the Smithsonian Hectospec Lensing Survey (SHELS) four degree field, and both objects have SHELS spectra with identification of quasars at z=3.33 (Geller et al., 2014). The system has radio and X-ray counterparts in FIRST/NVSS (4.2mJy at 1.4GHz), SZA (2.9mJy at 5GHz, 1.4mJy at 31GHz, Muchovej et al., 2010), and 2.82e-14mW/m2 from XMM-Newton (Rosen et al., 2016).

J1003+0651

This system has three GDR2 detections, centred on a SDSS spectroscopic galaxy at z=0.225. A feature around 4300Å is indicative of a quasar, and subtraction of the SDSS model galaxy template reveals quasar emission lines at z=2.56 (Figure 4.19). Our WHT data resolve two quasar traces at the same redshift, either side of the lensing galaxy.

J1238+2846

The WHT spectra show a shared broad emission line at 6410Å (and perhaps a line at 5210Å) for each component of this pair. The southern component has a BOSS spectrum clearly revealing much higher signal-to-noise versions of these emission lines, corresponding to CIII and CIV respectively. Interestingly the BOSS spectrum also shows strong Lyα and NV which are not present in our WHT spectrum. This is probably due to the candidate being targetted at the very start of the night at high airmass and with the slit aligned along the two images rather than the parallactic angle, reducing the amount of flux to the blue arm. The lensing galaxy is revealed most readily in the z-band and is verified in both the Pan-STARRS and DECaLS z-band data.

J1307+0642

This system was the only followed up *Chandra* double, and was also selected as spectroscopic galaxy with nearby *Gaia* detection. The *Chandra* data resolve two X-ray point sources coinciding with two optically blue point sources either side of a bright galaxy (see Figure 4.9). A SDSS spectrum reveals the lensing galaxy to be at z=0.23, however, no quasar emission lines are seen upon subtraction of the model spectrum. We targetted this system during our first observing run of GDR2-selected objects, however only a hint of an emission line at 4700Å was seen. Deeper spectra during our second observing run reveal clearly

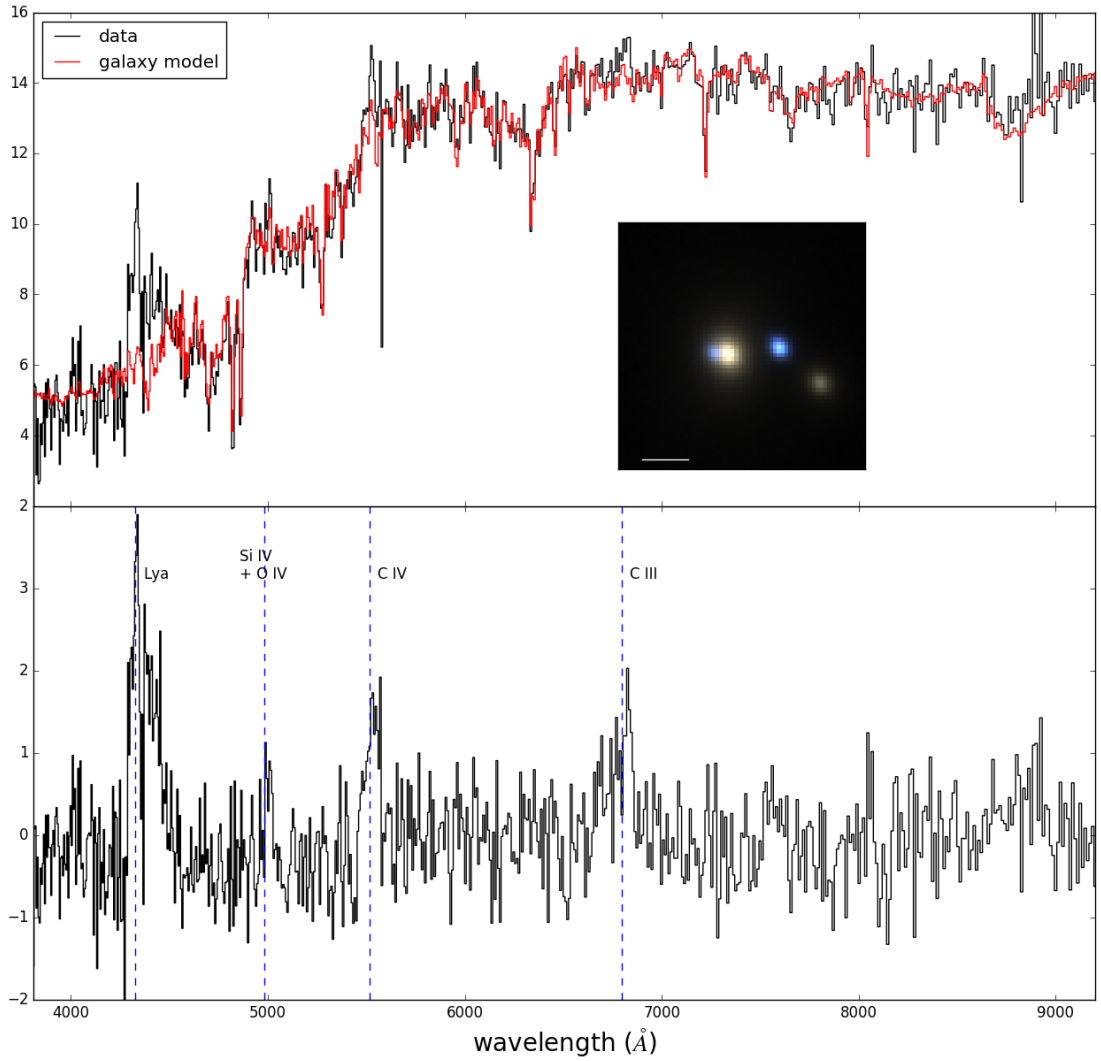

Fig. 4.19 SDSS galaxy spectrum and model for J1003+0651, with model subtraction showing quasar emission lines at z=2.56. The inset in the top figure is a HSC *gi* colour image showing the two blue quasar images. The white scale bar is 2".

resolved traces of quasar images at z=2.03. The initial *Chandra* imaging was for 3C281, which is situated less than 3 arcminutes from this system.

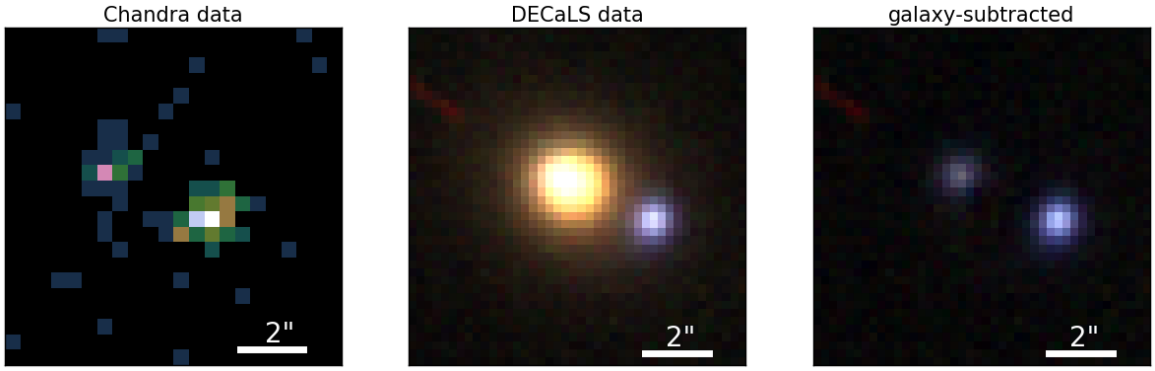

Fig. 4.20 *Left*: Archival *Chandra* imaging of J1307+0642; *middle*: DECaLS *grz* colour image; *right*: galaxy model subtracted *grz* image, showing the quasar counterimage.

J1418-1610

The blue arm reveals no broad emission lines, however as in the case of J1238+2846, it was observed at high airmass. The red arm reveals two prominent emission line at ∼5960 and ∼9260Å, suggesting MgII and Hγ at z=1.13. This is in agreement with the subsequent identification of Hδ and FeII (∼3200Å) in the stacked spectrum, and also with a UV excess as detected by GALEX.

J1524+4801

This doubly imaged lens was selected both by the unWISE modelling and the W1−W2>0.4 double *Gaia* detection search. Figure 4.8 shows that the two *Gaia* detections correspond to a quasar image (G=20.29, AEN=1.98), and the lensing galaxy (G=20.60, AEN=17.53). Surprisingly the lens galaxy is fainter (i=19.56) than most other galaxies with *Gaia* detections, suggesting a compact central region.

J1526-1400

This double has the lowest redshift source yet discovered for lensed quasars, z=0.65, and a particularly bright, low-redshift lensing galaxy at z=0.096. Similarly to J1003+0651 and J1524+4801, the lensing galaxy is detected by *Gaia*. Given the brightness of this lens (i=16.02), and that of J0416+7428, we can compare with how many bright lensing galaxies are expected based on the OM10 mocks. Figure 4.21 shows the number of lensed quasars

expected across the whole sky with multiple images detected by *Gaia* and lensing galaxy brighter than some magnitude.

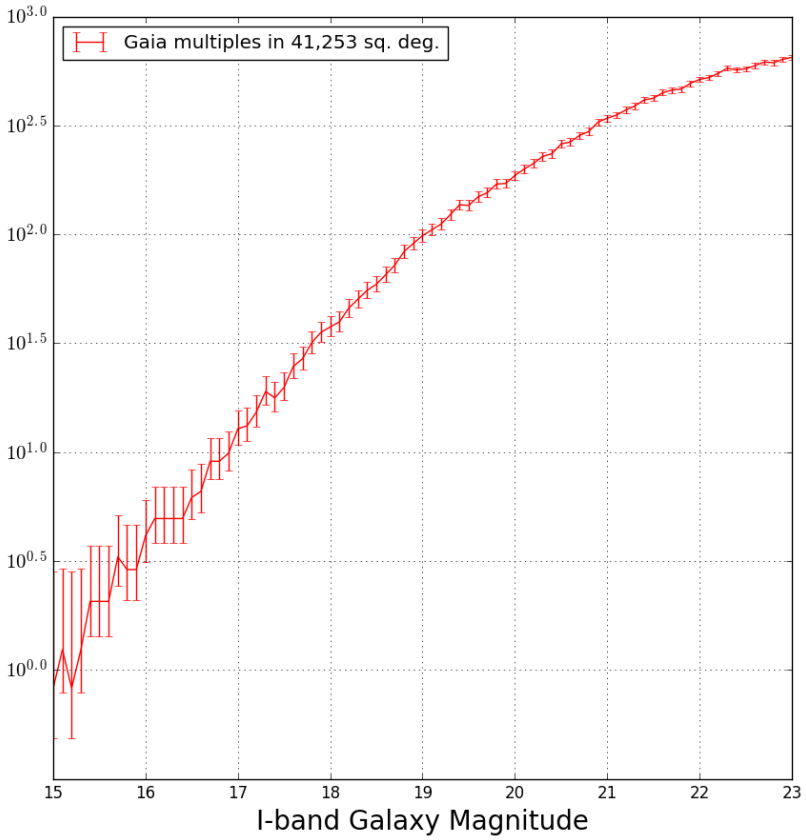

Fig. 4.21 Number of lensed quasars across the whole-sky with second (doubles) or third (quads) brightest images detected by *Gaia*, and lensing galaxy brighter than a certain magnitude.

With the two doubles presented here, and Q2237+030 (Huchra et al., 1985), we have 3 lenses with multiple *Gaia* detections, and lensing galaxies brighter than i=16.5. This seems to be consistent with the 4-7 expected across the whole sky based on OM10 (Figure 4.21), but it is perhaps surprising to have found all the lenses in such a sample given that our selections are mostly based on source colours. Investigating spectroscopic samples of bright galaxies up to z=0.1 will reveal if there is an overabundance of low-redshift lensing galaxies compared to the mocks.

J1537-3010

Our WHT spectra reveal that the eastern and southern images share a broad emission line at 4212Å. A second emission line at 5190Å has been identified with Subaru (Rusu, private

communication). This places the source at a redshift of $z = 1.72$, with the two lines being CIV and CIII respectively. The SIE+shear mass model provides a good fit, $\chi^2 \sim 5$ given 4 degrees of freedom. The majority of this derives from image B being half as bright as the model predicts. The shear has a magnitude of 0.07, 34 degrees East of North. This candidate was also independently selected by Delchambre et al. (2018) as GRAL153725327-301017053 and spectroscopically confirmed (Delchambre et al., private communication).

J1550+0221

This double has a BOSS spectrum, and was selected as a lens candidate independently by Spiniello et al. (2018) using imaging analysis of KiDS pixels. Surprisingly it was not selected by their *Gaia* multiplet method despite it passing their selection criteria.

J1752+0826

The WHT spectrum for this object was taken at the start of morning twilight, and at high airmass. The spectra reveal quasar emission lines at z=0.78, however the spectra are not deep enough to resolve two traces.

J1817+2729

This object was selected by the W1−W2>0.2, 4 *Gaia* detections search. One of these detections is due to a very nearby star. Given its high stellar density and apparent lack of a lensing galaxy or fourth image, it was given a low follow-up priority. However, we upgraded the priority given its selection by Delchambre et al. (2018) as GRAL181730853+272940139, as in the case of J2014-3024. Resolved spectra verify images A, C, and D are at a redshift of $z = 3.07$. Our SIE+shear model predicts a highly flattened mass distribution with $q = 0.21$ orientated 54 degrees East of North, and a strong shear of 0.27, -34 degrees East of North. The light from the galaxy is also highly elongated, $q = 0.1$, and in a remarkably similar direction to the mass (56 degrees East of North). The main contribution to the χ^2 is the flux ratio, with image B being 4 times fainter than predicted by our SIE+shear model. This is a saddle point and such images can be strongly demagnified by microlensing (Schechter and Wambsganss, 2002). We note that such a strong shear, orthogonal to the mass distribution likely suggests a limitation in the choice of lensing model. Rusu and Lemon (2018) discuss a more intricate mass model, based on deeper Subaru imaging, and suggest that the lensing galaxy is an edge-on disk. The lensing nature has been independently spectroscopically confirmed by Delchambre et al. (private communication).

J1949+7732

This lens is an XMM source (Pineau et al., 2011) and has a source redshift of $z = 1.63$. The SDSS data show that the north-eastern component is brightest in all bands, while the Pan-STARRS data clearly show the opposite. The *Gaia* magnitudes corroborate the Pan-STARRS flux ratios (G=18.71, 19.51 for A and B). Similarly to J0235-2433, it has both images detected by *Gaia*, and so a lightcurve will help reveal the nature of this flux ratio discrepancy, perhaps attributable to an ongoing microlensing event. The modelled unWISE magnitudes are similar for each component: W1,W2=14.94,14.03 for A and W1,W2=15.08,13.97 for B. We note that even though the WISE quasar fluxes should be unaffected by microlensing, they are likely contaminated by flux from the unmodelled lensing galaxy. Our simple mass model predicts a large magnification of $\sim$20, however, this is unreliable since the potentially microlensing-affected flux ratio has been used to constrain the model.

J2014-3024

This system was selected as a *Gaia* triple with W1$-$W2>0.3. It was originally given a low priority because of the lack of a fourth image or lensing galaxy and a poor unWISE pixel model–only one component is classified as a quasar. We upgraded the priority given its selection by Delchambre et al. (2018), as in the case of J1817+2729. The spectra of the two eastern PSFs are blended and show features of a quasar at $z = 2.35$, while the western PSF has a much redder spectrum, showing no quasar emission lines. Therefore, we can rule out the hypothesis that this is a quadruply imaged lensed quasar, but cannot rule out if the close pair are components of a doubly imaged quasar.

J2032-2358

Given the high airmass at which this target was observed, there is little signal from the blue arm. On the red arm, the single shared emission line can be identifed as MgII, since in one component there is the characteristic MgII absorption doublet. A corresponding signal can then be seen in the noisy blue spectra, corresponding to CIV (see Figure 4.7). This places the sources at $z = 1.64$, however no lensing galaxy is detected in the Pan-STARRS images.

J2145+6345

This object was discovered by our W1$-$W2>0.2, 4 *Gaia* detections search. Three spectra were extracted for this object, since components A and B could not be resolved. It has a similar configuration and brightness to PG1115+080 (Weymann et al., 1980). It lies at $|b|$=7

in a crowded stellar field with a *Gaia* density of 71,000 detections per square degree. While such regions are normally excluded from lens searches, proper motions from *Gaia* made our search in such regions more manageable by removing many high proper motion contaminant systems. No galaxy is revealed in the PSF subtraction of the Pan-STARRS data. The system is very bright in WISE (W1=12.08 in Vega) and corresponds to a faint ROSAT source (Voges et al., 1999) with 7 ROSAT photons within 30" of the lens. Furthermore, all images are optically bright (G=16.86, 17.26, 18.34 and 18.56), making it second only to PSJ0147+4630 (Berghea et al., 2017) in terms of the brightest fourth image. This makes the system ideal for high-cadence, high signal-to-noise monitoring to determine time delays for cosmography (Courbin et al., 2018). Our mass model (SIE+shear) is constrained exclusively by image positions and fluxes, as the lensing galaxy is not detected. It predicts a shear of 0.13, -36 degrees East of North, and an overall magnification of $\sim$21. The fitted galaxy position is at x, y = 0.206, 0.271" relative to the astrometry given in Appendix A.

J2350+3654

Figure 4.22 shows a *gi* Hyper-Suprime Cam (HSC) colour image of J2350+3654. A third blue object, C, is seen North-East of the lensing galaxy. Subtraction of the lensing galaxy and quasar images reveals two more sources, one to the West of the lensing galaxy, and one red source West of image A, the brighter image. The *i*-band magnitudes of A, B, and C are 20.82, 21.10, and 21.9. There also exists narrow band (NB515) HSC imaging of this system. The differences in *g-i* and *g-NB515* colours between the three components are: $\Delta(g-i)_{AB,AC} = -0.08, -0.62$ and $\Delta(g-NB515)_{AB,AC} = 0.28, -0.09$. The nature of C is still yet to be determined. It might be a third quasar image, but given the single lensing galaxy we would often expect a 4th image. It could also be a secondary source, such as the quasar host galaxy—as in SDSSJ1206+4332 (Agnello et al., 2016)—or another quasar. C could also be a foreground star. Deeper imaging and spectra of this system are required.

4.4 Discussion

We have observed 87 candidates identified amongst photometric quasar candidates with multiple *Gaia* detections, single *Gaia* detections offset from a galaxy, or multiple *Gaia* detections with similar modelled red WISE photometry. We have found 70 new lenses, 1 highly probable lens and 4 NIQs. 4 candidates are still unclassified, and 8 are contaminant systems. For the probable lens, J0203+1612, two blue point sources are seen either side of a galaxy, with a spectrum showing blended features of a low-redshift galaxy and a higher-redshift quasar. Our low contaminant rate arises from the large number of previously

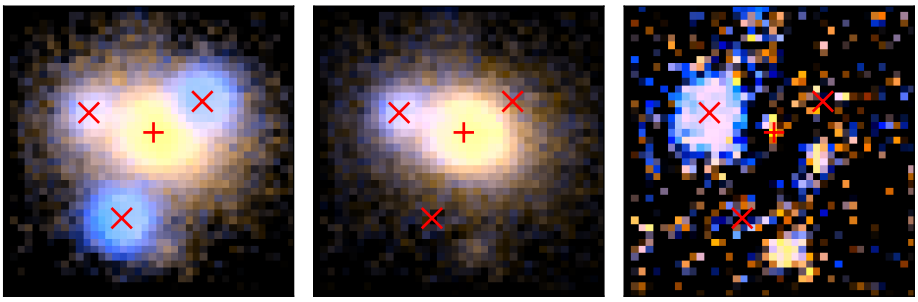

Fig. 4.22 *Left*: A 7"×7" *gi* HSC colour image of J2350+3654; *middle*: model for the confirmed quasar images (A and B) subtracted from the data; *right*: confirmed quasar and galaxy models subtracted from the data, revealing a bright blue point source and two other sources, one west of the lensing galaxy and one west of image A.

undiscovered bright lensed quasars in the Pan-STARRS footprint, coupled with a large reduction in typical contaminant systems by using *Gaia*'s catalogue information and unWISE pixel modelling. This modelling has now become particularly useful due to the increase in resolution and detection of small-separation pairs in *Gaia* DR2. The limited allocation of spectroscopic follow-up time since the second *Gaia* data release has led us to concentrate on the lens candidates that are most convincing, namely those with bright lensing galaxies. To build a statistical sample from *Gaia*, however, we must ensure that the lensed quasars with fainter lensing galaxies are confirmed. We are confident that these have been selected in our candidate list, since our lens selection techniques recover all previously known lensed quasars with 2 or more *Gaia* detections, which includes statistical samples unbiased by bright lensing galaxies (e.g. SQLS).

We investigate the bias in this current sample of lenses discovered with *Gaia* by comparing to a complete sample of mock lenses that would have images detected by *Gaia* with image separations between 1" and 4" (see Section 5 of Chapter 1 for details of the mock lens sample). Figure 4.23 shows the lensing galaxy brightness against source redshift for 64 of our 70 lenses confirmed from GDR2 (i.e., excluding the quads for which no lensing galaxy is seen in the Pan-STARRS residuals, and those with unreliable *i*-band galaxy magnitudes due to only seeing the lensing galaxy in the redder bands). Also overlaid is the mock sample, demonstrating that we are clearly biased towards lensed quasars with bright lensing galaxies, as expected. We note that the nearly identical quasar pairs identified throughout our campaign might partly represent the missing systems with fainter lens galaxies. Though deeper imaging is required to reveal potential lensing galaxies in these systems, we are still limited by lack of spectroscopic follow-up time to confirm candidates without obvious lensing galaxies in the relatively shallow Pan-STARRS imaging. A bias towards lower-redshift sources is

also present, explained both by the degeneracy with galaxy brightness and perhaps also by prioritisation of candidates showing a *u*-band excess when such data are available. Figure 4.23 also reveals that many lensed quasars detected by *Gaia* are expected to have faint lensing galaxies that would not be uncovered given the depth of current Pan-STARRS imaging. These lenses could be targetted by modelling deeper data, such as Dark Energy Survey data, or by looking for quasar pairs with similar variability within *Gaia* and/or LSST lightcurves.

The quad fraction of the sample presented here is 11.4% (8 in 70). While this is slightly lower than the expected quad fraction at *Gaia*'s magnitude limit of 18.8%, we are recovering all previously known quads with multiple *Gaia* detections bringing the total quad fraction of known lenses to ∼20.6%. The majority of our systems have fainter images (G>19), for which we expect a lower quad fraction due to magnification bias, and accordingly we see a smaller quad fraction than compared to a total *Gaia*-selected sample.

Figure 4.24 shows image separation versus source redshift for all known lensed quasars across the whole sky satisfying: 2 or at least 3 *Gaia* detections for doubles and quads respectively, G<20.7 for each detection, $|b|$>20, and image separations between 1" and 4". This amounts to 127 such systems, 47 of which have been presented in this thesis. We also plot the OM10 mock sample and histograms of the two parameters. The mock sample is normalised to the same area of sky in which the lenses are restricted to be. This shows that there are still ∼200 bright lensed quasars at modest separation left to be discovered, with ∼316 in total. These missing lenses are certainly being detected by *Gaia* since it detects all components of known lenses and pairs of point sources at these magnitudes and separations. The majority of these undiscovered lenses will be in the Southern hemisphere, as imaging and spectroscopic surveys for this area of sky are recent or yet to begin.

To manage the rapidly increasing number of lensed quasars (Figure 4.25), we have created an online database that will be kept up-to-date with all known lensed quasars. Each lens has multi-band imaging cutouts, a variety of catalogue information, and relevant survey links.

4.5 Conclusions

We have presented the discovery of 70 new gravitationally lensed quasars with resolved spectra from ISIS on the WHT. One lens candidate is likely to be a lensed quasar, however we have not been able to obtain spatially resolved spectra of the components. In total, we obtained a 81-90% success rate in confirming gravitationally lensed quasars, while several candidates require deeper observations to understand their nature. The particularly low contaminant rate from a purely photometric selection arises from our ability to remove contaminants using *Gaia* catalogue information and modelling of unWISE pixels.

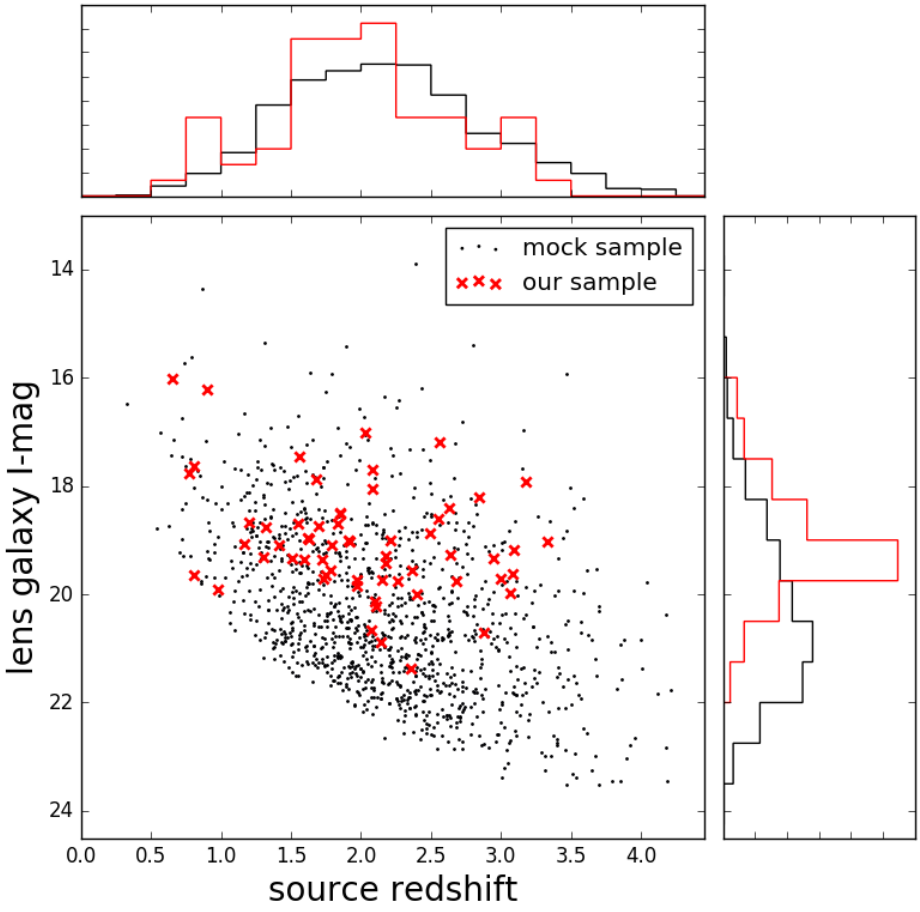

Fig. 4.23 Plot of lensing galaxy *i*-band magnitude against source redshift for 64 lensed quasars discovered with *Gaia* DR2 and reliable *i*-band galaxy magnitudes. A complete mock sample from OM10 with multiple *Gaia* detections is shown as black points. Our sample is clearly biased towards lenses with bright lensing galaxies.

The lens sample presented here is clearly a biased and incomplete sample, missing lensed quasars with fainter lensing galaxies and/or higher source redshifts. We have many candidates remaining which could fill this missing part of the parameter space. Future *Gaia* data releases will help confirm these lenses efficiently via: more precise proper motion measurements, correlation searches based on *Gaia* lightcurves, and 2-D PSF reconstruction techniques to search for lensing galaxies directly in the *Gaia* data (Harrison, 2011).

Building a complete sample of lensed quasars from *Gaia* at modest image separation (>1") and from uncrowded fields ($|b|$>20 across the whole sky) will provide a useful statistical sample of around 300 lensed quasars, an order of magnitude greater than SQLS, which can be used to impose constraints on cosmological parameters and massive galaxy evolution

(Finet and Surdej, 2016; Oguri et al., 2012). We currently know of approximately 120 lensed quasars in this sample.

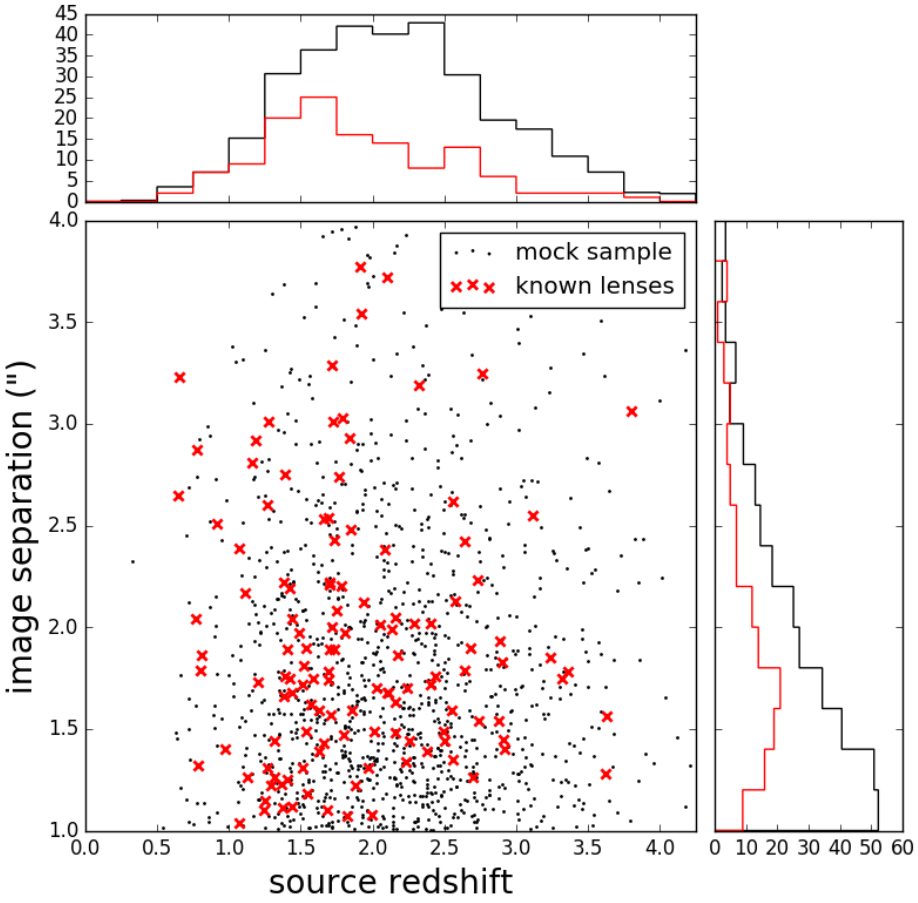

Fig. 4.24 Plot of image separation against source redshift for all known lensed quasars satisfying $|b|$>20, image separations between 1" and 4", and 2 (at least 3) *Gaia* detections brighter than 20.7 for doubles (quads). The image separations are in 0.2" bins and the source redshifts in 0.25 bins. The mocks are plotted with a frequency 4 times that of the known lens area, since the OM10 catalogue is 100,000 square degrees and sky area outside of the galactic plane is 65.7% of the full sky, i.e. 27,100 square degrees. There are 127 known lenses that meet the stated criteria, while mocks predict 307 in total.

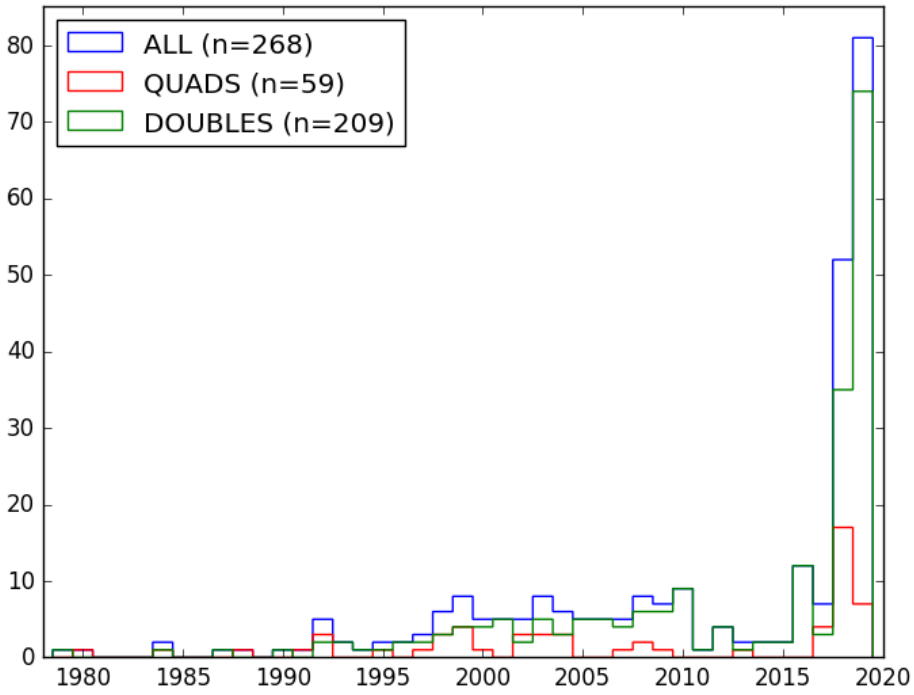

Fig. 4.25 Number of published lensed quasars discovered each year, split into doubles and quads.

Chapter 5

Variability from DES

A unique aspect of the Dark Energy Survey is its repeated observations of a large area of sky, typically 8 epochs in each band over 5 years. This allows us to extract variability information in the *grizY* bandpasses (with central wavelengths 4827, 6432, 7827, 9179, 9900Å respectively). Extracting variability information for the multiple components of nearby blends of objects offers a promising way to: (i) remove quasar+star systems from future follow-up of potential doubly imaged quasars (Kochanek et al., 2006); (ii) prioritise possible lenses amongst nearly identical quasar pairs by looking for similar variability, as has been done with targeted repeat observations of SDSS candidates (Sergeyev et al., 2016; Shalyapin et al., 2018); (iii) place constraints on time delays for lensed quasars in high-cadence fields (Kostrzewa-Rutkowska et al., 2018). However, applying variability analysis on pipeline magnitudes of close-separation pairs will lead to spurious results due to flux-sharing (Tewes et al., 2013) and variable seeing, and excludes applicability to all cases of blended sources that are not segmented by the source extraction software. This problem has been well-explored by teams dedicated to lensed quasar monitoring for extraction of lightcurves and hence time delays. Photometry has been extracted through fitting multiple PSFs (e.g., Goicoechea and Shalyapin, 2010; Koptelova et al., 2010), fitting multiple PSFs and parametric galaxy components (e.g., Hainline et al., 2013; Kochanek et al., 2006; Shalyapin and Goicoechea, 2017), difference imaging (e.g., Fohlmeister et al., 2013; Giannini et al., 2017), aperture photometry for wide-separation systems (e.g., Dahle et al., 2015; Ovaldsen et al., 2003), and non-parametric deconvolutional techniques (e.g., Bonvin et al., 2018; Burud et al., 2002; Vuissoz et al., 2007). In this Chapter we develop a parametric modelling pipeline to extract DES lightcurves in the *grizY* bandpasses, and discuss its applicability to lensed quasar follow-up.

5.1 A photometry pipeline for lensed quasars

We note that understanding the PSF is vital for deriving reliable photometry from each epoch. Tests using PSFEx (Bertin, 2011) reconstructions do not fit the PSFs of our systems precisely enough, and there is no knowledge of the uncertainty on the PSF model over which to marginalise. Using nearby stars or stacks of nearby stars as the PSF is also often inconsistent with the PSF of the system, perhaps due to spatial variations or brightness mismatches between the system PSF and the star PSFs, which can exhibit different shapes due to flux-dependent charge interactions (i.e., the brighter-fatter effect, Gruen et al., 2015; Walter, 2015). We therefore opt for an initial PSF as a Moffat profile fit to a nearby star, but we later allow the data from each epoch to fit this profile (with differences possibly due to a SED difference between the system components and the PSF star), and marginalise over the Moffat parameters. For systems with bright PSFs (G$<$18), this profile often fails to describe the PSF accurately and we remove the relevant frame from our analysis. For the remaining frames of these bright systems, the photometric precision is often $<$0.01 mag, and so only a few frames are needed to statistically verify variability. Poor Moffat fits are uncommon for the fainter systems, for which more frames are required for a robust detection of variability given the increased photometric uncertainties on fainter PSFs.

For the following, we use all single-epoch images with DES “Final Cut" processing from the first four years of DES (Morganson et al., 2018). The steps of the modelling pipeline are as follows:

1. 40$\times$40 pixel cutouts (10.5"$\times$10.5") of all single-epoch images centred on the relevant system are inspected, and any showing artefacts/cosmic rays/or significantly poor seeing (over 2 arcseconds FWHM based on the FITS header information) are excluded from the modelling.

2. To determine the zeropoint in each band, stellar objects on the same CCD chip are found by plotting $MAG\_AUTO - MAG\_PSF$ vs MAG_AUTO (as derived from SExtractor (Bertin and Arnouts, 1996)), fitting a line to the stellar locus, and selecting all objects within 0.05mag of this line and with catalogued magnitudes between 15.5 and 19. The sky background is estimated from a fit to the histogram of pixels between 5 and 25 arcseconds around each star, after a 5-σ clip. The background level is determined through the Bayesian model of Bijaoui (1980), however we also include some fraction of empty sky pixels. Following the notation of Bijaoui (1980), the (unnormalised) probability distribution of true sky flux values, i, is:

$$p(i) = \kappa\delta(i) \quad \text{if} \quad i = 0, \quad p(i) = \frac{1}{a}\mathrm{e}^{-i/a} \quad \text{if} \quad i > 0 \tag{5.1}$$

where κ describes the relevant contribution between empty sky pixels and pixels from faint objects, and the wings of PSFs and galaxies. Given a sky background s, and Gaussian noise σ, the observed flux (I) distribution is:

$$p(I) = \frac{\kappa}{2\pi\sigma^2}\exp\left(-\frac{(I-\sigma)^2}{2\sigma^2}\right) + \frac{1}{a}\exp\left(\frac{\sigma^2}{2a^2}\right)\exp\left(-\frac{(I-s)}{a}\right)\mathrm{erf}_c\left(\frac{\sigma}{a}-\frac{(I-s)}{\sigma}\right) \quad (5.2)$$

The parameter space is explored using EMCEE (Foreman-Mackey et al., 2013), so a true sky background and its uncertainty are inferred. The flux for each star is then the sum of the background-subtracted 5.4 arcsecond (20 pixel) circular aperture, and the flux uncertainty includes Poisson noise, sky background noise, and uncertainty in the subtracted background value. Finally we include a magnitude uncertainty of 0.003 in quadrature with the photometric uncertainty to account for possible systematic biases in bright stars, following Burke et al. (2018).

3. In each band we simultaneously fit the zeropoints of all frames. Since our goal is to measure variability, we set one frame's zeropoint to that of the average value derived from the calibration stars' catalogued magnitudes (Abbott et al., 2018). For any combination of zeropoints, each calibration star's best-fit magnitude is found by minimising the χ^2. Therefore, for N epochs in a given band, we perform an optimisation procedure to infer $N-1$ zeropoints. Any stars with reduced χ^2 above 100 are removed and the optimisation is repeated. This procedure is then iterated, removing stars with reduced χ^2 above 50, 25, 10, 6, and 4. This preferentially removes the fainter stars in the sample, perhaps due to intrinsic variability or because their photometry is more sensitive to seeing variations and contamination by nearby objects. Typically $\sim$80% of stars are retained after these iterations, and the zeropoints are then sampled with EMCEE. Uncertainties on these zeropoints are $\sim$0.001-0.003mag.

   The relative differences between these zeropoints are consistent with the relative differences of DES pipeline zeropoints (Burke et al., 2018) to $<$0.01 mag. However, the absolute magnitudes can differ by up to 0.02 mag. This is expected since we attempted no aperture corrections on the star fluxes. Instead, we will apply the same 5.4 arcsecond apertures on our model PSF components, since we only want to constrain relative fluxes.

4. After fitting a nearby PSF with a Moffat profile, the best seeing frame in each band is fit simultaneously with a combination of PSFs and Sersic profiles. Registrations

between the *g*- and *rizY*-bands are also modelled. Once the chains have converged, the best-fit model is used to set the registration of all other frames (again with a nearby star fit for the frame's Moffat parameters), and the PSF positions and galaxy parameters are constrained from all frames simultaneously using these registrations. After convergence, the new best-fit parameters are used to constrain the best-fitting Moffat profiles and registration on each frame individually, and subsequently all frames are again modelled simultaneously to infer PSF positions and galaxy parameters. Any poor-fitting frames are removed after visual inspection, and the Moffat fits and simultaneous frame fits are repeated. The convergence of each chain is visually checked at each stage. This provides a burnt-in chain of PSF positions and galaxy parameters.

5. For 50 samples of this model chain, the model PSF fluxes are determined in each frame through the same apertures as were applied to the zeropoint calibration stars (5.4 arcsecond circular apertures). However, since the Moffat parameters can affect these fluxes by $\sim$1%, we marginalise over all Moffat parameters and registration offsets, by sampling these parameters at each step of the model chain. The concatenated chain of fluxes for PSFs and galaxies (the sum of the brightest 200 unconvolved pixels), provides the magnitudes and their uncertainties at each epoch. We add an uncertainty of 0.005mag in quadrature with the sampled uncertainty to account for any remaining systematics (poor centring of calibration stars within their apertures, lack of modelling of host galaxies, etc.).

5.2 Example Application: ULASJ2343-0050

To demonstrate this modelling system and the individual steps, we show images from the pipeline's various stages for the lensed quasar ULASJ2343-0050 (Jackson et al., 2008). Figure 5.1 shows the individual epoch cutouts for ULASJ2343-0050 in the *grizY* bands. For some epochs, the object is at the edge of the chip, and so these epochs are removed from the analysis ($g7$, $i0$, and $z0$). In the case of $z4$, we remove it because of a nearby cosmic ray.

This initial visualisation step also immediately shows that the flux ratio between the two images is varying in all bands, since the earlier observations (time ordered in Figure 5.1) show the Eastern component is brightest, while the most recent observations show this image to be fainter.

Next, a nearby PSF is selected in each frame for modelling as a Moffat profile. This is done by showing a cutout centred on the system which can be made larger until a PSF star is seen (Figure 5.2). *Gaia* detections with AEN < 5 are overlaid during this step to prevent selection of likely binary stars, or compact galaxies.

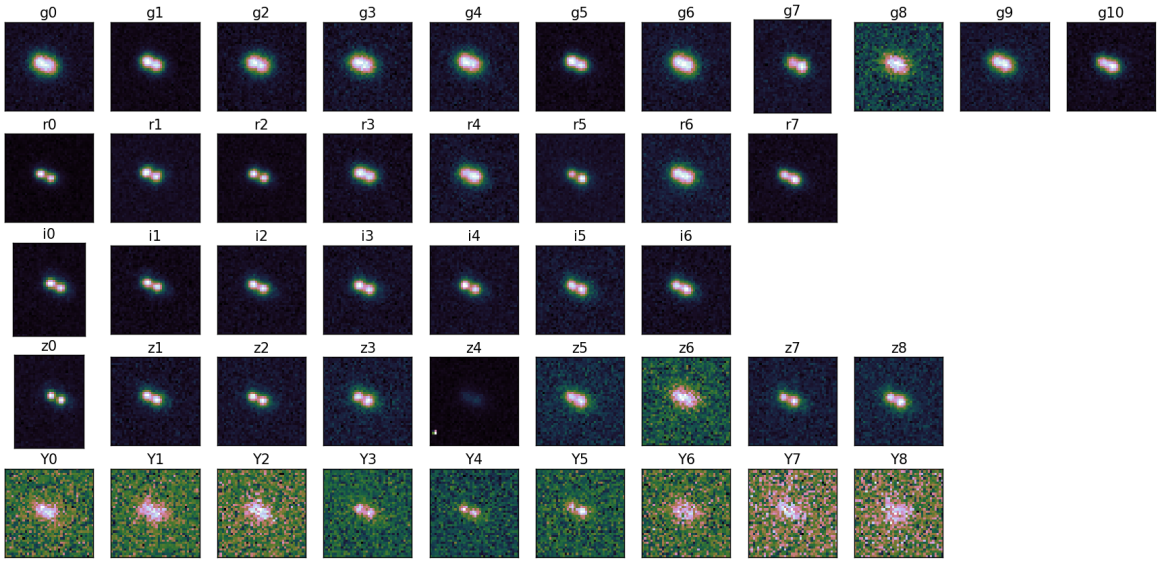

Fig. 5.1 All DES single-epoch observations of ULASJ2343-0050 from the first four years of DES data. Cutouts are 10.5"×10.5".

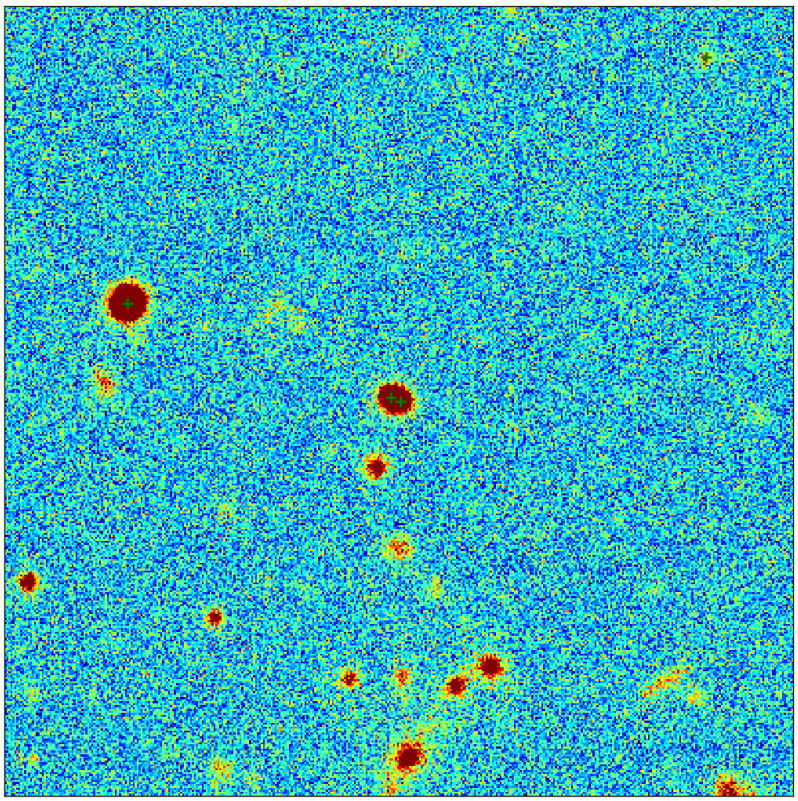

Fig. 5.2 The immediate field of ULASJ2343-0500 for a single-epoch. Overlaid are green crosses for all *Gaia* detections with AEN < 5. This helps selection of isolated stars for the PSF fitting. The field in this example is 100"×100".

Once the Moffat parameters are inferred for each frame, the best-seeing epoch from each band is selected via the modelled Moffat parameters. These 5 images are modelled simultaneously as two PSFs and one Sersic profile. The model and component subtractions are shown for ULASJ2343-0050 in Figure 5.3. These positions and galaxy parameters are then fixed, and the registration found for all other frames. A simultaneous model of all frames then provides updated positions and galaxy parameters. The PSF is then inferred for each frame using the best-fit parameters. The stacked data, model, residuals, and individual components are shown in Figure 5.4.

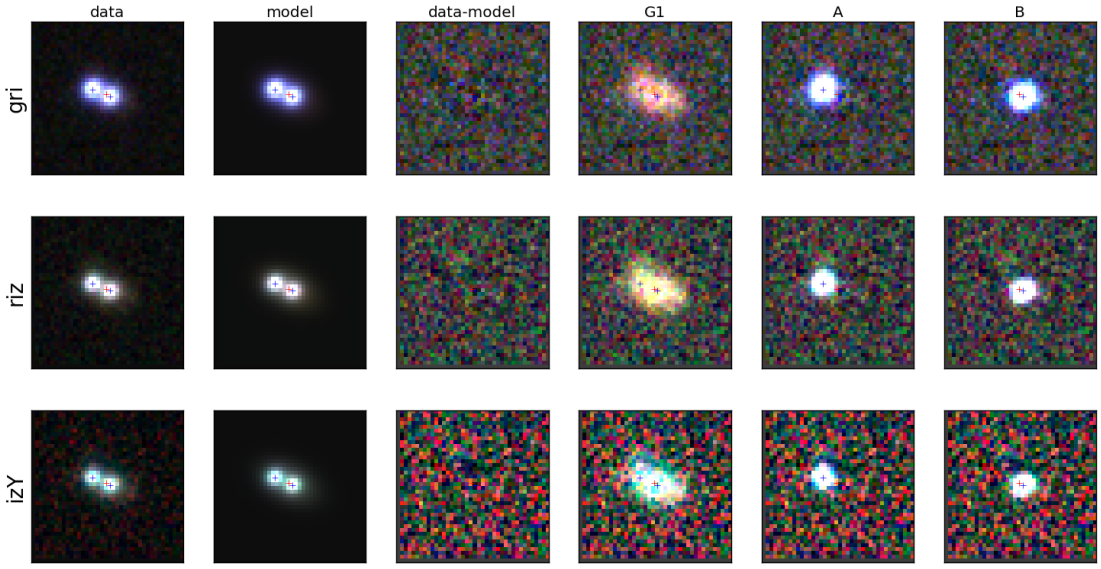

Fig. 5.3 ULASJ2343-0050 best-seeing data from each band, shown as *gri*, *riz*, and *izY* colour images. Model subtractions and subtractions of all but individual components are shown.

Table 5.1 shows the inferred positions for the two quasar images and lensing galaxy, with their sampled uncertainties. These values are typical for other lenses we will model with similarly bright images. Lightcurves from each band confirm the switching of the brightest image flux, as shown in the *g*- and *r*-band lightcurves in Figure 5.5.

Table 5.1 Astrometry and median photometry for ULASJ2343-0050 from the DES single-epoch modelling pipeline. The uncertainties on the photometry are the standard deviations of the lightcurves, showing image A to be more variable than B. We note that the photometric uncertainty has its own uncertainty, but these are similar for A and B.

Component	X (")	Y (")	*g*	*r*
A	-1.0065 $\pm$ 0.0014	0.3686 $\pm$ 0.0012	20.31 $\pm$ 0.26	20.55 $\pm$ 0.23
B	0.2402 $\pm$ 0.0014	-0.1545 $\pm$ 0.0012	20.48 $\pm$ 0.09	20.37 $\pm$ 0.10
G	0.000 $\pm$ 0.012	0.000 $\pm$ 0.008	21.26 $\pm$ 0.13	20.60 $\pm$ 0.07

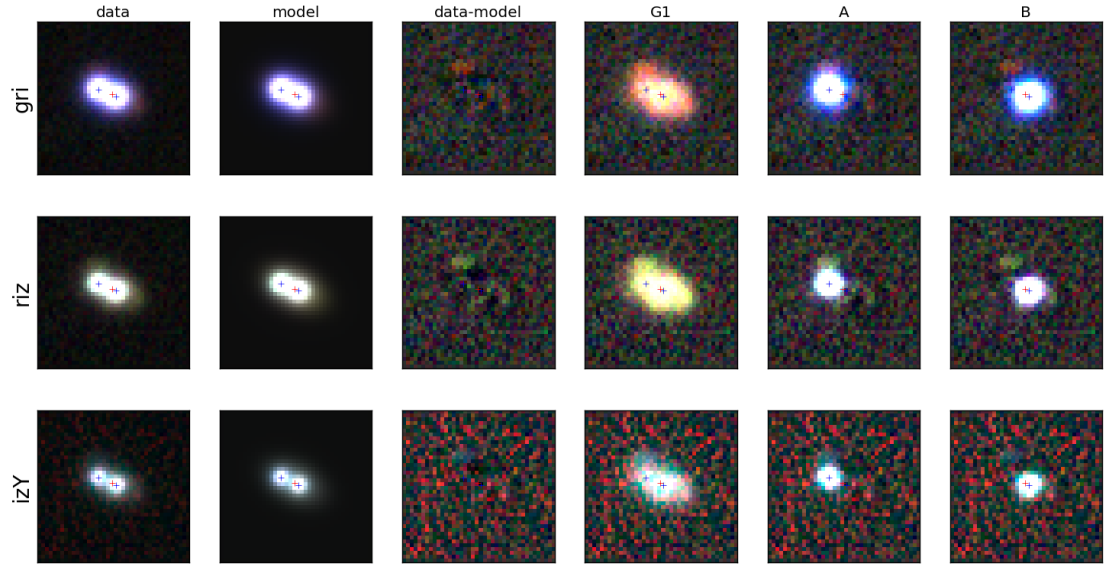

Fig. 5.4 As in Figure 5.3, but after shifting pixels in each epoch by the inferred registration and stacking. There are clear residuals North of the Eastern image and West of the Western image, likely associated with the lensing galaxy given their similar colour. These residuals are also seen in the Keck LRIS R-band imaging from Jackson et al. (2008).

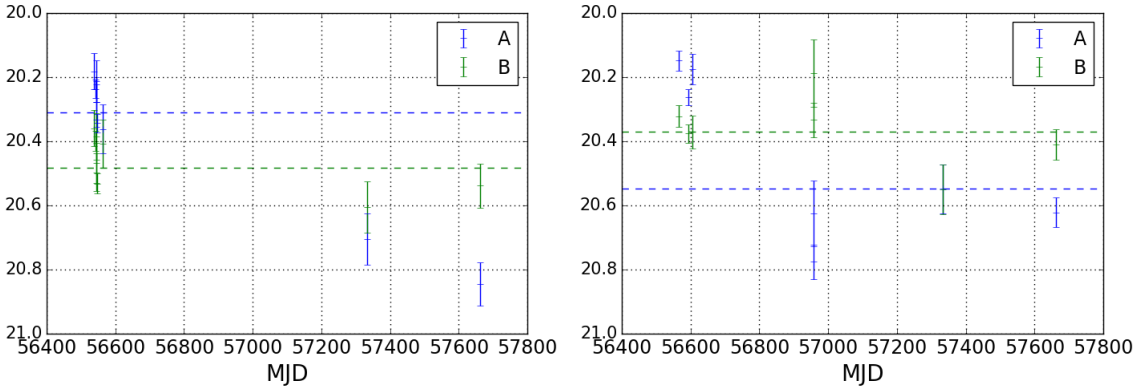

Fig. 5.5 *g*- and *r*-band lightcurves for ULASJ2343-0050. Image B is consistent with small variations, while A shows large variations attributed to extrinsic microlensing effects. The dashed lines are the median values of the lightcurves.

Using the median positions and uncertainties, we fit a SIE+shear model fixing the SIE position angle and ellipticity to the measured values from the light (q=0.572, PA=64.2 degrees E of N). We do not use the flux ratios to constrain the model. The free parameters for this model are the source position and Einstein radius. We find b=0.76" with χ^2/d.o.f. = 8.9/1. When fitting also for the shear, the model becomes underconstrained but the shear direction is well constrained to 165$\pm$5 degrees East of North and shear of 0.18$\pm$0.07, in agreement with the direction found by Jackson et al. (2008) (0.34 at 162 degrees East of North). These models suggest time delays of 25$\pm$3 days, with A varying first. Such a short time delay is unlikely to explain the flux ratio inversion in the lightcurves, suggesting significant microlensing of amplitude $\sim$0.5 mag. SDSS, *Gaia*, and Pan-STARRS all show image B to be brighter than image A, however our smooth models suggest A should be brighter. It seems, however, that A is normally fainter than B (consistent with early SDSS observations, and late DES observations) and the epochs showing it brighter than B are explained by a microlensing event. Later DES observations of this system will help decide the issue.

5.3 Variability of DES systems

5.3.1 Removing stellar contaminants

The most common contaminant in lens searches is quasars projected close to blue stars, mimicking doubly imaged quasars. While their optical colours can be similar, their SEDs vary towards redder wavelengths, as exploited by the modelling of unWISE pixels using *Gaia* positions to remove such systems from lens searches (Chapter 4). However, this modelling can only be applied to brighter systems with *Gaia* detections and high signal-to-noise detections in WISE.

We investigate how variability information can be used to further remove contaminant systems including stars. We take a sample of spectroscopically confirmed quasar+star pairs (Appendix B, Anguita et al., 2018; Treu et al., 2018) and derive their lightcurves following Chapter 5.1. We also repeat the analysis for all known lensed quasars within the DES footprint[1]. Example lightcurves with representative sampling and photometric uncertainties are shown in Figures 5.6 and 5.7 for a quasar+star system and lensed quasar, respectively. For our analysis we only retain systems with more than three photometric points over at least two observing seasons in at least three bands. To measure the variability of components in these systems, we take the reduced χ^2 after fitting all photometry to a single magnitude in each band, and report the average of these reduced χ^2 values. We expect values around

[1] https://www.ast.cam.ac.uk/ioa/research/lensedquasars/

1 for non-variable components, but we also note that for magnitudes at the single-epoch limiting magnitude for the survey, the photometric uncertainties naturally limit our detection of variability.

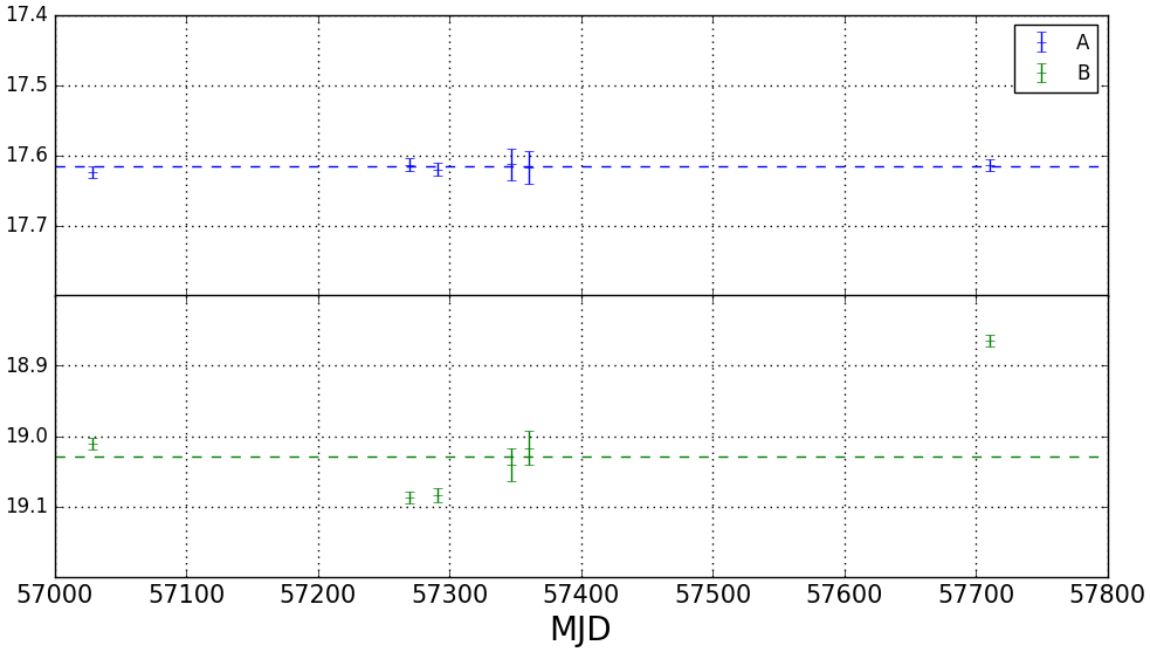

Fig. 5.6 DES z-band lightcurves for the projected star and quasar system DESJ0201-2043, clearly showing variability in the quasar component. Such lightcurves rely only on DES data, and as such are a useful way to remove contaminant systems from spectroscopic follow-up.

Figure 5.8 shows the average reduced χ^2, ${\chi_\nu}^2$, across all measured bands for the two most variable PSF components in a system, for a sample of 15 quasar+star systems, 16 lensed quasars, and 16 quasar pairs (all from STRIDES campaigns). The quasar pair sample may contain lensed quasars with faint, yet currently undetected, lensing galaxies, and are discussed further in Chapter 5.3.3. We expect the variability of the less variable object to be a good indicator of whether the system has only quasar components, or a non-variable quasar component. A cut retaining systems with average reduced $\chi^2 > 3.16$ removes 15 of the 16 stellar contaminant systems, while retaining all lensed quasars. Assuming that we can extend this analysis to all 24 systems we have spectroscopically classified as containing stars with the DES 6-year data, but are not currently able to due to lacking the number of good-fitting epochs in at least three bands, we would expect that the suggested cut can remove 22 systems. This would reduce our contaminant systems to 13, composed of 2 systems with stars, and the rest of star-forming galaxies and quasar-galaxy projections. Our confirmation rate of lensed quasars and quasar pairs would then increase from 34-45% to 51-70%, with the spread due to the inconclusive systems. We note, however, that ULASJ2343-0050 would not pass the

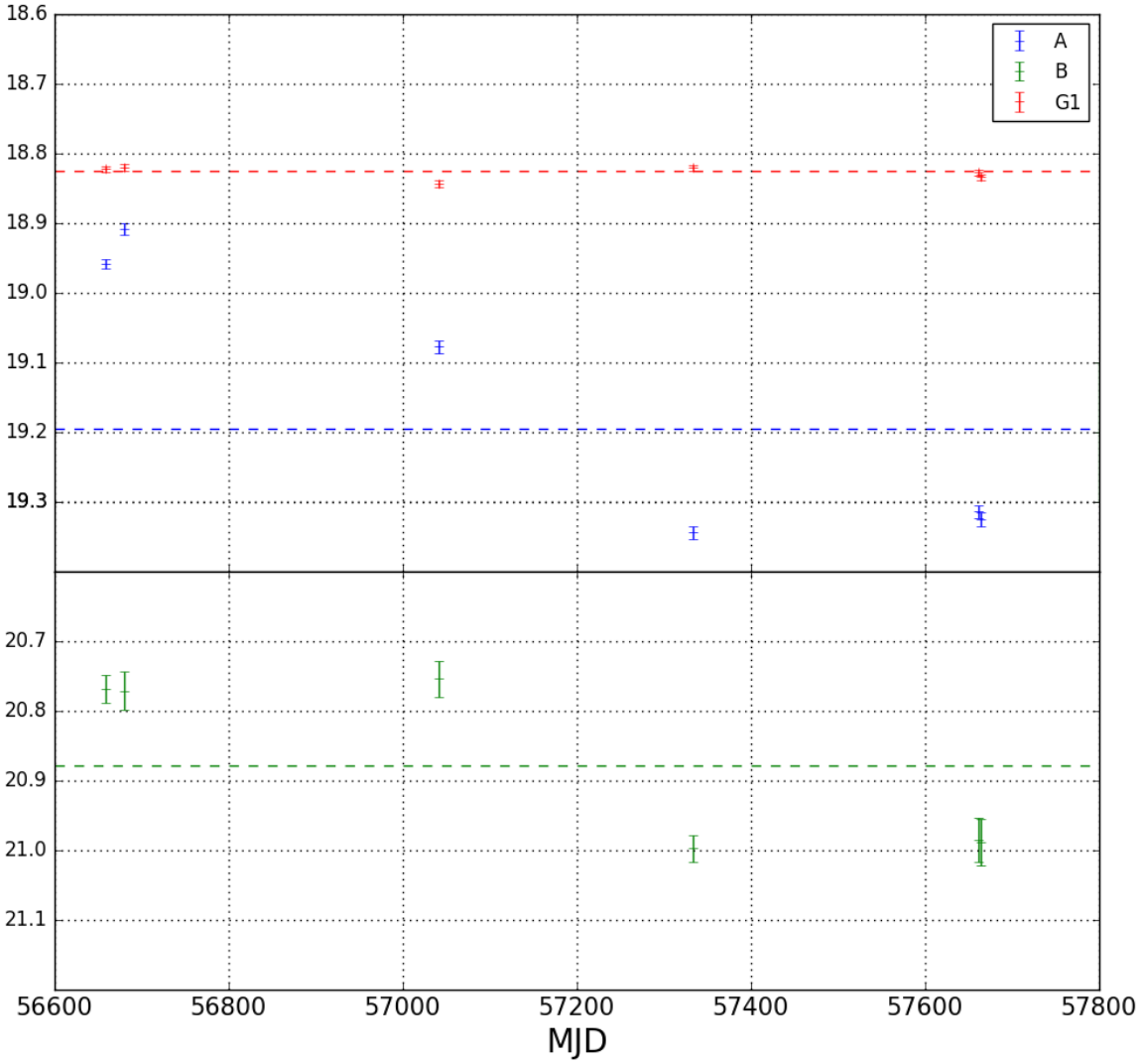

Fig. 5.7 DES *i*-band lightcurves for the lensed quasar system DESJ0150-4041, showing similar variations in the quasar images over a long baseline, and a lensing galaxy with consistent photometry.

variability selection. Further modelling of known lensed quasars will help us understand the limitations of using variability to discover new lensed quasars (see also the discussion in Section 5 of this Chapter).

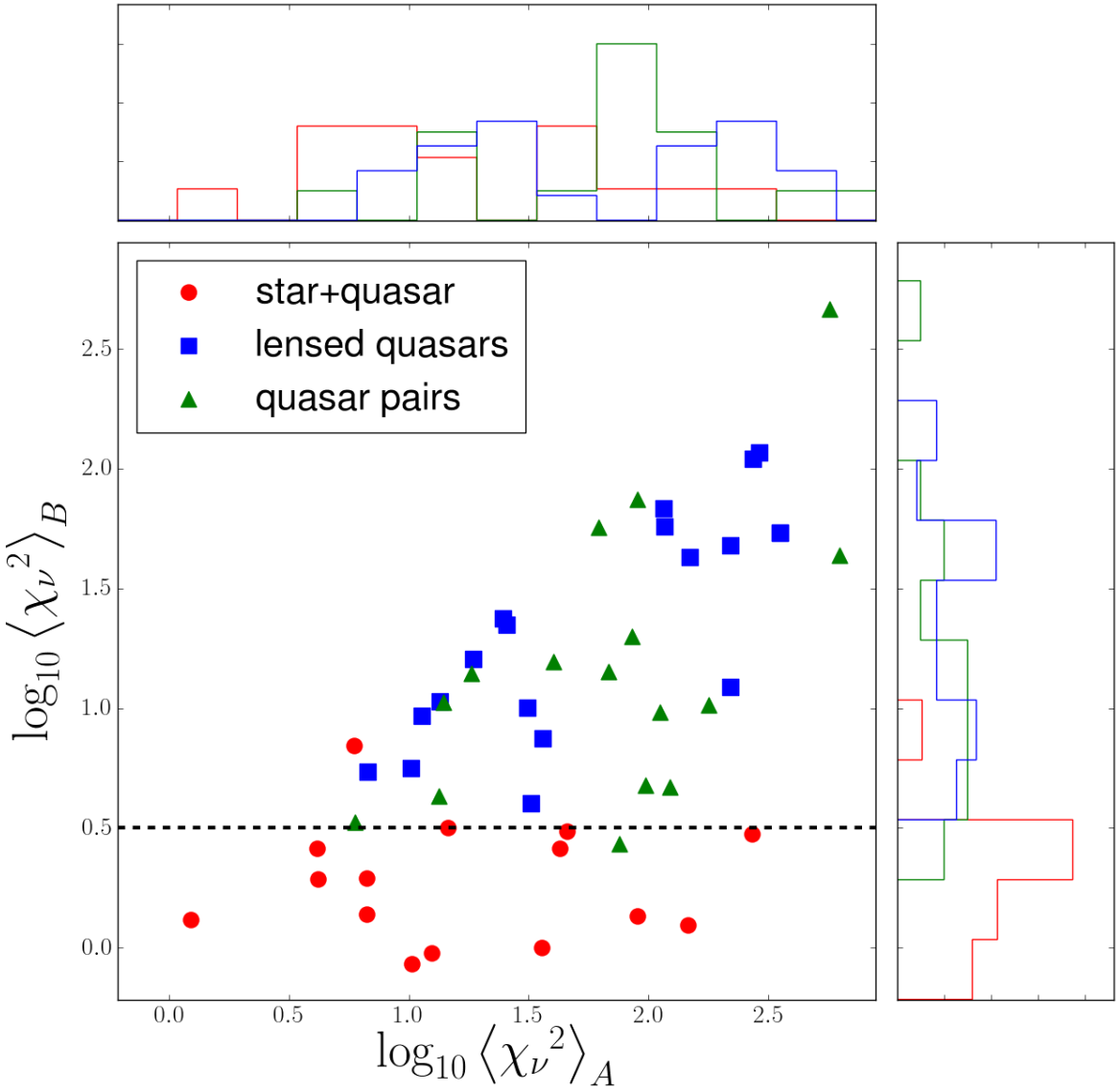

Fig. 5.8 Average reduced χ^2 over all bands containing three or more epochs of reliable photometry over at least two observing seasons. A cut of average $\log_{10}\chi^2$ >0.5 retains all modelled lensed quasars, while removing 94% of the contaminant systems containing stars.

The top histogram of Figure 5.8 shows the variability measure for the most variable component in each system. For the quasar+star pairs this is always the quasar component, and for the lensed quasars, this is generally the brighter image. The unlensed quasars from the quasar+star pairs are less variable than their lensed counterparts. This is not due to the

former set having fainter apparent magnitudes and hence being less significantly variable through the χ^2 statistic, because both sets have similar distributions of observed brightnesses. It is more likely explained by a combination of three factors: (i) the lensing magnification implies the intrinsic magnitudes of the lensed quasar sources are fainter than the counterparts in the quasar+star systems, and less luminous quasars are well-known to vary more (e.g., Hook et al., 1994; Kozłowski, 2016; Li et al., 2018); (ii) lensed quasars are susceptible to additional extrinsic variations through microlensing; and (iii) our unlensed quasar sample has a lower redshift distribution than the lensed quasars. Given that bluer quasar emission is intrinsically more variable, for a given observed wavelength range, a higher-redshift quasar will be more variable. Furthermore, there is a weak trend of increasing variability with increasing redshift at a fixed rest-frame wavelength (Li et al., 2018).

5.3.2 J0235-2433

This doubly imaged lensed quasar was suspected to have an image undergoing a long-term microlensing event due to a large discrepancy between the image flux ratio in the DES and Pan-STARRS data (Chapter 2.3.1). The DES lightcurves corroborate this interpretation. In all bands, image A decreases in brightness by $\sim$0.3mag from Year 2 to Year 4, while image B increases over the first year of this same period by 0.3mag and drops by 0.6mag in the following year. The z- and Y-band lightcurves include an epoch in Year 1, showing the two images are of similar magnitude, while in Year 3 the difference is 0.9mag. If the time delay were comparable to the baseline of our observations, then this could simply be an effect caused by the images sampling the source quasar at entirely different epochs. However, the source redshift is relatively low (z=1.44), the lensing galaxy is particularly bright implying a low redshift, and the separation is modest (2.04 arcseconds). Simple lens models for such systems are expected to have time delays under 50 days, much shorter than the 3 year observation baseline. The Y-band lightcurves (the band with the longest baseline) are shown in Figure 5.9, clearly showing that image B has undergone variations inconsistent with that of image A.

5.3.3 Nearly Identical Quasar Pairs

The Oguri and Marshall (2010) mock catalogue for lensed quasars with bright images, i.e. detected by *Gaia*, predicts $\sim$17% of lensing galaxies will have i-band magnitudes fainter than 22.4, namely a magnitude brighter than the DES DR1 coadd magnitude limit (*MAG_APER*_4, 1.95 arcsecond diameter, S/N=10). We might expect, then, that some of the quasar pairs identified in this work, and previous STRIDES publications, are doubly

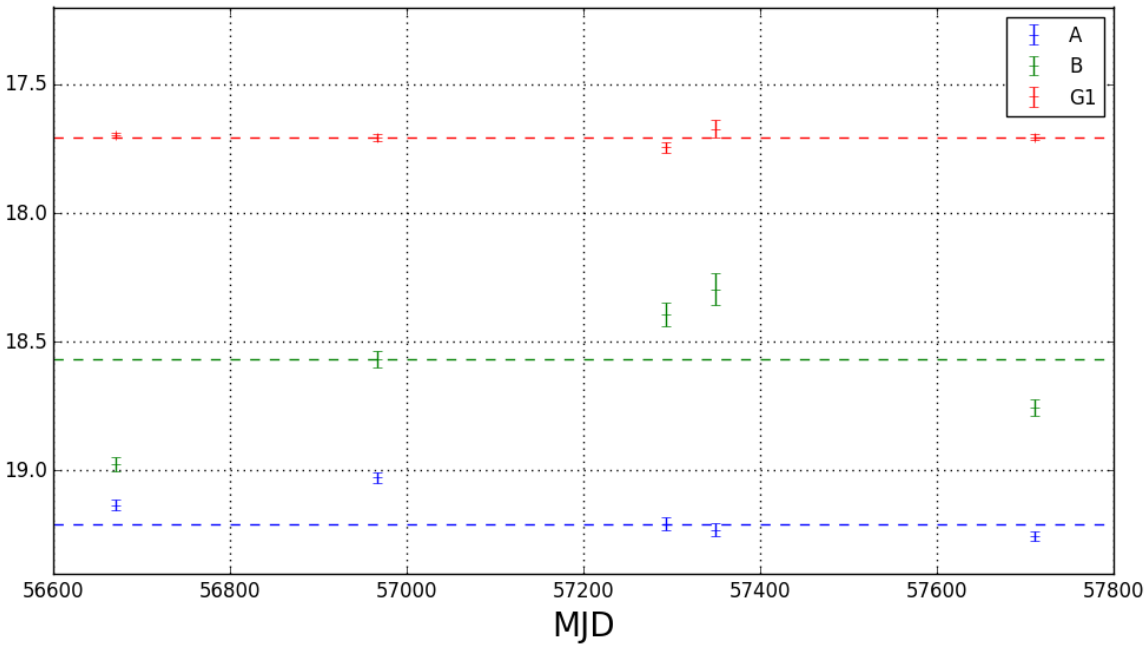

Fig. 5.9 DES *Y*-band lightcurves for the lensed quasar system J0235-2433, showing a likely microlensing event in image A over 3 years. Similar variations are seen in the other bands, and cannot be explained by the time delay difference without invoking multiple large variation and short-lived flares in the source quasar.

imaged lensed quasars. Obtaining deep, high-resolution imaging of all such pairs would be an expensive and potentially inefficient project. However, an indicator of the gravitational lensing hypothesis would be similar long-term variability in the multiple components of a system. Our variability pipeline allows us to consider such objects over a baseline of 4 years.

We model all the newly discovered quasar pairs with components at the same redshift from this work (see Table 2.8) and Anguita et al. (2018). The variability metric described in Section 5.3.1 is plotted for the components of these NIQs in Figure 5.8. They are clearly detected as having multiple variable components, and we might expect that if such systems were lensed quasars, the variability of the images would be similar. However, this neglects the effects of extrinsic variability due to microlensing, difference in time sampling of the true quasar lightcurve due to the time delay, and the different photometric precision due to flux differences. We inspect each pair's lightcurves, looking for similar long term variability, taking into account a possible time delay causing a shift in the variability. Candidates showing similar variability are DESJ0229+0320 (Figure 5.10) and DESJ2215-5204 (based only on 2 well-modelled epochs in each band), and those showing seemingly uncorrelated variability are DESJ0122+0358 and DESJ0313-2546. We warn that extrinsic variability,

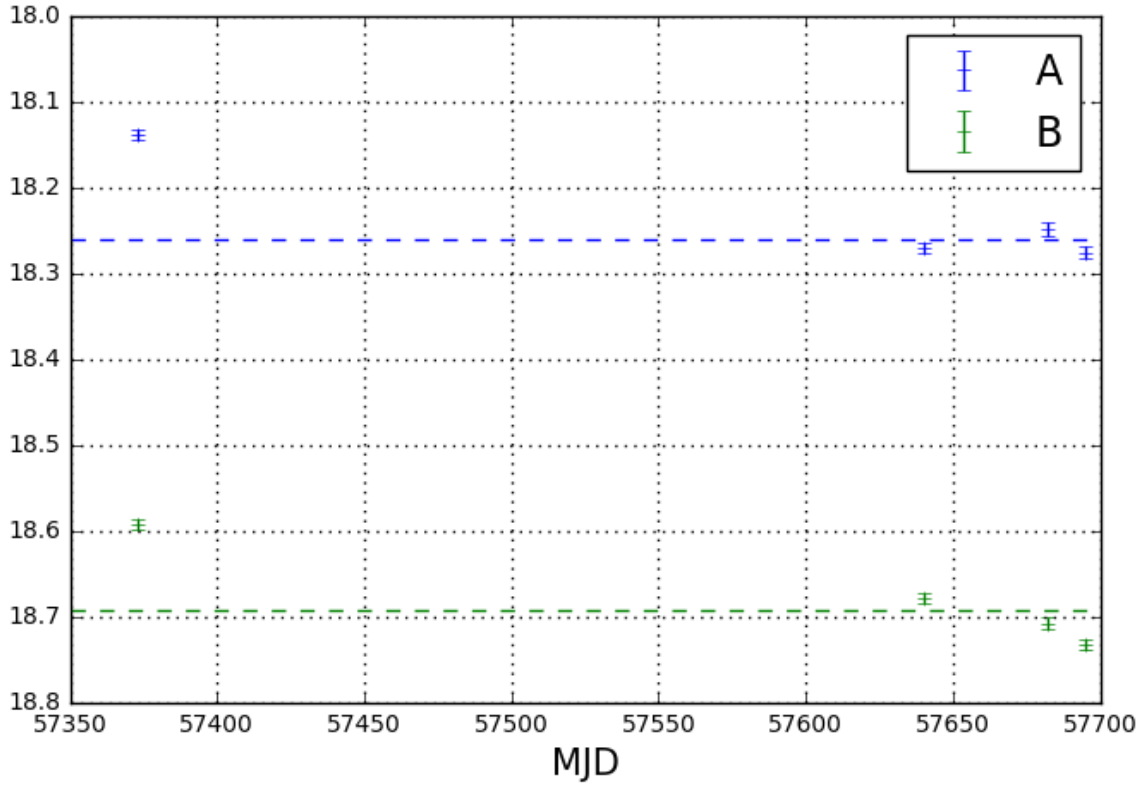

Fig. 5.10 DES *i*-band lightcurves for the components of J0229+0320, showing similar long-term variations. However, no lensing galaxy is seen in the stacked residuals suggesting a high-redshift lens or chance similar variations.

sampling differences due to the time delay, and chance correlations in distinct quasars could confuse the signs of lensing.

5.4 Variability Selection Bias

Our lightcurves have currently only been used to demonstrate the proof of concept of using variability to efficiently discover lensed quasars. Applying such a routine to all close pairs in DES is unfeasible due to the input time required by the user (e.g., from selecting PSF stars or inspecting residuals). Kochanek et al. (2006) suggested difference imaging would be an efficient way to select lensed quasars as extended variable objects. We did not implement such a pipeline since a good understanding of the PSF is required, and for DECam images we had to infer this from the data. We expect difference imaging will become an effective way to find lensed quasars as full focal plane PSF modelling is being pursued in weak lensing

studies. This naturally raises the question of selection effects from selecting the most variable systems.

Systems with the faintest intrinsic sources will have the most variable images. For a magnitude-limited survey there is a trade-off between faint sources being more variable, but also having less precise photometry. In practice, therefore, we expect quasar images with brightnesses near the magnitude limit of a survey to only be robustly detected through their variability if they are high-magnification images. This will cause a quad bias. We test these ideas using mock lightcurves for a DES-like survey, and determine how the reduced χ^2 cut from our DES analysis affects the discovered population. We take the OM10 mocks and generate lightcurves using the Damped Random Walk parameters and uncertainties from MacLeod et al. (2010) based on source magnitude and redshift. The photometric uncertainties are estimated based on all our *i*-band measured uncertainties for lensed quasar *i*-band image magnitudes between 18 and 22.5. Typical uncertainties for images with *i*=19, 20, 21, 22, and 23 are 0.01, 0.02, 0.04, 0.15, and 0.77 respectively. We assume a pessimistic cadence of one observation per year to understand the selection effects from mock DES data. The lightcurves are shifted by the relevant time delays and single-epoch magnitudes are sampled. The χ^2 statistic is generated as in Chapter 5.3.1 and a system is counted as discovered if at least two images have χ^2>3.16. In Figure 5.11, the number of quads and doubles passing this criterion is shown after different numbers of epochs. The numbers naturally increase with more epochs. For a 6 year survey like DES, we would expect variability to discover $\sim$54 quads, and $\sim$130 doubles. The middle panel of Figure 5.11 shows these numbers as a fraction of the total number of quads and doubles that have at least two images brighter than the measured 10σ single-epoch *i*-band depth of DES, i.e. 22.78. As expected, the quad fraction is higher due to magnification bias, since the variability of the source does not depend on the number of images produced. Requiring just the two brightest images of quads to be the ones detected for variability does not significantly change the results (as shown by the dashed lines in Figure 5.11), so the higher quad fraction is not due to having more images in quads, and hence having a higher probability of detecting at least two variable images.

The absolute numbers are conservative since we have only used one band. Using the *g*-band would be best for detecting variability, however this is the band for which we have found the PSF most difficult to model. Furthermore, we have only considered intrinsic variations as a method for detecting lensed quasars. Extrinsic variations from microlensing will make these lightcurves more variable, making our estimates more conservative.

This variability bias will have an impact on the subset of lensed quasars that will have their time delays measured via LSST. Early predictions from OM10 suggested up to 3,000 lensed quasars will have measured time delays in LSST. A tested prediction came from the Time

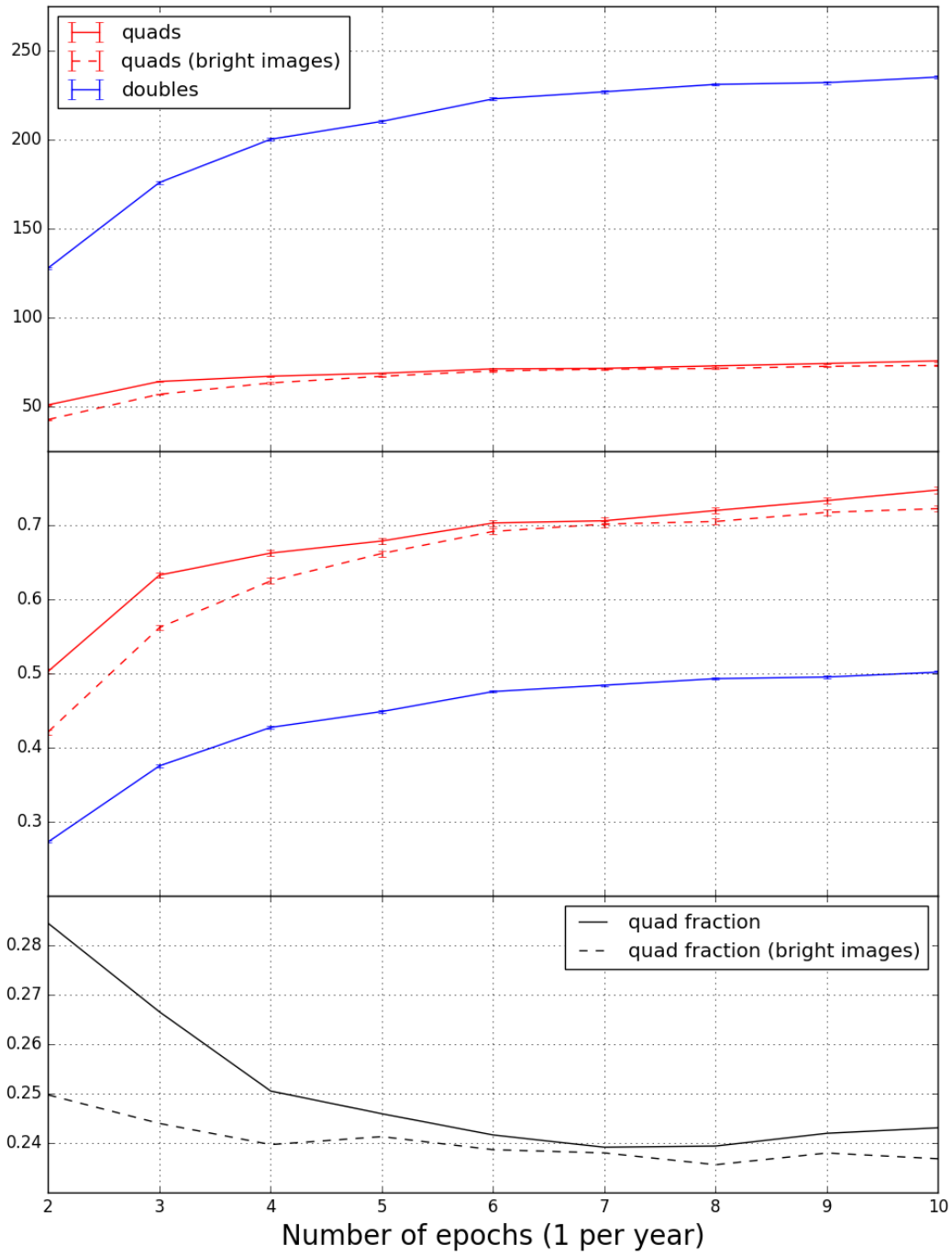

Fig. 5.11 *Top*: number of doubles and quads in 5,000 square degrees passing the variability threshold condition for at least two images given the number of epochs separated by 1 year. *Middle*: fraction of systems compared to all systems with at least two images brighter than the measured single-epoch *i*-band DES depth of 22.78. *Bottom*: quad fraction of lenses expected to be discovered with variability techniques. This is much higher than the magnitude-limited sample of lenses, which would have a quad fraction of $\sim$ 17.7%. Dashed lines for quads are limiting variability detection to just the two brightest images. This reduces the quad fraction by <1% for the DES 6 year survey, implying the magnification bias alone causes a 6% increase in quad fraction over the magnitude-limited sample.

Delay Challenge, which created thousands of mock LSST lensed quasar lightcurves with known time delays, then given to the community for blind time delay retrieval (Dobler et al., 2015; Liao et al., 2015). Based on teams' correct retrievals of time delays, approximately 400 robust measurements will be expected from LSST; however, the mock lightcurves drew variability parameters uniformly from observed ranges, rather than using their correlations with intrinsic luminosity. It is unclear how this would affect the numbers of robust time delay measurements, though the quad fraction within this sample will be higher because of the same causes of variability selection bias.

5.5 Conclusions

We have applied a parametric modelling pipeline (any combination of PSFs and galaxies) to model all available DES single-epoch images of a system in order to extract single-epoch magnitudes. Applying this to known lensed quasars and spectroscopically confirmed quasar+star pairs in the DES footprint, we provide a prescription for removing 94% of the latter from future spectroscopic follow-up campaigns while retaining all lensed quasars. We note that future campaigns targetting a complete sample of lensed quasars with difference imaging techniques—as might be applied to LSST—will need to take into account the variability bias of their search. This will require a good understanding of the variability distribution of the sources, and the magnifications due to realistic lensing galaxies. Current simulations based on DES imaging and cadence from the *i*-band show that such searches will be biased towards high magnification systems (i.e., quads) since there exists a strong anti-correlation between intrinsic luminosity and variability.

Since the Dark Energy Survey has extended its operations to a sixth year, we can soon extend the baseline of these studies by 50%, which will improve the removal of contaminant systems with non-variable stars, the prioritisation of follow-up of quasar pairs as potential lensed quasars, and the detection of lensing galaxies through deeper stacked imaging. Future improvements on extracting variability from single-epoch images requires better point spread function models, possibly through non-parametric reconstructions directly from the data, and an application of difference imaging and/or non-parametric modelling.

Chapter 6

Discussion and Conclusions

In the preceding chapters we have presented techniques for discovery and characterisation of gravitationally lensed quasars in wide-field surveys, making extensive use of *Gaia*'s unique space-based spatial resolution and cataloguing of bright point sources, in combination with modelling of WISE pixels, and further modelling and visual inspection of deep ground-based imaging from DES and Pan-STARRS. Our selection is able to recover over 95% of previously known lensed quasars while still discovering new lensed quasars with greater than 95% efficiency. This is an improvement over previous selection techniques, including those based on initial catalogues of spectroscopically confirmed quasars. The reason for this improvement is due to several factors: (i) *Gaia*'s deblending and ancillary information for close pairs of point sources; (ii) the unexplored areas of sky opened up by new all-sky surveys like *Gaia*, Pan-STARRS, and DES; (iii) the detailed modelling of optical pixels from such surveys before spectroscopic follow-up to prioritise candidates showing possible lens galaxy residuals after point source subtraction; and (iv) extending SED comparison to infrared wavelengths by modelling unWISE pixels with *Gaia* positional information. In this Chapter we compare our sample of new lensed quasars to known lensed quasars to identify any differences between the two sets. We then compare to an ideal mock catalogue of lensed quasars, and finally discuss prospects for future searches and conclude this thesis.

6.1 Comparison to Known Lenses

The current catalogue of all confirmed lensed quasars contains 266 systems. We divide these into three categories: lenses discovered in this thesis (105), previously discovered lenses with at least one *Gaia* detection (126), previously discovered lenses with no *Gaia* detections (35). This final category consists mostly of radio-selected lensed quasars, and some fainter systems from the BOSS quasar lens search (More et al., 2016). We will compare the simple properties

of image brightness, image separation, and source redshift for the first two samples. Such a comparison will elucidate selection effects of our sample or previous samples.

Figure 6.1 shows image separation against source redshift for our sample and previously known lenses with *Gaia* detections. There are 2 optically bright systems with image separations above 9" that are not shown on this plot: SDSSJ1029+2623 (Inada et al., 2006) and SDSSJ1004+4112 (Inada et al., 2003). For our lenses and the previous lens sample, the median source redshifts are z=1.85 and z=1.87, and median image separations are 2.04" and 1.70" respectively. The source redshift distributions show that the previous lens sample has a strong peak at $1.5 < z < 1.75$, and quickly drops for $1.75 < z < 2.00$. This variation cannot be attributed to selection bias since SDSS quasar selection was mostly incomplete for the redshift ranges $2.4 < z < 2.9$ and $3.5 < z < 4.5$ (Richards et al., 2002).

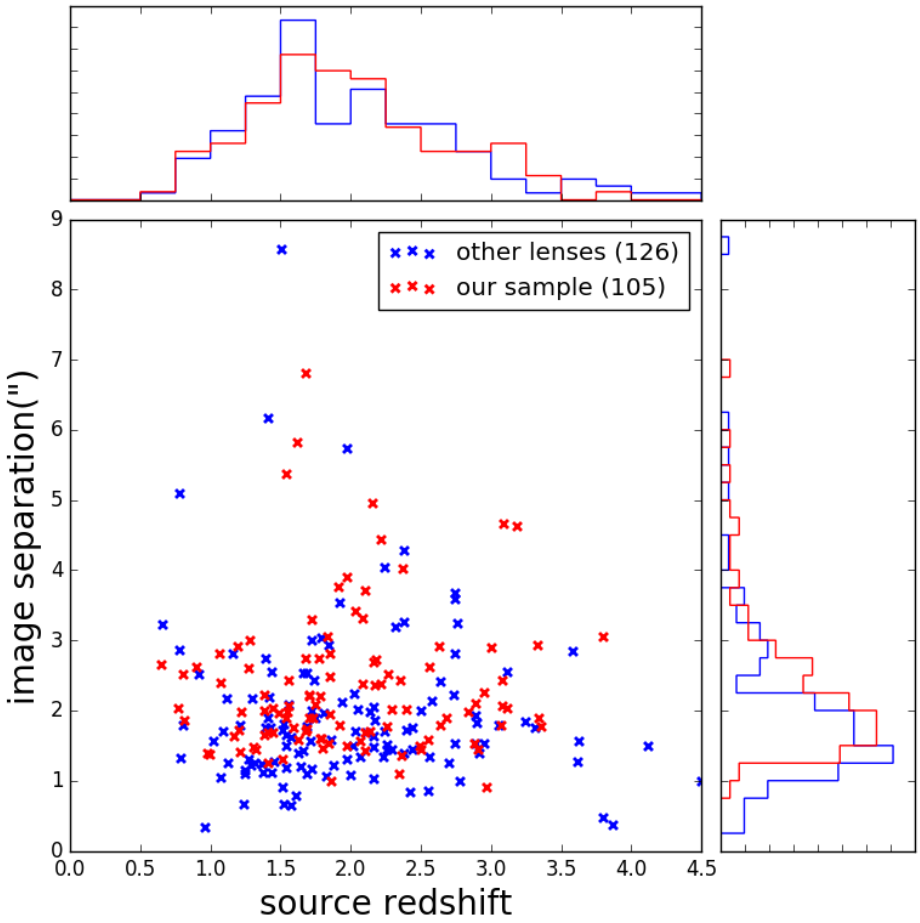

Fig. 6.1 Image separation against source redshift for our *Gaia*-selected sample and for all other lensed quasars with at least one *Gaia* detection. The separations of other lenses extends to smaller separations than our sample.

The image separation distribution of our sample is shifted higher than the previous lens sample. The previous lens sample extends to smaller separations due to the early follow-up of bright quasars, which contain many lenses due to magnification bias, and with more at small separations (since magnification does not vary with image separation). These sub-arcsecond lenses include APM08279+5255, Q1208+101, HE0512-3329, HE1113-0641, and HS0810+2554. Our sample is constructed by having visible lensing galaxies in ground-based imaging datasets, or, much less frequently, by having an arrangement of 4PSFs in a quad-like arrangement. However, the lensing galaxy brightness is strongly correlated with image separation because galaxy brightness and galaxy mass are correlated, and galaxy mass and image separation are correlated. This lens galaxy brightness-image separation correlation is shown in Figure 6.2 for all OM10 mocks that would pass a multiple *Gaia* detection condition (though the source brightness is not dependent on the plotted parameters). The number of lenses with separations between 0.5" and 1" compose 31% of the sample, but considering just lensed quasars with galaxies with $i < 20$, the fraction with image separations between 0.5" and 1" drops to just 2.3%. These results are further validated by the fact that the two smallest separation lenses in our sample are quads without obvious lensing galaxies: J0803+3908 (0.91") and J0608+4229 (1.10").

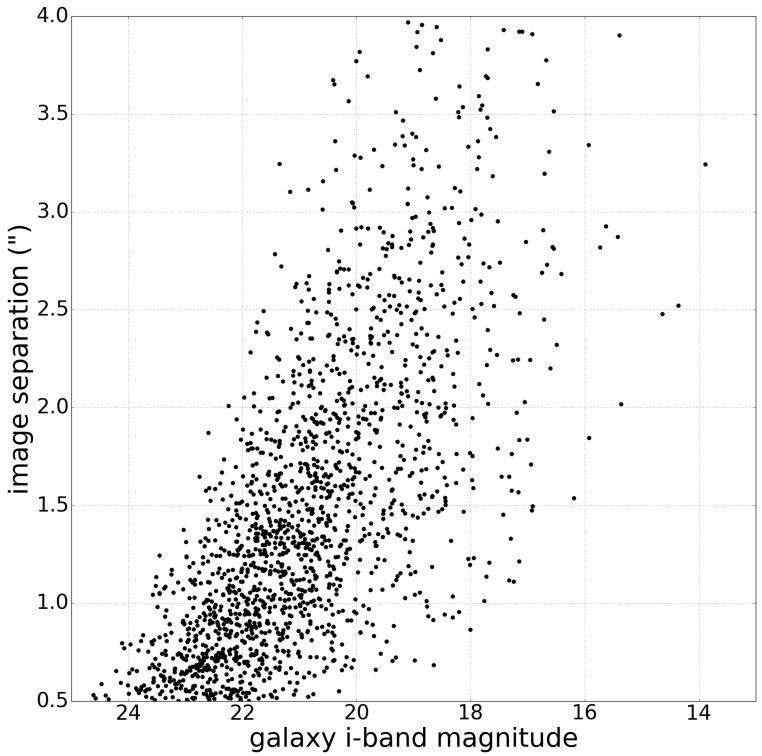

Fig. 6.2 Image separation against lensing galaxy *i*-band magnitude for OM10 mocks with multiple images detectable by *Gaia*.

Figure 6.3 shows the G-band magnitude of the brightest quasar image detected by *Gaia* against source redshift for the two samples. The median G-band magnitudes for our sample and the previous lens sample are G=19.48 and G=18.79 respectively. This difference is expected since the brightest lensed quasars across the sky have generally been early serendipitous discoveries (e.g., Walsh et al., 1979) or well-mined from spectroscopic quasar surveys. These bright lenses should also have a higher quad fraction. Indeed, the quad fractions for the two samples are 11.2% and 26.2% respectively. We note this is not indicative of our selection technique, since we recover the quads from the latter sample, but is purely due to extending our selection to fainter magnitudes for which the quad fraction drops, while other searches (including serendipitous discoveries) have been biased towards finding quads.

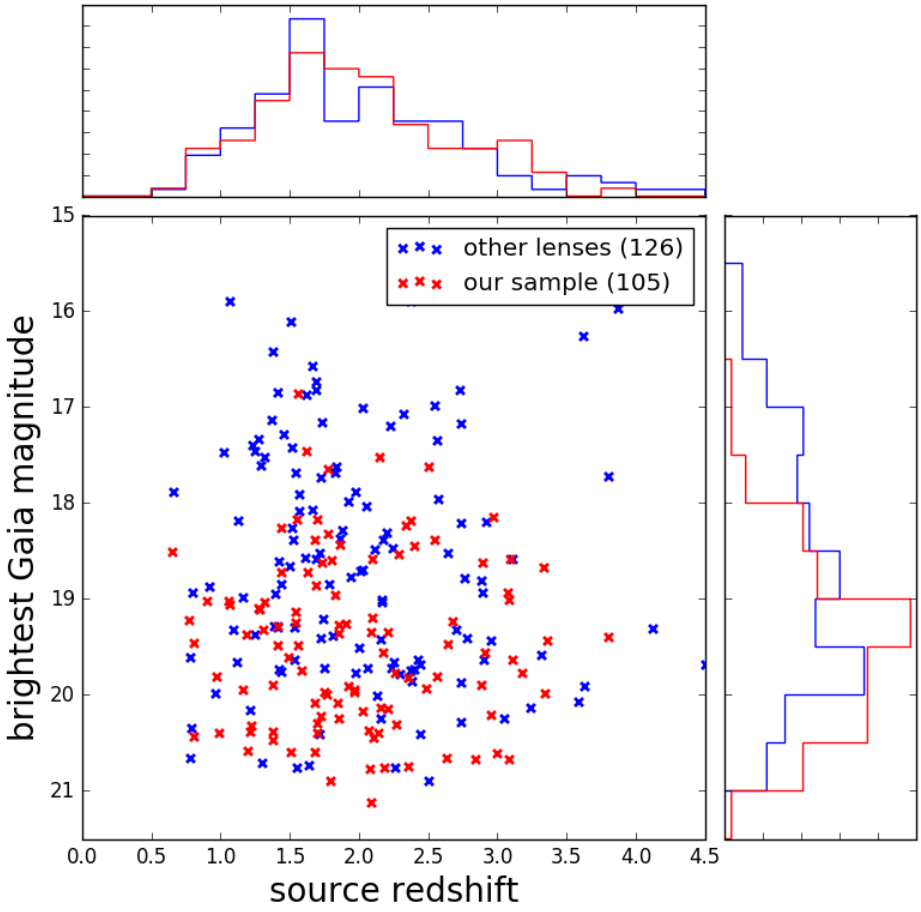

Fig. 6.3 Brightest *Gaia* detection magnitude against source redshift for our *Gaia*-selected sample and for all other lensed quasars with at least one *Gaia* detection.

6.2 Comparison to Mock Lenses

Since previous lens samples might themselves be biased, we now consider how the currently known lensed quasars compare to a complete sample of mock lensed quasars from OM10. Importantly, we can compare absolute numbers in different parameter bins to evaluate the completeness of our selection. We include previously known lensed quasars with multiple *Gaia* detections since our search criteria recover these. We already understand that our sample is biased towards larger image separations and brighter lensing galaxies than a complete sample, given the discussion in Chapter 4.4. We consider a fair sample of lenses that we would wish to discover completely using multiple *Gaia* detections to be those with image separations between 1" and 4". We must also decide what area of sky to consider for comparison to mock numbers. Our searches have focused primarily on lens candidates visible from the WHT ($28^\circ45'38''$N), i.e., the Pan-STARRS footprint, so we take our search area to be 30,939 square degrees. However, we have not searched the entirety of this footprint, and our search area has not been well-defined throughout this thesis, since we have used different local *Gaia* density thresholds for different searches. For simplicity we choose $|b|>15$, which reduces the search area to 23,549 square degrees (76.1% of Pan-STARRS has $|b|>15$). These criteria retain 107 known lensed quasars (93 doubles, 14 quads), with at least two (three) images with G < 20.7 for doubles (quads). From the mock sample with the same sky area, we retain 271 ± 3 lensed quasars (219 doubles, 52 quads).

We plot the image separation against source redshift for these two samples, for doubles in Figure 6.4, and quads in Figure 6.5. For the doubles, searches have now discovered almost all lensed quasars with source redshifts below z=1.5. However, at redshifts above this there is a clear discrepancy as the density of known doubles decreases with redshift, whereas that of mock lenses continues to increase to z=2.5. We can explain this through the anti-correlation between source redshift and lensing galaxy brightness, as seen in Figure 4.23. Since our searches have been biased towards lenses with bright lensing galaxies, detectable in Pan-STARRS/DES imaging, we are biased towards lower-redshift sources. Further biases from SDSS quasar lens searches such as SQLS are present since their initial spectroscopic quasar catalogue was restricted to $z < 2.2$ quasars. The known doubles seem to be $\approx$70% complete at image separations above 1.5" and become severely incomplete at smaller separations. This is because of the correlation between image separation and lens galaxy brightness, and, again, our bias towards following up lensed quasars with obvious lensing galaxies.

For the quad comparison, though the numbers are much smaller, it is clear that the completeness as a function of source redshift is less biased than for the doubles. This is because bright lensing galaxies are not needed to identify quads—three or four *Gaia* detections for a photometric quasar warrants modelling and spectroscopic follow-up. Bright

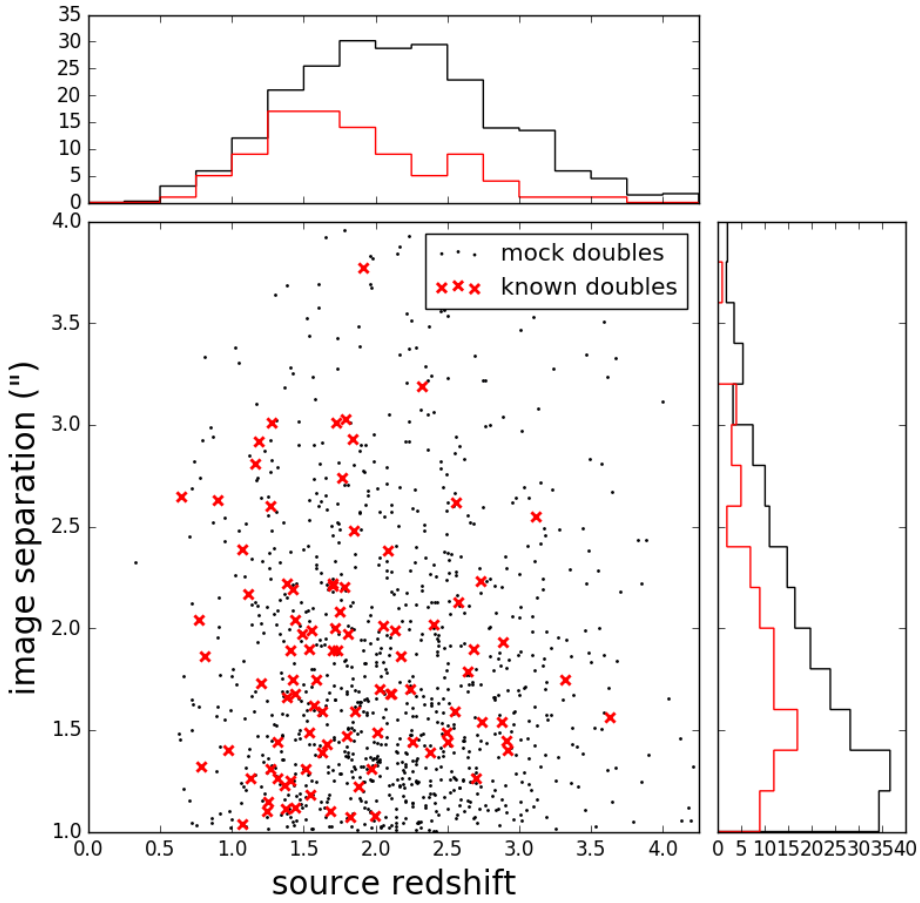

Fig. 6.4 Image separation against source redshift for doubles with image separations between 1" and 4", two *Gaia* detections with G<20.7, and $|b|$>15. Mocks from the OM10 catalogue with the same selection criteria are shown. The predicted number of doubles in this area is ∼219, while the known number is 108.

lensing galaxies are needed to efficiently identify doubles. The known quads are likely complete towards the larger separations (above 2.5"), though there is a large deficiency at smaller separations. This difference is perhaps surprising as the requirement of three *Gaia* detections should be a relatively efficient and complete way to identify the missing ≈30 quads. We explain this discrepancy with two ideas. Firstly, of the three brightest images in quads, one is always a saddle point and is often much fainter than smooth mass models (as used by OM10) predict (Schechter and Wambsganss, 2002). For some quads, this will dim the image below the *Gaia* threshold. Secondly, even though these image separations are above 1", this is the maximum image separation for the known lenses, or twice the Einstein radius in the case of the mocks. Therefore, there are certainly pairs of images within the quads which are separated by much less than this, and often less than the *Gaia* DR2

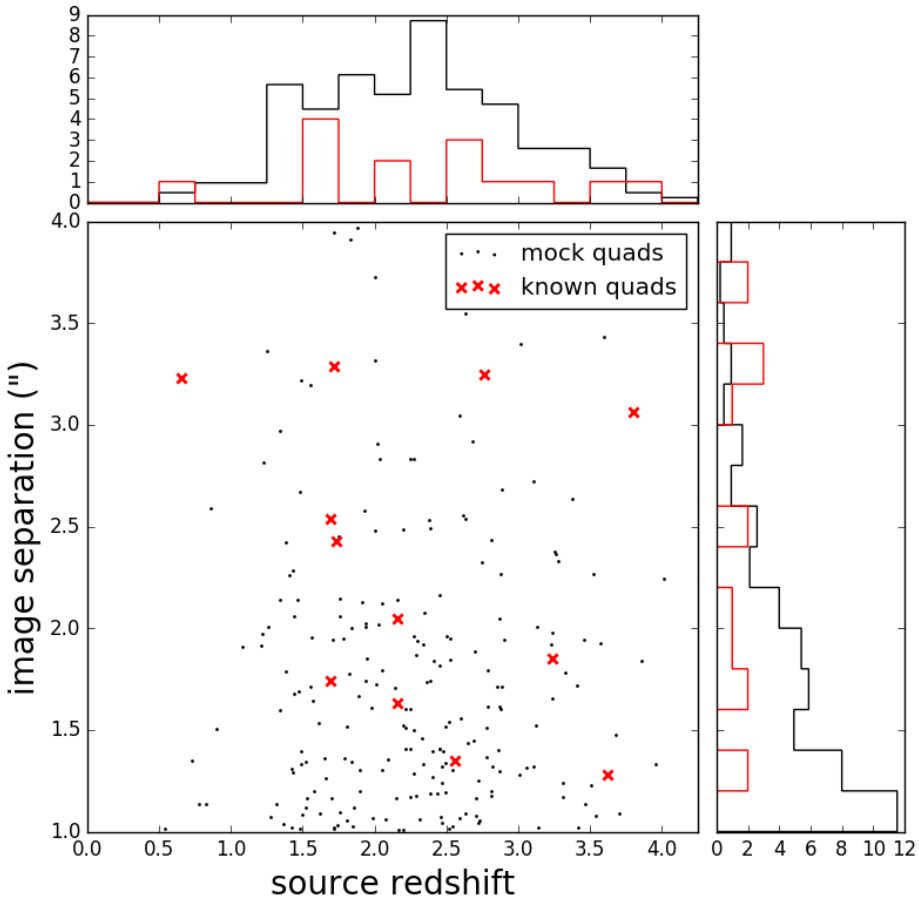

Fig. 6.5 Image separation against source redshift for quads with image separations between 1" and 4", at least three *Gaia* detections with G<20.7, and $|b|$>15. Mocks from the OM10 catalogue with the same selection criteria are shown. The predicted number of quads in this area is ∼52, while the known number is 22.

completeness limit of ∼0.5". By calculating the individual pair separations between the *Gaia*-detected images in the mocks and requiring at least three images all separated from each other by > 0.5", we retain only 40 quads. Even with microlensing, we are far from the observed number of 14 quads. The remaining discrepancy might be due to a larger separation required for completeness for quads due to the increase in local crowding. The 0.5" limit was reported just for binary stars (Arenou et al., 2018). We know of several quads with bright images *Gaia* could detect and are separated from the nearest image by over 0.5" but which are not catalogued. For example, HS0810+2554 has a bright image 0.8" from the nearest image, yet it is not in the GDR2 catalogue.

Finally, we compare the brightness of the images between our known lens sample and the mock sample. Figure 6.6 shows the second brightest image *Gaia* magnitude against

that of the brightest image. Current lenses are incomplete for brightest images fainter than G=17.5. The distribution of flux ratios between the mocks and known lenses appears similar, though the main discrepancy is due to systems with second brightest images with G<20.0, constituting 95 of the "missing" lenses (recalling 271 are predicted, while 107 are known).

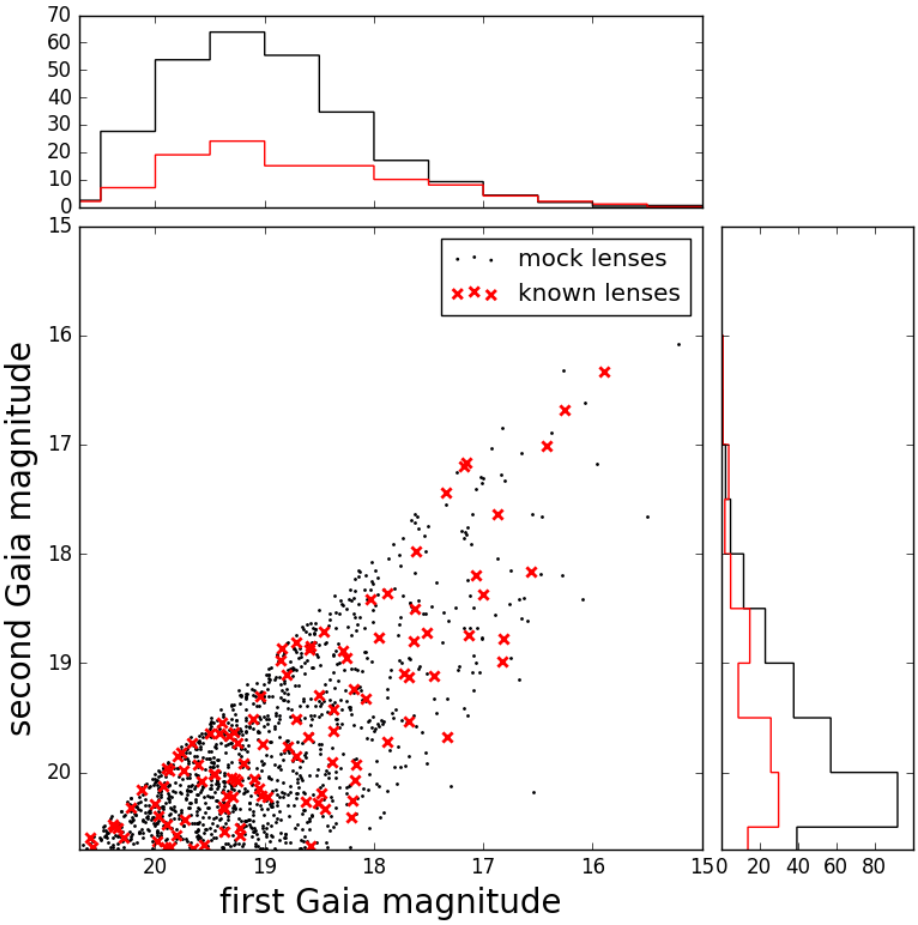

Fig. 6.6 Second brightest *Gaia* magnitude against brightest *Gaia* magnitude for known lensed quasars and the OM10 mock catalogue.

The incompletenesses and biases in our current lens sample are due to limited follow-up rather than bias in the selection method. Fainter lensing galaxies would make infrared SED comparison more robust and such lenses would be recovered by our selection, but we are limited by the available spectroscopic follow-up time. To create a statistical sample of lensed quasars from *Gaia* would require more rigorous selection criteria that can be applied to mock lensed quasars to fully understand our selection function. This would require an application of the *Gaia* detection, deblending, source extraction, and cataloguing routines considering scan angles and the realistic crowding of fields. A simpler route to a complete sample is to consider sources for which we know *Gaia* is complete, i.e., by considering wide-separation

doubles in regions of the sky with low stellar density (to fully trust the detection algorithm of *Gaia*). Such a selection has the added benefit that the lensing galaxies are bright and lens redshifts are more easily determined, which are crucial to the constraining power of image-separation statistics (Oguri et al., 2012).

6.3 Prospects for Future Searches

6.3.1 *Gaia*

At the time of writing, *Gaia* has only released 22 months of data from its nominal 60 month mission. Our analysis of known lensed quasars shows that *Gaia* is cataloguing all images of doubly imaged quasars down to $\sim$0.7", but it is still not cataloguing all images of quads. These missing quad images are likely detected by *Gaia* but are being given truncated windows that have not been released in GDR1 or GDR2. It is unclear whether they will be released in GDR3; nonetheless, the extra information from scan angles will improve completeness of quad image detection in any future data releases. With inclusion of the truncated windows, we expect that simple searches based on three or four *Gaia* detections around photometric and spectroscopic quasars should yield between 10 and 30 new, bright quads above 1" separation. This improved detection rate will naturally increase the number of contaminant systems; however, these are rarer and modelling based on purely *Gaia* information appears to be a promising way of determining whether positions and fluxes are consistent with lens models (Delchambre et al., 2018; Krone-Martins et al., 2018; Schechter and Wynne, 2019; Wynne and Schechter, 2018). The final *Gaia* data release will allow a reconstruction of two-dimensional images from the downloaded one-dimensional line spread functions, due to each having a different scan angle. This will allow for searches of images fainter than the *Gaia* catalogue limit, and also for characterisation and detection of the lensing galaxy or lensed quasar host galaxy, with a pixel scale of 0.06". A forward model will allow for reliable deblended single-epoch photometry from *Gaia*, and hence sparsely sampled lightcurves over a 5 year baseline. This will in turn provide useful information on characterising NIQs through similar variability, and prioritisation of highly variable systems for time delay monitoring. For the many expected lenses with small separations, the small time delays will allow characterisation of purely extrinsic variations, and ensemble modelling of several hundred lenses could provide competitive constraints on microlensing statistics before LSST.

6.3.2 Variability

Chapter 5 demonstrated the usefulness of variability information in a lensed quasar search. However, in our analysis we used a parametric model for each system, with user input of number of PSFs and galaxies. Thus our application is limited to a final-step prioritisation rather than a blind search within the whole of the DES footprint. Ideally, difference imaging would be used and any extended variable object would be flagged as a lensed quasar candidate. This removes contamination from any extended components which should remain constant in magnitude, but requires an accurate model of the PSF. In practice, we have found it difficult to find a PSF model for the quasar images based on nearby stars that fits the data to the noise, and often rely on inferring it from the lens candidate data. Weak lensing analyses also rely on good knowledge of the PSF, and developments within the DES weak lensing team of a PSF modelled on the full focal plane of each observation should offer a promising method to discover lensed quasars through variability alone. This technique will remove many of the biases from colour-cut based searches. In particular it will find the very rare, but perhaps more physically interesting, lensed quasars with high redshift sources and/or low redshift lensing galaxies.

Pan-STARRS data release 2 (Flewelling, 2018) provides single-epoch images for three quarters of the sky, with 5-10 epochs per band. A difference imaging search can therefore also be applied to Pan-STARRS, over a much wider area, albeit at a brighter magnitude limit than DES. Since this sort of search has only been applied once before, and to a small area of sky (Lacki et al., 2009), the density and types of contaminants are unclear, and will likely require strict data quality cuts.

By the mid-to-late 2020s, LSST will have provided deep and sufficiently high cadence imaging of the whole southern sky to find lensed quasars through variability and even to measure time delays. Liao et al. (2015) showed that we should expect at least 300 robust time delay measurements from LSST lightcurves of lensed quasars. As discussed in Chapter 5, variability selection effects from difference imaging will bias discoveries towards lens systems with large magnifications because intrinsically less luminous sources are more variable.

6.3.3 Machine Learning

Several recent lens discovery efforts have focused on using machine learning to identify lensed galaxies from image pixels. There is often more information in lensed galaxy pixels due to the extended arcs, compared to lensed quasars where often just two point sources are present, and thus the contaminants are different. Nonetheless, we should consider the

applicability of such an approach to mining lensed quasars beyond current methods. Jacobs et al. (2017) and Jacobs et al. (2019) have searched CFHTLS and DES, respectively, for strong lenses using convolutional neural nets. Such searches can be tuned to a certain purity/completeness trade-off, with the DES searches finding 88 likely lenses after visual inspection of 16,729 cutouts with an expected completeness of over 50% for the magnitude and source redshift range.

Gradient-boosted trees have been explored as a way to discover lensed quasars via pixel pattern recognition with estimates of a purity of 70 % and a completeness of 60 % at visual inspection (Agnello et al., 2015a), but the results are not borne out in practice with much higher contamination rates (Agnello et al., 2015b). These poor results are due to bright doubles masking any contribution from the lens features, especially when the image separation is comparable to the PSF FWHM of the imaging data. It is then impossible to distinguish these systems from star+quasar projections. Wide-separation quads are usually easy to identify, but again, at smaller separations the blending makes the systems appear very similar to star-forming galaxies.

Figure 6.7 shows two contaminant systems and two lensed quasars with particularly similar configurations and optical colours. Without modelling the pixels for exact SEDs or using extra information such as *Gaia* proper motions or modelled WISE colours, it is not possible to separate contaminants from lenses. These modelling steps will be necessary even after selection via machine learning on pixels.

Furthermore, while automated approaches will be required to find the majority of lensed quasars, visual inspection is still required, as evidenced by Metcalf et al. (2018), in which simulated lenses were injected into real KiDS data. Only human inspection was able to identify the single multiple-source lens in the sample.

6.3.4 Other Datasets

Ongoing spectroscopic surveys of quasars will help identify large numbers of potential lensed quasars, with automatic removal of star-forming galaxy contaminants (as SDSS quasar lens searches started from). For example, SDSS V will take spectra of over 400,000 X-ray bright quasars (based on eROSITA selection), WEAVE-QSO will take spectra of over 400,000 z>2 quasars, DESI will take spectra of over 2.5 million quasars, and 4MOST will obtain over 10 million low-resolution spectra of galaxies and active galactic nuclei. Since the lensing galaxy brightness is independent of source brightness, and since current searches are finding lenses with bright images, future searches will enter a new regime where the lensing galaxy magnitude dominates the flux of the lens system (see Figure 1.11). Spectroscopic galaxy

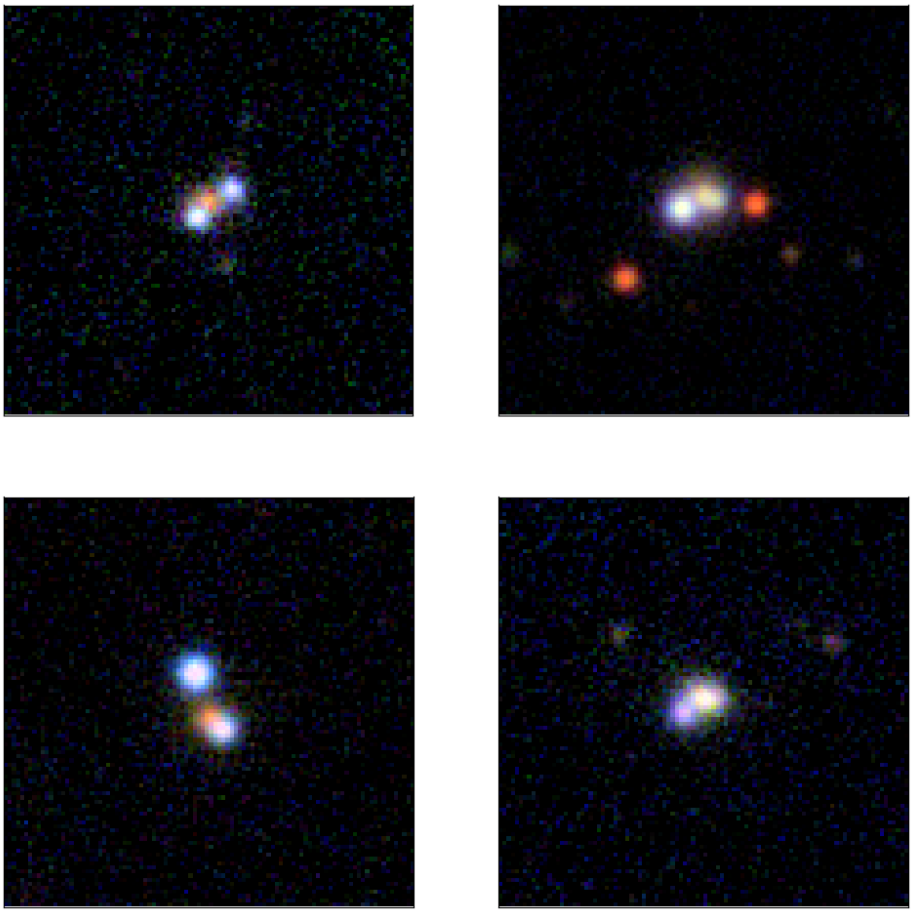

Fig. 6.7 *Top row*: contaminant systems with stars and quasars; *bottom row*: confirmed gravitationally lensed quasars. The optical data alone cannot distinguish lensed quasars from contaminants, and hence the need for ancillary information from *Gaia* or other wavelengths will be necessary.

surveys are therefore likely to uncover most of the new lensed quasars through searching for blended emission lines from a background quasar.

We also note that searches targetting high-redshift lensed quasars will become possible due to Euclid, LSST, and 4MOST, with careful consideration of the possible effects of lensing galaxies on the photometry (Fan et al., 2019; Pacucci and Loeb, 2019).

References

Abazajian, K.N. et al (2009). The Seventh Data Release of the Sloan Digital Sky Survey. ApJS, 182:543–558.

Abbott, B.P. et al (2016). Tests of General Relativity with GW150914. Phys. Rev. Lett., 116:221101.

Abbott, T.M.C. et al (2018). The Dark Energy Survey: Data Release 1. *The Astrophysical Journal Supplement Series*, 239:18.

Agnello, A. (2017). Quasar lenses and galactic streams: outlier selection and Gaia multiplet detection. MNRAS, 471:2013–2021.

Agnello, A. et al (2018a). Discovery and first models of the quadruply lensed quasar SDSS J1433+6007. MNRAS, 474:3391–3396.

Agnello, A. et al (2015a). Data mining for gravitationally lensed quasars. MNRAS, 448:1446–1462.

Agnello, A. et al (2018b). DES meets Gaia: discovery of strongly lensed quasars from a multiplet search. MNRAS, 479:4345–4354.

Agnello, A. et al (2018c). Quasar lenses and pairs in the VST-ATLAS and Gaia. MNRAS, 475:2086–2096.

Agnello, A. et al (2016). Spectroscopy and high-resolution imaging of the gravitational lens SDSS J1206+4332. MNRAS, 458:3830–3838.

Agnello, A. et al (2015b). Discovery of two gravitationally lensed quasars in the Dark Energy Survey. MNRAS, 454:1260–1265.

Aihara, H. et al (2018). The Hyper Suprime-Cam SSP Survey: Overview and survey design. *Publications of the Astronomical Society of Japan*, 70:S4.

Alam, S. et al (2015). The Eleventh and Twelfth Data Releases of the Sloan Digital Sky Survey: Final Data from SDSS-III. ApJS, 219:12.

Altschuler, D.R. (1986). A 5-GHz survey of radio sources. *Astronomy and Astrophysics Supplement Series*, 65:267–283.

Anguita, T. et al (2018). The STRong lensing Insights into the Dark Energy Survey (STRIDES) 2016 follow-up campaign - II. New quasar lenses from double component fitting. MNRAS, 480:5017–5028.

Arenou, F. et al (2018). Gaia Data Release 2: Catalogue validation. *ArXiv e-prints*.

Arenou, F. et al (2017). Gaia Data Release 1: Catalogue validation. *ArXiv e-prints*.

Auger, M.W. (2008). The environments of SLACS gravitational lenses. MNRAS, 383:L40–L44.

Auger, M.W. et al (2009). The Sloan Lens ACS Survey. IX. Colors, Lensing, and Stellar Masses of Early-Type Galaxies. ApJ, 705:1099–1115.

Auger, M.W. et al (2010). The Sloan Lens ACS Survey. X. Stellar, Dynamical, and Total Mass Correlations of Massive Early-type Galaxies. ApJ, 724:511–525.

Bade, N. et al (1997). RX J0911.4+0551: A new multiple QSO selected from the ROSAT All-Sky Survey. A&A, 317:L13–L16.

Baranec, C. et al (2014). Second generation Robo-AO instruments and systems. In *Adaptive Optics Systems IV*, volume 9148 of *Society of Photo-Optical Instrumentation Engineers (SPIE) Conference Series*, page 914812.

Bartelmann, M. and Schneider, P. (2001). Weak gravitational lensing. Phys. Rep., 340:291–472.

Bate, N.F. et al (2011). A Microlensing Measurement of Dark Matter Fractions in Three Lensing Galaxies. ApJ, 731:71.

Belokurov, V. et al (2016). Clouds, Streams and Bridges. Redrawing the blueprint of the Magellanic System with Gaia DR1. MNRAS.

Berghea, C.T. et al (2017). Discovery of the First Quadruple Gravitationally Lensed Quasar Candidate with Pan-STARRS. ApJ, 844:90.

Bertin, E. (2011). Automated Morphometry with SExtractor and PSFEx. In Evans, I.N. et al, editors, *Astronomical Data Analysis Software and Systems XX*, volume 442 of *Astronomical Society of the Pacific Conference Series*, page 435.

Bertin, E. and Arnouts, S. (1996). SExtractor: Software for source extraction. *Astronomy and Astrophysics Supplement Series*, 117:393–404.

Bijaoui, A. (1980). Sky background estimation and application. A&A, 84:81–84.

Birrer, S. et al (2019). H0LiCOW - IX. Cosmographic analysis of the doubly imaged quasar SDSS 1206+4332 and a new measurement of the Hubble constant. MNRAS, 484:4726–4753.

Blackburne, J.A. et al (2011). Sizes and Temperature Profiles of Quasar Accretion Disks from Chromatic Microlensing. ApJ, 729:34.

Bonvin, V. et al (2018). COSMOGRAIL. XVII. Time delays for the quadruply imaged quasar PG 1115+080. A&A, 616:A183.

Borguet, B. and Hutsemékers, D. (2010). A polar+equatorial wind model for broad absorption line quasars. I. Fitting the C IV BAL profiles. A&A, 515:A22.

Burbidge, G.R. and Burbidge, E.M. (1967). Limits to the Distance of the Quasi-Stellar Objects Deduced from Their Absorption Line Spectra. ApJ, 148:L107.

Burke, D.L. et al (2018). Forward Global Photometric Calibration of the Dark Energy Survey. AJ, 155:41.

Burke, W.L. (1981). Multiple Gravitational Imaging by Distributed Masses. ApJ, 244:L1.

Burud, I. et al (2002). Time delay and lens redshift for the doubly imaged BAL quasar SBS 1520+530. A&A, 391:481–486.

Carrasco, J.M. et al (2016). Gaia Data Release 1. Principles of the photometric calibration of the G band. A&A, 595:A7.

Chae, K.H. and Mao, S. (2003). Limits on the Evolution of Galaxies from the Statistics of Gravitational Lenses. ApJ, 599:L61–L64.

Chambers, K.C. et al (2016). The Pan-STARRS1 Surveys. *ArXiv e-prints*.

Chang, K. and Refsdal, S. (1979). Flux variations of QSO 0957 + 561 A, B and image splitting by stars near the light path. Nature, 282:561–564.

Chang, K. and Refsdal, S. (1984). Star disturbances in gravitational lens galaxies. A&A, 132:168–178.

Chen, G.C.F. et al (2016). SHARP - III. First use of adaptive-optics imaging to constrain cosmology with gravitational lens time delays. MNRAS, 462:3457–3475.

Choi, Y.Y., Park, C. and Vogeley, M.S. (2007). Internal and Collective Properties of Galaxies in the Sloan Digital Sky Survey. ApJ, 658:884–897.

Chwolson, O. (1924). Uber eine mogliche Form fiktiver Doppelsterne. *Astronomische Nachrichten*, 221:329.

Colla, G. et al (1970). A catalogue of 3235 radio sources at 408 MHz. *Astronomy and Astrophysics Supplement Series*, 1:281.

Collett, T.E. et al (2017). Core or Cusps: The Central Dark Matter Profile of a Strong Lensing Cluster with a Bright Central Image at Redshift 1. ApJ, 843:148.

Condon, J.J. et al (1998). The NRAO VLA Sky Survey. AJ, 115:1693–1716.

Courbin, F. et al (2018). COSMOGRAIL: the COSmological MOnitoring of GRAvItational Lenses. XVI. Time delays for the quadruply imaged quasar DES J0408-5354 with high-cadence photometric monitoring. A&A, 609:A71.

Courbin, F., Saha, P. and Schechter, P.L. (2002). *Quasar Lensing*, page 1.

Cowan, C.L. (1968). Concerning Redshifts in the Spectra of Quasi-Stellar Objects. ApJ, 154:L5.

Dahle, H. et al (2015). Time Delay Measurements for the Cluster-lensed Sextuple Quasar SDSS J2222+2745. ApJ, 813:67.

Davis, M.M. (1971). The NRAO 5-GHz radio source survey. I. A survey of faint sources. AJ, 76:980–992.

Dawson, K.S. et al (2013). The Baryon Oscillation Spectroscopic Survey of SDSS-III. AJ, 145:10.

de Jong, J.T.A. et al (2013). The Kilo-Degree Survey. *Experimental Astronomy*, 35:25–44.

Deason, A.J. et al (2017). The slight spin of the old stellar halo. *ArXiv e-prints*.

Delchambre, L. et al (2018). Gaia GraL: Gaia DR2 Gravitational Lens Systems. III. A systematic blind search for new lensed systems. *ArXiv e-prints*.

Ding, X. et al (2017). H0LiCOW VII. Cosmic evolution of the correlation between black hole mass and host galaxy luminosity. *ArXiv e-prints*.

DiPompeo, M.A. et al (2015). Quasar probabilities and redshifts from WISE mid-IR through GALEX UV photometry. MNRAS, 452:3124–3138.

Dobke, B.M., King, L.J. and Fellhauer, M. (2007). Steepened inner density profiles of group galaxies via interactions: an N-body analysis. MNRAS, 377:1503–1510.

Dobler, G. et al (2015). Strong Lens Time Delay Challenge. I. Experimental Design. ApJ, 799:168.

Einstein, A. (1936). Lens-Like Action of a Star by the Deviation of Light in the Gravitational Field. *Science*, 84:506–507.

Evans, I.N. et al (2010). The Chandra Source Catalog. *The Astrophysical Journal Supplement Series*, 189:37–82.

Fabian, A.C. (2012). Observational Evidence of Active Galactic Nuclei Feedback. *Annual Review of Astronomy and Astrophysics*, 50:455–489.

Fabricius, C. et al (2016). Gaia Data Release 1. Pre-processing and source list creation. A&A, 595:A3.

Falco, E.E., Gorenstein, M.V. and Shapiro, I.I. (1985). On model-dependent bounds on H 0 from gravitational images : application to Q 0957+561 A, B. ApJ, 289:L1–L4.

Fan, X. et al (2019). The Discovery of a Gravitationally Lensed Quasar at z = 6.51. ApJ, 870:L11.

Finet, F. and Surdej, J. (2016). Multiply imaged quasi-stellar objects in the Gaia survey. A&A, 590:A42.

Flaugher, B. et al (2015). The Dark Energy Camera. AJ, 150:150.

Flesch, E.W. (2015). The Half Million Quasars (HMQ) Catalogue. PASA, 32:e010.

Flewelling, H. (2018). Pan-STARRS Data Release 2. In *American Astronomical Society Meeting Abstracts #231*, volume 231 of *American Astronomical Society Meeting Abstracts*, page 436.01.

Fohlmeister, J. et al (2013). A Two-year Time Delay for the Lensed Quasar SDSS J1029+2623. ApJ, 764:186.

Foreman-Mackey, D. et al (2013). emcee: The MCMC Hammer. PASP, 125:306.

Gaia Collaboration et al (2018). Gaia Data Release 2. Summary of the contents and survey properties. A&A, 616:A1.

Gaia Collaboration et al (2016a). The Gaia mission. A&A, 595:A1.

Gaia Collaboration et al (2016b). The Gaia mission. A&A, 595:A1.

Geller, M.J. et al (2014). SHELS: A Complete Galaxy Redshift Survey with R $\approx=$ 20.6. ApJS, 213:35.

Giannini, E. et al (2017). MiNDSTEp differential photometry of the gravitationally lensed quasars WFI 2033-4723 and HE 0047-1756: microlensing and a new time delay. A&A, 597:A49.

Glikman, E., Helfand, D.J. and White, R.L. (2006). A Near-Infrared Spectral Template for Quasars. ApJ, 640:579–591.

Goicoechea, L.J. and Shalyapin, V.N. (2010). Time Delays in the Gravitationally Lensed Quasar H1413+117 (Cloverleaf). ApJ, 708:995–1001.

Górski, K.M. et al (2005). HEALPix: A Framework for High-Resolution Discretization and Fast Analysis of Data Distributed on the Sphere. ApJ, 622:759–771.

Gott, J. R., I. (1981). Are heavy halos made of low mass stars - A gravitational lens test. ApJ, 243:140–146.

Green, D.A. (2011a). A colour scheme for the display of astronomical intensity images. *Bulletin of the Astronomical Society of India*, 39:289–295.

Green, D.A. (2011b). A colour scheme for the display of astronomical intensity images. *Bulletin of the Astronomical Society of India*, 39:289–295.

Greenstein, J.L. (1963). Red-Shift of the Unusual Radio Source: 3C 48. Nature, 197:1041–1042.

Gruen, D. et al (2015). Characterization and correction of charge-induced pixel shifts in DECam. *Journal of Instrumentation*, 10:C05032.

Hainline, L.J. et al (2013). Time Delay and Accretion Disk Size Measurements in the Lensed Quasar SBS 0909+532 from Multiwavelength Microlensing Analysis. ApJ, 774:69.

Harrison, D.L. (2011). A fast 2D image reconstruction algorithm from 1D data for the Gaia mission. *Experimental Astronomy*, 31:157–175.

Hartley, P. et al (2019). Strong lensing reveals jets in a sub-microJy radio-quiet quasar. MNRAS, 485:3009–3023.

Hazard, C., Mackey, M.B. and Shimmins, A.J. (1963). Investigation of the Radio Source 3C 273 By The Method of Lunar Occultations. Nature, 197:1037–1039.

Hennawi, J.F. et al (2006). Binary Quasars in the Sloan Digital Sky Survey: Evidence for Excess Clustering on Small Scales. AJ, 131:1–23.

Hook, I.M. et al (1994). The Variability of Optically Selected Quasars. MNRAS, 268:305.

Hsueh, J.W. et al (2017). SHARP - IV. An apparent flux-ratio anomaly resolved by the edge-on disc in B0712+472. MNRAS, 469(3):3713–3721.

Huchra, J. et al (1985). 2237+0305 : a new and unusual gravitational lens. AJ, 90:691–696.

Inada, N. et al (2008). The Sloan Digital Sky Survey Quasar Lens Search. II. Statistical Lens Sample from the Third Data Release. AJ, 135:496–511.

Inada, N. et al (2007). Two New Gravitationally Lensed Double Quasars from the Sloan Digital Sky Survey. AJ, 133:206–213.

Inada, N. et al (2006). SDSS J1029+2623: A Gravitationally Lensed Quasar with an Image Separation of 22.5". ApJ, 653:L97–L100.

Inada, N. et al (2003). A gravitationally lensed quasar with quadruple images separated by 14.62arcseconds. Nature, 426:810–812.

Inada, N. et al (2010). The Sloan Digital Sky Survey Quasar Lens Search. IV. Statistical Lens Sample from the Fifth Data Release. AJ, 140:403–415.

Inada, N. et al (2012). The Sloan Digital Sky Survey Quasar Lens Search. V. Final Catalog from the Seventh Data Release. AJ, 143:119.

Inada, N. et al (2009). Five New High-Redshift Quasar Lenses from the Sloan Digital Sky Survey. AJ, 137:4118–4126.

Irwin, M.J. et al (1998). APM 08279+5255: an Ultraluminous Broad Absorption Line Quasar at a Redshift Z = 3.87. ApJ, 505:529–535.

Irwin, M.J. et al (1989). Photometric Variations in the Q2237+0305 System: First Detection of a Microlensing Event. AJ, 98:1989.

Jackson, N. (2013). Quasar lensing. *Bulletin of the Astronomical Society of India*, 41:19.

Jackson, N. and Browne, I.W.A. (2007). Improving efficiency in radio surveys for gravitational lenses. MNRAS, 374:168–175.

Jackson, N., Ofek, E.O. and Oguri, M. (2008). ULAS J234311.93-005034.0: a gravitational lens system selected from UKIDSS and SDSS. MNRAS, 387:741–746.

Jackson, N., Ofek, E.O. and Oguri, M. (2009). A new gravitational lens from the MUSCLES survey: ULASJ082016.1+081216. MNRAS, 398:1423–1427.

Jackson, N. et al (2012). New lensed quasars from the MUSCLES survey. MNRAS, 419:2014–2024.

Jacobs, C. et al (2019). Finding high-redshift strong lenses in DES using convolutional neural networks. MNRAS, 484:5330–5349.

Jacobs, C. et al (2017). Finding strong lenses in CFHTLS using convolutional neural networks. MNRAS, 471:167–181.

Jiménez-Vicente, J. et al (2015). Dark Matter Mass Fraction in Lens Galaxies: New Estimates from Microlensing. ApJ, 799:149.

Keeton, C.R. (2001). Computational Methods for Gravitational Lensing. *ArXiv Astrophysics e-prints*.

Keeton, C.R., Kochanek, C.S. and Falco, E.E. (1998). The Optical Properties of Gravitational Lens Galaxies as a Probe of Galaxy Structure and Evolution. ApJ, 509:561–578.

King, L.J. et al (1999). Gravitationally lensed radio sources in the Jodrell Bank-VLA Astrometric Survey. MNRAS, 307:225–235.

Kochanek, C.S. et al (1997). SBS 0909+532: A New Double Gravitational Lens or Binary Quasar?1,2,. ApJ, 479:678–683.

Kochanek, C.S. et al (2006). A Simple Method to Find All Lensed Quasars. ApJ, 637:L73–L76.

Koposov, S.E., Belokurov, V. and Torrealba, G. (2017). Gaia 1 and 2. A pair of new Galactic star clusters. *ArXiv e-prints*.

Koptelova, E. et al (2010). Intrinsic quasar variability and time delay determination in the lensed quasar UM673. MNRAS, 401:2805–2815.

Korista, K.T. et al (1993). Double Troughs in Broad Absorption Line Quasars and LY alpha –N V Line Locking. *The Astrophysical Journal Supplement Series*, 88:357.

Kormann, R., Schneider, P. and Bartelmann, M. (1994). Isothermal elliptical gravitational lens models. A&A, 284:285–299.

Kostrzewa-Rutkowska, Z. et al (2018). A gravitationally lensed quasar discovered in OGLE. MNRAS, 476:663–672.

Kozłowski, S. (2016). Revisiting Stochastic Variability of AGNs with Structure Functions. ApJ, 826:118.

Krone-Martins, A. et al (2018). Gaia DR2 Gravitational Lens Systems I: New lensed quasar candidates around known quasars. *ArXiv e-prints*.

Kuijken, K. et al (2019). The fourth data release of the Kilo-Degree Survey: ugri imaging and nine-band optical-IR photometry over 1000 square degrees. *arXiv e-prints*, page arXiv:1902.11265.

Kundić, T. et al (1997). A Robust Determination of the Time Delay in 0957+561A, B and a Measurement of the Global Value of Hubble's Constant. ApJ, 482:75–82.

Lacki, B.C. et al (2009). Difference Imaging of Lensed Quasar Candidates in the Sloan Digital Sky Survey Supernova Survey Region. ApJ, 698:428–438.

Lacy, M. and VLASS Survey Team, V.S.S.G. (2018). The VLA Sky Survey. In *American Astronomical Society Meeting Abstracts #231*, volume 231 of *American Astronomical Society Meeting Abstracts*, page 321.02.

Lang, D. (2014). unWISE: Unblurred Coadds of the WISE Imaging. AJ, 147:108.

Lang, D., Hogg, D.W. and Schlegel, D.J. (2016). WISE Photometry for 400 Million SDSS Sources. AJ, 151:36.

Lawrence, A. et al (2007). The UKIRT Infrared Deep Sky Survey (UKIDSS). MNRAS, 379:1599–1617.

Lemon, C.A. et al (2018). Gravitationally lensed quasars in Gaia - II. Discoveryof 24 lensed quasars. MNRAS, 479:5060–5074.

Li, Z. et al (2018). The Ensemble Photometric Variability of Over 10^5 Quasars in the Dark Energy Camera Legacy Survey and the Sloan Digital Sky Survey. ApJ, 861:6.

Liao, K. et al (2015). Strong Lens Time Delay Challenge. II. Results of TDC1. ApJ, 800:11.

Lindegren, L. et al (2016). Gaia Data Release 1. Astrometry: one billion positions, two million proper motions and parallaxes. A&A, 595:A4.

Lindegren, L. et al (2012). The astrometric core solution for the Gaia mission. Overview of models, algorithms, and software implementation. A&A, 538:A78.

Linder, E.V. (2011). Lensing time delays and cosmological complementarity. Phys. Rev. D, 84:123529.

Lucey, J.R. et al (2017). Serendipitous discovery of quadruply-imaged quasars: two diamonds. *ArXiv e-prints*.

Lucey, J.R. et al (2018). Serendipitous discovery of quadruply imaged quasars: two diamonds. MNRAS, 476:927–932.

Lynden-Bell, D. (1969). Galactic Nuclei as Collapsed Old Quasars. Nature, 223:690–694.

MacLeod, C.L. et al (2010). Modeling the Time Variability of SDSS Stripe 82 Quasars as a Damped Random Walk. ApJ, 721:1014–1033.

MacLeod, C.L. et al (2012). A Description of Quasar Variability Measured Using Repeated SDSS and POSS Imaging. ApJ, 753:106.

Magain, P. et al (1988). Discovery of a quadruply lensed quasar - The 'clover leaf' H1413 + 117. Nature, 334:325–327.

Mainzer, A. et al (2011a). Preliminary Results from NEOWISE: An Enhancement to the Wide-field Infrared Survey Explorer for Solar System Science. ApJ, 731:53.

Mainzer, A. et al (2011b). NEOWISE Observations of Near-Earth Objects: Preliminary Results. ApJ, 743:156.

Mao, S. and Schneider, P. (1998). Evidence for substructure in lens galaxies? MNRAS, 295(3):587–594.

Maoz, D. et al (1992). Gravitational Lensing of Quasars as Seen by the Hubble Space Telescope Snapshot Survey. ApJ, 394:51.

Maoz, D. et al (1993a). The Hubble Space Telescope Snapshot Survey. III. Further Observations in Search of Gravitationally Lensed Quasars. ApJ, 402:69.

Maoz, D. et al (1993b). The Hubble Space Telescope Snapshot Survey. IV. A Summary of the Search for Gravitationally Lensed Quasars. ApJ, 409:28.

Matthews, T.A. and Sandage, A.R. (1963). Optical Identification of 3C 48, 3C 196, and 3C 286 with Stellar Objects. ApJ, 138:30.

Mauch, T. et al (2003). SUMSS: a wide-field radio imaging survey of the southern sky - II. The source catalogue. MNRAS, 342:1117–1130.

McGreer, I.D. et al (2013). An HST Snapshot Survey for Gravitationally Lensed z=6 Quasars. In *American Astronomical Society Meeting Abstracts #221*, volume 221 of *American Astronomical Society Meeting Abstracts*, page 133.03.

Meisner, A.M., Lang, D. and Schlegel, D.J. (2017a). Deep Full-sky Coadds from Three Years of WISE and NEOWISE Observations. AJ, 154:161.

Meisner, A.M., Lang, D. and Schlegel, D.J. (2017b). Full-depth Coadds of the WISE and First-year NEOWISE-reactivation Images. AJ, 153:38.

Meisner, A.M., Lang, D.A. and Schlegel, D.J. (2018). More unWISE Coadd Epochs from 2016 NEOWISE-reactivation Imaging. *Research Notes of the American Astronomical Society*, 2:202.

Mendez, R.A., Silva, J.F. and Lobos, R. (2013). Analysis and Interpretation of the Cramér-Rao Lower-Bound in Astrometry: One-Dimensional Case. PASP, 125:580.

Metcalf, R.B. et al (2018). The Strong Gravitational Lens Finding Challenge. *arXiv e-prints*, page arXiv:1802.03609.

Moffat, A.F.J. (1969). A Theoretical Investigation of Focal Stellar Images in the Photographic Emulsion and Application to Photographic Photometry. A&A, 3:455.

More, A. et al (2016). The SDSS-III BOSS quasar lens survey: discovery of 13 gravitationally lensed quasars. MNRAS, 456:1595–1606.

Morgan, C.W. et al (2018). Accretion Disk Size Measurement and Time Delays in the Lensed Quasar WFI 2033-4723. ApJ, 869:106.

Morgan, N.D. et al (2004). WFI J2026-4536 and WFI J2033-4723: Two New Quadruple Gravitational Lenses. AJ, 127:2617–2630.

Morgan, N.D. et al (1999). CTQ 414: A New Gravitational Lens. AJ, 118:1444–1449.

Morganson, E. et al (2018). The Dark Energy Survey Image Processing Pipeline. *Publications of the Astronomical Society of the Pacific*, 130:074501.

Morokuma, T. et al (2007). Discovery of a Gravitationally Lensed Quasar from the Sloan Digital Sky Survey: SDSS J133222.62+034739.9. AJ, 133:214–219.

Mosquera, A.M., Muñoz, J.A. and Mediavilla, E. (2009). Detection of Chromatic Microlensing in Q 2237 + 0305 A. ApJ, 691:1292–1299.

Muchovej, S. et al (2010). Radio Sources from a 31 GHz Sky Survey with the Sunyaev-Zel'dovich Array. ApJ, 716:521–529.

Myers, S.T. et al (2003). The Cosmic Lens All-Sky Survey - I. Source selection and observations. MNRAS, 341:1–12.

Ofek, E.O. et al (2007). SDSS J131339.98+515128.3: a new gravitationally lensed quasar selected based on near-infrared excess. MNRAS, 382:412–418.

Oguri, M. et al (2008a). Mass models and environment of the new quadruply lensed quasar SDSS J1330+1810. MNRAS, 391:1973–1980.

Oguri, M. et al (2008b). Mass models and environment of the new quadruply lensed quasar SDSS J1330+1810. MNRAS, 391:1973–1980.

Oguri, M. et al (2006). The Sloan Digital Sky Survey Quasar Lens Search. I. Candidate Selection Algorithm. AJ, 132:999–1013.

Oguri, M. et al (2012). The Sloan Digital Sky Survey Quasar Lens Search. VI. Constraints on Dark Energy and the Evolution of Massive Galaxies. AJ, 143:120.

Oguri, M. and Marshall, P.J. (2010). Gravitationally lensed quasars and supernovae in future wide-field optical imaging surveys. MNRAS, 405:2579–2593.

Ostrovski, F. et al (2017). VDES J2325-5229 a z = 2.7 gravitationally lensed quasar discovered using morphology-independent supervised machine learning. MNRAS, 465:4325–4334.

Ovaldsen, J.E. et al (2003). New aperture photometry of QSO 0957+561; application to time delay and microlensing. A&A, 402:891–904.

Pacucci, F. and Loeb, A. (2019). Most Lensed Quasars at z > 6 are Missed by Current Surveys. ApJ, 870:L12.

Paczynski, B. (1986). Gravitational Microlensing by the Galactic Halo. ApJ, 304:1.

Padovani, P. et al (2017). Active galactic nuclei: what's in a name? *Astronomy and Astrophysics Review*, 25:2.

Pineau, F.X. et al (2011). Cross-correlation of the 2XMMi catalogue with Data Release 7 of the Sloan Digital Sky Survey. A&A, 527:A126.

Refsdal, S. (1964). On the possibility of determining Hubble's parameter and the masses of galaxies from the gravitational lens effect. MNRAS, 128:307.

Reimers, D. et al (2002). Discovery of a new quadruply lensed QSO: HS 0810+2554 - A brighter twin to PG 1115+080. A&A, 382:L26–L28.

Reis, R.C. et al (2014). Reflection from the strong gravity regime in a lensed quasar at redshift z = 0.658. Nature, 507:207–209.

Richards, G.T. et al (2002). Spectroscopic Target Selection in the Sloan Digital Sky Survey: The Quasar Sample. AJ, 123:2945–2975.

Riello, M. et al (2018). Gaia Data Release 2. Processing of the photometric data. A&A, 616:A3.

Rosen, S.R. et al (2016). The XMM-Newton serendipitous survey. VII. The third XMM-Newton serendipitous source catalogue. A&A, 590:A1.

Rusu, C.E. and Lemon, C.A. (2018). An Edge-on Disk in the Quadruply Lensed Quasar Cross GraL J181730853+272940139. *Research Notes of the American Astronomical Society*, 2:187.

Rusu, C.E. et al (2011). SDSS J133401.39+331534.3: A New Subarcsecond Gravitationally Lensed Quasar. ApJ, 738:30.

Rusu, C.E. et al (2016). Subaru Telescope adaptive optics observations of gravitationally lensed quasars in the Sloan Digital Sky Survey. MNRAS, 458:2–55.

Saha, P. and Williams, L.L.R. (2003). Qualitative Theory for Lensed QSOs. AJ, 125:2769–2782.

Salpeter, E.E. (1964). Accretion of Interstellar Matter by Massive Objects. ApJ, 140:796–800.

Schaffer, K.K. et al (2011). The First Public Release of South Pole Telescope Data: Maps of a 95 $\deg^2$ Field from 2008 Observations. ApJ, 743:90.

Schechter, P.L. et al (1997). The Quadruple Gravitational Lens PG 1115+080: Time Delays and Models. ApJ, 475:L85–L88.

Schechter, P.L. et al (2017). First Lensed Quasar Systems from the VST-ATLAS Survey: One Quad, Two Doubles, and Two Pairs of Lensless Twins. AJ, 153:219.

Schechter, P.L. and Wambsganss, J. (2002). Quasar Microlensing at High Magnification and the Role of Dark Matter: Enhanced Fluctuations and Suppressed Saddle Points. ApJ, 580:685–695.

Schechter, P.L. and Wynne, R.A. (2019). Even simpler modeling of quadruply lensed quasars (and random quartets) using Witt's hyperbola. *arXiv e-prints*, page arXiv:1901.08517.

Schlafly, E.F., Meisner, A.M. and Green, G.M. (2019). The unWISE Catalog: Two Billion Infrared Sources from Five Years of WISE Imaging. *The Astrophysical Journal Supplement Series*, 240:30.

Schmidt, M. (1963). 3C 273 : A Star-Like Object with Large Red-Shift. Nature, 197:1040.

Sergeyev, A.V. et al (2016). Discovery of the optically bright, wide separation double quasar SDSS J1442+4055. MNRAS, 456:1948–1954.

Sérsic, J.L. (1963). Influence of the atmospheric and instrumental dispersion on the brightness distribution in a galaxy. *Boletin de la Asociacion Argentina de Astronomia La Plata Argentina*, 6:41.

Shakura, N.I. and Sunyaev, R.A. (1973). Reprint of 1973A&A....24..337S. Black holes in binary systems. Observational appearance. A&A, 500:33–51.

Shalyapin, V.N. and Goicoechea, L.J. (2017). Doubly Imaged Quasar SDSS J1515+1511: Time Delay and Lensing Galaxies. ApJ, 836:14.

Shalyapin, V.N. et al (2018). Spectroscopic follow-up of double quasar candidates. MNRAS, 480:2853–2860.

Shanks, T. et al (2015). The VLT Survey Telescope ATLAS. MNRAS, 451:4238–4252.

Shu, Y. et al (2016). The BOSS Emission-line Lens Survey. IV. Smooth Lens Models for the BELLS GALLERY Sample. ApJ, 833:264.

Shu, Y. et al (2018). SDSS J0909+4449: A large-separation strongly lensed quasar at z 2.8 with three images. MNRAS, 481:L136–L140.

Sluse, D. et al (2017). H0LiCOW - II. Spectroscopic survey and galaxy-group identification of the strong gravitational lens system HE 0435-1223. MNRAS, 470:4838–4857.

Sluse, D. et al (2003). A quadruply imaged quasar with an optical Einstein ring candidate: 1RXS J113155.4-123155. A&A, 406:L43–L46.

Soldner, J.G.v. (1801). Johann georg von soldner and the gravitational bending of light, with an english translation of his essay on it published in 1801. *Foundations of Physics*, 8(11-12):927–950.

Spiniello, C. et al (2018). KiDS-SQuaD: The KiDS Strongly lensed Quasar Detection project. MNRAS, 480:1163–1173.

Stern, D. et al (2012). Mid-infrared Selection of Active Galactic Nuclei with the Wide-Field Infrared Survey Explorer. I. Characterizing WISE-selected Active Galactic Nuclei in COSMOS. ApJ, 753:30.

Stockton, A. (1980). The lens galaxy of the twin QSO 0957+561. ApJ, 242:L141–L144.

Stoughton, C. et al (2002). Sloan Digital Sky Survey: Early Data Release. AJ, 123:485–548.

Surdej, J., Claeskens, J.F. and Smette, A. (2002). A complete sample of gravitationally lensed quasars to be detected with gaia. Gaia WG meeting, IAGL.

Suyu, S.H. et al (2017). H0LiCOW - I. H_0 Lenses in COSMOGRAIL's Wellspring: program overview. MNRAS, 468:2590–2604.

Suyu, S.H. et al (2009). Dissecting the Gravitational Lens B1608+656. I. Lens Potential Reconstruction. ApJ, 691(1):277–298.

Tewes, M., Courbin, F. and Meylan, G. (2013). COSMOGRAIL: the COSmological MOnitoring of GRAvItational Lenses. XI. Techniques for time delay measurement in presence of microlensing. A&A, 553:A120.

The Dark Energy Survey Collaboration (2005). The Dark Energy Survey. *ArXiv Astrophysics e-prints*.

Tokovinin, A. et al (2016). SOAR Adaptive Module (SAM): Seeing Improvement with a UV Laser. *Publications of the Astronomical Society of the Pacific*, 128:125003.

Treu, T. et al (2018). The STRong lensing Insights into the Dark Energy Survey (STRIDES) 2016 follow-up campaign. I. Overview and classification of candidates selected by two techniques. MNRAS.

Treu, T. and Ellis, R.S. (2015). Gravitational Lensing: Einstein's unfinished symphony. *Contemporary Physics*, 56:17–34.

Treu, T. and Marshall, P.J. (2016). Time delay cosmography. *Astronomy and Astrophysics Review*, 24:11.

Turner, E.L., Ostriker, J.P. and Gott, III, J.R. (1984). The statistics of gravitational lenses - The distributions of image angular separations and lens redshifts. ApJ, 284:1–22.

Urry, C.M. and Padovani, P. (1995). Unified Schemes for Radio-Loud Active Galactic Nuclei. *Publications of the Astronomical Society of the Pacific*, 107:803.

Voges, W. et al (1999). The ROSAT all-sky survey bright source catalogue. A&A, 349:389–405.

Vuissoz, C. et al (2007). COSMOGRAIL: the COSmological MOnitoring of GRAvItational Lenses. V. The time delay in SDSS J1650+4251. A&A, 464:845–851.

Walsh, D., Carswell, R.F. and Weymann, R.J. (1979). 0957 + 561 A, B - Twin quasistellar objects or gravitational lens. Nature, 279:381–384.

Walter, C.W. (2015). The Brighter-Fatter and other sensor effects in CCD simulations for precision astronomy. *Journal of Instrumentation*, 10:C05015.

Wang, L. et al (2017). SDSS J1640+1932: a spectacular galaxy-quasar strong lens system. MNRAS, 468:3757–3763.

Weymann, R.J. et al (1980). An Optical Three-Way Split - Triple Quasar PG1115+08. *Science News*, 118:4.

Williams, P.R. et al (2018). Discovery of three strongly lensed quasars in the Sloan Digital Sky Survey. MNRAS, 477:L70–L74.

Winn, J.N. et al (2002). PMN J1632-0033: A New Gravitationally Lensed Quasar. AJ, 123:10–19.

Wright, E.L. et al (2010). The Wide-field Infrared Survey Explorer (WISE): Mission Description and Initial On-orbit Performance. AJ, 140:1868–1881.

Wu, X.B. et al (2012). SDSS Quasars in the WISE Preliminary Data Release and Quasar Candidate Selection with Optical/Infrared Colors. AJ, 144:49.

Wynne, R.A. and Schechter, P.L. (2018). Robust modeling of quadruply lensed quasars (and random quartets) using Witt's hyperbola. *ArXiv e-prints*.

Young, P. et al (1980). The double quasar Q0957+561 A, B: a gravitational lens image formed by a galaxy at z=0.39. ApJ, 241:507–520.

Zwicky, F. (1937). Nebulae as Gravitational Lenses. *Physical Review*, 51:290–290.

Appendix A

Lens Photometry and Astrometry

The following tables list modelled photometry and astrometry of the lensed quasars presented in this thesis. Table A.1 presents photometry and astrometry for Pan-STARRS+*Gaia*-DR1-selected lensed quasars. Table A.2 provides the astrometry from the best available imaging data and DES photometry for DES+*Gaia*-DR1-selected lensed quasars. The uncertainties on quasar photometry reflect the standard deviation of single epoch magnitude values, or in the case of only one epoch fitting being retained, the uncertainty on that single epoch magnitude. In the case of the lens galaxy, the photometry and uncertainty are given for the most precise single epoch band. Table A.3 presents photometry and astrometry for Pan-STARRS+*Gaia*-DR2-selected lensed quasars.

Table A.1 Pan-STARRS astrometry and photometry of the *Gaia* DR1+Pan-STARRS-selected lensed quasars. Magnitudes are in the AB sytem.

	component	α (")	δ (")	g	r	i	z	Y
J0011–0845	A	0.46 ± 0.02	1.24 ± 0.01	20.90 ± 0.01	20.67 ± 0.01	20.69 ± 0.01	20.64 ± 0.03	20.78 ± 0.05
	B	-0.48 ± 0.10	-0.44 ± 0.10	21.03 ± 0.02	20.78 ± 0.06	21.02 ± 0.09	20.41 ± 0.23	20.52 ± 0.14
	G	0.00 ± 0.05	0.00 ± 0.04	22.71 ± 0.22	20.85 ± 0.12	20.32 ± 0.09	20.03 ± 0.15	19.89 ± 0.17
J0028+0631	A	0.44 ± 0.01	2.09 ± 0.01	18.82 ± 0.01	18.75 ± 0.01	18.98 ± 0.01	19.23 ± 0.01	19.11 ± 0.02
	B	-0.23 ± 0.01	-0.59 ± 0.10	20.65 ± 0.01	20.39 ± 0.02	20.89 ± 0.04	21.07 ± 0.07	20.73 ± 0.07
	G	0.00 ± 0.01	0.00 ± 0.01	20.23 ± 0.02	19.11 ± 0.12	18.44 ± 0.01	18.19 ± 0.01	18.00 ± 0.02
J0030–1525	A	-1.09 ± 0.01	0.86 ± 0.01	19.54 ± 0.01	19.22 ± 0.01	19.07 ± 0.01	18.86 ± 0.01	18.87 ± 0.01
	B	-1.05 ± 0.19	-0.92 ± 0.01	20.11 ± 0.01	19.78 ± 0.01	19.74 ± 0.01	19.66 ± 0.01	19.89 ± 0.02
	G	0.00 ± 0.09	0.01 ± 0.09	20.58 ± 0.02	19.34 ± 0.012	18.88 ± 0.01	18.53 ± 0.01	18.37 ± 0.02
J0123–0455	A	1.20 ± 0.01	0.93 ± 0.01	19.08 ± 0.01	19.11 ± 0.01	19.87 ± 0.01	19.67 ± 0.01	20.06 ± 0.03
	B	-0.43 ± 0.01	-0.25 ± 0.01	19.77 ± 0.01	19.47 ± 0.02	20.59 ± 0.07	19.98 ± 0.07	20.46 ± 0.24
	G	0.00 ± 0.01	0.00 ± 0.01	20.28 ± 0.04	19.12 ± 0.03	18.15 ± 0.02	18.17 ± 0.02	17.80 ± 0.03
J0140–1152	A	0.57 ± 0.01	0.11 ± 0.01	19.54 ± 0.01	19.08 ± 0.01	18.87 ± 0.01	19.09 ± 0.01	18.92 ± 0.02
	B	-0.81 ± 0.01	-0.30 ± 0.01	19.62 ± 0.01	19.30 ± 0.01	19.16 ± 0.01	19.23 ± 0.01	19.16 ± 0.02
	G	0.00 ± 0.02	0.00 ± 0.01	20.18 ± 0.02	18.92 ± 0.02	18.53 ± 0.01	18.38 ± 0.03	17.87 ± 0.02
J0146–1133	A	0.34 ± 0.01	-1.20 ± 0.01	18.91 ± 0.01	18.74 ± 0.01	18.79 ± 0.01	18.74 ± 0.01	18.83 ± 0.01
	B	-0.35 ± 0.01	0.33 ± 0.01	19.17 ± 0.01	18.85 ± 0.01	18.90 ± 0.01	18.83 ± 0.01	19.12 ± 0.03
	G	0.00 ± 0.01	0.00 ± 0.01	20.32 ± 0.03	19.30 ± 0.02	18.70 ± 0.02	18.52 ± 0.02	18.24 ± 0.02
J0235–2433	A	0.48 ± 0.01	-1.30 ± 0.01	19.73 ± 0.02	19.47 ± 0.02	19.58 ± 0.02	19.90 ± 0.03	19.66 ± 0.05
	B	0.06 ± 0.01	0.71 ± 0.01	20.24 ± 0.03	19.93 ± 0.02	19.41 ± 0.02	20.16 ± 0.03	19.55 ± 0.07
	G	0.00 ± 0.01	0.00 ± 0.01	19.43 ± 0.03	18.43 ± 0.02	18.10 ± 0.01	17.92 ± 0.01	17.59 ± 0.02
J0259–2338	A	-2.29 ± 0.01	0.19 ± 0.01	19.09 ± 0.02	19.00 ± 0.02	19.66 ± 0.02	19.20 ± 0.02	19.06 ± 0.09
	B	0.59 ± 0.01	-0.22 ± 0.01	19.83 ± 0.03	19.79 ± 0.04	20.26 ± 0.03	20.06 ± 0.05	19.58 ± 0.13
	G	0.00 ± 0.01	0.00 ± 0.01	21.69 ± 0.25	19.44 ± 0.04	18.72 ± 0.02	18.13 ± 0.02	18.15 ± 0.05
J0417+3325	A	0.54 ± 0.01	1.01 ± 0.02	20.35 ± 0.01	19.64 ± 0.01	19.41 ± 0.01	19.14 ± 0.01	19.04 ± 0.01
	B	-0.46 ± 0.01	-0.23 ± 0.01	21.10 ± 0.02	20.22 ± 0.02	19.93 ± 0.03	19.59 ± 0.03	19.39 ± 0.04
	G	0.00 ± 0.01	0.00 ± 0.01	20.58 ± 0.02	19.33 ± 0.01	18.54 ± 0.01	18.07 ± 0.02	17.93 ± 0.02
J0630–1201	A	0.01 ± 0.01	0.00 ± 0.01	20.50 ± 0.01	19.69 ± 0.01	19.60 ± 0.01	19.12 ± 0.01	19.14 ± 0.02
	B	0.53 ± 0.01	-0.58 ± 0.01	20.58 ± 0.02	19.86 ± 0.02	19.44 ± 0.01	19.18 ± 0.02	19.12 ± 0.02
	C	-0.31 ± 0.01	1.13 ± 0.01	20.48 ± 0.01	19.65 ± 0.01	19.44 ± 0.01	19.16 ± 0.01	19.05 ± 0.01
J0840+3550	A	-2.04 ± 0.01	0.56 ± 0.01	20.38 ± 0.01	20.58 ± 0.01	19.92 ± 0.01	19.99 ± 0.01	20.34 ± 0.01
	B	0.64 ± 0.04	-0.14 ± 0.03	21.59 ± 0.05	22.06 ± 0.15	21.75 ± 0.20	21.96 ± 0.23	22.43 ± 0.48
	G	0.00 ± 0.02	0.00 ± 0.01	19.48 ± 0.02	18.54 ± 0.01	18.03 ± 0.01	17.69 ± 0.01	17.65 ± 0.01
J0941+0518	A	-3.02 ± 0.01	-2.18 ± 0.01	19.39 ± 0.01	18.96 ± 0.01	18.66 ± 0.01	18.85 ± 0.01	18.76 ± 0.01
	B	0.97 ± 0.01	1.46 ± 0.01	20.16 ± 0.01	19.93 ± 0.01	19.68 ± 0.01	19.86 ± 0.01	19.65 ± 0.02
	G	0.01 ± 0.01	0.00 ± 0.01	19.43 ± 0.01	18.08 ± 0.01	17.51 ± 0.01	17.16 ± 0.01	16.85 ± 0.01
J0949+4208	A	1.04 ± 0.01	1.77 ± 0.09	19.10 ± 0.02	19.02 ± 0.01	19.61 ± 0.03	19.53 ± 0.02	19.75 ± 0.04
	B	-0.31 ± 0.01	-0.42 ± 0.01	20.19 ± 0.02	19.99 ± 0.02	19.66 ± 0.02	19.90 ± 0.03	19.97 ± 0.05
	G	0.00 ± 0.02	0.00 ± 0.04	20.87 ± 0.12	19.59 ± 0.04	19.19 ± 0.05	18.54 ± 0.02	18.45 ± 0.04
J1508+3844	A	-0.50 ± 0.03	0.70 ± 0.03	22.18 ± 0.02	21.95 ± 0.04	21.58 ± 0.06	21.27 ± 0.07	21.09 ± 0.12
	B	0.96 ± 0.03	-0.19 ± 0.03	22.14 ± 0.02	21.79 ± 0.03	21.28 ± 0.05	20.93 ± 0.04	21.38 ± 0.11
	G	0.00 ± 0.04	0.00 ± 0.05	22.47 ± 0.10	21.22 ± 0.05	20.04 ± 0.05	19.72 ± 0.04	19.39 ± 0.05
J1602+4526	A	1.99 ± 0.01	0.38 ± 0.01	19.99 ± 0.01	20.39 ± 0.01	20.20 ± 0.01	19.92 ± 0.01	20.05 ± 0.01
	B	-0.52 ± 0.02	-0.60 ± 0.02	20.93 ± 0.01	21.19 ± 0.04	21.11 ± 0.03	20.72 ± 0.04	20.98 ± 0.08
	G	0.00 ± 0.01	0.00 ± 0.01	20.67 ± 0.03	19.27 ± 0.02	18.67 ± 0.02	18.24 ± 0.02	18.04 ± 0.02
J1606–2333	A	-0.88 ± 0.01	0.30 ± 0.01	19.24 ± 0.01	19.11 ± 0.01	18.80 ± 0.01	18.88 ± 0.01	18.92 ± 0.05
	B	0.76 ± 0.01	-0.27 ± 0.01	19.42 ± 0.01	19.33 ± 0.01	18.99 ± 0.01	19.08 ± 0.02	19.12 ± 0.06
	C	-0.07 ± 0.01	-0.60 ± 0.01	19.79 ± 0.01	19.51 ± 0.02	19.22 ± 0.01	19.23 ± 0.02	19.27 ± 0.06
	D	0.24 ± 0.01	0.48 ± 0.01	20.23 ± 0.03	19.95 ± 0.03	19.46 ± 0.02	19.59 ± 0.02	19.66 ± 0.07
	G	0.00 ± 0.05	0.00 ± 0.05	21.67 ± 0.29	21.40 ± 0.25	20.85 ± 0.17	21.08 ± 0.29	19.75 ± 0.19
J1640+1045	A	-0.37 ± 0.01	-0.36 ± 0.01	18.69 ± 0.01	18.73 ± 0.01	18.49 ± 0.01	18.28 ± 0.01	18.34 ± 0.01
	B	1.44 ± 0.01	0.92 ± 0.01	20.31 ± 0.01	20.34 ± 0.01	19.96 ± 0.01	19.89 ± 0.01	19.87 ± 0.01
	G	0.00 ± 0.01	0.00 ± 0.01	20.66 ± 0.04	19.25 ± 0.02	18.67 ± 0.01	18.66 ± 0.02	18.29 ± 0.02

J1709+3828	A	0.75 ± 0.01	-0.44 ± 0.02	21.49 ± 0.02	20.68 ± 0.01	20.70 ± 0.03	20.89 ± 0.05	21.29 ± 0.23
	B	-0.05 ± 0.01	1.06 ± 0.01	21.21 ± 0.01	20.65 ± 0.01	20.60 ± 0.02	20.91 ± 0.03	20.72 ± 0.07
	G	0.00 ± 0.02	0.00 ± 0.02	21.57 ± 0.04	20.06 ± 0.02	19.36 ± 0.02	18.98 ± 0.02	18.79 ± 0.03
J1710+4332	A	0.29 ± 0.01	1.67 ± 0.01	20.89 ± 0.01	21.09 ± 0.01	21.43 ± 0.01	21.20 ± 0.02	20.20 ± 0.02
	B	-0.17 ± 0.02	-0.72 ± 0.02	21.89 ± 0.01	21.99 ± 0.04	22.06 ± 0.07	21.34 ± 0.12	20.18 ± 0.15
	G	0.00 ± 0.05	0.00 ± 0.06	—	21.60 ± 0.08	20.60 ± 0.09	20.22 ± 0.09	20.38 ± 0.18
J1721+8842	A	-0.54 ± 0.01	-1.80 ± 0.01	19.45 ± 0.01	19.50 ± 0.02	19.14 ± 0.03	19.39 ± 0.02	19.14 ± 0.05
	B	-2.13 ± 0.01	-0.71 ± 0.01	20.57 ± 0.02	20.45 ± 0.02	20.18 ± 0.03	20.15 ± 0.03	19.88 ± 0.05
	C	1.88 ± 0.01	-1.10 ± 0.01	20.13 ± 0.01	20.04 ± 0.02	19.90 ± 0.03	19.91 ± 0.02	19.71 ± 0.05
	D	0.06 ± 0.02	1.69 ± 0.02	21.69 ± 0.04	21.43 ± 0.03	21.02 ± 0.05	21.18 ± 0.04	21.11 ± 0.08
	G	0.00 ± 0.01	0.00 ± 0.02	18.89 ± 0.02	18.47 ± 0.02	18.02 ± 0.03	17.97 ± 0.02	18.01 ± 0.04
J1831+5447	A	1.47 ± 0.01	1.10 ± 0.01	19.32 ± 0.01	19.14 ± 0.03	19.22 ± 0.02	19.08 ± 0.04	19.21 ± 0.06
	B	-0.37 ± 0.01	-0.27 ± 0.01	20.55 ± 0.03	20.07 ± 0.04	20.02 ± 0.03	19.58 ± 0.05	19.76 ± 0.08
	G	0.00 ± 0.02	0.00 ± 0.01	20.21 ± 0.07	18.95 ± 0.04	18.17 ± 0.01	17.76 ± 0.02	17.45 ± 0.03
J2124+1632	A	-0.04 ± 0.01	2.55 ± 0.01	18.99 ± 0.01	18.66 ± 0.01	18.80 ± 0.02	18.93 ± 0.03	19.08 ± 0.06
	B	0.13 ± 0.01	-0.46 ± 0.01	19.24 ± 0.02	19.16 ± 0.02	18.93 ± 0.03	19.34 ± 0.03	19.34 ± 0.08
	G	0.00 ± 0.01	0.00 ± 0.01	20.44 ± 0.10	18.88 ± 0.04	18.40 ± 0.04	18.03 ± 0.04	17.89 ± 0.05
J2305+3714	A	1.18 ± 0.01	-0.83 ± 0.01	17.96 ± 0.01	17.68 ± 0.01	17.34 ± 0.01	17.30 ± 0.01	17.28 ± 0.02
	B	-0.25 ± 0.01	0.84 ± 0.01	18.94 ± 0.01	18.99 ± 0.01	18.54 ± 0.01	18.51 ± 0.01	18.46 ± 0.02
	G	0.00 ± 0.02	0.00 ± 0.02	22.14 ± 0.43	18.59 ± 0.04	18.32 ± 0.03	18.05 ± 0.03	17.81 ± 0.05
J2332−1852	A	1.35 ± 0.01	0.43 ± 0.01	20.27 ± 0.01	20.24 ± 0.01	19.24 ± 0.01	19.68 ± 0.01	19.15 ± 0.01
	B	-0.43 ± 0.01	-0.41 ± 0.01	20.59 ± 0.01	20.59 ± 0.01	19.88 ± 0.03	20.21 ± 0.03	19.44 ± 0.03
	G	0.00 ± 0.02	0.00 ± 0.02	—	21.01 ± 0.05	18.93 ± 0.04	19.40 ± 0.04	18.71 ± 0.04

Table A.2 Astrometry and photometry of *Gaia* DR1 + DES selected lensed quasars. Magnitudes are in the AB sytem. All photometry is from DES. Astrometry is from NIRC2 (DESJ0245-0556, DESJ0246-1845, DESJ0340-2545), SOAR (DESJ0053-2012, DESJ0150-4041, DESJ0407-1931, DESJ0501-4118, DESJ0600-4649), or DES (DESJ0112-1650, DESJ2349-4518). The photometric uncertainties are the standard deviation of magnitudes across all measured epochs.

	component	α (")	δ (")	g	r	i	z	Y
J0053-2012	A	1.828 ± 0.001	-0.662 ± 0.001	20.22±0.04	19.44±0.02	19.32±0.03	19.06±0.02	19.16±0.01
	B	-0.263±0.001	-0.264±0.001	20.12±0.04	19.34±0.01	19.23±0.03	18.99±0.02	19.06±0.01
	C	-0.981±0.001	0.472±0.001	20.30±0.06	19.49±0.01	19.37±0.03	19.12±0.03	19.23±0.01
	D	0.95±0.01	1.46±0.01	22.49±0.07	21.92±0.04	21.76±0.05	21.63±0.14	21.29±0.12
	G1	0.86±0.02	0.90±0.03	23.53±0.37	21.65±0.06	21.22±0.05	20.25±0.05	20.12±0.09
	G2	-2.39±0.02	-1.91±0.02	22.58±0.04	21.80±0.03	20.98±0.03	20.44±0.03	20.28±0.03
J0112-1650	A	0.928±0.001	0.140±0.001	20.64±0.03	20.10±0.05	20.08±0.04	19.84±0.16	19.67±0.27
	B	-0.325 ± 0.002	-0.486 ± 0.002	20.99±0.13	20.70±0.06	20.65±0.09	20.55±0.08	20.59±0.75
	C	-0.089 ± 0.004	0.684 ± 0.004	23.39±0.20	21.78±0.09	21.25±0.02	20.96±0.06	21.05±0.36
	G1	0.00 ± 0.01	0.00 ± 0.01	—	20.55±0.05	19.78±0.04	19.24±0.04	18.52±0.10
J0150-4041	A	-1.643±0.001	-0.003±0.001	19.78±0.04	19.64±0.13	19.19±0.18	19.01±0.16	18.98±0.01
	B	1.163±0.005	0.028±0.005	21.31±0.01	21.20±0.09	20.87±0.11	20.77±0.13	20.78±0.02
	G1	0.480±0.004	-0.025±0.003	21.38±0.02	19.43±0.01	18.82±0.01	18.43±0.01	18.37±0.01
J0245-0556	A	0.00	0.00	19.38±4.89	19.24±0.04	19.27±0.05	19.42±0.05	19.44±0.04
	B	1.1300±0.005	-1.5300±0.005	19.97±0.01	19.73±0.06	19.80±0.13	19.93±0.08	20.00±0.05
	G	0.9148±0.005	-1.196±0.005	20.99±0.03	19.57±0.01	18.92±0.01	18.69±0.01	18.55±0.02
J0246-1845	A	0.00	0.00	18.66±0.01	18.63±0.01	18.39±0.01	18.49±0.03	18.53±0.02
	B	0.0430±0.005	-0.9966±0.005	19.38±0.01	19.39±0.01	19.11±0.01	19.15±0.01	19.20±0.04
	G	0.011±0.005	-0.709±0.005	—	—	—	—	—
J0340-2545	A	0.00	0.00	18.42±0.06	18.44±0.02	18.31±0.07	18.49±0.08	18.66±0.02
	B	-3.102±0.005	5.985±0.005	19.85±0.13	19.74±0.07	19.51±0.06	19.82±0.08	19.84±0.11
	C	0.807±0.005	3.078±0.005	21.12±0.09	21.18±0.06	21.01±0.06	21.42±0.25	21.68±0.49
	G1	0.720±0.005	2.758±0.005	22.51±0.10	20.46±0.01	19.67±0.01	19.24±0.01	19.08±0.01
	G2	-2.960±0.005	3.263±0.005	21.91±0.01	20.23±0.01	19.47±0.01	19.12±0.01	18.92±0.01
	G3	-2.798±0.005	5.631±0.005	22.31±0.05	20.54±0.01	19.95±0.01	19.47±0.01	19.34±0.03
J0407-1931	A	-0.179±0.002	-1.530±0.002	20.42±0.08	20.34±0.05	20.23±0.06	20.05±0.04	20.00±0.18
	B	0.14±0.01	1.04±0.01	21.58±0.17	21.89±0.05	21.44±0.70	21.56±0.09	21.62±1.08
	G1	0.037±0.003	0.488±0.003	20.99±0.01	19.35±0.00	18.93±0.00	18.66±0.01	18.50±0.03
J0501-4118	A	-1.247±0.001	-1.050±0.001	18.84±0.01	18.79±0.01	18.61±0.01	18.38±0.01	18.47±0.04
	B	2.396±0.001	-1.680±0.001	19.10±0.01	19.06±0.01	18.88±0.01	18.68±0.04	18.75±0.07
	G1	1.538±0.005	-0.754±0.005	21.08±0.02	19.52±0.01	18.94±0.01	18.52±0.01	18.48±0.01
J0600-4649	A	-1.392±0.002	-0.223±0.002	19.36±0.01	19.34±0.01	19.17±0.06	18.90±0.05	19.04±0.07
	B	0.948±0.009	0.138±0.009	21.66±0.01	21.58±0.01	21.40±0.12	21.09±0.08	21.18±0.21
	G1	0.443±0.010	0.086±0.007	—	20.61±0.02	19.54±0.01	19.12±0.01	19.01±0.01
J2349-4518	A	-1.399±0.001	-0.619±0.001	18.83±0.01	18.62±0.01	18.81±0.03	18.29±0.05	—
	B	0.705±0.001	-0.217±0.001	21.25±0.01	20.90±0.01	21.05±0.04	20.47±0.06	—
	G1	0.00±0.03	0.00±0.02	22.55±0.37	21.73±0.10	20.62±0.05	20.00±0.04	—

Table A.3 Pan-STARRS astrometry and photometry of *Gaia* DR2+Pan-STARRS-selected lensed quasars. Magnitudes are in the AB sytem.

	component	α (")	δ (")	g	r	i	z	Y
J0013+5119	A	-0.83 ± 0.01	1.55 ± 0.02	20.86 ± 0.01	20.62 ± 0.01	20.49 ± 0.01	20.39 ± 0.02	20.17 ± 0.02
	B	-0.02 ± 0.01	-1.28 ± 0.02	21.31 ± 0.01	20.77 ± 0.02	20.54 ± 0.02	20.36 ± 0.03	20.29 ± 0.05
	G	0.00 ± 0.01	0.00 ± 0.02	20.55 ± 0.02	19.11 ± 0.02	18.41 ± 0.02	18.11 ± 0.02	17.81 ± 0.02
J0047+2514	A	0.77 ± 0.02	-1.05 ± 0.02	21.03 ± 0.01	20.68 ± 0.01	20.74 ± 0.02	20.80 ± 0.03	20.75 ± 0.04
	B	-0.21 ± 0.02	0.39 ± 0.02	21.36 ± 0.05	21.47 ± 0.12	21.74 ± 0.28	—	—
	G	0.00 ± 0.02	0.00 ± 0.02	21.20 ± 0.07	19.34 ± 0.03	18.68 ± 0.03	18.44 ± 0.03	18.28 ± 0.05
J0102+2445	A	1.73 ± 0.01	-0.71 ± 0.01	19.37 ± 0.01	19.35 ± 0.01	19.21 ± 0.01	19.00± 0.01	19.11 ± 0.01
	B	-0.23 ± 0.01	0.34 ± 0.01	20.90 ± 0.02	20.74 ± 0.05	20.69 ± 0.06	20.04 ± 0.04	20.37 ± 0.08
	G	0.00 ± 0.01	0.00 ± 0.01	19.69 ± 0.02	18.45 ± 0.02	17.70 ± 0.02	17.59 ± 0.02	17.36 ± 0.02
J0124-0033	A	-0.84 ± 0.02	-1.06 ± 0.02	21.59 ± 0.02	21.15 ± 0.02	21.70 ± 0.03	21.93 ± 0.07	21.45 ± 0.1
	B	0.30 ± 0.02	0.56 ± 0.02	21.14 ± 0.06	21.21 ± 0.07	21.11 ± 0.06	21.03 ± 0.16	20.68 ± 0.19
	G	0.00 ± 0.01	0.00 ± 0.02	19.92 ± 0.03	18.64 ± 0.01	18.20 ± 0.01	17.91 ± 0.01	17.75 ± 0.02
J0203+1612	A	0.85 ± 0.02	1.53 ± 0.02	21.22 ± 0.01	20.53 ± 0.01	20.37 ± 0.01	19.93 ± 0.01	20.02 ± 0.02
	B	-0.46 ± 0.02	-0.87 ± 0.02	22.08 ± 0.03	21.11 ± 0.03	20.97 ± 0.04	20.67 ± 0.05	20.47 ± 0.1
	G	0.00 ± 0.02	0.00 ± 0.03	21.71 ± 0.04	20.22 ± 0.04	19.30 ± 0.04	18.81 ± 0.04	18.78 ± 0.05
J0228+3953	A	1.03 ± 0.01	0.19 ± 0.01	19.99 ± 0.02	19.76 ± 0.03	19.90 ± 0.03	19.32 ± 0.04	19.32 ± 0.04
	B	-0.45 ± 0.01	-0.31 ± 0.01	20.65 ± 0.02	20.36 ± 0.04	20.15 ± 0.04	19.92 ± 0.05	19.87 ± 0.09
	G	0.00 ± 0.03	0.00 ± 0.03	—	21.05 ± 0.19	20.66 ± 0.17	19.85 ± 0.16	19.54 ± 0.18
J0347-2154	A	0.38 ± 0.01	1.32 ± 0.01	19.39 ± 0.01	19.24 ± 0.01	19.48 ± 0.01	19.35 ± 0.01	19.40 ± 0.02
	B	-0.18 ± 0.01	-0.51 ± 0.01	20.45 ± 0.02	20.29 ± 0.05	20.48 ± 0.07	20.72 ± 0.14	20.89 ± 0.31
	G	0.00 ± 0.01	0.00 ± 0.01	19.23 ± 0.02	17.97 ± 0.01	17.63 ± 0.01	17.32 ± 0.01	17.08 ± 0.02
J0401-2514	A	0.10 ± 0.01	1.01 ± 0.01	18.78 ± 0.02	18.48 ± 0.02	18.56 ± 0.05	18.60 ± 0.06	18.74 ± 0.08
	B	0.03 ± 0.01	-0.40 ± 0.01	20.25 ± 0.05	19.80 ± 0.05	20.09 ± 0.07	20.10 ± 0.11	20.05 ± 0.15
	G	0.00 ± 0.02	0.00 ± 0.04	—	19.97 ± 0.15	18.76 ± 0.08	18.42 ± 0.08	18.04 ± 0.06
J0416+7428	A	-1.85 ± 0.01	-0.73 ± 0.01	20.32 ± 0.01	19.56 ± 0.01	19.48 ± 0.01	19.16 ± 0.01	18.82 ± 0.01
	B	0.63 ± 0.01	0.16 ± 0.01	20.32 ± 0.02	19.30 ± 0.01	19.00± 0.01	18.55 ± 0.01	18.14 ± 0.02
	G	0.00 ± 0.01	0.00 ± 0.01	17.85 ± 0.01	16.83 ± 0.01	16.22 ± 0.01	15.86 ± 0.01	15.58 ± 0.01
J0440-0905	A	0.20 ± 0.01	-1.20 ± 0.01	19.36 ± 0.01	19.23 ± 0.01	19.09 ± 0.01	18.91 ± 0.01	19.03 ± 0.01
	B	-0.27 ± 0.01	0.42 ± 0.01	20.16 ± 0.02	20.11 ± 0.03	19.75 ± 0.04	19.60 ± 0.04	19.67 ± 0.07
	G	0.00 ± 0.03	0.00 ± 0.03	21.86 ± 0.16	20.31 ± 0.06	20.13 ± 0.11	19.90 ± 0.21	19.25 ± 0.07
J0504-2446	A	-0.55 ± 0.01	0.23 ± 0.01	19.76 ± 0.01	19.84 ± 0.02	19.50 ± 0.02	19.56 ± 0.03	19.56 ± 0.09
	B	1.03 ± 0.01	-1.08 ± 0.01	21.00± 0.01	20.76 ± 0.01	20.11 ± 0.02	19.87 ± 0.02	19.64 ± 0.02
	G	0.00 ± 0.01	0.00 ± 0.01	19.65 ± 0.03	18.37 ± 0.02	17.76 ± 0.03	17.42 ± 0.03	17.15 ± 0.03
J0544+4350	A	0.00 ± 0.01	0.00 ± 0.01	20.15 ± 0.01	19.64 ± 0.01	19.27 ± 0.01	19.20 ± 0.01	19.00± 0.01
	B	-2.00 ± 0.01	-0.20 ± 0.01	20.99 ± 0.01	20.27 ± 0.01	19.85 ± 0.01	19.74 ± 0.01	19.53 ± 0.0
J0607-2152	A	-0.26 ± 0.01	0.71 ± 0.01	19.59 ± 0.01	19.06 ± 0.01	19.01 ± 0.01	18.93 ± 0.01	19.21 ± 0.04
	B	0.77 ± 0.01	-0.07 ± 0.01	21.69 ± 0.06	20.94 ± 0.03	20.68 ± 0.04	20.66 ± 0.05	21.18 ± 0.15
	C	-0.52 ± 0.01	-0.78 ± 0.01	21.51 ± 0.04	20.67 ± 0.02	20.56 ± 0.03	20.42 ± 0.03	20.63 ± 0.06
	D	-1.15 ± 0.01	0.19 ± 0.01	22.86 ± 0.25	21.97 ± 0.10	21.93 ± 0.08	21.31 ± 0.07	21.02 ± 0.12
	G	0.00 ± 0.04	0.00 ± 0.03	20.78 ± 0.10	19.91 ± 0.05	19.32 ± 0.04	18.89 ± 0.03	18.48 ± 0.04
J0608+4229	A	0.00 ± 0.01	0.00 ± 0.01	19.03 ± 0.01	18.42 ± 0.01	18.02 ± 0.01	18.01 ± 0.02	17.55 ± 0.02
	B	-0.58 ± 0.01	0.62 ± 0.01	20.91 ± 0.05	20.12 ± 0.03	19.54 ± 0.01	19.19 ± 0.02	18.71 ± 0.02
	C	-1.23 ± 0.01	-0.22 ± 0.01	21.16 ± 0.02	20.44 ± 0.01	19.78 ± 0.01	19.48 ± 0.01	19.00± 0.01
	D	-0.21 ± 0.01	-0.45 ± 0.01	21.48 ± 0.18	21.96 ± 0.37	20.36 ± 0.07	19.50 ± 0.08	19.06 ± 0.09
J0635+6452	A	0.03 ± 0.01	-2.62 ± 0.01	19.20 ± 0.01	19.03 ± 0.01	18.81 ± 0.01	18.81 ± 0.01	18.63 ± 0.01
	B	-0.02 ± 0.01	0.47 ± 0.01	21.64 ± 0.05	21.00± 0.08	21.20 ± 0.16	—	—
	G	0.00 ± 0.01	0.00 ± 0.02	20.99 ± 0.05	19.71 ± 0.04	18.69 ± 0.03	18.41 ± 0.02	17.92 ± 0.03
J0643+2725	A	0.70 ± 0.01	-1.53 ± 0.01	20.53 ± 0.01	19.65 ± 0.01	19.31 ± 0.01	19.17 ± 0.01	19.22 ± 0.01
	B	-0.25 ± 0.01	0.67 ± 0.01	20.32 ± 0.02	19.78 ± 0.02	19.25 ± 0.02	19.13 ± 0.06	19.07 ± 0.06
	G	0.00 ± 0.01	0.00 ± 0.01	19.36 ± 0.02	18.01 ± 0.01	17.46 ± 0.01	17.13 ± 0.02	17.20 ± 0.02
J0659+1629	A	-1.82 ± 0.01	1.05 ± 0.01	18.89 ± 0.01	18.40 ± 0.01	18.65 ± 0.01	18.77 ± 0.01	18.36 ± 0.01
	B	-0.70 ± 0.01	2.01 ± 0.01	20.40 ± 0.01	19.92 ± 0.01	20.13 ± 0.01	20.23 ± 0.01	19.75 ± 0.01
	C	-1.73 ± 0.01	-0.87 ± 0.01	20.17 ± 0.01	19.72 ± 0.01	19.99 ± 0.01	20.01 ± 0.01	19.69 ± 0.01
	D	2.95 ± 0.01	-1.20 ± 0.01	20.29 ± 0.01	19.81 ± 0.01	19.88 ± 0.01	19.84 ± 0.01	19.62 ± 0.0
	G	0.00 ± 0.01	0.00 ± 0.02	22.62 ± 0.09	20.49 ± 0.04	19.18 ± 0.04	18.86 ± 0.04	18.33 ± 0.04
J0740+0635	A	0.99 ± 0.01	-0.02 ± 0.01	18.71 ± 0.01	18.31 ± 0.01	17.86 ± 0.01	17.55 ± 0.01	17.29 ± 0.01
	B	-0.65 ± 0.01	-0.00 ± 0.01	19.96 ± 0.01	19.74 ± 0.01	19.22 ± 0.01	19.04 ± 0.01	18.71 ± 0.01
	G	0.00 ± 0.01	0.00 ± 0.01	20.94 ± 0.09	19.35 ± 0.04	19.56 ± 0.15	18.68 ± 0.06	19.12 ± 0.07

J0803+3908	A	0.00 ± 0.01	0.00 ± 0.01	19.27 ± 0.05	18.95 ± 0.03	18.42 ± 0.02	18.47 ± 0.03	18.04 ± 0.05
	B	-0.12 ± 0.01	0.41 ± 0.01	18.30 ± 0.02	18.37 ± 0.02	18.31 ± 0.02	17.97 ± 0.02	17.74 ± 0.04
	C	0.29 ± 0.01	1.19 ± 0.01	18.95 ± 0.01	18.89 ± 0.01	18.78 ± 0.01	18.58 ± 0.01	18.49 ± 0.01
	D	0.84 ± 0.01	0.38 ± 0.01	20.60 ± 0.02	19.90 ± 0.01	19.66 ± 0.01	19.25 ± 0.01	19.38 ± 0.03
J0816+2339	A	0.00 ± 0.02	0.00 ± 0.02	20.89 ± 0.01	20.60 ± 0.01	20.66 ± 0.01	20.48 ± 0.01	20.25 ± 0.02
	B	-1.35 ± 0.02	-1.42 ± 0.02	21.16 ± 0.01	20.84 ± 0.01	20.71 ± 0.01	20.71 ± 0.01	20.38 ± 0.02
J0818-2613	A	-2.75 ± 0.01	0.11 ± 0.01	18.55 ± 0.02	17.93 ± 0.01	17.52 ± 0.01	17.10 ± 0.01	17.08 ± 0.01
	B	-2.58 ± 0.01	-0.52 ± 0.01	18.51 ± 0.02	17.89 ± 0.01	17.45 ± 0.01	17.02 ± 0.01	17.01 ± 0.01
	C	1.81 ± 0.01	-4.15 ± 0.01	20.45 ± 0.01	19.91 ± 0.01	19.42 ± 0.01	19.02 ± 0.01	18.96 ± 0.0
	D	1.29 ± 0.01	1.41 ± 0.01	20.62 ± 0.01	20.13 ± 0.01	19.61 ± 0.01	19.16 ± 0.01	19.18 ± 0.01
	G	0.00 ± 0.04	0.00 ± 0.04	21.40 ± 0.08	19.93 ± 0.09	19.73 ± 0.06	18.56 ± 0.07	18.19 ± 0.07
J0826+7002	A	-3.30 ± 0.01	-0.90 ± 0.01	17.90 ± 0.01	17.86 ± 0.01	17.64 ± 0.01	17.86 ± 0.01	17.94 ± 0.01
	B	-1.77 ± 0.01	4.73 ± 0.01	19.34 ± 0.01	19.30 ± 0.01	19.21 ± 0.01	19.30 ± 0.01	19.40 ± 0.0
	G	0.00 ± 0.01	0.00 ± 0.01	20.79 ± 0.01	19.47 ± 0.02	18.96 ± 0.01	18.67 ± 0.01	18.44 ± 0.02
	G2	-3.65 ± 0.01	0.35 ± 0.01	19.45 ± 0.02	17.77 ± 0.01	17.42 ± 0.01	17.05 ± 0.01	16.73 ± 0.01
	G3	-4.87 ± 0.03	1.98 ± 0.02	21.78 ± 0.13	21.26 ± 0.19	20.63 ± 0.15	20.30 ± 0.22	20.17 ± 0.18
J0833+0331	A	0.00 ± 0.01	0.00 ± 0.01	20.13 ± 0.01	20.23 ± 0.01	19.76 ± 0.01	19.88 ± 0.01	19.84 ± 0.01
	B	-1.32 ± 0.01	-0.51 ± 0.01	20.87 ± 0.01	20.78 ± 0.01	20.31 ± 0.01	20.13 ± 0.01	19.97 ± 0.02
J0834-2933	A	-0.33 ± 0.01	-1.09 ± 0.01	19.81 ± 0.01	19.78 ± 0.01	19.70 ± 0.02	19.39 ± 0.03	19.69 ± 0.17
	B	0.56 ± 0.01	0.51 ± 0.01	20.43 ± 0.02	20.31 ± 0.04	20.01 ± 0.05	19.79 ± 0.06	—
	G	0.00 ± 0.02	0.00 ± 0.03	20.84 ± 0.07	19.61 ± 0.05	19.03 ± 0.05	18.74 ± 0.05	18.75 ± 0.07
J0904+3343	A	0.63 ± 0.01	-0.85 ± 0.01	20.59 ± 0.01	20.20 ± 0.01	19.80 ± 0.01	19.43 ± 0.01	19.23 ± 0.01
	B	-0.35 ± 0.01	0.19 ± 0.01	21.16 ± 0.03	20.57 ± 0.04	19.59 ± 0.03	19.31 ± 0.03	19.36 ± 0.04
	C	-7.12 ± 0.01	2.96 ± 0.01	20.51 ± 0.01	20.37 ± 0.01	20.12 ± 0.01	20.04 ± 0.01	19.91 ± 0.01
	G	0.00 ± 0.01	0.00 ± 0.01	20.61 ± 0.02	19.14 ± 0.01	18.87 ± 0.02	18.74 ± 0.02	18.30 ± 0.03
J0907+6224	A	1.46 ± 0.01	1.18 ± 0.01	19.69 ± 0.02	19.47 ± 0.02	18.90 ± 0.02	18.86 ± 0.02	18.78 ± 0.05
	B	-0.41 ± 0.01	-0.46 ± 0.01	20.51 ± 0.04	20.51 ± 0.04	19.94 ± 0.04	19.98 ± 0.06	20.01 ± 0.12
	G	0.00 ± 0.01	0.00 ± 0.01	21.51 ± 0.10	19.32 ± 0.03	18.49 ± 0.03	18.05 ± 0.03	18.02 ± 0.03
J0918-0220	A	1.72 ± 0.02	-0.08 ± 0.02	20.89 ± 0.01	20.90 ± 0.01	20.52 ± 0.01	20.47 ± 0.02	21.08 ± 0.04
	B	-0.41 ± 0.02	0.16 ± 0.02	21.60 ± 0.04	21.78 ± 0.19	20.73 ± 0.22	21.19 ± 0.31	19.81 ± 0.13
	G	0.00 ± 0.03	0.00 ± 0.03	21.99 ± 0.10	20.25 ± 0.06	19.65 ± 0.08	19.04 ± 0.05	19.59 ± 0.15
J0921+3020	A	1.72 ± 0.01	-1.87 ± 0.01	18.79 ± 0.01	18.57 ± 0.01	18.50 ± 0.01	18.50 ± 0.01	18.41 ± 0.01
	B	-0.41 ± 0.01	0.19 ± 0.01	21.55 ± 0.05	20.94 ± 0.07	20.96 ± 0.11	21.14 ± 0.17	20.98 ± 0.19
	G	0.00 ± 0.02	0.00 ± 0.01	20.98 ± 0.06	19.77 ± 0.05	19.03 ± 0.04	18.66 ± 0.05	18.45 ± 0.05
J0924+4235	A	2.24 ± 0.01	2.72 ± 0.01	19.96 ± 0.01	19.44 ± 0.01	19.54 ± 0.01	19.56 ± 0.01	19.45 ± 0.01
	B	-0.55 ± 0.01	-0.97 ± 0.01	21.57 ± 0.02	21.17 ± 0.02	20.82 ± 0.02	21.16 ± 0.04	20.92 ± 0.09
	G	0.00 ± 0.01	0.00 ± 0.01	20.39 ± 0.02	18.69 ± 0.01	17.92 ± 0.01	17.58 ± 0.01	17.42 ± 0.01
J0937+5835	A	-0.17 ± 0.02	-0.67 ± 0.03	21.06 ± 0.05	20.80 ± 0.03	20.85 ± 0.06	20.51 ± 0.06	—
	B	0.34 ± 0.02	0.70 ± 0.03	21.46 ± 0.06	21.19 ± 0.04	21.01 ± 0.07	20.70 ± 0.08	—
	G	0.00 ± 0.04	0.00 ± 0.06	21.76 ± 0.16	21.12 ± 0.07	20.23 ± 0.04	19.80 ± 0.04	19.29 ± 0.1
J0954-1421	A	-0.85 ± 0.01	-0.10 ± 0.01	19.73 ± 0.01	19.42 ± 0.01	19.65 ± 0.02	19.68 ± 0.03	19.79 ± 0.05
	B	0.55 ± 0.01	-0.14 ± 0.01	20.41 ± 0.01	20.12 ± 0.02	19.89 ± 0.03	19.81 ± 0.05	19.94 ± 0.09
	G	0.00 ± 0.05	0.00 ± 0.04	21.13 ± 0.07	20.61 ± 0.06	19.92 ± 0.05	19.02 ± 0.03	18.32 ± 0.06
J1003+0651	A	2.17 ± 0.01	0.28 ± 0.01	20.20 ± 0.01	19.97 ± 0.01	19.98 ± 0.01	19.89 ± 0.01	19.70 ± 0.01
	B	-0.14 ± 0.01	-0.03 ± 0.01	21.54 ± 0.08	20.48 ± 0.09	19.98 ± 0.08	19.32 ± 0.05	19.74 ± 0.1
	G	0.00 ± 0.01	0.00 ± 0.01	18.70 ± 0.01	17.59 ± 0.01	17.18 ± 0.01	17.07 ± 0.01	16.69 ± 0.01
	G2	3.78 ± 0.01	-1.09 ± 0.01	20.72 ± 0.03	19.57 ± 0.03	19.12 ± 0.03	18.93 ± 0.04	18.70 ± 0.04
J1008+0046	A	-0.08 ± 0.01	0.45 ± 0.02	20.96 ± 0.05	20.57 ± 0.06	20.47 ± 0.08	20.40 ± 0.09	20.95 ± 0.25
	B	0.15 ± 0.01	-0.84 ± 0.02	20.74 ± 0.02	20.47 ± 0.03	20.24 ± 0.03	20.35 ± 0.04	20.30 ± 0.07
	G	0.00 ± 0.02	0.00 ± 0.03	20.98 ± 0.08	19.86 ± 0.04	19.33 ± 0.03	19.07 ± 0.03	18.75 ± 0.03
J1008+0929	A	-0.20 ± 0.01	-1.51 ± 0.01	19.30 ± 0.01	19.01 ± 0.01	18.79 ± 0.01	18.72 ± 0.01	18.68 ± 0.01
	B	0.17 ± 0.01	0.37 ± 0.01	21.07 ± 0.03	20.65 ± 0.05	20.47 ± 0.10	20.51 ± 0.14	20.28 ± 0.11
	G	0.00 ± 0.02	0.00 ± 0.03	21.93 ± 0.13	20.98 ± 0.10	19.63 ± 0.06	18.96 ± 0.04	18.94 ± 0.04
J1025-2246	A	-1.16 ± 0.01	-3.30 ± 0.01	20.01 ± 0.01	19.95 ± 0.01	20.01 ± 0.01	19.76 ± 0.01	19.75 ± 0.01
	B	0.14 ± 0.01	0.46 ± 0.01	20.99 ± 0.01	21.04 ± 0.03	21.33 ± 0.16	20.57 ± 0.12	19.83 ± 0.08
	G	0.00 ± 0.06	0.00 ± 0.07	—	21.35 ± 0.09	19.73 ± 0.07	19.20 ± 0.07	20.11 ± 0.22
J1045+3433	A	0.04 ± 0.01	-0.86 ± 0.01	20.66 ± 0.02	20.37 ± 0.02	20.39 ± 0.01	20.57 ± 0.06	20.32 ± 0.07
	B	-0.45 ± 0.01	0.50 ± 0.01	20.87 ± 0.05	20.74 ± 0.04	20.81 ± 0.03	21.01 ± 0.14	—
	G	0.00 ± 0.10	0.00 ± 0.15	21.63 ± 0.11	21.96 ± 0.22	21.83 ± 0.13	20.63 ± 0.13	20.41 ± 0.19
J1102+3421	A	-0.45 ± 0.01	-0.29 ± 0.01	19.32 ± 0.01	19.77 ± 0.01	20.27 ± 0.02	19.20 ± 0.01	19.27 ± 0.01
	B	0.66 ± 0.01	0.34 ± 0.01	20.04 ± 0.01	20.16 ± 0.02	20.61 ± 0.03	19.49 ± 0.01	19.47 ± 0.01
	G	0.00 ± 0.02	0.00 ± 0.01	—	19.28 ± 0.01	19.10 ± 0.01	21.80 ± 0.15	—

J1137-1245	A	1.68 ± 0.01	0.80 ± 0.01	19.47 ± 0.01	19.51 ± 0.01	19.42 ± 0.01	19.20 ± 0.01	19.30 ± 0.01
	B	-0.47 ± 0.01	-0.26 ± 0.01	21.26 ± 0.02	20.86 ± 0.03	20.80 ± 0.05	20.19 ± 0.05	20.55 ± 0.08
	G	0.00 ± 0.02	0.00 ± 0.02	21.24 ± 0.04	20.71 ± 0.05	19.43 ± 0.03	19.13 ± 0.04	18.68 ± 0.04
J1206-2543	A	1.23 ± 0.01	0.68 ± 0.01	19.99 ± 0.01	19.88 ± 0.01	19.58 ± 0.01	19.64 ± 0.02	19.60 ± 0.01
	B	-0.71 ± 0.01	-0.09 ± 0.01	20.30 ± 0.02	20.35 ± 0.04	20.14 ± 0.05	20.47 ± 0.13	20.17 ± 0.09
	G	0.00 ± 0.04	0.00 ± 0.03	21.47 ± 0.14	20.65 ± 0.08	19.65 ± 0.07	19.10 ± 0.07	19.16 ± 0.07
J1209-1929	A	1.25 ± 0.01	0.06 ± 0.01	19.77 ± 0.01	19.66 ± 0.01	19.43 ± 0.01	19.52 ± 0.02	19.33 ± 0.01
	B	-0.21 ± 0.01	-0.01 ± 0.01	∼20.84	20.90 ± 0.42	∼20.68	∼20.68	∼20.32
	G	0.00 ± 0.26	0.00 ± 0.08	—	—	—	—	—
‘ J1233-0227	A	-0.37 ± 0.01	-1.03 ± 0.01	20.14 ± 0.01	19.92 ± 0.01	19.35 ± 0.01	19.40 ± 0.01	19.54 ± 0.02
	B	0.54 ± 0.01	0.43 ± 0.01	20.63 ± 0.02	20.10 ± 0.02	19.50 ± 0.02	19.28 ± 0.02	19.35 ± 0.02
	G	0.00 ± 0.03	0.00 ± 0.03	20.26 ± 0.05	19.10 ± 0.04	19.35 ± 0.06	18.89 ± 0.05	18.62 ± 0.05
J1237+3340	A	-0.43 ± 0.02	-0.98 ± 0.02	20.93 ± 0.01	21.20 ± 0.04	20.79 ± 0.04	21.35 ± 0.07	21.41 ± 0.17
	B	-0.09 ± 0.02	0.61 ± 0.02	21.63 ± 0.05	—	21.64 ± 0.20	20.96 ± 0.14	—
	G	0.00 ± 0.02	0.00 ± 0.03	22.25 ± 0.22	19.83 ± 0.04	19.10 ± 0.05	19.08 ± 0.04	18.44 ± 0.05
J1238+2846	A	-0.22 ± 0.01	1.54 ± 0.02	20.76 ± 0.01	20.62 ± 0.01	20.52 ± 0.01	20.49 ± 0.02	20.39 ± 0.02
	B	0.22 ± 0.01	-0.84 ± 0.02	20.71 ± 0.01	20.64 ± 0.01	20.47 ± 0.01	20.50 ± 0.03	20.09 ± 0.04
	G	0.00 ± 0.05	0.00 ± 0.07	—	22.08 ± 0.16	21.38 ± 0.15	20.28 ± 0.15	20.09 ± 0.12
J1255+0737	A	-0.15 ± 0.01	-1.18 ± 0.01	21.00± 0.01	20.82 ± 0.01	20.61 ± 0.02	20.11 ± 0.02	20.40 ± 0.04
	B	-0.39 ± 0.01	0.49 ± 0.01	21.70 ± 0.05	21.34 ± 0.05	20.94 ± 0.07	20.28 ± 0.06	20.39 ± 0.09
	G	0.00 ± 0.06	0.00 ± 0.09	21.89 ± 0.21	22.10 ± 0.25	20.88 ± 0.14	20.48 ± 0.16	19.89 ± 0.15
J1303+1816	A	-0.53 ± 0.01	-1.62 ± 0.01	22.30 ± 0.13	21.70 ± 0.12	21.10 ± 0.11	21.00± 0.11	20.75 ± 0.14
	B	-0.24 ± 0.01	0.58 ± 0.01	19.78 ± 0.05	19.26 ± 0.05	19.09 ± 0.05	18.90 ± 0.05	18.03 ± 0.05
	G	0.00 ± 0.02	0.00 ± 0.01	21.37 ± 0.05	19.86 ± 0.03	19.33 ± 0.07	19.23 ± 0.09	18.79 ± 0.03
J1307+0642	A	2.66 ± 0.01	-1.17 ± 0.01	20.39 ± 0.01	20.16 ± 0.01	20.03 ± 0.01	19.83 ± 0.01	19.83 ± 0.01
	B	-0.53 ± 0.01	0.29 ± 0.01	21.78 ± 0.05	21.24 ± 0.07	21.27 ± 0.09	20.88 ± 0.10	20.79 ± 0.17
	G	0.00 ± 0.01	0.00 ± 0.01	19.01 ± 0.01	17.58 ± 0.01	17.02 ± 0.01	16.75 ± 0.01	16.47 ± 0.01
J1326+3020	A	1.69 ± 0.01	-0.15 ± 0.01	20.55 ± 0.01	20.70 ± 0.01	20.26 ± 0.01	20.56 ± 0.02	20.64 ± 0.05
	B	-0.18 ± 0.01	-0.33 ± 0.01	22.66 ± 0.09	21.38 ± 0.09	20.66 ± 0.08	20.65 ± 0.12	20.41 ± 0.11
	G	0.00 ± 0.02	0.00 ± 0.02	20.10 ± 0.03	18.93 ± 0.01	18.52 ± 0.02	18.12 ± 0.02	18.01 ± 0.03
J1329-2807	A	1.45 ± 0.01	0.28 ± 0.01	19.57 ± 0.01	18.94 ± 0.01	18.90 ± 0.01	18.64 ± 0.01	18.58 ± 0.01
	B	-0.45 ± 0.01	-0.11 ± 0.01	20.70 ± 0.01	20.50 ± 0.06	20.42 ± 0.18	20.01 ± 0.13	19.91 ± 0.16
	G	0.00 ± 0.07	0.00 ± 0.04	—	21.26 ± 0.14	19.75 ± 0.08	19.62 ± 0.09	19.19 ± 0.09
J1344+6200	A	2.54 ± 0.01	2.51 ± 0.01	19.97 ± 0.01	19.97 ± 0.01	19.95 ± 0.01	19.65 ± 0.01	19.69 ± 0.01
	B	-0.67 ± 0.01	-0.55 ± 0.01	20.78 ± 0.01	20.74 ± 0.02	20.69 ± 0.03	20.46 ± 0.06	20.60 ± 0.11
	G	0.00 ± 0.02	0.00 ± 0.01	21.41 ± 0.05	20.03 ± 0.03	19.01 ± 0.03	18.38 ± 0.03	18.68 ± 0.03
J1408+0422	A	0.40 ± 0.02	1.90 ± 0.02	20.48 ± 0.01	20.30 ± 0.01	20.17 ± 0.01	20.30 ± 0.01	20.07 ± 0.02
	B	0.10 ± 0.02	-0.90 ± 0.02	21.65 ± 0.02	21.60 ± 0.04	21.93 ± 0.12	21.48 ± 0.08	21.61 ± 0.25
	G	0.00 ± 0.02	0.00 ± 0.03	—	20.82 ± 0.09	19.72 ± 0.08	19.51 ± 0.08	19.00± 0.09
J1418-1610	A	0.00 ± 0.01	0.00 ± 0.01	18.90 ± 0.01	18.57 ± 0.01	18.45 ± 0.01	18.64 ± 0.01	18.43 ± 0.01
	B	1.91 ± 0.01	1.47 ± 0.01	19.23 ± 0.01	18.92 ± 0.01	18.93 ± 0.01	18.88 ± 0.01	18.89 ± 0.0
J1428+0500	A	0.00 ± 0.01	0.00 ± 0.01	20.17 ± 0.02	19.91 ± 0.01	19.94 ± 0.02	19.86 ± 0.04	19.80 ± 0.09
	B	0.96 ± 0.01	2.01 ± 0.01	20.11 ± 0.02	20.03 ± 0.01	20.12 ± 0.02	19.96 ± 0.04	19.80 ± 0.08
J1515+3137	A	0.32 ± 0.01	-0.90 ± 0.01	20.41 ± 0.01	20.23 ± 0.03	19.84 ± 0.02	19.67 ± 0.02	19.69 ± 0.04
	B	-0.30 ± 0.01	0.49 ± 0.01	21.23 ± 0.05	21.09 ± 0.17	20.42 ± 0.13	20.27 ± 0.13	20.06 ± 0.18
	G	0.00 ± 0.03	0.00 ± 0.06	21.16 ± 0.07	19.87 ± 0.03	19.85 ± 0.06	19.46 ± 0.05	19.03 ± 0.06
J1518+4658	A	-0.31 ± 0.01	0.78 ± 0.01	19.86 ± 0.01	19.67 ± 0.01	19.72 ± 0.02	19.46 ± 0.03	19.29 ± 0.04
	B	-0.18 ± 0.01	-0.57 ± 0.01	21.15 ± 0.04	20.97 ± 0.08	21.08 ± 0.12	20.39 ± 0.09	20.73 ± 0.17
	G	0.00 ± 0.02	0.00 ± 0.03	21.61 ± 0.13	20.25 ± 0.05	19.56 ± 0.03	19.57 ± 0.07	19.25 ± 0.07
J1524+4801	A	-1.19 ± 0.02	-0.91 ± 0.01	21.08 ± 0.01	20.62 ± 0.01	20.05 ± 0.01	19.96 ± 0.01	19.67 ± 0.01
	B	0.83 ± 0.02	-0.00 ± 0.01	22.18 ± 0.07	21.77 ± 0.14	21.00± 0.06	20.77 ± 0.07	20.39 ± 0.07
	G	0.00 ± 0.02	0.00 ± 0.01	20.52 ± 0.03	19.26 ± 0.03	18.73 ± 0.03	18.53 ± 0.03	18.27 ± 0.07
J1526-1400	A	-1.54 ± 0.01	-0.78 ± 0.01	19.77 ± 0.01	19.46 ± 0.02	19.04 ± 0.01	19.00 ± 0.01	18.89 ± 0.01
	B	1.10 ± 0.01	-0.38 ± 0.01	20.26 ± 0.0	20.39 ± 0.03	19.37 ± 0.02	19.54 ± 0.04	19.38 ± 0.05
	G	0.00 ± 0.01	0.00 ± 0.01	17.25 ± 0.01	16.33 ± 0.01	16.02 ± 0.01	15.51 ± 0.01	15.4 ± 0.01
	G2	1.74 ± 0.01	-3.25 ± 0.01	18.44 ± 0.01	17.6 ± 0.01	17.32 ± 0.01	16.79 ± 0.01	16.75 ± 0.03
J1537-3010	A	-1.42 ± 0.01	-0.82 ± 0.01	20.16 ± 0.01	20.08 ± 0.01	19.79 ± 0.01	19.80 ± 0.02	19.65 ± 0.02
	B	0.52 ± 0.01	-1.07 ± 0.01	20.45 ± 0.02	20.38 ± 0.02	20.01 ± 0.03	20.02 ± 0.04	19.89 ± 0.05
	C	1.38 ± 0.01	0.90 ± 0.01	20.23 ± 0.01	20.24 ± 0.01	19.91 ± 0.01	19.89 ± 0.02	19.69 ± 0.02
	D	-0.76 ± 0.01	1.02 ± 0.01	21.24 ± 0.03	20.99 ± 0.03	20.65 ± 0.04	20.48 ± 0.05	20.45 ± 0.06
	G	0.00 ± 0.04	0.00 ± 0.06	20.63 ± 0.07	20.18 ± 0.07	19.35 ± 0.06	18.98 ± 0.06	18.78 ± 0.05
J1548-2914	A	0.60 ± 0.01	1.07 ± 0.01	18.81 ± 0.01	18.42 ± 0.01	18.04 ± 0.01	18.16 ± 0.01	18.41 ± 0.01
	B	-0.28 ± 0.01	-0.64 ± 0.01	20.55 ± 0.01	19.87 ± 0.02	19.37 ± 0.02	19.30 ± 0.03	19.37 ± 0.04
	G	0.00 ± 0.05	0.00 ± 0.05	—	19.51 ± 0.03	18.69 ± 0.03	18.38 ± 0.03	18.21 ± 0.02

J1550+0221	A	1.39 ± 0.01	-0.05 ± 0.01	18.64 ± 0.01	18.56 ± 0.01	18.47 ± 0.01	18.27 ± 0.01	18.18 ± 0.01
	B	-0.61 ± 0.01	-0.15 ± 0.01	20.81 ± 0.01	20.46 ± 0.01	20.17 ± 0.02	19.73 ± 0.01	19.93 ± 0.05
	G	0.00 ± 0.06	0.00 ± 0.03	21.04 ± 0.05	—	20.01 ± 0.09	—	18.73 ± 0.07
J1553+3149	A	-1.08 ± 0.01	-0.38 ± 0.01	18.54 ± 0.01	18.47 ± 0.01	18.30 ± 0.02	18.14 ± 0.02	18.06 ± 0.04
	B	0.37 ± 0.01	0.30 ± 0.01	19.55 ± 0.02	19.65 ± 0.02	19.38 ± 0.02	19.27 ± 0.03	19.12 ± 0.05
	G	0.00 ± 0.02	0.00 ± 0.02	21.18 ± 0.26	19.20 ± 0.05	18.61 ± 0.05	18.39 ± 0.05	18.32 ± 0.07
J1554+5817	A	0.00 ± 0.01	0.00 ± 0.01	19.02 ± 0.01	19.16 ± 0.01	18.69 ± 0.01	18.86 ± 0.01	18.99 ± 0.01
	B	-1.31 ± 0.01	0.47 ± 0.01	19.96 ± 0.01	19.84 ± 0.01	19.54 ± 0.01	19.63 ± 0.01	19.74 ± 0.01
J1612+3920	A	0.75 ± 0.01	1.74 ± 0.01	20.24 ± 0.01	20.09 ± 0.01	20.06 ± 0.01	19.95 ± 0.01	19.93 ± 0.01
	B	-0.44 ± 0.01	-0.72 ± 0.01	21.81 ± 0.04	21.89 ± 0.07	21.55 ± 0.06	21.41 ± 0.09	—
	G	0.00 ± 0.01	0.00 ± 0.01	19.26 ± 0.01	18.22 ± 0.01	17.87 ± 0.01	17.52 ± 0.01	17.36 ± 0.01
J1616+1415	A	-0.28 ± 0.01	-0.86 ± 0.01	20.10 ± 0.01	19.74 ± 0.01	19.60 ± 0.01	19.57 ± 0.02	19.45 ± 0.03
	B	0.35 ± 0.01	0.57 ± 0.01	20.59 ± 0.02	20.26 ± 0.01	20.07 ± 0.02	19.95 ± 0.04	19.86 ± 0.04
	G	0.00 ± 0.05	0.00 ± 0.08	21.16 ± 0.08	21.19 ± 0.06	20.70 ± 0.09	20.02 ± 0.07	19.53 ± 0.09
	G2	-2.11 ± 0.02	-3.86 ± 0.03	23.91 ± 0.08	22.16 ± 0.13	21.33 ± 0.23	20.77 ± 0.24	20.66 ± 0.27
J1623+7533	A	-0.64 ± 0.01	-1.07 ± 0.02	—	19.81 ± 0.01	19.73 ± 0.01	19.57 ± 0.01	—
	B	0.03 ± 0.01	0.63 ± 0.02	—	20.55 ± 0.03	20.68 ± 0.06	20.23 ± 0.06	—
	G	0.00 ± 0.02	0.00 ± 0.02	—	19.87 ± 0.04	19.27 ± 0.04	19.11 ± 0.04	—
J1627-0224	A	-0.86 ± 0.01	2.74 ± 0.01	19.72 ± 0.01	19.53 ± 0.01	19.13 ± 0.01	19.11 ± 0.01	19.02 ± 0.01
	B	0.75 ± 0.01	-0.66 ± 0.01	20.51 ± 0.01	20.32 ± 0.01	19.93 ± 0.01	19.95 ± 0.01	19.86 ± 0.02
	G	0.00 ± 0.01	0.00 ± 0.01	21.48 ± 0.05	20.09 ± 0.03	19.01 ± 0.03	18.54 ± 0.03	18.30 ± 0.03
J1653+5155	A	0.39 ± 0.01	-1.06 ± 0.01	20.06 ± 0.01	19.91 ± 0.01	—	20.09 ± 0.01	—
	B	-0.41 ± 0.01	0.25 ± 0.01	20.95 ± 0.01	20.64 ± 0.03	—	19.87 ± 0.03	—
	G	0.00 ± 0.02	0.00 ± 0.01	21.46 ± 0.03	20.10 ± 0.02	—	19.07 ± 0.02	—
J1817+2729	A	0.67 ± 0.01	0.42 ± 0.01	19.26 ± 0.01	18.87 ± 0.01	18.49 ± 0.01	18.47 ± 0.01	18.22 ± 0.03
	B	0.84 ± 0.01	-0.43 ± 0.01	22.41 ± 0.13	21.84 ± 0.12	21.57 ± 0.10	21.80 ± 0.30	21.16 ± 0.23
	C	-0.61 ± 0.01	-0.84 ± 0.01	20.35 ± 0.01	19.93 ± 0.01	19.60 ± 0.01	19.56 ± 0.01	19.29 ± 0.02
	D	-0.60 ± 0.01	0.64 ± 0.01	21.59 ± 0.05	20.82 ± 0.04	20.45 ± 0.04	20.30 ± 0.06	19.84 ± 0.06
	G	0.00 ± 0.03	0.00 ± 0.03	22.16 ± 0.21	20.58 ± 0.06	19.97 ± 0.05	19.44 ± 0.11	19.25 ± 0.15
J1949+7732	A	0.51 ± 0.01	-0.51 ± 0.01	18.96 ± 0.03	18.56 ± 0.03	18.82 ± 0.04	18.70 ± 0.05	18.73 ± 0.1
	B	-0.77 ± 0.01	0.44 ± 0.01	19.88 ± 0.02	19.69 ± 0.03	19.51 ± 0.04	19.31 ± 0.05	19.33 ± 0.09
	G	0.00 ± 0.02	0.00 ± 0.02	—	19.55 ± 0.10	18.98 ± 0.10	18.59 ± 0.09	18.32 ± 0.11
J2014-3024	A	0.00 ± 0.01	0.00 ± 0.01	19.14 ± 0.01	18.95 ± 0.01	18.72 ± 0.01	18.56 ± 0.04	18.23 ± 0.07
	B	1.00 ± 0.01	0.17 ± 0.01	19.49 ± 0.01	19.17 ± 0.01	19.03 ± 0.01	18.91 ± 0.04	18.91 ± 0.06
	C	2.18 ± 0.01	1.18 ± 0.01	19.36 ± 0.01	19.02 ± 0.01	18.86 ± 0.01	18.82 ± 0.03	18.54 ± 0.06
J2032-2358	A	0.00 ± 0.01	0.00 ± 0.01	19.48 ± 0.01	19.21 ± 0.01	18.86 ± 0.01	18.71 ± 0.03	18.84 ± 0.06
	B	1.91 ± 0.01	0.09 ± 0.01	19.80 ± 0.01	19.56 ± 0.01	19.25 ± 0.01	19.33 ± 0.02	19.44 ± 0.05
J2132+2603	A	0.83 ± 0.01	0.76 ± 0.01	19.43 ± 0.03	19.48 ± 0.02	19.44 ± 0.03	19.31 ± 0.04	18.87 ± 0.08
	B	-0.51 ± 0.01	-0.39 ± 0.01	20.63 ± 0.05	20.74 ± 0.04	20.61 ± 0.07	20.44 ± 0.09	20.01 ± 0.14
	G	0.00 ± 0.04	0.00 ± 0.04	21.30 ± 0.24	20.77 ± 0.13	19.75 ± 0.08	19.37 ± 0.08	19.01 ± 0.12
J2145+6345	A	0.00 ± 0.01	0.00 ± 0.01	17.79 ± 0.01	17.28 ± 0.01	16.71 ± 0.01	16.69 ± 0.01	16.54 ± 0.01
	B	0.33 ± 0.01	-0.56 ± 0.01	17.70 ± 0.01	17.04 ± 0.01	16.51 ± 0.01	16.46 ± 0.01	16.26 ± 0.01
	C	1.87 ± 0.01	-0.88 ± 0.01	18.82 ± 0.01	18.32 ± 0.01	17.82 ± 0.01	17.79 ± 0.01	17.52 ± 0.0
	D	1.37 ± 0.01	0.81 ± 0.01	19.14 ± 0.01	18.55 ± 0.01	18.08 ± 0.01	17.91 ± 0.01	17.72 ± 0.0
J2212+3144	A	0.00 ± 0.01	0.00 ± 0.01	19.60 ± 0.02	19.55 ± 0.01	19.17 ± 0.02	18.91 ± 0.03	19.18 ± 0.11
	B	-0.69 ± 0.01	2.56 ± 0.01	20.21 ± 0.01	20.19 ± 0.01	19.79 ± 0.01	19.82 ± 0.02	20.02 ± 0.09
J2250+2117	A	-1.48 ± 0.01	-0.16 ± 0.01	18.58 ± 0.01	18.32 ± 0.01	18.02 ± 0.01	18.13 ± 0.02	18.12 ± 0.05
	B	0.37 ± 0.01	0.04 ± 0.01	20.39 ± 0.02	19.87 ± 0.02	19.72 ± 0.04	19.96 ± 0.07	19.72 ± 0.11
	G	0.00 ± 0.05	0.00 ± 0.02	—	—	19.71 ± 0.09	19.07 ± 0.09	19.32 ± 0.18
J2316+0610	A	-1.41 ± 0.01	1.38 ± 0.01	20.35 ± 0.01	20.15 ± 0.01	19.95 ± 0.01	19.71 ± 0.01	19.96 ± 0.01
	B	0.37 ± 0.01	-0.06 ± 0.01	20.99 ± 0.02	20.70 ± 0.04	20.74 ± 0.09	20.32 ± 0.08	20.55 ± 0.2
	G	0.00 ± 0.02	0.00 ± 0.02	—	20.93 ± 0.07	19.81 ± 0.05	19.55 ± 0.05	19.40 ± 0.1
J2350+3654	A	-0.68 ± 0.02	-2.00 ± 0.02	21.17 ± 0.01	21.03 ± 0.01	20.82 ± 0.01	20.72 ± 0.01	20.77 ± 0.02
	B	1.14 ± 0.02	0.77 ± 0.02	21.40 ± 0.01	21.52 ± 0.04	21.10 ± 0.02	20.76 ± 0.03	21.19 ± 0.08
	C	-1.58 ± 0.02	0.44 ± 0.02	22.74 ± 0.04	22.80 ± 0.12	21.90 ± 0.04	21.79 ± 0.06	21.16 ± 0.06
	G	0.00 ± 0.02	0.00 ± 0.02	20.38 ± 0.01	18.96 ± 0.01	18.06 ± 0.01	17.72 ± 0.01	17.55 ± 0.01

Appendix B

Inconclusive/Contaminant Systems

Tables B.1 and B.2 list all inconclusive systems and contaminant systems, respectively, each with spectroscopic follow-up.

Table B.1 Inconclusive DES-selected candidates.

Name	R.A.	Dec.	spectrum	imaging	outcome
DESJ0149-6532	27.2900250	-65.5403840	EFOSC2	-	low flux, inconclusive
DESJ0428-2933	67.1001427	-29.5551883	EFOSC2	-	z=0.74? QSO + another? inconclusive
DESJ0451-2147	72.8056670	-21.7967430	EFOSC2	-	possible NIQ z=1.07? inconclusive

Table B.2 Spectroscopically confirmed DES contaminant systems.

Name	R.A.	Dec.	spectrum	imaging	outcome
DESJ0058-3947	14.5548610	-39.7899300	EFOSC2	SOAR	z=0.51 QSO + star
DESJ0343-3309	55.9238000	-33.1556000	EFOSC2	SOAR	z=1.58 QSO + star
DESJ0418-5722	64.7171719	-57.3698405	EFOSC2	-	z=2.02 QSO + other
DESJ0455-5412	73.9221950	-54.2067050	EFOSC2	SOAR	QSO (z=1.01?) + other
DESJ0512-1817	78.1131200	-18.2982970	ESI	-	z=0.343 emission line galaxies
DESJ0559-3428	89.8474080	-34.4721310	EFOSC2	SOAR	z=0.75 QSO + other
DESJ2047-4801	311.8620590	-48.0299640	EFOSC2	-	z=0.71 QSO + star
DESJ2332-4934	353.0429680	-49.5685220	EFOSC2	-	z=0.74 QSO + star